Universiteit Gent
Faculteit Wetenschappen
Vakgroep Vastestofwetenschappen

Magnetic resonance study of dopant related defects in X-ray storage phosphors

door

ir. Frank Loncke

Promotoren:

Prof. Dr. Freddy Callens
Prof. Dr. Paul Matthys

Proefschrift voorgelegd tot het behalen van de graad van

Doctor in de Wetenschappen : Fysica

Leden van de examencommissie

Voorzitter

Prof. Dr. Jan Ryckebusch (Ghent University, department of of Subatomic and Radiation Physics)

Leescommissie

Prof. Dr. Freddy Callens (Ghent University, department of Solid State Sciences)
Prof. Dr. Etienne Goovaerts (University of Antwerp, Physics departement)
Prof. Dr. Paul Matthys (Ghent University, department of Solid State Sciences)
Prod. Dr. Dirk Poelman (Ghent University, department of Solid State Sciences)

Overige leden van de examenjury

Dr. Paul Leblans (Agfa HealthCare NV)
Prof. Dr. Luc Van Hoorebeke (Ghent University, department. of Subatomic and Radiation Physics)
Prof. Dr. Ir. Henk Vrielinck (Ghent University, department of Solid State Sciences)


This research has been conducted at the EPR/ENDOR research group at the Departement of Solid State Sciences (Ghent University), in close collaboration with Agfa HealthCare NV (Mortsel)

Dankwoord

Dit werk is de wetenschappelijke vrucht van zes jaar assistentschap. Tijdens deze periode heb ik het genoegen gehad om met verschillende boeiende mensen samen te werken en ik zou hen bij deze graag kort willen bedanken.

In de eerste plaats, mijn promotoren Prof. Dr. Freddy Callens en Prof. Dr. P. Matthys. Dank je wel voor het vertrouwen, de kritische opmerkingen, het nalezen van schrijfsels,... Heel in het bijzonder wil ik Prof. Dr. Ir. Henk Vrielinck bedanken voor de dagelijkse begeleiding, hulp en supervisie.
Dank je wel aan Jean-Pierre Tahon, Paul Leblans, Luc Struye en Jens Lenaerts van Agfa HealthCare NV, voor de leuke interacties, verrijkende vergaderingen en vlotte medewerking aan mijn soms rare ingevingen.
Verder wil ik alle leden van de vakgroep Vastestofwetenschappen bedanken, in het bijzonder Marc, Nadine en Elly voor hun hulp in de administratieve UGent doolhof en Nico en Olivier voor hun technische bijstand bij computer- dan wel XRD/SEM-problemen.
Ik vergeet natuurlijk niet mijn partners-in-crime van de EPR/ENDOR groep : dank je wel aan Hendrik (zodat ik niet de flauwste grappenmaker was), Adela (om mij gezelschap te houden en Dmitry (for still not understanding Dutch).
Ik heb ongetwijfeld nog mensen vergeten te bedanken, de EPR mensen van Antwerpen bijvoorbeeld (onder leiding van Prof. Dr. E. Goovaerts en Prof. Dr. S. Van Doorslaer) die me steeds hielpen met de W band metingen, Chou, die me onvindbare artikels kon bezorgen, ...

Ik wil ook mijn familie en vrienden bedanken, die uit sympathie geregeld deden alsof mijn onderzoek hen interesseerde en dan eens vroegen hoever ik nu eigenlijk stond, met die platen.

Een grote dank je wel aan mijn ouders, aan wie ik alles te danken heb, voor hun onvoorwaardelijke steun aan en geloof in hun grote jongen.
En ten slotte, dank je wel aan mijn spiksplinternieuwe vrouw Griet, om mij simpelweg gelukkig te maken.

LIST OF ABBREVIATIONS

ν	frequency
ν_L	Larmor frequency
B	magnetic field
CCD	charge-coupled device
CE	conversion efficiency
CR	computed radiography
DFT	density functional theory
DR	direct digital radiography
EM	electromagnetic
ENDOR	electron-nuclear double resonance
EPR	electron paramagnetic resonance
ES	EasySpin
ESO	extended Stevens operators
FWHM	full width at half maximum
HF	hyperfine
IP	imaging plate
LED	light-emitting diode
LT	low temperature
MTF	modulation transfer function
MW	microwave
NIP	needle image plate
NMR	nuclear magnetic resonance
NN	nearest neighbour
NNN	next-nearest neighbour
PM	photomultiplier
P(S)L	photo(stimulated) luminescence
PVD	physical vapour deposition
RE	rare-earth

RF	radiofreqency
RT	room temperature
SE	stimulation energy
SH	spin Hamiltonian
SHF	superhyperfine
SO	spin operators
S/N	signal-to-noise
T	temperature
TL	thermoluminescence
TM	transition metal
V	vacancy
ZFS	zero field splitting

CONTENTS

SAMENVATTING

Wanneer men een kristal doteert met een vreemd ion, kan dit een enorme invloed hebben op zijn elektronische, optische, magnetische, ... eigenschappen. Het onderzoek naar dit soort defecten die deze eigenschappen karakteriseren, kent dan ook een lange en vruchtbare geschiedenis. Er werd hierbij gebruik gemaakt van verschillende spectroscopische technieken, waaronder elektronen paramagnetische resonantie (EPR) en elektronen nucleaire dubbele resonantie (ENDOR). Deze laatste zijn zeer geschikt voor het bestuderen van paramagnetische defecten met een lage concentratie. In deze doctoraatsthesis worden ze gebruikt voor de karakterisering van verscheidene ionen in X-stralen opslagfosforen, die o.a. gebruikt worden in de digitale radiografie.

Digitale beeldplaten kenden sinds hun ontdekking in het begin van de jaren 80 een groot succes. Ze vervingen al snel de traditionele natte-film technologie in de radiografie afdeling van veel ziekenhuizen. De actieve laag van een digitale beeldplaat is een X-stralen fosfor en wanneer deze bestraald wordt, worden stabiele defecten gecreëerd. De concentratie van deze defecten is evenredig met de ontvangen dosis en de defecten vormen zo het latente beeld in de plaat. Wanneer de defecten bestraald worden met licht met een bepaalde golflengte, recombineren de vrijgemaakte elektronen en gaten. Aangezien deze recombinatie gepaard gaat met de emissie van licht, wordt dit proces foto-gestimuleerde luminescentie (photostimulated luminescence, PSL) genoemd. De plaat kan zo pixelgewijs uitgelezen worden en men verkrijgt tenslotte het digitale beeld.

De eerste generatie digitale beeldplaten hadden als actieve laag een BaFBr:Eu^{2+} poeder, met een lage resolutie tot gevolg. Agfa-Gevaert NV ontdekte eind de jaren 90 de zogenaamde digitale naaldplaten en commercialiseerde ze in 2005. Deze bestonden uit een laag opgedampte CsBr:Eu^{2+} naaldkristallen, die alle loodrecht op het vlak van de plaat gericht staan. Intensief onderzoek heeft ervoor gezorgd dat de processen en de defecten in BaFBr:Eu^{2+} reeds goed gekend zijn. Dit is echter nog niet het geval voor de CsBr naaldplaten. In dit doctoraatswerk willen we, geïnspireerd door de successen behaald met EPR en ENDOR aan het BaFBr onderzoek, een bijdrage leveren aan het begrijpen van de defecten en processen die achter het opslag- en uitleesprocédé zitten.

In het begin van het onderzoek leverde de specifieke morfologie van de naaldplaten de nodige experimentele uitdagingen op. Daarom concentreerden we ons eerst op verpoederde naaldplaten, hoewel die ook typische problemen met zich meebrachten. Naarmate het onderzoek vorderde, werd het opdampprocédé geoptimaliseerd, wat langzaam aan leidde tot betere en reproduceerbare resultaten. Ondertussen werd ook begonnen met het onderzoek van andere X-stralen opslagfosforen : elpasolieten en K_2YF_5.
In hexagonale en kubische $Cs_2NaM^{III}F_6$ elpasolieten hebben we het Fe^{3+} ion gekarakteriseerd. Hoewel Fe^{3+} een onzuiverheid is zonder nuttige eigenschappen, bleek het uitstekend geschikt om de omgeving van het trivalente M^{III} kation te onderzoeken. In de kubische elpasolieten heeft de Fe^{3+} positie kubische symmetrie. In hexagonale kristallen kan het ijzer ion op twee plaatsen zitten, die beide beschouwd kunnen worden als een kubus die ofwel uitgerekt, ofwel ingedrukt werd langs een trigonale symmetrie as. We konden de tekens bepalen van alle EPR parameters, door gebruik te maken van 2D ENDOR en W band metingen bij (zeer) lage temperaturen. Deze ervaring bleek later van cruciaal belang bij de analyse van de naaldplaten. Onze resultaten kunnen gebruikt worden om het ijzerion sneller en beter te identificeren in de vele andere materialen waarin het als onzuiverheid voorkomt. De beschikbaarheid van EPR parameters van eenzelfde Fe^{3+} ion op drie zeer gelijkaardige plaatsen kan tevens benut worden als uitgangspunt voor of controle van theoretische berekeningen. Dit is reeds het geval met onze vroegere resultaten over Cr^{3+} gedopeerde elpasolieten.
De microscopische structuur van zeldzame aarden in K_2YF_5 kristallen wordt voornamelijk bepaald door de weinig voorkomende zevenvoudige F^- omringing van het trivalente kation. We konden aantonen dat zowel Gd^{3+} als Ce^{3+} monokliene symmetry vertonen. Hieruit leidden we af dat het kristalrooster een Pnam symmetrie heeft en hiermee beslechtten we definitief een discussie in de literatuur. Zverev *et al.* konden deze informatie recent al gebruiken als basis voor hun studie van stralingsgeïnduceerde defecten in K_2YF_5. De bepaling van de EPR parameters van Gd^{3+} was een eerste kennismaking met S = 7/2 systemen. Hoewel voor Gd^{3+} dezelfde spin Hamiltoniaan gebruikt wordt als voor Eu^{2+}, was de EPR analyse voor K_2YF_5:Gd^{3+} beduidend eenvoudiger: (i) de eenkristallen leverden angulaire variaties in drie vlakken, (ii) er is slechts één Gd^{3+} defect aanwezig en (iii) alle spectra konden opgemeten worden op kamertemperatuur.
Met de bekomen ervaring en de steeds beter wordende naaldplaten, konden de resultaten niet uitblijven. Algauw bleek dat het opdampen van de laag zorgde voor de aanwezigheid van defecten die niet in Bridgman gegroeide eenkristallen gevonden werden. Aangezien uit vroegere literatuur bleek dat water een voordelige invloed had op de gevoeligheid van de plaat, rijpte het idee dat water een

rol speelde in de vorming van deze defecten.
Bij kamertemperatuur konden we het tetragonale Eu^{2+} gerelateerde AA-EPR centrum detecteren. We bewezen dat de gevoeligheid van de plaat lineair correleert met de intensiteit van het EPR spectrum (en dus de concentratie van het defect). Met andere woorden, het AA-EPR centrum is van cruciaal belang voor de werking van de naaldplaat.
Met ENDOR metingen kan men de omgeving van een defect in kaart brengen. Hiervoor moet echter de temperatuur verlaagd worden, wat een drastische verandering in het EPR spectrum teweegbrengt. Analyse leerde dat het spectrum is opgebouwd uit de bijdrages van een tetragonaal (AA-EPR I) en een orthorhombisch (AA-EPR II) defect. Het is niet duidelijk of beide defecten transformeren tot AA-EPR dan wel of AA-EPR II (of enkel het bijhorende spectrum) verdwijnt bij hogere temperaturen.
Met de kennis van het EPR spectrum was het mogelijk de ENDOR spectra te analyseren. De specifieke morfologie van de platen speelde opnieuw een belemmerende rol in de analyse. In beide defecten werd er, naast de verwachte Eu interactie, ook een ^1H interactie waargenomen, die afkomstig is van waterstofkernen op ongeveer 3.3 Å van het Eu^{2+} ion verwijderd. De richting van de Eu-H binding is verschillend voor beide defecten: in AA-EPR I is deze binding lichtjes gedraaid ten opzichte van een <100> kristal as, terwijl de binding in AA-EPR II langs <110> gericht is. Momenteel hebben we nog geen allesverklarend model voor de AA-EPR-achtige defecten. Alles wijst er echter op dat water een stabiliserende invloed heeft op het Eu^{2+} ion. We veronderstellen dat de watermolecule kation vacatures opvult, zodat Eu^{2+} niet kan aggregeren.
Wanneer we de naaldplaten annealen op 300°C, kunnen deze watermolecules diffunderen en kunnen de Eu^{2+} ionen aggregeren tot $Cs_xEu_yBr_z$ microfases. Overannealen op 600°C zorgt ervoor dat het Eu^{2+} in een toestand komt die vergelijkbaar is met die van het eenkristal, waarin geen Eu^{2+} gerelateerd EPR signaal kan gedetecteerd worden.
X-bestraling met hoge doses vernietigt onomkeerbaar de AA-EPR-achtige defecten. We konden geen nieuwe defecten vinden na bestraling en/of belichting van de naaldplaten onder verschillende omstandigheden.

CHAPTER 1

INTRODUCTION

"Last time I got all the way through it, I got dehydrated."
— DR. N. CRANE

Doping a solid has a tremendous impact on its electronic, optical, structural and magnetic properties. Research on the related defects has a long established history and combines many different investigation methods. Among the most suitable methods to investigate paramagnetic defects with low concentrations in solids, are Electron Paramagnetic Resonance (EPR) and Electron Nuclear Double Resonance (ENDOR).
Since the early 1980s, digital imaging plates based on an X-ray storage phosphor layer, are in many hospitals rapidly replacing the conventional screen/film technology. When irradiating an X-ray phosphor, stable defects (latent image) are created, the concentration of which is correlated with the absorbed dose. When the defects are stimulated by light with an adapted wavelength, the released electrons and holes recombine accompanied by the emission of light. This process is called photostimulated luminescence (PSL). The plate can be read out pixel-by-pixel generating the X-ray image.
The traditional BaFBr:Eu^{2+} powder based plates suffer from a lack of resolution and in the early 1990s, physical vapour deposited (PVD) CsBr:Eu^{2+} needle image plates (NIPs) were proposed by Agfa-Gevaert NV to counter this problem. Whereas the defects in the BaFBr powder plate are by now well-known and understood, there still exists a lack of information about the defects involved in the working of the NIPs. In the present work we want to make a contribution to the elucidation of the physics behind the NIPs, in analogy with the successful EPR/ENDOR work on BaFBr:Eu^{2+}.
In the beginning of our PhD the partially ordered NIPs posed considerable experimental challenges and we first focussed on powdered NIPs although the latter also caused problems. E.g. there was some unknown underlying defect around

$g \approx 2$ and present in varying concentrations. Later, improved plate material gradually led to better and reproducible results.
In parallel, other X-ray storage phosphors became the subject of our interest. These materials appeared excellent 'teaching material' to gain experience and helped us later during the analysis of the NIP results. Our study on iron doped elpasolites showed e.g. that (i) 2D ENDOR can help unravelling complicated EPR/ENDOR spectra and that (ii) W band results are in several respects complementary to our Q band data ; e.g. the sign of spin Hamiltonian parameters could be determined and peaks inaccessible with the Q band setup, could be revealed. The work on Gd^{3+} doped K_2YF_5 introduced us in the study of $S = 7/2$ systems. Although the same spin Hamiltonian has to be used for both Gd^{3+} and Eu^{2+}, the EPR analysis of Gd^{3+} in K_2YF_5 was nonetheless simpler than for Eu^{2+} in NIPs : (i) single crystals were available, allowing full angular variations in three planes, (ii) only a single centre was present and (iii) all experiments could be performed at room temperature (RT).
Using plate material, we succeeded in analyzing the RT and low temperature spectra of the NIPs. At RT we found a tetragonal Eu^{2+} defect the concentration of which is closely related to the sensitivity of the plates. At low temperatures, two Eu^{2+} defects are present with a different symmetry. The specific morphology of the plates, however, complicated the ENDOR analysis and a definitive model could not be established. We could however demonstrate a positive influence of the presence of water during the PVD procedure on the plate sensitivity. Apparently, water prevents the Eu^{2+} ions in NIPs to decay to the same the state as in single crystals (which show no X-ray storage properties).

Structure of the thesis

In the next two chapters, details are given about both the theoretical (Chapter 2) and experimental background (Chapter 3) of this work. Chapter 4 deals with the work on iron doped elpasolites whereas Chapter 5 shows the results on rare-earth doped K_2YF_5. Chapter 6 contains the core of this PhD thesis : the study of Eu^{2+} doped CsBr NIPs. The first sections deal with the motivation for this study and contain an overview of the existing literature. In sections 6.5 to 6.9 our own EPR/ENDOR results are presented and discussed. The last chapter summarizes all results and provides an outlook to the future.

CHAPTER 2

ELECTRON PARAMAGNETIC RESONANCE

"This is boring, yet difficult."
— DR. N. CRANE

In this chapter we give an introduction on the theoretical aspects of *electron paramagnetic resonance* (EPR). Also the terms *EMR* (electron magnetic resonance) and *ESR* (electron spin resonance) are sometimes used in the literature, but EMR can strictly speaking also refer to, for example, (anti)ferromagnetic resonance ((A)FMR). The name ESR originates from the work on free radicals, where the electron magnetic moment is solely due to the electron spin of the unpaired electron(s), the orbital angular momentum being totally quenched. We chose to use the term EPR, which encompasses ESR, but is not so general as EMR. More detailed information about EPR, both from a practical and a theoretical point of view, abounds in various textbooks, e.g. [1, 2, 3, 4, 5].

2.1 PREHISTORY OF EPR

Classically, electrons are moving charges around a nucleus. They possess angular momentum and accordingly a *magnetic moment*. The magnetic moment of one electron (with mass m_e and charge -e) can be classically calculated to be

$$\vec{\mu} = -\frac{e}{2m_e}\vec{l} \tag{2.1}$$

with $\vec{l}$ its orbital momentum $\vec{l} = \vec{r} \times \vec{p}$.
In 1897, *Zeeman* [6] discovered the Zeeman effect : certain spectral lines can split into several components in the presence of a static magnetic field .
In 1913 the first successful quantum theory of atomic structure was developed by *Niels Bohr* [7]. In this article he combined successfully the atomic model of

Rutherford with the quantum theory on radiation of Planck [1]. He developed this theory for one-electron atoms from four postulates, from which one [2] reads

> Instead of the infinity of orbits which would be possible in classical mechanics, it is only possible for an electron to move in an orbit for which its orbital angular momentum l is an integral multiple of $\hbar(=\frac{h}{2\pi})$.

In 1921, Otto Stern suggested that magnetic moments of atoms could be measured by detecting the deflection of an atomic beam by an inhomogeneous magnetic field, with the field gradient perpendicular to the incoming beam. Such an experiment was carried out in 1922 by *Stern and Gerlach* [9]. The experiment was carried out with a beam of silver atoms from a hot oven which were deposited on a glass substrate. The silver atoms allowed Stern and Gerlach to study the magnetic properties of a single electron because these atoms have a single outer electron which moves in the Coulomb potential caused by the 47 protons of the nucleus shielded by the 46 inner electrons. Since this electron has zero orbital angular momentum, one would expect there to be no interaction with an external magnetic field. They observed that the beam splits up in two discrete components, instead of the classically expected continuous spectrum. The quantization of the magnetic moment of the atoms, postulated by Bohr, explains the discrete levels, while the even number of levels indicates that half-integer values of angular momentum must exist.
In 1925, *Uhlenbeck and Goudsmit* [10] postulated the existence of a new intrinsic property of particles that behaved like an angular momentum, as a means of correctly explaining the results of Stern and Gerlach. This intrinsic property, which has a value of $\frac{\hbar}{2}$ was later termed *spin* by Pauli, however, the image of a spinning sphere is not likely an accurate one. This new property needs to be viewed as an intrinsic property like mass and charge that is typical to a given type of particle. Note that, unlike mass and charge, there is no classical analogue to spin.
In 1944 Yevgeny K. Zavoisky [11] detected at the Kazan State University for the first time *electron paramagnetic resonance* (EPR) absorption in paramagnetic sub-

[1] For more information about the early days of quantum theory, see e.g. [8]

[2] The other three postulates are :

1. An electron in an atom moves in a circular orbit about the nucleus under the influence of the Coulomb attraction between the electron and the nucleus, obeying the laws of classical mechanics.

2. Despite the fact that it is constantly accelerating, an electron moving in such an allowed orbit does not radiate electromagnetic energy. Thus, its total energy E remains constant.

3. Electromagnetic radiation is emitted if an electron, initially moving in an orbit of total energy E_i, discontinuously changes its motion so that it moves in an orbit of total energy E_j. The frequency of the emitted radiation ν is equal to the quantity (E_j - E_i) divided by Planck's constant (h).

stances. In his experiments, he used manganese and copper sulfates. It is worth [12] to mention another effort of Zavoisky which preceded his discovery of EPR. In 1940 he started a project to measure the nuclear magnetic resonance (NMR) phenomenon. In May 1941 he observed proton magnetic resonance, but he failed to detect a reproducible signal. Presumably he could not obtain the homogeneous magnetic field required for NMR experiments.

2.2 Introduction to EPR : the Zeeman effect for a free electron

The magnetic moment $\vec{\mu}_e$ of the free electron, associated with the intrinsic spin of the electron, interacts with an externally applied magnetic field $\vec{B}$ and the energy of this magnetic dipole is given by the classical expression :

$$E = -\vec{B} \cdot \vec{\mu}_e \tag{2.2}$$

Quantum-mechanically one has to replace $\vec{\mu}_e$ with the corresponding operator[3] :

$$\hat{\vec{\mu}}_e = -g_e \beta_e \hat{\vec{S}} \tag{2.3}$$

with $\beta_e = \frac{e\hbar}{2m_e}$ the Bohrmagneton and $g_e = 2.0023...$, the g value for the free electron. The corresponding Hamiltonian

$$\hat{H} = g_e \beta_e \vec{B} \cdot \hat{\vec{S}} \tag{2.4}$$

becomes

$$\hat{H} = g_e \beta_e B \hat{S}_z \tag{2.5}$$

when the magnetic field is along the z axis ($\vec{B} = B\vec{e_z}$). The corresponding eigenvalues are

$$E(|M_S = \frac{1}{2} >) = \frac{1}{2} g_e \beta_e B \tag{2.6}$$

$$E(|M_S = -\frac{1}{2} >) = -\frac{1}{2} g_e \beta_e B \tag{2.7}$$

In figure 2.1 we have depicted the change of the energy eigenvalues as a function of the magnetic field. When this two level system is placed in a electromagnetic (EM) field with frequency ν, a magnetic dipole transition can occur if the energy of the energy quantum $h\nu$ satifies the following resonance condition :

$$h\nu = \Delta E = g_e \beta_e B \tag{2.8}$$

[3] $\hbar\hat{\vec{S}} = \hat{\vec{s}}$, so $S = \frac{1}{2}$

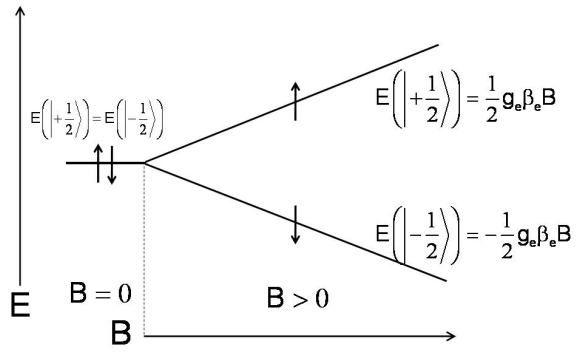

Figure 2.1. The Zeeman effect of a free electron.

When B varies between 0.1 T and 10 T (this range can be obtained with commercially available magnets), these transitions lie in the microwave (MW) range of the EM spectrum. The absorption spectrum can be obtained in two different ways: one could change the MW frequency and keep the magnetic field constant, or one could keep the MW frequency constant and vary the magnetic field. Because of technical reasons (see section 3.2) the latter procedure is applied.

2.3 ATOMIC DEFECTS IN LATTICES : A QUANTUM-MECHANICAL DESCRIPTION

Generally, both an impurity ion and an intrinsic deviation from the perfect lattice structure are considered as defects in a solid. Here, the description will be restricted to the first kind, since impurity ions are the main topic of this work. An ion is basically a charged atom, and consists of a (positively charged) nucleus surrounded by electrons. These electrons fill electronic shells and the outermost shell contains the valence electrons.
Several approximations are needed to describe quantum-mechanically an atom in a crystalline environment. The Born-Oppenheimer approximation eliminates the nuclear degrees of freedom, i.e. the nuclei are assumed to be fixed on the time scale of electron motions. A further simplication is restricting the quantum-mechanical description to the valence electrons, assuming them to be present in the mean field of the central nucleus and closed shell core electrons. Another assumption is that the interaction of the defect with the crystal lattice can be accounted for by introducing a crystal potential.
The Hamiltonian $\hat{H}$ describing an atom with nuclear charge $+Ze$ and N valence electrons in a homogeneous magnetic field $\vec{B}$, then [13] consists of the following contributions. We ordered them with decreasing magnitude in case of rare earth

ions[4].

The kinetic energy of the valence electrons

$$\hat{H}_{\text{kin}} = -\sum_{i=1}^{N} \frac{\hbar^2}{2m_{\text{e}}} \nabla_i^2 \tag{2.9}$$

The Coulomb attraction between the nucleus and the valence electrons

$$\hat{H}_{\text{Coul1}} = -\sum_{i=1}^{N} \frac{Ze^2}{4\pi\epsilon_0 r_{\text{i}}} \tag{2.10}$$

The Coulomb repulsion between the core electrons and the valence electrons

$$\hat{H}_{\text{Coul2}} = \sum_{i=1}^{N} \hat{U}(\vec{r}_{\text{i}}) \tag{2.11}$$

The electron-electron repulsion originating from the Coulomb repulsion between the electrons mutually

$$\hat{H}_{\text{e-e}} = \sum_{i>j}^{N} \frac{e^2}{4\pi\epsilon_0 r_{\text{ij}}} \tag{2.12}$$

This Hamiltonian is usually split into a maximal spherically symmetrical part and a minimal non-spherical interaction part :

$$\hat{H}_{\text{e-e}} = \hat{H}_{\text{e-e,SS}} + \hat{H}_{\text{e-e,NS}} \tag{2.13}$$

The spin-orbit coupling of the individual valence electrons[5]

$$\hat{H}_{\text{SO}} = \sum_{i=1}^{N} \xi(r_{\text{i}}) \hat{\vec{L}}_{\text{i}} \cdot \hat{\vec{S}}_{\text{i}} \tag{2.14}$$

The spin-spin interaction $\hat{H}_{\text{SS}}$ between the magnetic moments of the valence electrons

The crystal field potential which represents the Coulomb interaction between the valence electrons and the lattice ions

$$\hat{H}_{\text{CF}} = \sum_{i=1}^{N} \hat{V}_c(\vec{r}_i) \tag{2.15}$$

[4]The relative size of crystal field depends and can vary several orders of magnitude. Here we assumed a *weak* crystal field, which is the case for rare earth ions.

[5]$\hbar\hat{\vec{L}} = \hat{\vec{l}}$

Its explicit form depends on the local symmetry, characterized by the point-symmetry group. The *crystalline field approximation* where only the electrostatic interaction between the defect and its neighbours (simplified to point charges) is considered, leads to good qualitative results since such an approximation imposes the correct symmetry to the system. For quantitative calculations, also covalent bonding should be taken into account.

The electron Zeeman interaction of the valence electrons with the external magnetic field

$$\hat{H}_{\mathrm{EZ}} = \sum_{i=1}^{N} \beta_{\mathrm{e}} \vec{B} \cdot (\hat{\vec{L}}_{\mathrm{i}} + g_{\mathrm{e}} \hat{\vec{S}}_{\mathrm{i}}) \tag{2.16}$$

The hyperfine (HF) interaction reflecting the interaction between the magnetic moments of the valence electrons with the nuclear spin I, when $I \neq 0$

$$\hat{H}_{\mathrm{HF}} = \sum_{i=1}^{N} \hat{H}_{\mathrm{magn}}(\vec{r}_{\mathrm{i}}, \hat{\vec{S}}_{\mathrm{i}}, \hat{\vec{I}}) \tag{2.17}$$

The superhyperfine (SHF) interaction describing the interaction between the magnetic moments of the valence electrons with the nuclear spin I_{n} of the neighbouring nuclei, when $I_{\mathrm{n}} \neq 0$.

$$\hat{H}_{\mathrm{SHF}} = \sum_{n} \sum_{i=1}^{N} \hat{H}_{\mathrm{magn}}(\vec{r}_{\mathrm{i}}, \hat{\vec{S}}_{\mathrm{i}}, \hat{\vec{I}}_{\mathrm{n}}) \tag{2.18}$$

The nuclear quadrupole interaction which arises from the finite extension and aspherical shape of the nuclear charge distribution of each interacting nucleus with $I_{\mathrm{n}} > \frac{1}{2}$

$$\hat{H}_{\mathrm{Q}} = \sum_{n} \hat{H}_{\mathrm{Q,n}} \tag{2.19}$$

The nuclear Zeeman interaction expressing the effect of the external magnetic field on the nuclear magnetic moment I_{n} of the neighbouring nuclei, when $I_{\mathrm{n}} \neq 0$

$$\hat{H}_{\mathrm{NZ}} = \sum_{n} \hat{H}_{\mathrm{NZ,n}} \tag{2.20}$$

To understand the electronic structure of an atom, we will sequentially examine the effects of the largest terms. In the *central field approximation* the Hamiltonian consists of the first three terms plus the spherical symmetric part of $\hat{H}_{\text{e-e}}$:

$\hat{H}_0 = \hat{H}_{\text{kin}} + \hat{H}_{\text{Coul1}} + \hat{H}_{\text{Coul2}} + \hat{H}_{\text{e-e,SS}}$. Then, a non-spherical perturbation is applied (non-spherical part of $\hat{H}_{\text{e-e}}$: $\hat{H}_{\text{e-e,NS}}$). In the undisturbed system, the multi-electron problem (again, only considering the valence electrons) is reduced to a sum of one-electron problems and the eigenstates are anti-symmetric linear combinations of one-electron wave functions, the so-called Slater determinants. A specific distribution of the valence electrons over one-electron wave functions or orbitals is called an electron *configuration*. The non-spherical part of $\hat{H}_{\text{e-e}}$ couples the individual L_{i}'s and S_{i}'s to a total L and S. This coupling scheme is called the Russell-Saunders coupling. The allowed combinations of the operators $\hat{L}$ and $\hat{S}$ are called *terms* and labelled as ${}^{2S+1}L$. The total energy[6] of the lowest configuration is generally about 10^{15} Hz lower than that of the next configuration, while the energy separations between different terms is about 10^{14} Hz.
$\hat{\vec{L}}$ and $\hat{\vec{S}}$ are coupled via $\hat{H}_{\text{SO}}$ to the total momentum $\hat{\vec{J}}$. Since L and S are good quantum numbers for a term and since only matrix elements between wave functions for a single term are needed in the lowest-order perturbation approach, (2.14) can be replaced by $\hat{H}_{\text{SO}} = \lambda \hat{\vec{L}} \cdot \hat{\vec{S}}$. J can take up values $J = L + S, L + S - 1, ..., |L - S|$ and J states are $(2J + 1)$ degenerate. The energy difference between the ${}^{2S+1}L_J$ states is typically around 10^{13} Hz and the ground state is found via Hund's rules[7]. The spin-spin interaction $\hat{H}_{\text{SS}}$ is about 2 orders of magnitude smaller than $\hat{H}_{\text{SO}}$ and produces no additional splitting of the J-states.
The remaining interactions, including the weak crystal field, are much smaller and can cause further splitting of the ground state.

2.4 The spin Hamiltonian formalism

Even in the approximated picture, sketched in the previous section, the solution of the complete Schrödinger equation of a defect in a crystalline matrix, is too complicated to be used for analyzing EPR spectra, all the more since the relative size of the contributions are dependent of the specific case (host, dopant and magnetic field).
In a typical EPR experiment, the energy differences between states which can be overcome via MW radiation, will not exceed 300 GHz (custom-built high-

[6] In this work all EPR parameters (except g which is dimensionless) will be expressed in MHz so we preferred to use Hz as energy unit. A transformation table for energy units can be found in Appendix B on page 163

[7] Hund's rules to find the term ${}^{2S+1}L_J$ with the lowest energy :
(i) S maximal
(ii) L maximal
(iii) $J = |L - S|$ for (less then) half-filled shells or $J = L + S$ for more than half-filled shells

frequency spectrometers). Consequently, in thermal equilibrium we can confine ourselves to the states coming from the splitting of the degenerate ground state. It is common practice to use a so-called *spin Hamiltonian (SH)* for the analysis of EPR spectra : an effective Hamiltonian which only contains (electron and nuclear) spin interactions, characterized by one or more coupling coefficients, called *spin-Hamiltonian parameters*. These parameters contain information about not only the ground state and can be used as starting point for theoretical calculations.

The concept [14] of a spin-Hamiltonian was originally proposed by Van Vleck [15, 16] (in 1939-40, thus before the first EPR experiment) and Pryce [17]. Pryce's approach was based on perturbation calculations applied to the lowest orbital singlet well separated from the next excited state within the ground state multiplet, ^{2S+1}L, of an iron group ($3d^n$) ion in a paramagnetic crystal, split by $\hat{H}_{\mathrm{CF}}$ (2.15). The SH has now become a basic theoretical concept for explaining spectra not only in EPR but also in other experimental techniques, like nuclear magnetic resonance, Mössbauer spectroscopy, optical absorption, ...

When a certain number of energy levels is regarded as an isolated set, an effective electron-spin operator, $\vec{S^*}$, is introduced so that exactly $2S^* + 1$ electronic energy levels are obtained. Furthermore, all interactions with surrounding nuclei should be included in the SH, so the SH describes a system of $(2S^* + 1)\prod_j (2I_j + 1)$ levels. The SH parameters are determined by demanding that the energy levels of the real, complete Hamiltonian are reproduced. Mixing of the 'isolated' set of energy levels with higher-lying states (by interactions that are not explicitly considered in the spin Hamiltonian) make the SH parameters diverge from the values they would have if the system really was isolated.

The effective electron-spin operator, $\vec{S^*}$, is expressed in a certain *reference frame* and in solids this reference frame is often the crystal lattice. This means that for a cubic crystal, for example, $\hat{S}^*_x$, $\hat{S}^*_y$ and $\hat{S}^*_z$ are projections of $\vec{S^*}$ on the three [100] crystal axes.

Sometimes a SH parameter can be understood as an expectation value (energy) of the full Hamiltonian operating on the orbital part of the electronic ground state wave function, in which case the spin operator corresponds to a true (physical) spin operator. In general, however, the SH parameters do not have a direct physical interpretation related to the ground state alone. Their values can then only indirectly yield information about physically relevant parameters (e.g. via perturbation theory) and the operators are *effective* operators.

For the sake of simplicity, we will further on simply adopt the notation S for the effective spin and $\hat{H}$ for the effective spin Hamiltonian.

2.5 THE SPIN HAMILTONIAN

In the most general form [13], the terms of $\hat{H}$ have the form $A_{ijk}\vec{B}^i\hat{\vec{S}}^j\hat{\vec{I}}^k$, but a lot of these terms have no physical meaning. The coefficients i, j and k must obey certain restrictions due to various space and time symmetry requirements. Time reversal, e.g., imposes i+j+k=even.
In this work, the following SH will be used, in which all terms do have a direct physical interpretation

$$\hat{H} = \hat{H}_{EZ} + \hat{H}_{ZFS} + \hat{H}_{HF} + \hat{H}_{NZ} + \hat{H}_{Q} \tag{2.21}$$

The various terms will be briefly discussed in the following subsections.

2.5.1 The electron Zeeman interaction

The first term in (2.21) describes the interaction of the external magnetic field $\vec{B}$ with the (effective) spin $\hat{\vec{S}}$:

$$\hat{H}_{EZ} = \beta_e \vec{B} \cdot \bar{\bar{g}} \cdot \hat{\vec{S}} \tag{2.22}$$

$\bar{\bar{g}}$ is assumed to be a symmetrical tensor and differs from g_e in (2.3) since the spin-orbit coupling has to be taken into account. The components can be calculated by evaluating (2.16) in the effective spin multiplet.

2.5.2 The zero field splitting

$\hat{H}_{ZFS}$ influences only systems with $S > \frac{1}{2}$. Its physical origin is the influence of the electrical crystal field felt by the spins through the spin-orbit interaction as well as the magnetic dipole-dipole interaction between the unpaired electrons. This leads to a splitting of the energies in zero magnetic field, called the *zero field splitting*, or alternatively the *fine-structure splitting*.
One should take great care not to mix up $\hat{H}_{ZFS}$ from the (effective) SH in (2.21) and $\hat{H}_{CF}$ from (2.15) on page 11. In literature [14, 18], there exists a lot of confusion between both Hamiltonians although they differ in several important aspects. Crystal field splitting in (2.15) (sometimes also called fine structure splitting) refers to the effect of the electrostatic potential of neighbouring ions on the p, d or f valence electron levels of the central ion. It results in a lifting of the degeneracy of the ^{2S+1}L many electron levels, which may be observed in optics as fine structure on the transitions between such levels. Moreover, both Hamiltonians apparently take the same form, both being expressed in terms of, e.g., Extended Stevens Operators (ESO, see further). Hence, the ZFS in EPR is very often called crystal field

splitting, although there is a clear distinction. Indeed, crystal field splitting is the direct, first order effect of the crystal potential, acting on the orbital momentum of the valence electrons, whereas ZFS is an indirect, second order effect. It acts on the effective spin ground state (orbital momentum zero) by mixing in higher excited states through spin orbit coupling.

The principal directions of $\hat{H}_{\text{ZFS}}$ correspond to the reference frame axes

For paramagnetic systems with $S < 2$,

$$\hat{H}_{\text{ZFS}} = \hat{\vec{S}} \cdot \bar{\bar{D}} \cdot \hat{\vec{S}} \tag{2.23}$$

$\bar{\bar{D}}$ is traceless ($D_{\text{x}} + D_{\text{y}} + D_{\text{z}} = 0$) and vanishes if the defect has perfect cubic symmetry. For defects with *axial* symmetry, a single parameter D describes the axial distortion, and orthorhombic symmetries introduce an extra term E. When expressing (2.23) in terms of D and E we get :

$$\begin{aligned}
\hat{H}_{\text{ZFS}} &= \hat{\vec{S}} \cdot \begin{bmatrix} D_{\text{x}} & 0 & 0 \\ 0 & D_{\text{y}} & 0 \\ 0 & 0 & D_{\text{z}} \end{bmatrix} \cdot \hat{\vec{S}} \\
&= \hat{\vec{S}} \cdot \begin{bmatrix} -\frac{1}{3}D + E & 0 & 0 \\ 0 & -\frac{1}{3}D - E & 0 \\ 0 & 0 & \frac{2}{3}D \end{bmatrix} \cdot \hat{\vec{S}} \\
&= D(\hat{S_{\text{z}}}^2 - \frac{1}{3}S(S+1)) + E(\hat{S_{\text{x}}}^2 - \hat{S_{\text{y}}}^2)
\end{aligned} \tag{2.24}$$

For $S \geq 2$ terms in $\vec{S}_i^4 (i = x, y, z)$ should also be included and for axial symmetries $\hat{H}_{\text{ZFS}}$ expands to

$$\begin{aligned}
\hat{H}_{\text{ZFS}} &= \hat{\vec{S}} \cdot \bar{\bar{D}} \cdot \hat{\vec{S}} \\
&+ \frac{a}{6}\left[\hat{S_{\text{x}}}^4 + \hat{S_{\text{y}}}^4 + \hat{S_{\text{z}}}^4 - \frac{1}{5}S(S+1)(3S^2+3S-1)\right] \\
&+ \frac{F}{180}\left[35\hat{S_{\text{z}}}^4 - (30S(S+1)-25)\hat{S_{\text{z}}}^2 - 6S(S+1) + 3S^2(S+1)^2\right]
\end{aligned} \tag{2.25}$$

with $\bar{\bar{D}} = 0$ and $F = 0$ in cubic fields. For lower than axial symmetries extra terms should be included.
For $S \geq 3$ terms in $\vec{S}_i^6 (i = x, y, z)$ should also be included.

Expressions like (2.25) can be found by calculating the crystal potential arising from the Coulomb attraction from the neighbouring nuclei up to a certain order, as nicely illustrated in [1].

The principal directions of $\hat{H}_{\text{ZFS}}$ do not correspond to the reference frame axes

When the ZFS tensor is tilted with respect to the defect frame, things get more complicated. When $S < 2$, this can be solved by rotating the $\bar{\bar{D}}$ tensor : if $[R]$ is the rotation matrix from axes system 1 to axes system 2, than $\bar{\bar{D}}_2 = [R]\,\bar{\bar{D}}_1\,[R]^{\text{T}}$. For higher spin systems, however, the solution is not that simple and extra terms should be included.

In general, for lower symmetries and high spin, $\hat{H}_{\text{ZFS}}$ counts many higher order terms in $\hat{S}_i (i \in \{x, y, z\})$ and it is convenient to group such terms into combinations of spin operators, each such operator being the equivalent of a combination of spherical harmonics. This has the advantage that the appropriate SH can generally be written down without detailed calculation, since it must reflect the symmetry of the crystal field. If the latter has trigonal symmetry, for example, it is only necessary to include the spin operators corresponding to spherical harmonics with threefold or higher symmetry about the trigonal axis. The number of such spin operators is further limited by the more general restriction that ZFS spin operators of odd order are excluded because they are not invariant under time reversal (see section 2.5). Also operators of order higher than $2S$ can be omitted since they only cause a general shift of all levels.

Several different operators were defined in such way, e.g. the extended Stevens operators (ESO)[8] $\hat{O}_k^q$, the normalized Stevens operators $\hat{\hat{O}}_k^q$ and the Buckmaster & Smith-Thornly operators $\hat{O}_l^{\pm m}$. These different operators and corresponding parameters in $\hat{H}_{\text{ZFS}}$ are used higgledy-piggledy, resulting in a lot of confusion and problems when comparing literature coming from different sources (see e.g. [21, 22]). Effort has been made to compile and standardize results, e.g. for rare-earth centres in various crystals by Rudowicz and Madhu [23].

In this work and in our articles, we chose to use the *extended Stevens operators* $\hat{O}_k^q$, so that

$$\hat{H}_{\text{ZFS}} = \sum_k \sum_{-k \le q \le k} B_k^q \hat{O}_k^q \tag{2.26}$$

since in the literature, the ESO are the most common ones. Moreover, in EasySpin, the program we use for simulating and fitting spectra (see section 3.1 on page 27 and in Appendix A), the ESO are preprogrammed and can be readily introduced in programs.

[8] The prefix 'extended' comes from the fact that the matrix elements for $q < 0$ only were defined much later than the original paper from Stevens [19], see e.g. [20]

The extended Stevens operators

$\hat{O}_k^q$ is a linear combination of terms up to the k-th order in S and $\hat{S}_i (i \in \{x, y, z\})$. Their explicit form can be found in [4, 24][9]. The explicit form of the ESOs for $k = 2, 4$ with $q \geq 0$ are

$$\begin{cases} \hat{O}_2^0 = & 3\hat{S}_z^2 - S(S+1) \\ \hat{O}_2^1 = & \frac{1}{4}\left(\hat{S}_z\left(\hat{S}_+ + \hat{S}_-\right) + \left(\hat{S}_+ + \hat{S}_-\right)\hat{S}_z\right) \\ \hat{O}_2^2 = & \frac{1}{2}\left(\hat{S}_+^2 + \hat{S}_-^2\right) \\ \hat{O}_4^0 = & 35\hat{S}_z^{\,4} - (30S(S+1) - 25)\hat{S}_z^{\,2} - 6S(S+1) + 3S^2(S+1)^2 \\ \hat{O}_4^1 = & \frac{1}{4}\left(7\hat{S}_z^3 - (3S(S+1)+1)\hat{S}_z\right)\left(\hat{S}_+ + \hat{S}_-\right) + \cdots \\ & \frac{1}{4}\left(\hat{S}_+ + \hat{S}_-\right)\left(7\hat{S}_z^3 - (3S(S+1)+1)\hat{S}_z\right) \\ \hat{O}_4^2 = & \frac{1}{4}\left(\left(7\hat{S}_z^2 - S(S+1) - 5\right)\left(\hat{S}_+^2 + \hat{S}_-^2\right) + \left(\hat{S}_+^2 + \hat{S}_-^2\right)\left(7\hat{S}_z^2 - S(S+1) - 5\right)\right) \\ \hat{O}_4^3 = & \frac{1}{4}\left(\hat{S}_z\left(\hat{S}_+^3 + \hat{S}_-^3\right) + \left(\hat{S}_+^3 + \hat{S}_-^3\right)\hat{S}_z\right) \\ \hat{O}_4^4 = & \frac{1}{2}\left(\hat{S}_+^4 + \hat{S}_-^4\right) \end{cases} \tag{2.27}$$

In general all $\hat{O}_k^q$ $(-k \leq q \leq k)$ should be included in (2.26) with $k \leq 2S$ (as already mentioned in the previous subsection), but symmetry drastically restricts the number of terms. We will demonstrate this with two selected examples :

- For an orthorhombic $S = 1$ system, $\hat{H}_{\text{ZFS}}$ simplifies to

  $$\hat{H}_{\text{ZFS}} = B_2^0\hat{O}_2^0 + B_2^2\hat{O}_2^2 \tag{2.28}$$

  and with (2.24) one sees that

  $$B_2^0 = \frac{D}{3} \qquad\qquad B_2^2 = E \tag{2.29}$$

- In a cubic $S = 5/2$ system $D = E = 0$ and

  $$\hat{H}_{\text{ZFS}} = B_4^0\left(\hat{O}_4^0 + 5\hat{O}_4^4\right) \tag{2.30}$$

  and only B_4^0 has to be found ($B_4^4 = 5B_4^0$).
  For a tetragonal $S = 5/2$ system

  $$\hat{H}_{\text{ZFS}} = B_2^0\hat{O}_2^0 + B_4^0\hat{O}_4^0 + B_4^4\hat{O}_4^4 \tag{2.31}$$

  three parameters define the ZFS interaction. With (2.25) and (2.27) one can calculate ([4], page 437) that

  $$B_4^0 = \frac{a}{120} + \frac{F}{180} \qquad\qquad B_4^4 = \frac{a}{24} \tag{2.32}$$

[9] Note that there are some typos in the most used reference for the ESO ([4]) as discussed in [24]

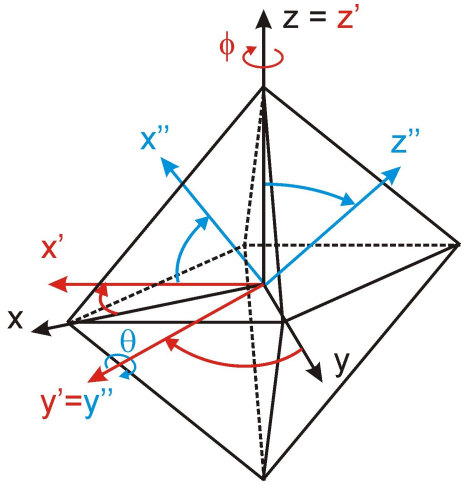

Figure 2.2. Transformation of a octahedral defect from an axes frame with z along a tetragonal symmetry (black) axis to a frame with z along a trigonal symmetry axis (blue), via an azimuthal angle $\phi = 45°$ and a polar angle $\theta = 54.74°$

Transformation of the ESO between different axes frames

As the ESO depend on $\hat{S}_i (i \in \{x, y, z\})$ the corresponding B_k^q parameters depend on the orientation of this axes frame in the defect frame. The values of B_k^q in one axes frame differ from these in another and these values can be calculated via transformation formulas. If one is only interested in rotating one high symmetry axis (e.g. for systems with axial symmetry), then the original axes frame can be transformed to a new axes frame via a rotation around an azimuthal angle ϕ about the original z axis and around a polar angle θ about the new y axis. If transformation of the axes in the plane perpendicular to this main axis is also required, an extra rotation about an angle α around the z'' axis is needed. This is not treated in [20] and will also be omitted here. The transformation matrices $\mathbf{S_k}(\phi,\theta)$ connect the ESO in the original axes frame (in curly brackets) with the SO in the new axes frame (in square brackets) via

$$\left\{\hat{O}_k^q\right\} = \mathbf{S_k}(\phi,\theta) \left[\hat{O}_k^q\right] \tag{2.33}$$

Their explicit form can be found in [20]. For $k = 2$ and $q > 0$ one has

$$\begin{Bmatrix} \hat{O}_2^2 \\ \hat{O}_2^1 \\ \hat{O}_2^0 \end{Bmatrix} = \begin{bmatrix} cos(2\phi)\left(cos^2(\theta)+1\right)/2 & sin(2\theta)cos(2\phi) & sin^2(\theta)cos(2\phi)/2 \\ -sin(2\theta)cos(\phi)/4 & cos(2\theta)cos(\phi) & sin(2\theta)cos(\phi)/4 \\ 3sin^2(\theta)/2 & -3sin(2\theta) & \left(3cos^2(\theta)-1\right)/2 \end{bmatrix} \cdot \begin{bmatrix} \hat{O}_2^2 \\ \hat{O}_2^1 \\ \hat{O}_2^0 \end{bmatrix} \tag{2.34}$$

The transformation of the ESOs between two axes systems can be illustrated via

equation (2.30) :

$$\hat{H}_{\text{ZFS}} = B_4^0 \left(\hat{O}_4^0 + 5\hat{O}_4^4 \right)$$

Here we implicitly assumed that $\hat{S}_z$ corresponds to a tetragonal ([100]) symmetry axis. If, on the other hand, we take the z axis as a trigonal ([111]) symmetry axis, this equation transforms into

$$\hat{H}_{\text{ZFS}} = -\frac{2}{3} B_4^0 \left(\hat{O}_4^0 + 20\sqrt{2}\hat{O}_4^3 \right) \tag{2.35}$$

or, if we use the notation with brackets :

$$\begin{aligned} \left[B_4^0\right] &= -\frac{2}{3} \left\{B_4^0\right\} \\ \left[B_4^3\right] &= -\frac{40\sqrt{2}}{3} \left\{B_4^0\right\} = 20\sqrt{2} \left[B_4^0\right] \\ \left[B_4^4\right] &= 0 \end{aligned} \tag{2.36}$$

This can be calculated via evaluating $\mathbf{S_k(\phi,\theta)}$ with $k = 4$ and $\phi = 45°$ and $\theta = 54.74°$ (the explicit forms can be found in [20]) and ϕ and θ are illustrated in figure 2.2.

The absolute sign of the ZFS parameters

It should be noted that from EPR measurements of the positions of the spectral lines ideally only the relative signs of the B_k^q's can be determined, as well as their magnitudes. There is an ambiguity in the overall sign, but this can be solved by lowering T, so population differences become visible. This will be illustrated and further elaborated in sections 4.5.3 and 6.6.

2.5.3 The (super)hyperfine interaction

The interactions between the valence electrons and the magnetic moment of the central nucleus and surrounding nuclei are called the hyperfine (HF) and super-hyperfine (SHF) interactions respectively. In the SH this interaction is represented by

$$\hat{H}_{\text{HF}} = \hat{\vec{S}} \cdot \bar{\bar{A}} \cdot \hat{\vec{I}} \tag{2.37}$$

for each nucleus. For its physical interpretation, the (S)HF tensor $\bar{\bar{A}}$ is often divided into an isotropic part and an anisotropic part :

$$\bar{\bar{A}} = A_{\text{iso}} \bar{\bar{1}} + \bar{\bar{A}}_{\text{aniso}} \tag{2.38}$$

with $A_{iso} = \frac{2\mu_0}{3} g_\mathrm{e} g_\mathrm{N} \beta_\mathrm{e} \beta_\mathrm{N} \rho_S(\vec{0})$. $\rho_S(\vec{0})$ is interpreted as the spin density at the nucleus and is in first order only non-zero for s-electrons. The anisotropic part can be interpreted in terms of dipole interactions and can be approximated by

$$\bar{\bar{A}}_\mathrm{aniso} = \frac{\mu_0}{4\pi} g_\mathrm{e} g_\mathrm{N} \beta_\mathrm{e} \beta_\mathrm{N} \frac{1}{r^3} \begin{bmatrix} -1 & 0 & 0 \\ 0 & -1 & 0 \\ 0 & 0 & 2 \end{bmatrix} \tag{2.39}$$

where r is the distance between the valence electrons and the interacting nucleus. In many cases, the HF and SHF structure of several nuclei overlap in the EPR spectrum, and the (S)HF tensors cannot be retrieved from EPR alone.

2.5.4 The nuclear Zeeman interaction

To first order, $\hat{H}_\mathrm{NZ}$ causes an equal energy shift of two levels between which an EPR transition is allowed, because it only influences the nuclear spin levels, via

$$\hat{H}_\mathrm{NZ} = -\beta_\mathrm{N} g_N \vec{B} \cdot \hat{\vec{I}} \tag{2.40}$$

The (isotropic) nuclear g factor, g_N, is characteristic for each nucleus and can be used to identify different nuclei (see below).

2.5.5 The quadrupole interaction

$\hat{H}_\mathrm{Q}$ is also in most cases in first order invisible[10] in EPR spectra and only applies for $I \geq 1$. The general form is

$$\hat{H}_\mathrm{Q} = \hat{\vec{I}} \cdot \bar{\bar{Q}} \cdot \hat{\vec{I}} \tag{2.41}$$

$\bar{\bar{Q}}$ is traceless and can be described by the electric field gradient q and the asymmetry factor η :

$$\bar{\bar{Q}} = \begin{bmatrix} Q_\mathrm{x} & 0 & 0 \\ 0 & Q_\mathrm{y} & 0 \\ 0 & 0 & Q_\mathrm{z} \end{bmatrix} = Q \begin{bmatrix} -(1-\eta) & 0 & 0 \\ 0 & -(1+\eta) & 0 \\ 0 & 0 & 2 \end{bmatrix} \tag{2.42}$$

with

$$Q = \frac{e^2 q \tilde{Q}}{4I(2I-1)} \tag{2.43}$$

$\tilde{Q}$, the electric quadrupole moment, is specific for each isotope.

[10] The line positioning as well as the appearance of $\Delta(m_\mathrm{I}) \neq 0$ lines in EPR spectra correlates with the Q/A ratio [2]

2.6 SATURATION AND RELAXATION DURING AN EPR EXPERIMENT

Consider the following ground state energy levels $E_1, E_2, \ldots$ in thermal equilibrium. The number of systems N_i that occupy a certain energy level E_i is given by the Boltzmann distribution:

$$N_i \sim e^{-\frac{E_i}{kT}} \tag{2.44}$$

The absorbed MW power in a transition between two energy levels $E_1 < E_2$ during an EMR experiment is proportional to the population difference

$$n = N_1 - N_2 = N_1 \left(1 - e^{-\frac{\Delta E}{kT}}\right) \tag{2.45}$$

where $\Delta E = E_2 - E_1$ and the EMR signal thus increases with decreasing temperature. This does not mean nevertheless that all EMR measurements are performed at low temperature (LT), since a good knowledge of the system at room temperature (RT) can be of great importance for practical applications.
When a radiation field supplies energy quanta $h\nu = \Delta E$, the transition probabilities $W_{1\to 2}$ and $W_{2\to 1}$ are equal, but since $N_1 > N_2$, there are more transitions from E_1 to E_2 and the net effect is that the system absorbs energy. However, when ignoring the spontaneous decay back to the lowest energy level, these transitions quickly equalise the population levels and there no longer is net absorption. This is called *saturation* of a transition.
In real systems, various *relaxation* mechanisms allow deexcitation of E_2 to E_1 and saturation of an energy level only occurs when the rate of transitions induced by the radiation field is larger than the relaxation rate. As the relaxation time[11] depends on the system and on the temperature, both temperature and radiation power should be tuned for optimal measuring conditions.

2.7 ENDOR SPECTROSCOPY

In many cases, the EPR spectrum alone is not sufficient to fully structurally characterize the system, since EPR comes with some inherent problems. For some of these, NMR has a clear advantage over EPR.

- As already mentioned in section 2.5.3, (S)HF interactions can cause many narrow lines to overlap to form one inhomogeneously[12] broadened EPR line where no information about the (S)HF interaction can be extracted from.

[11] There are in general two main contributions to the relaxation time : a T-dependent spin-lattice relaxation and a T-independent spin-spin relaxation.

[12] The inhomogeneous linewidth is caused by overlapping of several (S)HF lines, each of which having a smaller homogeneous linewidth.

- Also the number of lines in EPR can blur things, since it scales multiplicatively with the number of involved nuclei : for N nuclei (with nuclear spin I_k) the number of EPR transitions is given by

$$n_{EPR} = 2S \prod_{k=1}^{N} (2I_k + 1) \tag{2.46}$$

  while in an NMR experiment only

$$n_{NMR} = (2S + 1) \sum_{k=1}^{N} 2I_k \tag{2.47}$$

  transitions are allowed for this system.

- Another advantage of NMR over EPR includes the easy identification of the interacting nucleus, since the magnetic field dependence of each NMR line correlates with g_N.

However, there also is a major drawback to NMR experiments: the signals are typically much less intense than EPR signals, because (i) the probability for a transition between nuclear-spin levels is smaller and (ii) the population difference between two nuclear-spin levels is smaller (Boltzmann distribution, see Section 2.6). Typically, one needs minimal centre concentrations of 10^{19} cm^{-3} [13], which is several orders of magnitude more than in EPR experiments (10^{14}-10^{16} cm^{-3}, see section 3.2.4).
Electron Nuclear Double Resonance (ENDOR) combines the advantages of both techniques by inducing an EPR and an NMR transition at the same time. This makes it a very powerful tool to study paramagnetic defects in great detail. One starts by saturating an EPR transition (typically via high MW power and low temperature), consequently extra relaxation paths are created by simultaneous radiofrequent (RF) irradiation: via nuclear spin flips the concerned electron spin levels can desaturate in additional ways. This desaturation can be monitored via the change of intensity of the EPR signal. A detailed description about all the involved relaxation processes can be found in various textbooks (e.g. [13, 4]). Here we restrict ourselves by mentioning that the different relaxation processes are usually strongly temperature-dependent and for many paramagnetic systems, ENDOR can consequently only be detected in a very narrow temperature range.

2.8 Selection rules in EPR and ENDOR

For complicated systems with several interacting nuclei, the ground state can consist of a large number of energy levels, so a lot of EPR and ENDOR transiti-

ons can be expected. Nevertheless, only a few transitions are allowed and these allowed transitions obey certain *selection rules*.
Let us illustrate this with an isotropic system with spin S and no interaction nuclei. During an EPR experiment we have the simultaneous interaction of $\vec{S}$ with the static magnetic field $\vec{B} = B\vec{e_z}$ and with a MW field perpendicular to the static magnetic field $\vec{B_1}(t) = B_1 cos(\omega t)\vec{e_x} + B_1 cos(\omega t)\vec{e_y}$. Using (2.22) we get

$$\hat{H} = g_e\beta_e B\hat{S}_z + g_e\beta_e B_1(cos(\omega t)\hat{S}_x + sin(\omega t)\hat{S}_y) \tag{2.48}$$
$$= g_e\beta_e B\hat{S}_z + g_e\beta_e B_1(e^{-i\omega t}\hat{S}_+ + e^{i\omega t}\hat{S}_-) \tag{2.49}$$
$$= \hat{H}_0 + \hat{H}_1(t) \tag{2.50}$$

Using time-dependent perturbation theory ($\hat{H}_0 >> \hat{H}_1(t)$) one can deduce that the transition probability between level $|M_S>$ and $|M'_S>$ is zero, unless $|M_S - M'_S| = 1$.

In general, when several unpaired electrons interact with surrounding nuclei (with nuclear spin I), the following selection rules apply :

$$\text{EPR selection rules} \begin{cases} |\Delta M_S| = 1 \\ \Delta M_I = 0 \end{cases} \tag{2.51}$$

$$\text{ENDOR selection rules} \begin{cases} \Delta M_S = 0 \\ |\Delta M_I| = 1 \end{cases} \tag{2.52}$$

2.9 EPR AND ENDOR : A SIMPLE EXAMPLE

We want to conclude this chapter by illustrating EPR and ENDOR with the simplest example containing ZFS, HF and quadrupole interaction. Consider an axially symmetric centre $S = 1$ which interacts with one nucleus with $I = 1$ (e.g. ^{14}N). For simplicity, we assume $\bar{\bar{g}}$ and $\bar{\bar{A}}$ isotropic, $\bar{\bar{D}}$ and $\bar{\bar{Q}}$ axial along the same z axis and finally, the external magnetic field $\vec{B}$ is oriented along this z axis. The SH for this system follows from (2.21) and can be written as

$$\hat{H} = g\beta_e B\hat{S}_z + D\left(\hat{S}_z^2 - \frac{1}{3}\hat{S}^2\right) + A\hat{\vec{S}}\cdot\hat{\vec{I}} - \beta_N g_N B\hat{I}_z + Q\left(3\hat{I}_z^2 - \hat{I}^2\right) \tag{2.53}$$

In first order, the energy levels can be calculated to be

$$E(M_S, M_I) = g\beta_e B M_S + \frac{D}{3}\left(3M_S^2 - 2\right) + AM_S M_I - \beta_N g_N B M_I + 3Q\left(3M_I^2 - 2\right) \tag{2.54}$$

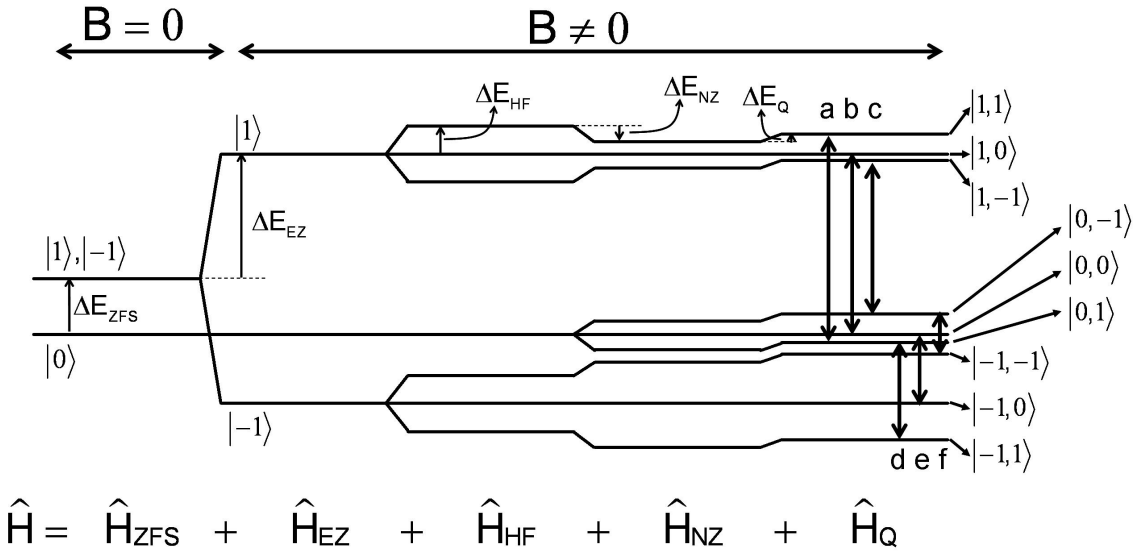

Figure 2.3. Energy level scheme of the system defined in section 2.9, for the case that $|\Delta E_{\mathrm{EZ}}| = g\beta_{\mathrm{e}}B > |\Delta E_{\mathrm{ZFS}}| = D > |\Delta E_{\mathrm{HF}}| = A > |\Delta E_{\mathrm{NZ}}| = g\beta_{\mathrm{N}}B > |\Delta E_{\mathrm{Q}}| = Q > 0$.
The eigenstates are labelled $|M_{\mathrm{S}}(, M_{\mathrm{I}})>$ and the allowed (by (2.51)) EPR transitions are symbolised by a $\updownarrow$.

and we get 9 different $|M_{\mathrm{S}}, M_{\mathrm{I}}>$ energy levels, which we will name '1' (the lowest in energy, $|-1,1>$) to '9' (highest energy, $|1,1>$) in the following. In figure 2.3 the energy level scheme is drawn.
Six allowed EPR transitions ($|\Delta M_{\mathrm{S}} = 1|$ and $\Delta M_{\mathrm{I}} = 0$) occur in this system. They are indicated with $\updownarrow$ and labelled a to f in figure 2.3 and their position can be easily calculated via (2.54).
The EPR transition a, between energy levels 4 and 9, spans an energy difference of

$$\Delta E = g\beta_{\mathrm{e}}B + D + A \tag{2.55}$$

and has the smallest resonance field in the EPR spectrum :

$$B_{\mathrm{a}} = \frac{h\nu_{\mathrm{MW}}}{g\beta_{\mathrm{e}}} - \frac{D}{g\beta_{\mathrm{e}}} - \frac{A}{g\beta_{\mathrm{e}}} \tag{2.56}$$

When saturating this EPR transition, 2 NMR transitions (between levels 8-9 and 4-5) can be seen in the ENDOR spectrum. The energy differences between these levels are

$$\begin{cases} \Delta E_{8\text{-}9} &= A - g_{\mathrm{N}}\beta_{\mathrm{N}}B + 3Q \\ \Delta E_{4\text{-}5} &= g_{\mathrm{N}}\beta_{\mathrm{N}}B - 3Q \end{cases} \tag{2.57}$$

and the resonance frequencies can be found[13] at

$$\begin{cases} \nu_{8\text{-}9} &= \frac{1}{h}\left|A - g_{\mathrm{N}}\beta_{\mathrm{N}}B + 3Q\right| \\ \nu_{4\text{-}5} &= \frac{1}{h}\left|g_{\mathrm{N}}\beta_{\mathrm{N}}B - 3Q\right| \end{cases} \tag{2.58}$$

When saturating transition b, on the other hand, 4 NMR transitions are visible in the ENDOR spectrum.

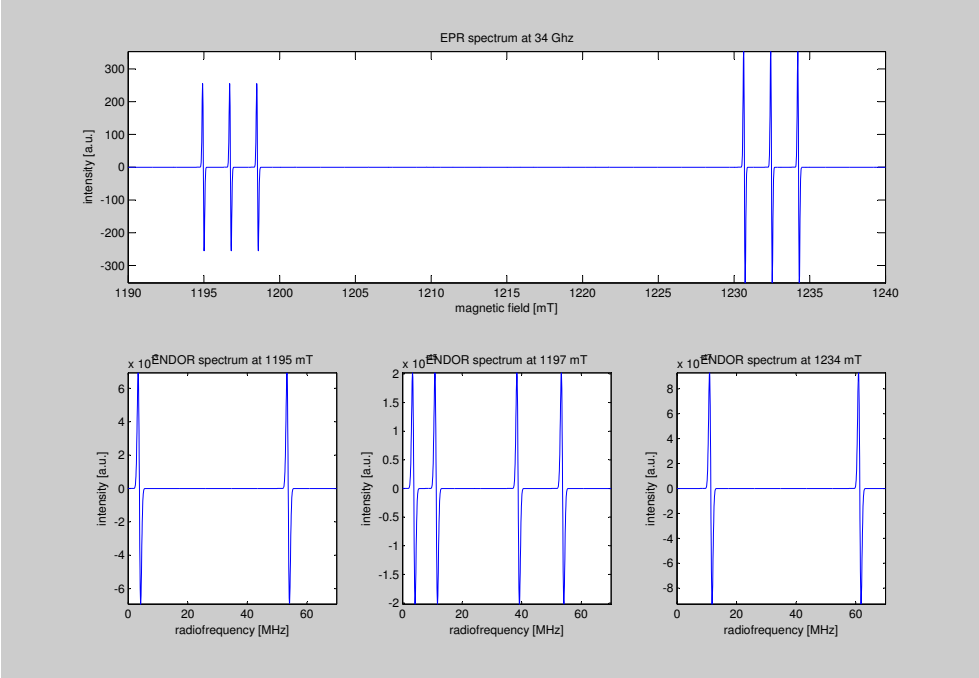

Figure 2.4. Output of the program example.m

In figure 2.4 the EPR spectrum and three ENDOR spectra (on EPR transition a, b and f respectively) of the centre are shown, with the magnetic field along the z axis. The spectra are simulated with the EasySpin (see section 3.1 on page 27) program *example.m*[14] and we gave every parameter an arbitrary value (obeying the conditions imposed in figure 2.3). The simulations are performed via exact matrix diagonalization. For this simple case is the correspondence with our first order calculations very good, both in EPR and ENDOR.

[13]Since all energies (in J) have to be divided by h to find the right frequency, one prefers to express *a priori* A, Q and D in units of $(M)Hz$, as already noted earlier.

[14]The source code of this program can be found in appendix A.

CHAPTER 3

EXPERIMENTAL PROCEDURES

"Friends! Help! A guinea pig tricked me! "
— DR. J. ZOIDBERG

3.1 SOFTWARE

During the research a lot of software was used, e.g. Matlab, Carine Crystallography v3.1, MS Excel, ...
For this work, we chose to elaborate on *EasySpin* (ES) [25]. ES is written and maintained by Stefan Stoll, currently at the University of California, Davis, and is free for non-commercial use and downloadable at www.easyspin.org.

Function name	Description
sop	Generate spin matrices
stev	Generate extended Stevens operator matrices
levels	Calculate energy levels
resfields	Calculate resonance fields
eprload	Import of experimental data
eulang	Conversion from rotation matrices to Euler angles
pepper	Solid-state cw EPR spectra simulation
salt	ENDOR spectra simulation

Table 3.1. Selected EasySpin functions

ES is a Matlab toolbox for simulating and fitting EPR and ENDOR spectra. It supplements the numerical and visualisation power of Matlab with the best computational methods devised by EPR spectroscopists. ES can be combined with Matlab's functionality, e.g. optimization functions like *fminsearch* for least-squares fitting of simulated spectra/fields. The simulations can be done by exact matrix

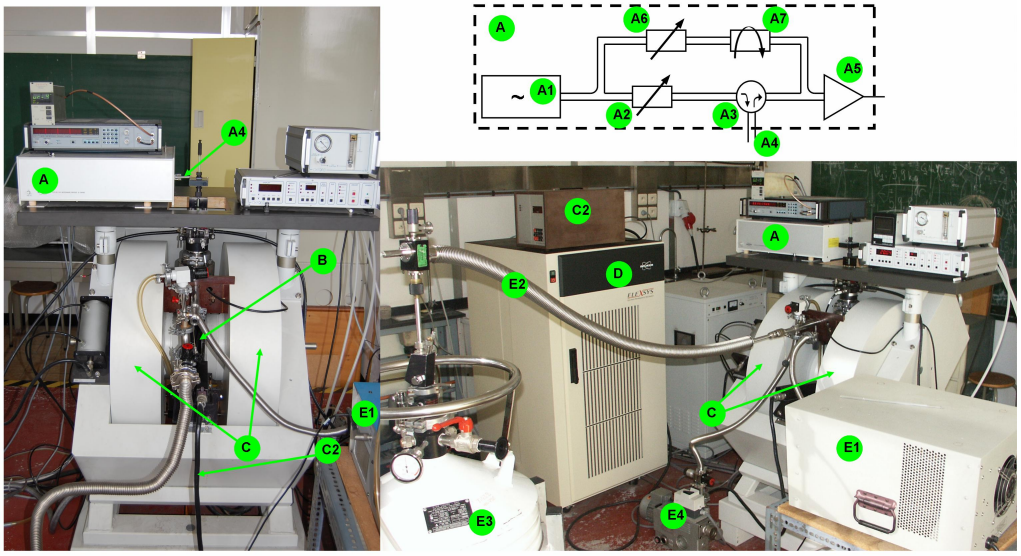

Figure 3.1. Two pictures of the Q band spectrometer of our group, the upper drawing is a block scheme of the MW bridge.

diagonalization or by perturbation theory. The latter can substantially shorten the computational time. Both continuous wave and pulse liquid- and solid-state EPR and ENDOR can be simulated. An important quality of ES is that spin systems with an arbitrary number of electron and nuclear spins are supported. As a consequence, self-written programs (programming can be learned fairly easily thanks to the accessible and well-documented Matlab programming environment), can easily be extended or modified according the specific spin system. In table 3.1 a few important ES functions are listed.
Some of the programs used in this work are shown in Appendix A along with sufficient comments, to illustrate various features of ES and to serve as a small tutorial for the starting EPR programmer. The simulations in this work were performed with version 2.7.1 (2008-02-12). During the writing of this thesis, version 3.0.0 was released, with some important changes[1], so care should be taken when copying the programs from Appendix A.

3.2 EPR SPECTROMETER

3.2.1 Principles of design

As the price of a commercial EPR spectrometer suggests (starting around 300.000 euro), there is a complex electronical, mechanical and computational structure

[1] A major change is for example that the order of outputs of 'eprload' has changed from [spc,Params,B] to [B,spc,Params].

needed for the correct functioning of an EPR spectrometer. Descriptions of the experimental EPR set-up can be found on diverse levels of detail, both in EPR-related books ([3, 26]) and in the manuals of the spectrometers (e.g. [27]).
In this section, only what is necessary to understand the basic operation of an EPR spectrometer will be discussed. In this simplified picture, the EPR spectrometer consists of 4 major parts, indicated in figure 3.1 : the MW bridge (A), the cavity (B), the electromagnet (C) and the console (D).
The *microwave bridge* (A, see block scheme in 3.1) contains the MW source (A1) as a first component. Due to practical constraints, neither its frequency nor power can easily be varied. Therefore the next component is a variable attenuator (A2) to control the power of the microwaves which, via the circulator (A3) and through an external waveguide (A4), attain the sample in the cavity (B). The reflected microwaves are directed to the detector via the circulator, which prevents back flow to the MW source. The detector (A5) is a diode, which converts the MW power to an electrical current. At lower (resp. higher) power levels, the diode current is proportional to (resp. to the square root of) the MW power and the detector is called a square law (resp. linear) detector, since the electrical power is proportional to the square of the current. For quantitative signal intensity measurements as well as optimal sensitivity, the diode should operate in the linear region. To insure that the detector operates at that level, some of the source power (bias) is guided into the reference arm, where a second attenuator (A6) controls the power level (and consequently the diode current) for optimal performance. There is also a phase shifter (A7) to insure that the reference arm microwaves are in phase with the reflected signal microwaves when the two signals combine at the detector diode.
The *cavity* (B) contains the sample and is placed between the poles of the electromagnet. A cavity is simply a metal box with a rectangular or cylindrical shape which can store MW energy, at a certain frequency, called the resonance frequency ν_{res}. At this frequency, the reflection coefficient of the cavity is minimal, and the microwaves remaining inside the cavity form a standing wave. The quality factor, Q,

$$\begin{aligned} Q &= 2\pi \frac{energy\ stored}{energy\ dissipated\ per\ cycle} \\ &= \frac{\nu_{\text{res}}}{\Delta\nu} \end{aligned} \tag{3.1}$$

quantifies how efficiently the cavity can store MW energy. ν_{res} and $\Delta\nu$ are illustrated in figure 3.2. EPR cavities have a Q factor of the order 10^3-10^4. Standing electromagnetic waves have their electric and magnetic field components exactly out of phase and we can use the spatial separation of the electric and magnetic

fields in a cavity to great advantage. If we place our sample in the electric field minimum and the magnetic field maximum, we minimize the dielectric losses and maximize the magnetic dipole transition probability, thus obtaining the biggest signals and the highest sensitivity. When the resonance condition $\Delta E = h\nu_{\text{res}}$ is fulfilled, the sample absorbs MW energy quanta, changing Q and thus also the reflection coefficient of the cavity. These changes of the reflected MW power constitute the EPR signal in the detector (A5). Since the MW frequency cannot be varied easily, due to both practical constraints on the MW bridge and the use of a resonance cavity, the MW frequency is kept constant in EPR experiments. The dimensions of the waveguides, cavity and maximum sample size are adapted to this frequency and each EPR spectrometer is named by its frequency 'band'. The most common EPR spectrometers have $\nu \approx 9.5$ GHz and are labelled 'X band EPR spectrometers' (see section 3.2.5).

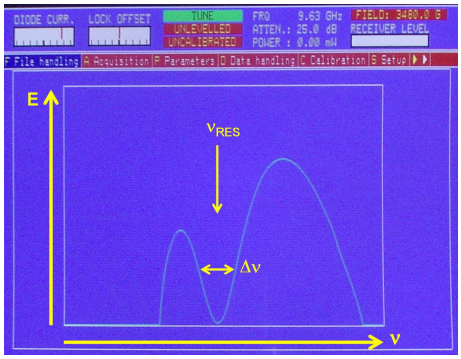

Figure 3.2. Screen shot of the ESP300E X band spectrometer in tuning mode, showing the energy density in the cavity as a function of the MW frequency. For clarity, an axes frame and both ν_{RES} and $\Delta\nu$ are (approximately) sketched in yellow.

The *electromagnet* (C) provides the static magnetic field $\vec{B}$. Its direction is perpendicular to that of the excitation microwave field $\vec{B}_1$ and its magnitude is slowly varied in a linear way. Via a built-in Hall probe, the console adjusts the current to the desired field trough the magnetic coils. Since this Hall probe, however, is not exactly positioned at the place of the sample, the measured field can differ several Gauss with the actual field at the sample. Therefore, an extra calibration is carried out with an external Gauss probe (C2) which is placed in the vicinity of the sample and a calibration sample with a well-documented g value. For lower MW frequencies, e.g., α,α'-Diphenyl-β-Picryl-Hydrazyl, better known as DPPH (g = 2.0036) is very well suited.
To improve the signal-to-noise (S/N) ratio, $\vec{B}$ is modulated at high frequency (1-100 kHz) by a small $\vec{B}_{\text{m}}$ (≈0.1 mT) ($\vec{B}_{\text{m}} \parallel \vec{B}$), generated by a modulation frequency

source which supplies a current to the modulation coils. A side effect of this modulation is that the output of the detector is proportional to the first derivative of the absorption signal. It should be noted, lastly, that B_{m} should not exceed $\frac{1}{3}$ to $\frac{1}{2}$ of the linewidth to avoid line broadening and corresponding loss of resolution ([26], page 482).

3.2.2 ENDOR extension to the EPR spectrometer

The low power RF signal, generated by a synthesiser, passes an RF amplifer (E1 in figure 3.1) and is fed to a coil inside the cavity, which produces the NMR excitation field $\vec{B}_2 \perp \left(\vec{B}_1, \vec{B}\right)$. The amplitude of the EPR signal is recorded as a function of the RF frequency. In accordance to EPR, the RF signal is modulated to enhance the S/N ratio and again the first derivative of the ENDOR absorption is recorded.

3.2.3 Cryogenics

For measurements at low temperatures liquid N_2 (for temperatures down to 77 K) or liquid He (T = 4.2 K) are used. With an external pump, the liquid He is transferred via the transfer line (E2) from the vessel (E3) to the cavity (B) (inside the cryostat)[2]. An extra pump (E4) is used for measurements at T $<$ 4 K. Special care has to be taken when transferring/rotating the sample if the temperature of the cavity is lower than RT, to avoid any contaminations (present in air) entering the cavity.

3.2.4 Sensitivity of the spectrometer

The theoretical minimum number of spins N to be detected with a S/N ratio of 1 is ([13], page 33)

$$N = \sqrt{\frac{A \cdot T}{P_{\mathrm{MW}}}} \frac{T \cdot \Delta\omega_{1/2}}{\omega_0 \cdot S(S+1)} \cdot \frac{1}{\eta \cdot Q} \tag{3.2}$$

The first factor in (3.2) is determined by the detection system, where A represents several constants and system dependent parameters and P_{MW} the MW power. The second factor depends on the sample, containing the linewidth ($\Delta\omega_{1/2}$), the Larmor frequency (ω_0) and the electron spin S. The last factor contains the quality factor Q and the filling factor η.
In practice, one needs arounds 10^{14}-10^{16} spins/cm^{-3}. This number depends, of course, on the details of the spin system and several aspects should be taken into account :

[2] In X band the liquid He first fills a chamber, from where it goes in to the cryostat to the cavity.

MW frequency Theoretically, the sensitivity should increase with increasing MW frequency. Experiment shows however that this gain is seldom fully reached in practice due to practical difficulties.

The influence of the filling factor η It seems very obvious : the more sample available, the more signal one can obtain, but the practical advantage can also work in the opposite way. When very little material is available, higher frequencies can be necessary to have a non-negligible η and/or a good S/N ratio. This is illustrated for the samples in focus of this doctoral research in figure 3.10. On the other hand, e.g., in-vivo experiments in mice demand cavity sizes that only L band spectrometers ($\nu \approx 1.5$ GHz) can provide.

Number of paramagnetic centra in the sample The intermolecular interaction between electron spins cannot be neglected anymore in case of higher concentration of paramagnetic centres. The corresponding EPR lines will broaden and the spectra will lose resolution. Generally, a minimum 'diamagnetic dilution' of 1:10^2 - 1:10^4 is recommended.

3.2.5 The used spectrometers

EPR spectra were measured in X, Q ($\nu \approx 34$ GHz) and W ($\nu \approx 95$ GHz) band. Spectrometers in the first two bands are located in our lab (the technical details can be found in table 3.2) and both have ENDOR facilities, while the latter spectrometer is shared between the ECM (Prof. Dr. Goovaerts) and the SIBAC (Prof. Dr. Van Doorslaer) group at the University of Antwerp.

3.2.6 A multi-frequency approach

Recording spectra at several MW frequencies has several advantages, of which the *sensitivity* issue has already been discussed in section 3.2.4.
An important advantage is the ability to discriminate between frequency dependent (e.g. $\hat{H}_{\mathrm{EZ}}$) and frequency independent (e.g. $\hat{H}_{\mathrm{(S)HF}}$ and $\hat{H}_{\mathrm{ZFS}}$) contributions.
Table 3.3 illustrates how a higher frequency also can enhance the *spectral resolution* for defects with a small g anisotropy. This is very useful when several radical spectra overlap, as e.g. in irradiated sugars.
On the other hand, certain ions (e.g. Ce^{3+}, see chapter 5) are preferably measured at lower frequencies (X band). Due to their *effective g values* which can be much lower than 2, they can have very high resonance fields (see table 3.3) at high frequencies, which cannot always be attained by the electromagnet of the corresponding spectrometer (Q band magnet limit = 1.5 T).
Here we will focus on the specific advantages of measuring high-spin systems in

	X band	Q band
Spectrometer	ESP300E	ELEXSYS E500 (Bruker)
MW bridge (MW source)	ER042MRH (klystron)	ER051 (Gunn-diode) (Bruker)
EPR cavity	4102ST (rectangular)	ER 5106 QTW (cilindrical)
ENDOR cavity	ESP353E (rectangular)	ER 5106 QTE (cilindrical) (Bruker)
T control	ITC4	ITC503 (Oxford Instruments)
RF amplifier	3200L (ENI, 2 models)	
Gauss probe	ER035M (Bruker)	
Cryostat	ESR10	CF935 (Oxford Instruments)
Frequency counter	5350B (HP)	548B (EIP)
Electromagnet	B-E30	ER073 (Bruker)
Magnetic field limit	1.5 T	1.5 T
Operation software	ESP300E	xEpr (Bruker)

Table 3.2. Technical specifications of the EPR spectrometers at the Department of Solid State Sciences, Gent.

g values	X band (ν = 9.5 GHz)	Q band (ν = 34 GHz)
1.00	678.75	2429.22
1.99	341.08	1220.71
2.00	339.38	1214.61
2.01	337.69	1208.57
4.00	169.69	607.31

Table 3.3. Resonance field (in mT) for several effective g values in X and Q band

different bands, since illustrations of the advantages of multi-frequency EPR on S = 1/2 systems abound in EPR textbooks, articles and theses.

High-spin systems in different bands

$\hat{H}_{\mathrm{ZFS}}$ can cause significant changes in the EPR spectrum. Varying the band of the spectrometer does not only affect the spectrum via the magnetic field (field dependence of the lines and magnetic field limit) but also via the MW quantum. The relative size of the MW quantum with respect to the ZFS of the levels, will determine if all allowed EPR transitions are possible. In other words, different MW quanta can allow to detect different energy transitions of a particular system.

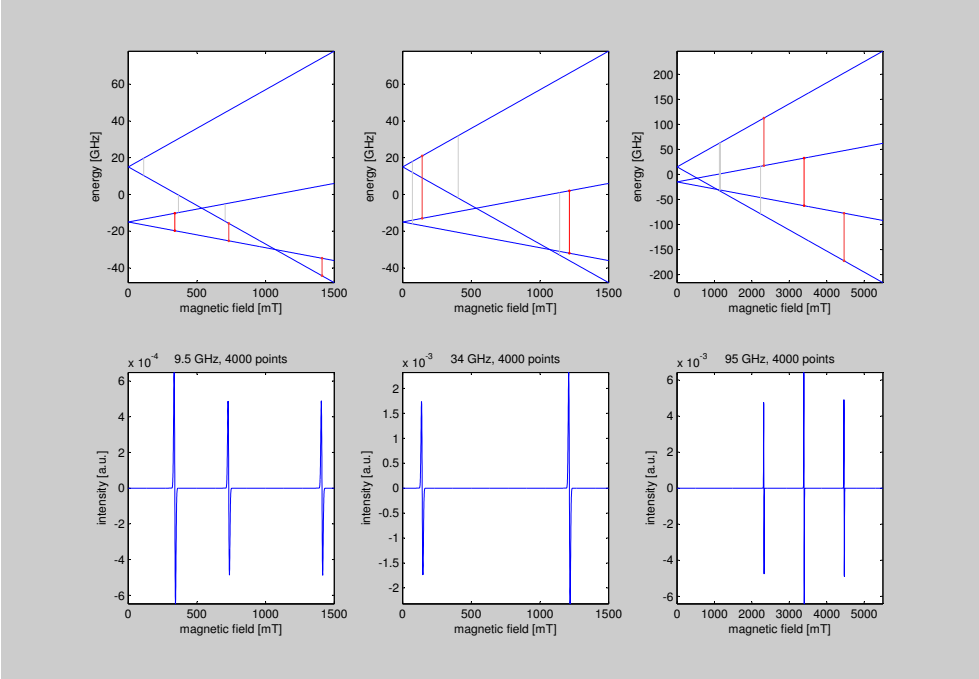

Figure 3.3. Output of the program frequencies.m

This can be illustrated by an simple example ignoring all (S)HF interaction. Consider an axial S=3/2 system[3] with an isotropic g value ($g = 2$). For this system, the following SH suffices :

$$\hat{H} = g\beta_{\mathrm{e}}\vec{B}\cdot\hat{\vec{S}} + \hat{\vec{S}}\cdot\bar{\bar{D}}\cdot\hat{\vec{S}} \tag{3.3}$$

which simplifies to

$$\hat{H} = g\beta_{\mathrm{e}}B\hat{S}_{\mathrm{z}} + D(\hat{S}_{\mathrm{z}}{}^2 - \frac{1}{3}S(S+1)) \tag{3.4}$$

[3]We chose S = 3/2, and not S = 1 (which would be the simplest case), so the M_S=$|-\frac{1}{2}> \leftrightarrow |\frac{1}{2}>$ transition, located at g = 2 is visible if the ZFS is smaller than the MW quantum.

when $\vec{B}||z$. In this orientation, the line positions can easily be calculated exactly via :

$$E = h\nu = g\beta_e B M_S + D(M_S^2 - \frac{1}{3}S(S+1)) \tag{3.5}$$

which gives the following energy levels

$$\begin{cases} E(|\frac{3}{2}>) = \frac{3}{2}g\beta_e B + D \\ E(|\frac{1}{2}>) = \frac{1}{2}g\beta_e B - D \\ E(|-\frac{1}{2}>) = -\frac{1}{2}g\beta_e B - D \\ E(|-\frac{3}{2}>) = -\frac{3}{2}g\beta_e B + D \end{cases} \tag{3.6}$$

In zero field ($B = 0$), the $|\pm -\frac{1}{2}>$ and $|\pm -\frac{3}{2}>$ energy levels are split by $2D$. To illustrate the effect of different bands, we chose $2D$=30 GHz, so $\nu_X < 2D < \nu_Q (< \nu_W)$. The energy differences between EPR allowed (ΔM_S=1) energy levels are

$$\begin{cases} M_{\frac{3}{2}} \leftrightarrow M_{\frac{1}{2}} & h\nu = g\beta_e B + 2D \\ M_{\frac{1}{2}} \leftrightarrow M_{-\frac{1}{2}} & h\nu = g\beta_e B \\ M_{-\frac{1}{2}} \leftrightarrow M_{-\frac{3}{2}} & h\nu = |g\beta_e B - 2D| \end{cases} \tag{3.7}$$

Via the ES program *frequencies.m* (see Appendix) we simulated the EPR spectrum in the z orientation in different bands. In figure 3.3 simulation in X (ν = 9.5 GHz), Q (ν = 34 GHz) resp. W (ν = 95 GHz) band are shown. The upper picture shows the energy level diagram, together with allowed (in red) and forbidden (in gray) transitions, the lower picture shows the corresponding EPR spectrum, taking into account the magnetic field limit for each band. In the appendix the used ES routines are explained.
Both simulation and calculations show that in X band 3 transitions occur : the $|-\frac{1}{2}> \leftrightarrow |\frac{1}{2}>$ transition at $B = \frac{h\nu}{g\beta_e}$ and two times the $|-\frac{1}{2}> \leftrightarrow |-\frac{3}{2}>$ transition[4]: at $B = \frac{2D}{g\beta_e} \pm \frac{h\nu}{g\beta_e}$. Both at Q band and at W band, all transitions occur once, but in Q band the $|-\frac{1}{2}> \leftrightarrow |-\frac{3}{2}>$ transition is cut off by the magnet's field limit ($B <$ 1.5 T).

3.3 X-RAY IRRADIATION AND DIFFRACTION

3.3.1 X-ray diffraction

The X-ray diffraction set-up (D8, Bruker) works with the Cu-Kα line, providing 'soft' X-rays with a wavelength of 1.54 Å(E = 8.05 keV). X-rays are generated by

[4]This transition is called a 'looping transition', since in the angular variation (see section 3.5.2) the $|-\frac{1}{2}> \leftrightarrow |-\frac{3}{2}>$ resonance line forms a loop.

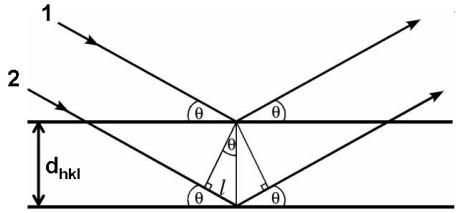

Figure 3.4. Illustration of Bragg's law (3.8). The pathway difference between incoming ray 1 and 2 is $2l = 2 \cdot d_{\text{hkl}} \cdot sin\theta$.

an X-ray tube : a vacuum tube that uses a high voltage to accelerate electrons released by a hot cathode to a high velocity. When soft X-rays hit a substrate, the electrons around the atoms start to oscillate with the same frequency as the incoming X-ray beam. Generally, there will be destructive interference of the outgoing waves in almost all directions, but when atoms are regularly arranged (in a single crystal) constructive interference can occur in certain directions. When incident X-rays (wavelength λ) make an angle θ with parallel (hkl)-planes of a lattice (with an interplanar distance d_{hkl}), a diffracted beam will leave the sample under the same angle θ only when

$$2 \cdot d_{\text{hkl}} \cdot sin\theta = n \cdot \lambda, \tag{3.8}$$

with n an integral number. (3.8) is called Bragg's law and is illustrated in figure 3.4. In a typical diffractometer, both the X-ray source and the X-ray detector are mounted under the same angle θ with the substrate plane. This means that only crystallographic planes parallel to the substrate plane can be measured.
In a powder, all crystallographic planes can be found parallel to the substrate plane and a so-called a $\theta/2\theta$ spectrum (2θ is the angle between the incoming and the diffracted beam) can be recorded. An example is given in figure 3.5. The reflected X-ray beam intensity is measured as a function of 2θ and for distinct 2θ positions, corresponding to the various crystallographic planes, peaks with a specific intensity are observed.
If one mounts a single crystal on a goniometer, the set-up can be used to orient the crystal, since every (hkl) plane has a particular 2θ. Plotting the diffraction intensity of a certain (hkl) reflection (with source and detector kept constant at the specific θ) at a large number of different orientations (changing ϕ and χ, see figure 3.6a) of the crystals, results in a pole figure. Pole figures are a type of stereographic projections. A stereographic projection gives information pertaining to the 3D structure and angles relating structural features in a two dimensional graphic. For crystallography we are interested mainly in the orientation of crystallographic planes through their normals. In most stereographic projections a sphere is considered that surrounds a crystal (see figure 3.6b). Normals to the

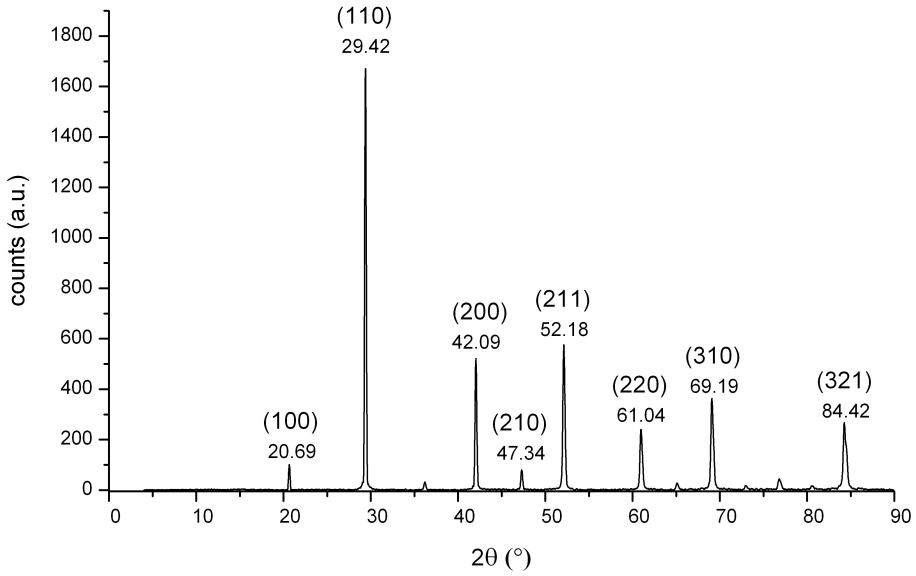

Figure 3.5. $\theta/2\theta$ spectrum of a powdered CsBr NIP (CB 12708_23). The corresponding crystallographic plane is indicated in brackets for the most intense diffraction peaks.

crystallographic planes intersect the sphere at a pole and the projection of these poles on a plane is called the pole figure. Via scanning the full range of ϕ and χ at a fixed 2θ, one determines at which (ϕ,χ) angle combinations for the sample the corresponding (hkl) plane is in a horizontal position with respect to the source and the detector. A pole figure of a randomly oriented CsBr crystal is shown in figure 3.6c. From that pole figure, recorded for $2\theta = 42.09°$ (see figure 3.5), one can deduct the azimuthal angle ϕ and the declination angle χ over which the crystal should be rotated to have a <100> orientation perpendicular to the plane.

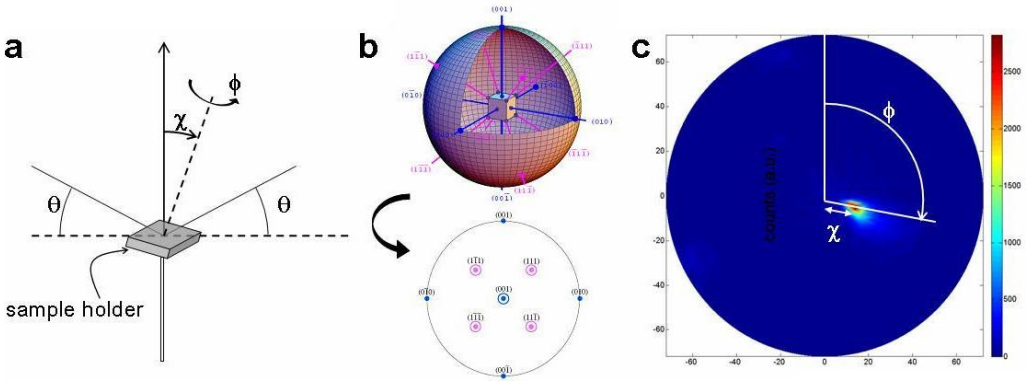

Figure 3.6.

a Representations of the angles ϕ, χ and θ in a goniometer.

b Construction of a pole figure from a single crystal.

c (200) pole figure of a CsBr single crystal. A crystallographic <100> axis is oriented perpendicular to the sample holder, when χ = 15° and ϕ = 153°

3.3.2 X-ray irradiation

Hard X-rays can create defects in lattices, e.g. F centres (an electron trapped in an anion vacancy) and change the valence state of defect ions (e.g. Eu^{2+} can change to Eu^{3+} upon irradiation).
In Ghent only X-ray irradiation outside the EPR setup (*ex situ*) is possible. The Philips tungsten anode X-ray tube (with a thin (<0.2 mm) beryllium window) was usually operated at 60 kV and 40 mA, at dose rates up to 1.3 kGy per minute. Apart from irradiation at RT, irradiation at liquid nitrogen temperature can also be performed using a special dewar. By precooling the EPR cavity with liquid He, the rise in sample temperature upon transfer into the cavity can be limited (to $\approx$ 100K).
In section 6.6.5 measurements are reported after T = 10 K irradiation. These were performed at the university of Oslo, in the lab of Prof. Dr. E. Sagstuen, where a Philips X-irradiation 100kV generator and side-window X-ray tubes (Cr and W) are available. *In situ* irradiation can be performed, from RT down to 10K through a thin (0.2 mm) aluminum window in the vacuum shield, at a typical dose rate of 0.5 kGy per minute.

3.4 NEEDLE IMAGE PLATES : NIPS

Most of the work performed in the framework of this PhD thesis is on Eu doped CsBr needle image plates, that act as X-ray phosphors in medical radiography. In this section, we will first discuss the composition of the commercial imaging plates (subsection 3.4.1). Subsequently, the production (3.4.2) and constitution (3.4.3 and 3.4.4) of the active layer will be explained.

3.4.1 Medical imaging plates

Commercial imaging plates for computed radiography consist of various layers. In figure 3.7 a simplified picture of such a plate is shown, where only the most important layers are shown. An organic top layer protects the plate against humidity and scratches. No EPR signal was detected of this layer, but it is possible that a (small) signal after irradiation remained hidden under the large EPR signals at $g \sim 2$. The production of the PSL active part, the CsBr:Eu phosphor layer, will be discussed in the following subsection.
From now on, if we speak about NIPs, we will only refer to the CsBr:Eu needles, and neglect the other layers, since either they are removed before measuring (Al support) or they do not contribute (or at most hardly) to the EPR and ENDOR spectra.

Figure 3.7. Construction of a commercial NIP.
1. Organic protection layer
2. CsBr:Eu needles
3. Adhesive layer
4. Aluminum support

Less relevant layers, e.g. an anti-reflective coating, have been omitted.

3.4.2 Production of NIPs

Property [unit]	Value
Melting temperature [°C]	636
Crystal structure	Pm3m (CsCl structure)
Lattice constant [Å]	4.29
Density [g/cm^3]	4.44
Bandgap [eV]	7.3
Solubility [g/l H_2O]	1243

Table 3.4. Physical properties of CsBr

CsBr has a simple cubic crystal structure and table 3.4 shows some relevant physical properties of CsBr. Binderless Eu-doped CsBr needles are produced via chemical vapour deposition. In a controlled Ar-atmosphere (around 5 mPa), two separate[5] crucibles with CsBr and with Eu containing salts (e.g. EuOBr) are heated above 450°C. The atoms pile up on the substrate, which is slightly heated and mounted to a rotating plate. On top of a 10 μm thick polycrystalline seedling layer the typical needle structure starts to grow. Eu concentrations up to 0.1 mol% can be attained. Varying the deposition parameters (crucible and substrate temperature, Ar pressure, Eu dopant, ...) allows tuning the appearance of the NIP (needle diameter, Eu concentration, Eu^{2+} vs. Eu^{3+} ratio, layer thickness, ...). The needles are oriented perpendicular to the substrate and have a typical height of around 350 μm and a diameter of around 4-5 μm. More technical information can

[5]Because of their different vapour pressure, both components are evapourated in different crucibles.

e.g. be found in US PATENT 7126135 ('Radiation pretreated stimulable phosphor screen or panel', 2006) and in US PATENT 7422765 ('Binderless storage phosphor screen with needle shaped crystals', 2008).
Both in-house experience as literature (e.g. [28]) taught that after-treatment may increase the sensitivity (PSL intensity) by a factor 4. This treatment boils down to heating the NIP on air for 4 hours at 170°C and will be discussed in detail in Chapter 6. Here we just want to note that this treatment does not affect the morphology of a NIP.

3.4.3 SEM images

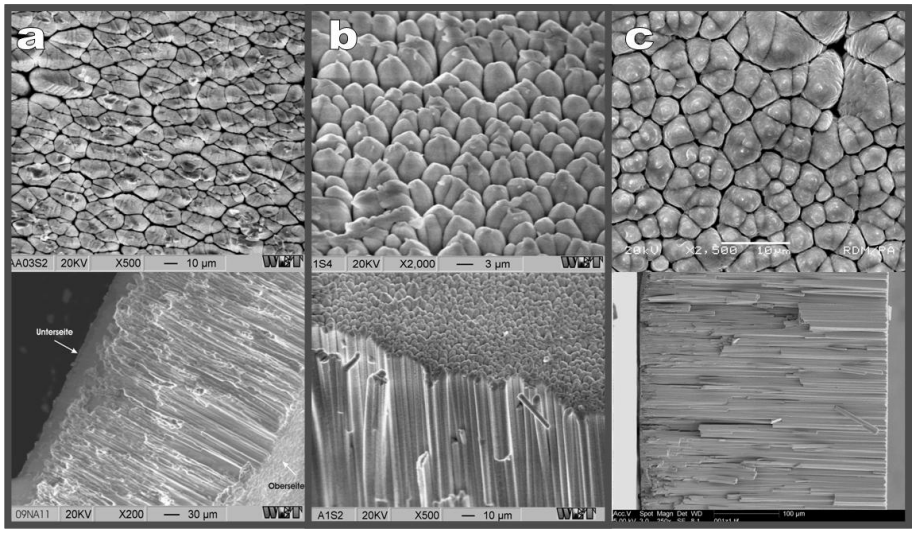

Figure 3.8. SEM micrographs of 3 NIPs. The upper two (a and b) were recorded by M. Weidner at University of Erlangen, c was recorded at Agfa HealthCare NV. Notice the different length scale of the pictures.
a. CB 12708 In the lower picture the polycrystalline seedling layer (see sec 3.4.2) can be seen at the bottom side ('Unterseite')
b. CB 74436
c. CB 74315
The latter two are more recent plates, showing more regular and thinner needles.

SEM (scanning electron microscopy) provides pictures with a high magnification and high resolution. The very large depth of field of the SEM micrographs yields a characteristic three-dimensional appearance useful for understanding the surface structure of a sample. SEM measurements were performed at Agfa HealthCare NV, at the University of Erlangen or in-house on a FEI Quanta FEG 200. Figure 3.8 shows the progress made by Agfa HealthCare NV during the PhD (2004-2009) on the quality of the needles. While older batches (CB 1****) have

more irregularly shaped needles, newer batches (CB 7****) show regular needles of smaller diameter, leading to a higher resolution to the NIP. For EPR purposes, the regularity of the needles was of lesser importance, but in general larger spacings between the needles lead to lower filling factors and should be avoided.

3.4.4 XRD images

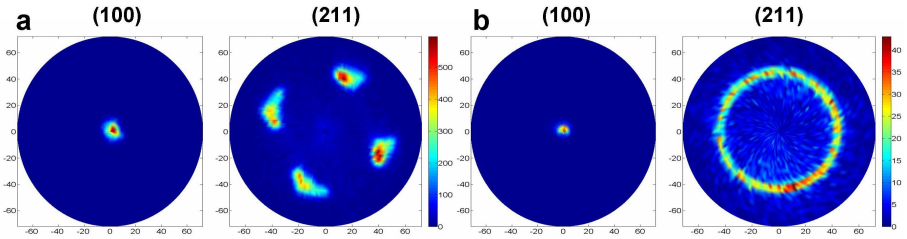

Figure 3.9. XRD pole figure of NIPs : (100) and (211) orientation.
a CB 12708_73
b CB 75516

The *pole figures* of NIPs revealed interesting information about the structure of these plates. In figure 3.9 pole diagrams for a (100) and (211) orientation are shown for two different NIPs. Since CsBr has a simple cubic structure the knowledge of these two directions[6] is sufficient to identify the orientation of the sample.
Figure 3.9 shows that the needle axis is oriented with a very narrow distribution along a <100> crystal axis, so when orienting the magnetic field parallel with the needles (i.e. perpendicular to the plate) a <100> (quasi) single crystal spectrum can be recorded. As CsBr has a cubic structure, this implies that this spectrum is composed of - possibly coinciding - [100], [010] and [001] subspectra.
The degree of in-plane orientation of the needles appeared to differ from plate to plate. Some plates have a pronounced in-plane orientation (figure 3.9a), while for other plates the needles are oriented in a random way (figure 3.9b). When the magnetic field is aligned parallel with such a plate, a so-called *2D powder spectrum* is recorded. This means that all orientations belonging to $\{100\}$ planes are present to a certain extent.

[6]The (211) direction is preferred over the (111) direction since the intensity of the corresponding 2θ peak is much higher. This can be seen in figure 3.6 : the (111) peak is the small unlabelled peak at 36,24°.

3.5 PRACTICAL ASPECTS OF EPR

The first provision for every EPR experiment, is to get the sample in the cavity. In Q band the sample is placed in a quartz tube or glued on a quartz rod. Clear fused quartz is qualitively sufficient, but sometimes suprasil tubes/rods are used for its higher resistance to irradiation.

Single crystal Crystals have to be oriented via XRD (see section 3.3.1) and subsequently cut/sawn to fit into the cavity. Due to the high bulk-surface ratio, hardly any surface effects can be seen in single crystal spectra.

3D powder To obtain a maximal filling factor, a powder should fill a tube over a length exceeding the active region of the cavity. To make powder of NIPs, pieces were crushed in a clean mortar with a pestle. To check whether this procedure did not affect the morphology of the defects, pressure up to 10^5 kPa was applied to the powder (via a AC Hydraulic A/S Hand-hydralic press Model PJ16H) and no difference in the EPR spectrum was found.

NIP Pieces of NIP were carefully cut from their support and placed in a tube or on a rod, with the plane parallel to the axis of the tube or rod. In that way, both a <100> and a 2D powder spectrum can be recorded with a 90° interval (see next subsection), since all used spectrometers are equipped with at least one goniometer, allowing 360° rotation of the sample around an axis perpendicular to the magnetic field. Since the NIPs have a limited height (around 1 mm) several pieces of NIP had to be stacked on top of each other in order to have a reasonable filling factor in X band (see figure 3.10) and extra inhomogeneity is inevitable.

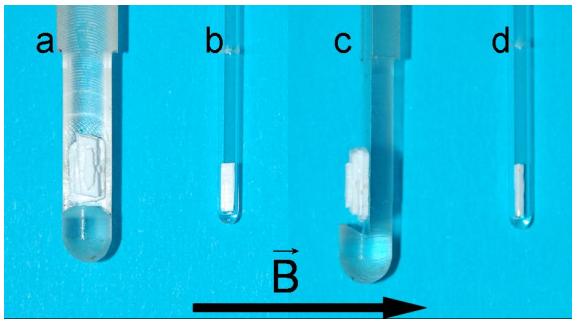

Figure 3.10. NIP mounted on an X band rod (a and c) and in a Q band tube (b and d). When the $\vec{B}$ is oriented parallel with the NIP (a and b) a 2D powder spectrum is recorded, when $\vec{B}$ is perpendicular to the NIP (c and d), a <100> single crystal spectrum is recorded.

3.5.1 Single crystal vs. 2D powder vs. 3D powder

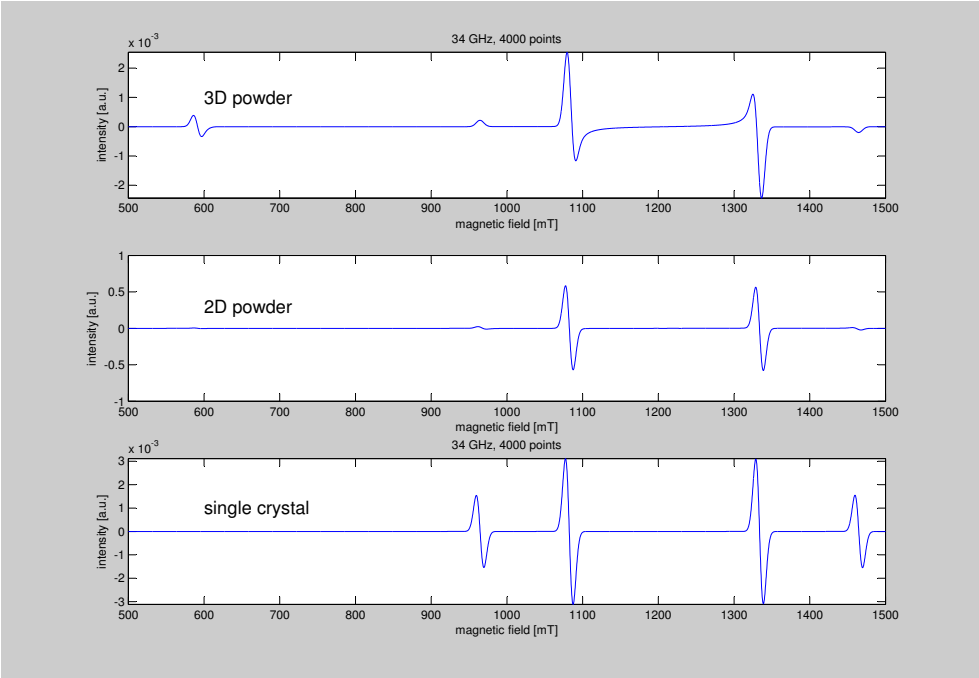

Figure 3.11. Output of the program samples.m

We illustrate the difference in spectrum between the 3 aforementioned types of samples (and the possibility to simulate these different kind of samples with ES) via a simple example in Q band. Let us consider an axial centre, with the following properties :

$$\begin{cases} S = 1 \\ g = 2 \\ D = 7000 MHz \end{cases} \tag{3.9}$$

No (S)HF was included and $S = 1$ was chosen in order to limit the number of EPR lines in the angular variation. D is kept smaller in comparison with the previous example (see page 34), because we want the full spectrum to appear in the magnetic field limit (B $<$ 1.5 T). Via the ES program *samples.m* (see Appendix) we simulated the EPR spectrum of this centre in a 3D powder (upper part of figure 3.11), in a 2D powder (middle part) and in a single crystal (with $\vec{B}$ parallel to the $<$100$>$ axis, lowest part of figure 3.11).
A full powder contains (in the ideal case[7]) every possible orientation of the sam-

[7]for very small samples, e.g. W band, one should take care that the powder grains are sufficiently small

ple and in general, only the principal values of the interactions can be determined and not the principal axes. In case of a large ZFS interaction it may be difficult to detect (parts of) a signal, since the intensity can be low at particular fields.
A 2D powder in NIPS is found when a the magnetic field is oriented along the plane of the NIP and only orientations belonging to a $\{100\}$ plane are present (see section 3.4.4).
In the lower part of figure 3.11 the single crystal spectrum is shown with $\vec{B}$ along a <100> crystal axis. The spectrum of a single crystal only contains one crystal orientation, but this does not mean that it only contains the contribution from one orientation of the defect. This phenomenon is called *site splitting* and can thoroughly complicate the EPR spectrum. A single crystal usually contains several symmetry-related defects. These defects can be transformed into each other by the symmetry operations of the crystal's point group and although they are chemically identical, magnetically they are not, since the corresponding principal axes of their EPR interaction tensors (like $\bar{\bar{g}}$, $\bar{\bar{D}}$, ...) have different relative orientations with respect to the applied magnetic field causing different EPR signals. In many EPR books this aspect of EMR spectroscopy is barely mentioned (e.g. in [29]), but more information can be found in [30] and in [31]. In the latter, the site splitting for with all possible symmetries in a NaCl lattice is illustrated using the g tensor.
In our simple example (3.9) the main symmetry axis of the D tensor (only the ZFS shows anisotropy) is along a <100> axis, so in the single crystal, centres can be found with either their x, y or z orientation along the considered <100> crystal axis. This means the single crystal spectrum is the composition of three EPR spectra : with $\vec{B}$ parallel to x, y and z respectively. This means the <100> spectrum counts a maximum of six lines : three orientations, each showing two ($|M_S = 0> \leftrightarrow |M_S = 1>$ and $|M_S = 0> \leftrightarrow |M_S = -1>$) transitions.

3.5.2 Angular variation

Since EPR and ENDOR belong to the few orientation sensitive techniques, this advantage should be maximally exploited via the use of single crystals. A so called *angular variation* of a single crystal will always lead to more information than a powder spectrum or than one single crystal orientation. To illustrate this, the angular variation in a (100) plane of the centre defined in (3.9) is simulated with *angvar.m* and shown in figure 3.12. 0° and 90° correspond to a <100> and a <010> axis, which are equivalent orientations in a cubic crystal, and the spectrum was simulated with a 5° interval. Due to site splitting, three orientations of the defect are present at <100> (x, y and z) and the angular variation follow six

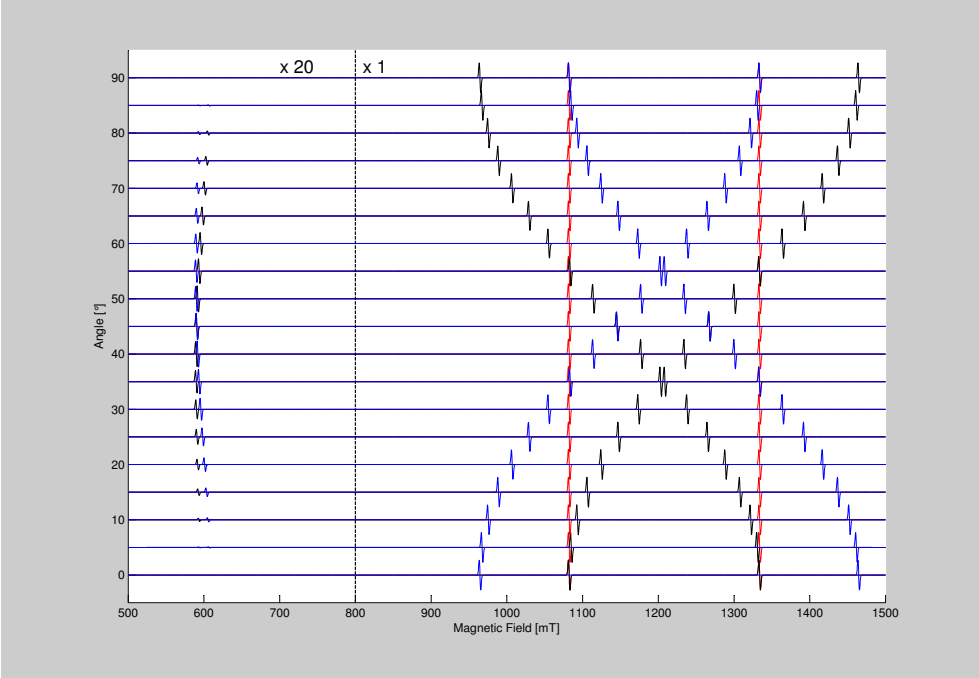

Figure 3.12. Output of the program angvar.m

possible pathways (from 0° to 90°) :

$$\begin{array}{lll} x \rightarrow y & y \rightarrow x & z \rightarrow x \\ x \rightarrow z & y \rightarrow z & z \rightarrow y \end{array}$$

Because of the equivalence of the x and y axes, only 4 transitions are present at <100> and the six pathways reduce to three

$$\begin{array}{ll} x \rightarrow y & \text{(in red, equivalent with } y \rightarrow x\text{)} \\ z \rightarrow x & \text{(in black, equivalent with } z \rightarrow y\text{)} \\ x \rightarrow z & \text{(in blue, equivalent with } y \rightarrow z\text{)} \end{array} \tag{3.10}$$

At orientations not along a principal axis of the defect, certain transitions with $|\Delta M_S| > 1$ obtain a non-zero transition probability. They appear in the low-field region and may also pop up in the 2D and 3D powder spectrum (compare figures 3.11 and 3.12)

3.6 CRYSTAL GROWTH

As already illustrated in previous sections, single crystals can significantly help the analysis of different systems. Crystals can be grown via various methods.

3.6.1 Hydrothermal crystal growth

Both the fluoroelpasolites in chapter 3 and the K_2YF_5 crystals from chapter 4 were grown under hydrothermal conditions, by Dr. N. M. Khaidukov, from the Institute of General and Inorganic Chemistry in Moscou. Hydrothermal synthesis is the use of aqueous solvents or mineralizers under high temperature and high pressure to dissolve and recrystallize materials that are relatively insoluble under ordinary conditions. Usually, the dissolution is carried out at the lower hotter zone (nutrient zone) and crystallization is carried out at the upper colder zone (growth zone). The convection currents created by the T gradient carry the material from the nutrient zone to the growth zone.

3.6.2 Bridgman crystal growth

At the Department of Solid State Sciences in Gent, various CsX (X = Br, Cl or I) single crystals have been grown via the Bridgman technique. The results on the experiments on these crystals will be reported in section 6.8.Growth started from pure CsX powder, CsX powder with Eu dopants and/or oxygen or from crushed NIPs.

Figure 3.13. Bridgman setup with two furnaces at constant temperature. The inset shows an undoped Bridgman grown CsBr single crystal.

The Bridgman growth method is basically a controlled freezing process taking place under liquid - solid equilibrium conditions. The growth takes place under

a temperature gradient, and the mechanism is to produce a single nucleus from which a single crystal will propagate and grow. Various temperature gradients can be used (see [32], page 51). In our setup (see figure 3.13) two furnaces with a constant temperature were used. The upper furnace has $T > T_{melt}$, while the lower has $T < T_{melt}$. A clean vacuum quartz ampoule, containing powder of the host material (e.g. CsBr) with or without a small amount of dopant, is entering the furnace from the top with the tip first and is lowered at a low and constant speed ($\approx$2mm/h) into the setup. The crystal growth starts from the tip, and after slowly cooling down the setup and removing the quartz, a single crystal can be retrieved (the inset of figure 3.13 shows an undoped CsBr single crystal). Via this technique cilindrical single crystals can be grown with diameters up to 4 cm and lengths up to 10 cm and more. At the Department of Solid State Sciences, three Bridgman lines are available, with two types of steering : either the temperature of both furnaces can be set (as in figure 3.13) or the percentage of maximum current through the heating coils is varied. While for the first a knowledge of the melt temperature suffices, for the latter experience is needed. In this respect, it seemed useful to collect in table 3.5 the settings for this setup for several (binary) crystals grown in our lab.

crystal	T_{melt}	percentage maximum current	
		upper furnace	lower furnace
NaCl	801	72	40
NaBr	747	68	40
NaI	661	62	40
KCl	770	70	40
KBr	734	64	40
KI	681	63	40
RbCl	718	64	40
RbBr	693	63	40
RbI	647	68	40
AgCl	455	50	22
AgBr	430	49	19
CsBr	636	60	40
CsCl	646	60	40
CsI	626	60	40

Table 3.5. Setting Bridgman setups in the Department of Solid State Sciences in Gent

For Eu doping of CsBr, mostly CEBLA was used. This is a mixture of Eu containing salts, produced by Agfa HealthCare NV and used by them for producing the

NIPs via PVD. For CsCl and CsI, $EuCl_2$ respectively EuI_2 were used and special care (working under a controlled atmosphere) had to been taken to combat the high hygroscopicity of these dopants.

CHAPTER 4

FE^{3+} IN FLUOROELPASOLITES

"If it isn't doctor ironside"
— DR. J. WILSON

4.1 INTRODUCTION

Since the early 1970s, perovskites and elpasolites have been intensively investigated with special focus firstly on synthesis and structure (e.g. [33, 34]). Nowadays, research activities concerning structural properties, concentrate on phase transitions and crystal structure determination ([35, 36, 37]). In 1979, interesting optical properties have been found [38] in Cr^{3+} doped K_2NaAlF_6 and the research focus became more and more optically oriented ([39, 40] and many others). Among the optical applications of elpasolites doped with rare earth (RE) and transition metal (TM) ions, we find e.g. tuneable lasers in the near IR, vacuum UV scintillators and mid IR emitters. Trivalent cations can be built in without charge compensation, making elpasolites appropiate candidates for host materials when high dopant concentrations are needed. Recent research [41] shows furthermore that Pr^{3+} or Ce^{3+} doped Cs_2NaYF_6 show promising X-ray storage phosphor characteristics.
EPR and ENDOR spectroscopy have become valuable tools from both a structural and an optical point of view, and a countless number of elpasolites with different dopants have been the subject of EMR investigations (see e.g. [42, 43, 44] or more recently [45, 46]). Also in our lab three fluoroelpasolites have been studied recently. Both Cs_2NaAlF_6 and Cs_2NaGaF_6 were initially doped with Cr^{3+} and the EPR/ENDOR results on the Cr^{3+} defects are described in [46, 47], while the results on Er^{3+} doped Cs_2NaYF_6 can be found in [48]. Unfortunately, in all these crystals an Fe^{3+} contamination is encountered, as can be the case in many other interesting materials : in YAG:Ce films [49], in ZnSe:Co [50], in CaB_6 [51], ... The

precise effect of this impurity on the (optical, electrical, ...) properties of such materials is not always fully understood or predictable. It is in any case important to be able to detect and identify these impurities, a task for which EPR and ENDOR are particularly well suited. In this chapter, we will describe the analysis of Fe^{3+} impurity centres in three elpasolite crystals. The complete EPR and ENDOR analysis can be found in [52]. In this chapter we will mainly focus on the ZFS of the Fe^{3+} ion.

4.2 CRYSTAL STRUCTURE

Fluoroelpasolites have the general form $A_2{}^{I}B^{I}M^{III}F_6$, where A and B are monovalent cations and M a trivalent cation. For their respective ionic radii, the following rule applies :

$$r_A > r_B > r_M \tag{4.1}$$

They are linked to perovskites with general form $A^{I}C^{II}F_3$ and the substitution of the C^{II} ions by differently charged B^{I} and M^{III} ions leads to a doubling of the lattice constant. With regard to the crystal structure, the fluoroelpasolites can be classified in two classes, depending on the Goldschmidt tolerance factor [53] :

$$t = \sqrt{2}\frac{r_A + r_F}{r_B + r_M + 2r_F} \tag{4.2}$$

When $0.88 \leq t \leq 1$, e.g. Cs_2NaYF_6 (lattice constant a = 9.08 Å), the crystal has a *cubic* structure, when $1 \leq t \leq 1.06$ a *hexagonal* structure, as is the case for both Cs_2NaAlF_6 ($a = b$ = 6.19 Å, c = 29.9 Å) and Cs_2NaGaF_6 ($a = b$ = 6.24 Å, c = 30.3 Å). The complete crystal structure has been described in length elsewhere. Explanatory pictures can be found in [44] (hexagonal crystals) and in [42] (cubic crystals). When entering the elpasolite crystal, the Fe^{3+} impurity subsitutes for the M^{3+} ion. In a cubic elpasolite the M^{3+} position, being surrounded by 6 equivalent fluorine ions, has perfect octahedral symmetry. It has been shown on the other hand, that in hexagonal crystals two inequivalent sites exist for the M^{3+} ion. Both have nearly octahedral symmetry, one slightly compressed and the other slightly elongated along the crystallographic c axis. We will from now on refer to them as sites R (from regular), C (compressed) and E (elongated) respectively. In figure 4.1 the three different sites are illustrated, indicating the nearest three neighbouring shells.

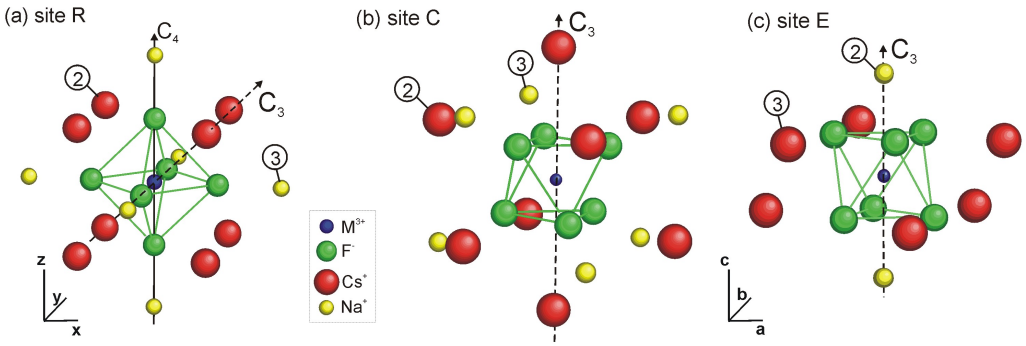

Figure 4.1. Lattice surroundings of the M^{3+} ion in a cubic elpasolite in the regular octahedral site R (a) and in a hexagonal elpasolite in the trigonally compressed site C (b) and in the trigonally elongated site E (c).
In all cases the crystal axes and a trigonal and/or tetragonal symmetry axis are indicated. The c axis is the trigonal symmetry axis in the hexagonal crystals.
The second and third shells, consisting solely of either Cs^+- or Na^+-ions, have also been indicated; the first shell (consisting of 6 F^--ions) is the same for the three sites.

4.3 The spin Hamiltonian of Fe^{3+}

The Fe^{3+} ion has an (Ar)$3d^5$ configuration and a $^6S_{5/2}$ ground state. S-state ions, like Fe^{3+} and Eu^{2+}, have a nearly isotropic g value close to g_e, since there is no orbital momentum.
No HF interaction is visible in the EPR spectrum of iron, since ^{57}Fe, the only magnetic isotope, has only 2% of natural abundance, so only SHF and quadrupole interaction with neighbouring nuclei has to be accounted for.
For $S = 5/2$ terms up to $k = 4$ should be included in $\hat{H}_{\text{ZFS}}$ and for the cubic case we can use $\hat{H}_{\text{ZFS}} = B_4^0\left(\hat{O}_4^0 + 5\hat{O}_4^4\right)$ (equation (2.30), page 18) or $\hat{H}_{\text{ZFS}} = -\frac{2}{3}B_4^0\left(\hat{O}_4^0 + 20\sqrt{2}\hat{O}_4^3\right)$ (equation (2.35), page 20) when the z axis of $\hat{H}_{\text{ZFS}}$ is taken along a tetragonal or trigonal symmetry axis respectively. Here we will use (2.35) for easier comparison with the hexagonal case, so the value of B_4^0 in the next subsection is valid when the z axis is along a trigonal symmetry axis. In the hexagonal crystals we will use $\hat{H}_{\text{ZFS}} = B_2^0\hat{O}_2^0 + B_4^0\hat{O}_4^0 + B_4^3\hat{O}_4^3$.

4.4 The Fe^{3+} ion in the cubic elpasolite Cs_2NaYF_6

For this crystal, the X band setup offered the best opportunity to orient the sample. The <100> spectrum at 8K is shown in figure 4.2. For an Fe^{3+} impurity at a site with cubic symmetry, five allowed unsplit EPR lines are expected. This five

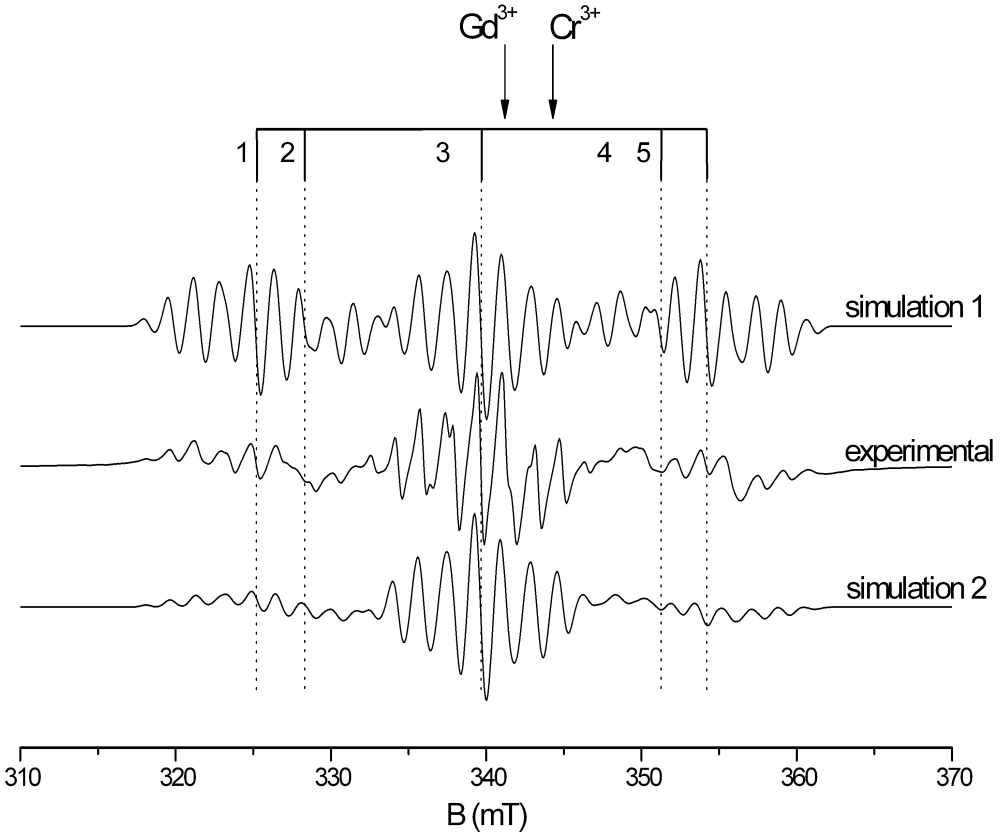

Figure 4.2. EPR spectrum of Cs_2NaYF_6:Fe^{3+}, with $\vec{B}||<100>$ at X band (ν = 9.513 GHz, T = 8K). The middle spectrum represents the experimental spectrum. The upper spectrum (simulation 1) shows a simulation without strain in B_4^0, the lower spectrum (simulation 2) with a gaussian distribution (FWHM = 0.37 MHz) in B_4^0. At the top the five lines due to the ZFS are indicated. The magnetic field positions of the g values of the Gd^{3+} and Cr^{3+} impurities are indicated with an arrow to show that the spectra of these impurities could not be resolved in X band.

lines structure cannot easily be recognised in the multiline EPR spectrum, due to the additional splitting as a result of the SHF interaction with the six ^{19}F nuclei in the first shell. Because of this, the EPR spectrum is quite complex and the SHF tensor for this interaction had to be deduced from the ENDOR analysis.

4.4.1 ^{19}F ENDOR analysis

In the ENDOR spectrum, interactions with the first coordination shell of the Fe^{3+} ion, consisting of 6 equivalent ^{19}F nuclei, are observed. The cubic symmetry of the centre requires that their A tensors are axially symmetric around the metal-ligand axis. For $\vec{B}||<100>$ the unpaired electrons of Fe^{3+} interact with two sets of equivalent ^{19}F nuclei: 2 nuclei along the $<100>$ axis and 4 nuclei in the equatorial

plane with interaction constants $A_\perp$ and $A_{||}$ respectively. When saturating an $M_S \leftrightarrow M_S + 1$ EPR transition, the following two ENDOR lines are expected for each set of equivalent ^{19}F nuclei ($I = \frac{1}{2}$) :

$$\begin{cases} \nu &= \frac{1}{h} \left| A M_S - \nu_L \right| \\ \nu &= \frac{1}{h} \left| A \left(M_S + 1 \right) - \nu_L \right| \end{cases} \tag{4.3}$$

with $\nu_L = g_N \beta_N B$ the Larmor frequency. $A_\perp$ and $A_{||}$ were determined by fitting resonance positions in the X band ENDOR spectra with $\vec{B}||<100>$ at different field positions and the obtained parameters are

$$\begin{cases} A_\perp &= 44.5 \text{ MHz} \\ A_{||} &= 103.7 \text{ MHz} \\ \Theta &= 54°11' \end{cases} \tag{4.4}$$

with Θ the angle between the C_3 axis and the principle $A\left(^{19}F\right)$ direction. An ENDOR angular variation at Q band confirmed these values. In principle, their absolute signs cannot be determined from the ENDOR spectra, so we assumed that $A\left(^{19}F\right) > 0$, in agreement with literature from analogous systems.

4.4.2 EPR analysis

The obtained SHF parameters enabled us to unravel the EPR spectrum and to extract the isotropic g factor and one independent ZFS parameter : B_4^0. The values are listed in table 4.1.

	Cs_2NaYF_6:Fe^{3+}	Cs_2NaAlF_6:Fe^{3+}		Cs_2NaGaF_6:Fe^{3+}	
Site	R	C	E	C	E
g	2.0028_{20}	2.0023_{18}	2.0022_{18}	2.0023_{10}	2.0023_{12}
B_2^0[MHz]	-	$215.5_{3.4}$	$-244.7_{3.7}$	$180.0_{2.6}$	$-216.3_{2.8}$
B_4^0[MHz]	-0.90_{3}	-0.98_{13}	-1.14_{16}	-0.95_{11}	-1.19_{14}
B_4^3[MHz]	$20\sqrt{2}B_4^0$	$-27.4_{4.0}$	$-36.4_{9.5}$	$-28.3_{4.1}$	$-37.2_{6.7}$

Table 4.1. g value and ZFS parameters of Fe^{3+} in three elpasolites (errors in the last digits given as subscripts)

The simulated EPR spectrum (simulation 1 in figure 4.2), however, shows a remarkable difference in the intensities of the outer SHF packets, as compared to the experimental spectrum. This discrepancy is removed to a large extent by allowing for a (gaussian) distribution in the B_4^0 parameter retaining cubic symmetry ($B_4^3 = 20\sqrt{2}B_4^0$). This may reflect random strain in the crystal. In simulation 2

such a gaussian distribution in the ZFS parameters is taken into account, with FWHM = 0.37 MHz. This simulation agrees much better with experiment, regarding line intensities.
The remaining differences may be attributed to overlap with the spectra of Gd^{3+} and Cr^{3+} impurities, whose presence was proved by W band measurements (figure 4.3). In X (see figure 4.2) and Q band their EPR spectra overlap because their g values are close to 2 when $\vec{B}||<100>$ (2.0028 (Fe^{3+}), 1.992 (Gd^{3+}) and 1.958 (Cr^{3+}) respectively), but by using the high spectral resolution in W band (see section 3.2.6), we could resolve the three components in the spectrum.

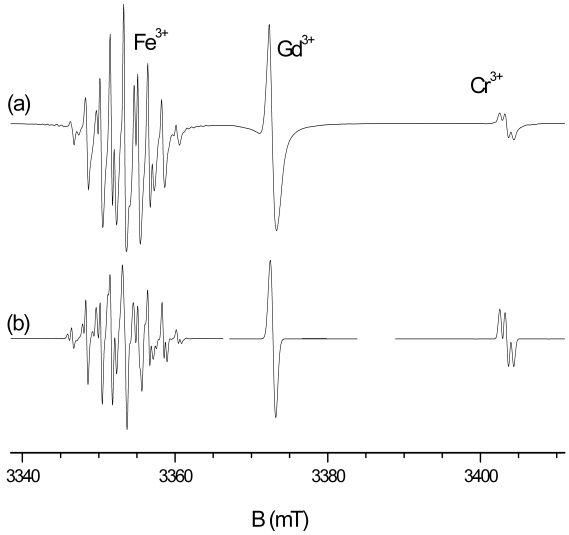

Figure 4.3. Experimental (a) and simulated (b) W band (ν = 94.01 GHz) EPR spectrum of Cs_2NaYF_6:Fe^{3+},Gd^{3+},Cr^{3+} at a random magnetic field orientation. The simulation parameters are taken from [52] and [42]. The spectra of the three components are centred around their effective g value.

4.4.3 2D ENDOR analysis

From the EPR analysis alone, only the size of the ZFS parameter could be obtained. This is illustrated in figure 4.4 where all SHF interaction is neglected. In this figure, both the energy level scheme and the EPR spectrum are simulated for $\vec{B}||<100>$ with $|B_4^0|$ = 0.90 MHz and $B_4^3 = 20\sqrt{2}B_4^0$. We see that the EPR spectrum when $B_4^0 > 0$ (the left side of figure 4.4) is identical to the EPR spectrum when $B_4^0 < 0$ (right side of figure 4.4). However, the lowest field position (B = 324.5 mT) corresponds to the $M_S = \frac{1}{2} \leftrightarrow M_S = \frac{3}{2}$ transition when $B_4^0 > 0$ but to the $-\frac{1}{2} \leftrightarrow -\frac{3}{2}$ transition when $B_4^0 < 0$. In other words, when saturating the EPR transition at 324.5 mT, different NMR transitions will be visible in the ENDOR spectrum (see equation (4.3)).

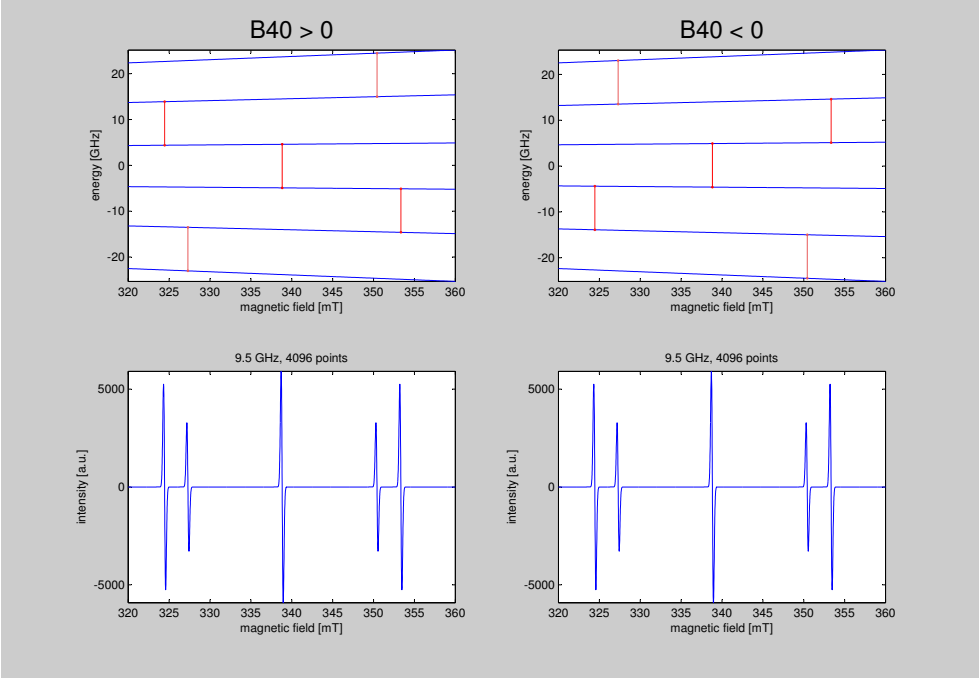

Figure 4.4. Simulation (with ES) of both the energy levels with the allowed (in red) EPR transitions (on top) and the EPR spectrum (at the bottom) in X band (ν = 9.5 GHz) of Cs_2NaYF_6:Fe^{3+} with $\vec{B}$||<100>. $B_4^0 > 0$ at the left and $B_4^0 < 0$ at the right, while in both cases $|B_4^0|$ = 0.90 MHz and $B_4^3 = 20\sqrt{2}B_4^0$.

The difference in ENDOR can thus be used to determine the sign of the ZFS parameters relative to the sign of the SHF parameters. Also for these crystals, we assume that $A\left(^{19}F\right) > 0$. At Q band a complete field variation of the ENDOR spectrum was recorded for $\vec{B}$ approximately along <100>. This is represented in the 2D ENDOR plot in figure 4.5. On top the complex EPR spectrum is shown in this orientation.

The figure gives a clear overview of which M_S states are involved in the saturated EPR transitions at each magnetic field position. ENDOR transitions within the $M_S = \frac{5}{2}$ state, for example, are most efficiently excited in the low field wing of the EPR spectrum, which can only be explained when $B_4^0 < 0$.

Also the variation of the ENDOR line positions as a function of the magnetic field strength can easily be explained from equation (4.3), which for positive ^{19}F principal SHF values predicts that the ENDOR frequency within negative (positive) M_S states goes up (down) with increasing magnetic field.

In conclusion, we could deduce that, if $A\left(^{19}F\right) > 0$ then $B_4^0 < 0$, as noted in table 4.1.

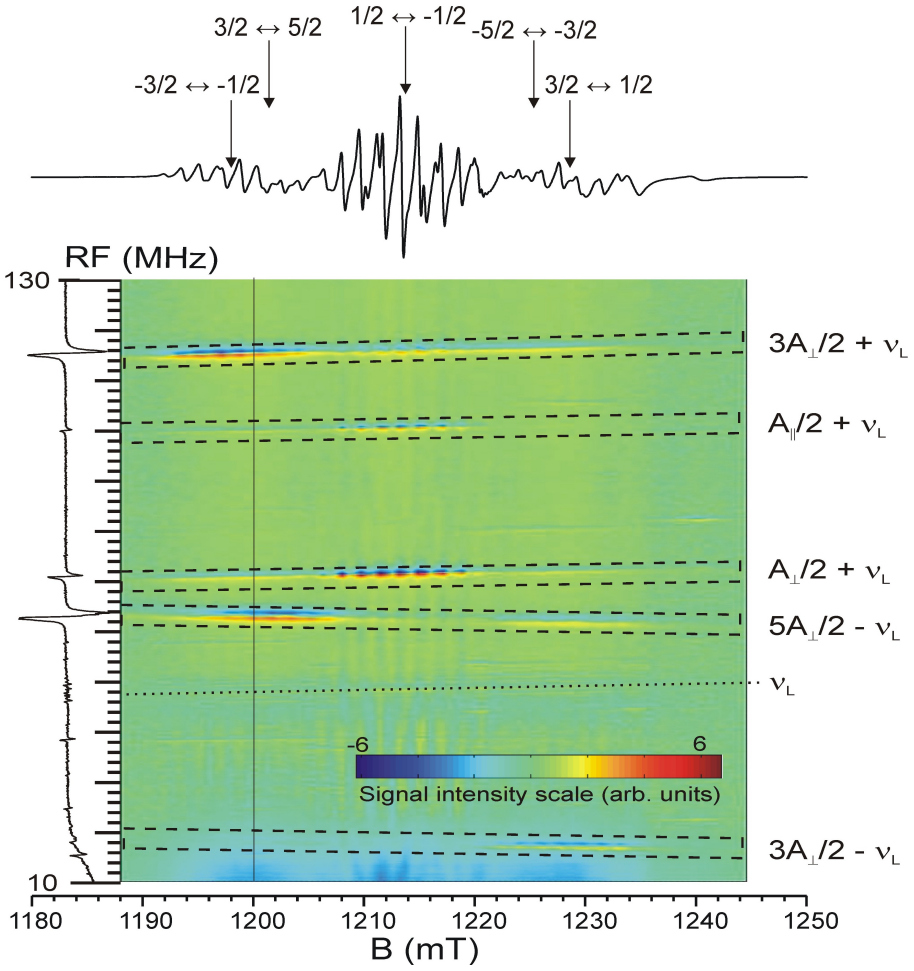

Figure 4.5. Two dimensional intensity (square root of intensity for contrast enhancement) plot of first derivative ENDOR spectra as a function of magnetic field for Cs_2NaYF_6:Fe^{3+} at ν = 34.010 GHz and T = 12 K. The EPR spectrum is shown on the top and the ENDOR spectrum at B = 1200 mT (indicated with full line in the 2D plot) is shown on the left. The transitions are labelled with the first order expression of their ENDOR frequency (see (4.3)). The position of ν_L is marked as well.

4.5 FE^{3+} IN THE HEXAGONAL ELPASOLITES Cs_2NaGaF_6 AND Cs_2NaAlF_6

4.5.1 EPR analysis

For both crystals EPR spectra were recorded at Q band and the angular variation of Cs_2NaAlF_6 in a plane containing the c axis is shown in figure 4.6. For $\vec{B}||c$, all six surrounding ^{19}F nuclei are equivalent, thus forming a 7 line SHF pattern, with 1:6:15:20:15:6:1 ratios. Since the ZFS is larger than in the cubic crystals, ten zero field split SHF packets are expected, as there are two inequivalent Fe^{3+} sites (see

figure 4.1). Only eight are visible, though, since the $|\frac{1}{2} > \rightarrow |-\frac{1}{2} >$ transitions for both sites overlap and one SHF packet is hidden under the more intense Cr^{3+} lines (all resonance lines in figure 4.6 which show no SHF splitting). The two EPR spectra can be well separated and linked to sites E and C, on the basis of their distinct ^{23}Na ENDOR spectra.

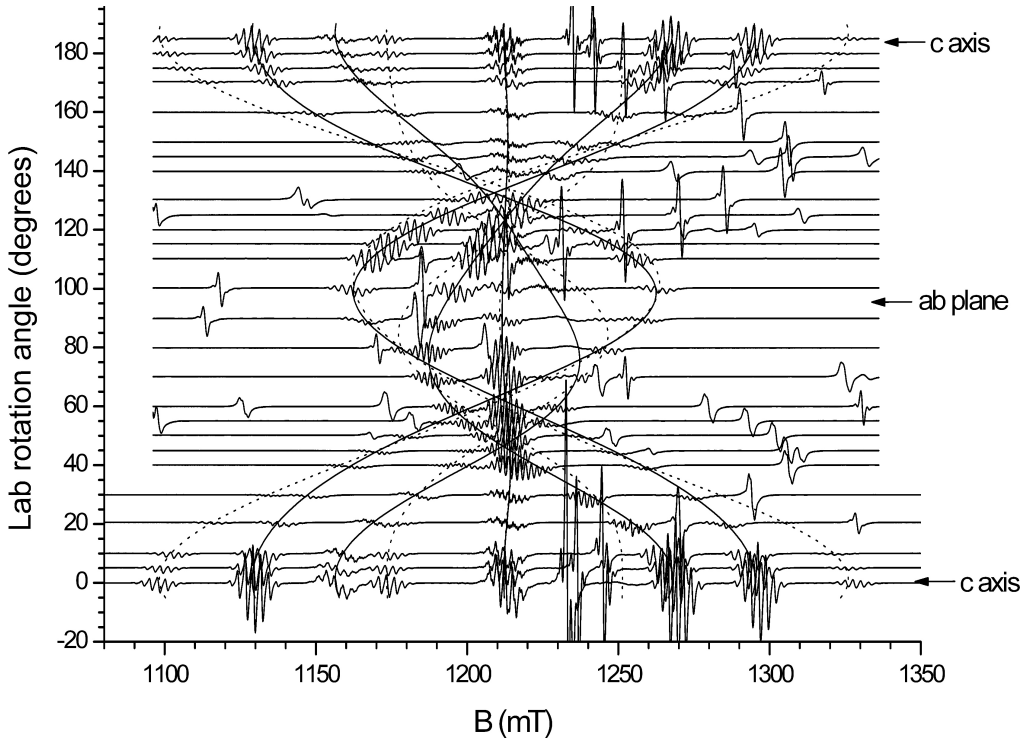

Figure 4.6. Q band EPR angular variation of Cs_2NaAlF_6:Fe^{3+} at 10K and ν = 33.97 GHz. The additional resonances which show no SHF splitting, belong to Cr^{3+} centres. The dashed (solid) lines represent the simulation of the central lines of the SHF packets of site E (site C).

4.5.2 ^{23}Na ENDOR analysis

In figure 4.1 the different ^{23}Na environment is clearly visible for the two hexagonal sites: site C has six ^{23}Na ions in the third shell forming a distorted octahedron, while site E has two ^{23}Na ions along the c axis. In the ^{23}Na ENDOR spectrum with $\vec{B}||c$ this difference is clearly visible.
For site E, the ^{23}Na ENDOR spectrum consists of two widely split triplets (separated by $A_{||}$). This is illustrated for Cs_2NaGaF_6 in figure 4.7. Six equivalent ^{23}Na nuclei on off-axis positions with a smaller (further away than in site E) SHF interaction characterize site C. The corresponding ENDOR spectra are broader and show a smaller splitting (e.g. ENDOR spectrum at B = 1145.1 mT in figure 4.7).

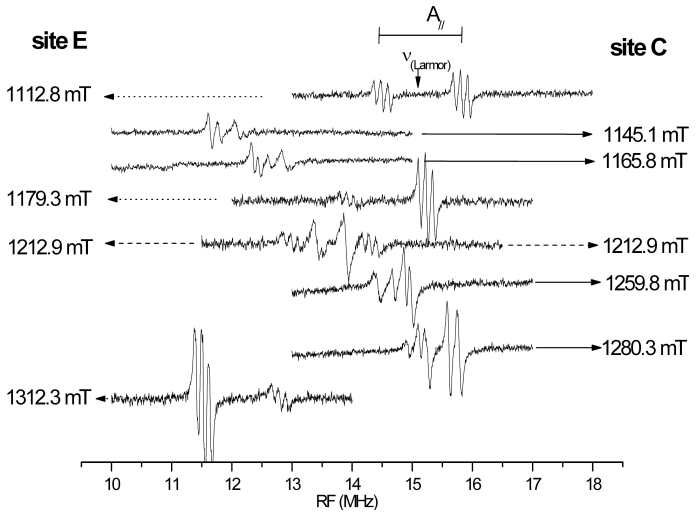

Figure 4.7. ^{23}Na ENDOR spectra of site C and site E in Cs_2NaGaF_6, recorded at various field positions at T = 10 K (indicated on the left: solid arrows for site C, dashed arrows for site E). At 1212.9 mT the lines for the sites coincide and the typical ^{23}Na ENDOR spectrum of both sites is present.

Based on these qualitative differences between the ENDOR spectra, we could assign each EPR transition to a particular site and at B = 1212.9 mT the spectra of both sites clearly overlap. The spectra with $\vec{B}$ in the ab plane were decomposed in an analogous way. The g value and ZFS parameters could be obtained for both sites, as listed in table 4.1. They were used to simulate the central line of the SHF packets of both sites in figure 4.6. Since the SHF packets were this time well separated, a detailed analysis of the strain was not necessary to obtain the ZFS parameters.
As for the cubic crystal, X band or Q band frequencies only allowed to determine the signs of the B_k^q parameters relative to that of the ^{19}F SHF parameters.

4.5.3 W band analysis

We used W band measurements to check the assumption that $A\left(^{19}F\right) > 0$. The MW quantum at W band is large enough to observe thermal population effects at low temperatures. Indeed, the states with high M_S become depopulated at low temperatures and high field, which allows to determine the absolute sign of the ZFS parameters. With equations (3.5) and (2.29) one can easily calculate that the energy of each M_S level equals

$$E\left(M_S\right) = g\beta_e B M_S + B_2^0(3M_S^2 - S(S+1)) \tag{4.5}$$

In table 4.2 these levels are calculated both for Q and W band assuming resonance conditions for $g = 2$, so $g\beta_e B$ = 34 GHz and 94 GHz respectively. The

absorbed MW power in an EPR transition is proportional to the population difference (equation (2.45)) of the two involved states and one can use these energy differences to calculate the absorbed MW power in both bands at 5 K and RT (T = 300 K). At W band and at 5 K the absorption ratio between the $-\frac{5}{2} \leftrightarrow -\frac{3}{2}$ transition on the one hand and $\frac{5}{2} \leftrightarrow \frac{3}{2}$ on the other hand is clearly much higher (35.9) than at 300 K (1.03).

M_S	Energy (GHz)		population			
	Q	W	Q	W	Q	W
			300 K	300 K	5 K	5 K
$\frac{5}{2}$	87.0	237.0	0.973	0.928	0.195	0.011
$\frac{3}{2}$	51.5	141.5	0.979	0.942	0.274	0.027
...	...	...	...	...	...	
$-\frac{3}{2}$	-50.5	-140.5	0.995	0.985	0.732	0.411
$-\frac{5}{2}$	-83.0	-233.0	1	1	1	1

Table 4.2. Population of M_S eigenstates in Q and W band at 5 K and 300 K, normalized to the population of the $M_S = -\frac{5}{2}$ level. B_2^0 is approximated as 200 MHz and contributes only to a smaller extent to the energy value.

In figure 4.8 these effects are shown for Cs_2NaAlF_6 with $\vec{B}$ close to c. From the relative intensity differences between 100 K and 5 K, we could derive the absolute[1] signs of the ZFS parameters by comparing, for example, the two lowest lying SHF packets of site E : lying centred around 3240 mT (packet 1) and around 3320 mT (packet 2). When lowering the temperature, the intensity of packet 2 decreases in comparison with the intensity of packet 1, meaning that SHF packet 2 corresponds to EPR transitions between M_S manifolds with higher energy than packet 1. Simulations (comparable to those in figure 4.4) of the different possible sign assignations for the ZFS parameters showed that the signs correspond perfectly with those acquired with the aforementioned supposition. This assures that the sign attributions are correct.

4.6 Discussion and conclusion

Considering the parameters in table 4.1, B_2^0 appears to be a very clear marker for the distortion of the site. Its sign seems to depend on the type of distortion: for the elongated E site $B_2^0 < 0$ and for the compressed C site $B_2^0 > 0$. Moreover, the magnitudes of B_2^0 are larger in site E than in site C and larger in Cs_2NaAlF_6 than

[1] This still implies that one knows the sign of the g values, but as already stated for an S-state ion g is close to g_e, thus $g > 0$.

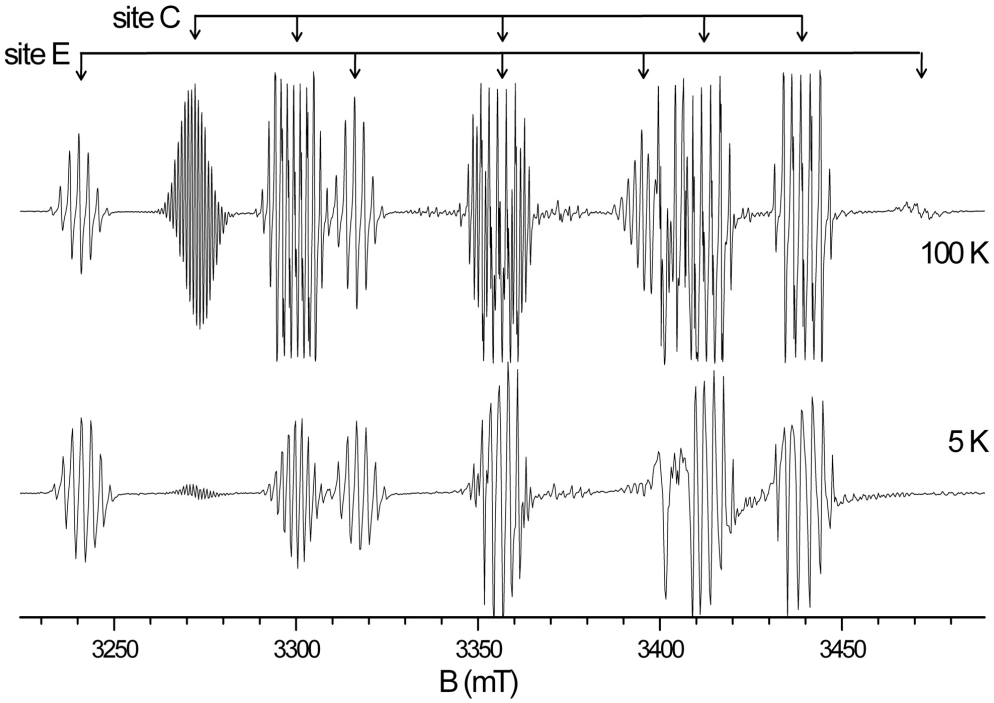

Figure 4.8. W band EPR spectrum of Cs_2NaAlF_6:Fe^{3+} with ν = 94.067 GHz and $\vec{B}$ close to c when T = 100 K and T = 5 K. On top is indicated to which site each SHF packet belongs and the intense line around 3400 mT could be attributed to Cr^{3+}. The spectra have been normalized with respect to the low field signal around 3240 mT.

in Cs_2NaGaF_6. The latter is in contrast with the structure of the undoped crystal: the deviation from a perfect octaëder is (for both sites) larger in Cs_2NaGaF_6 than in Cs_2NaAlF_6 (calculated with [35] and [36], see [47], page 86). Probably, Fe^{3+} induces a bigger distortion in Cs_2NaAlF_6 because its ionic radius in a sixfold coordination (r = 69 pm) matches better with the radius of Ga^{3+} (r = 62 pm) than with Al^{3+} (r = 53 pm).
Finally, for all sites we found that B_4^0 is negative in the trigonal reference frame and curiously, within the error, we found no deviation from cubic symmetry in the B_4^3 parameters in the hexagonal crystals ($B_4^3/B_4^0 \approx -20\sqrt{2}$).
Besides the structural information about the Fe^{3+} impurity, its ZFS and SHF parameters (and these of other dopants) can be used as a starting point for testing the reliability of theoretical ab initio , e.g. density functional theory (DFT), calculations of g, HF and ZFS parameters (e.g. [54]).

In this chapter, we characterized three different Fe^{3+} defects. Fe^{3+} is an S-state ion ($^6S_{5/2}$ ground state), as is Eu^{2+} ($^8S_{7/2}$ ground state), with S = 5/2. The high

spin causes a complex ZFS, which will also be encountered in the analysis of Eu^{2+} (S = 7/2) spectra. We could determine both the sign and the value of the SH parameters, using 2D ENDOR and/or variation in population ratios of the energy levels at high field and low temperature. These experimental procedures will also be used to characterize the Eu^{2+} defects in CsBr needle image plates in chapter 5.

CHAPTER 5

RARE EARTH IONS IN K_2YF_5

"Oh, must be a full moon, my hand goes magnetic."
— DR. C. TODD

5.1 INTRODUCTION

Recently it has been discovered that K_2YF_5 crystals singly doped with optically active RE ions are promising phosphors for thermoluminescence (TL) dosimetry. Such TL phosphors show relatively high sensitivity to ionizing radiation and low fading, while for some K_2YF_5:RE combinations the shape of the TL glow curves depends on the type of radiation, which offers possibilities for discriminating mixed radiation fields [55, 56, 57]. The latter is illustrated in figure 5.1 for $K_2YF_5:Ce^{3+}$

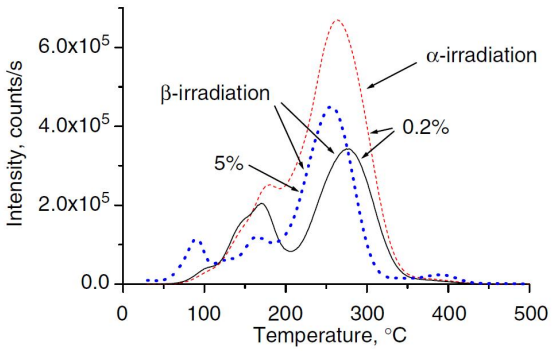

Figure 5.1. TL glow curves of K_2YF_5 doped with 0.2 at% Ce^{3+} following α and β irradiation to a 1 Gy dose and with 5.0 at% Ce^{3+} following β irradiation to a 0.3 Gy dose at the 5°C/s heating rate (from [57]).

In order to understand the TL mechanisms in these crystals, the microscopic structure of stable trapped electron and trapped hole centres, created upon ex-

posure to radiation, has to be determined and their thermal annealing behaviour has to be followed. The knowledge of the crystal symmetry is very important for the identification of these irradiation defects. Single crystal XRD studies have led to the conclusion that the space group of the orthorhombic K_2YF_5 lattice (a = 1.0791, b = 0.660 and c = 0.725 nm) is either Pnam or $Pna2_1$ [58, 59] whereas for the K_2GdF_5 compound Pnam symmetry was established [60]. These two crystal symmetry types are closely related. Rb_2ZnCl_4, for example, undergoes a phase transition [61] from Pnam to $Pna2_1$ when lowering the temperature from above 303 K to lower than 189 K. It is hard to distinguish both symmetries using only the data from powder XRD measurements [62]. On the other hand, the site for the Y^{3+} ions in K_2YF_5 which are substituted by RE^{3+} ions has been reported to have C_{2v} [63, 64], near-to C_{3v} [59] or even C_1 symmetry [58]. In order to elucidate this problem, K_2YF_5 crystals containing Ce^{3+} and Gd^{3+} as paramagnetic probes have been studied with EPR. In this context it should be noted that, from the viewpoint of charge and ionic radius matching, low concentrations of these RE^{3+} ions are not expected to change the local site symmetry, when they substitute for Y^{3+}.

5.2 Y^{3+} SITE SYMMETRY IN THE PNAM AND THE $PNA2_1$ CRYSTAL STRUCTURE OF K_2YF_5

From XRD studies it is known that the Y^{3+} ions are heptacoordinated and YF_7 polyhedra form chains running along the c axis by sharing two F^- ions with each adjacent polyhedron (see figure 5.2a). Six of the F^- ions in the first shell form a distorted octahedron around the Y^{3+} ion, and the connection to the seventh F^- ion is nearly parallel with the b axis. In both space groups, the unit cell contains four formula units, which can be transformed into one another by the crystal symmetry operations, as shown in figure 5.2b :

1. (x,y,z) : unity operator
2. (-x,-y,1/2+z) : twofold screw axis c
3. (1/2-x,1/2+y,1/2+z) : bc mirror plane + translation over (a/2,b/2,c/2)
4. (1/2+x,1/2-y,z) : ac mirror plane + translation over (a/2,b/2,0)

These restrictions imply a $Pna2_1$ structure and triclinic C_1 symmetry for the Y^{3+} ion. In the case of the Pnam space group, I (figure 5.2b) is a centre of inversion symmetry. This means[1] that the YF_7 polyhedra have a horizontal mirror plane

[1]The calculations can be found in [65].

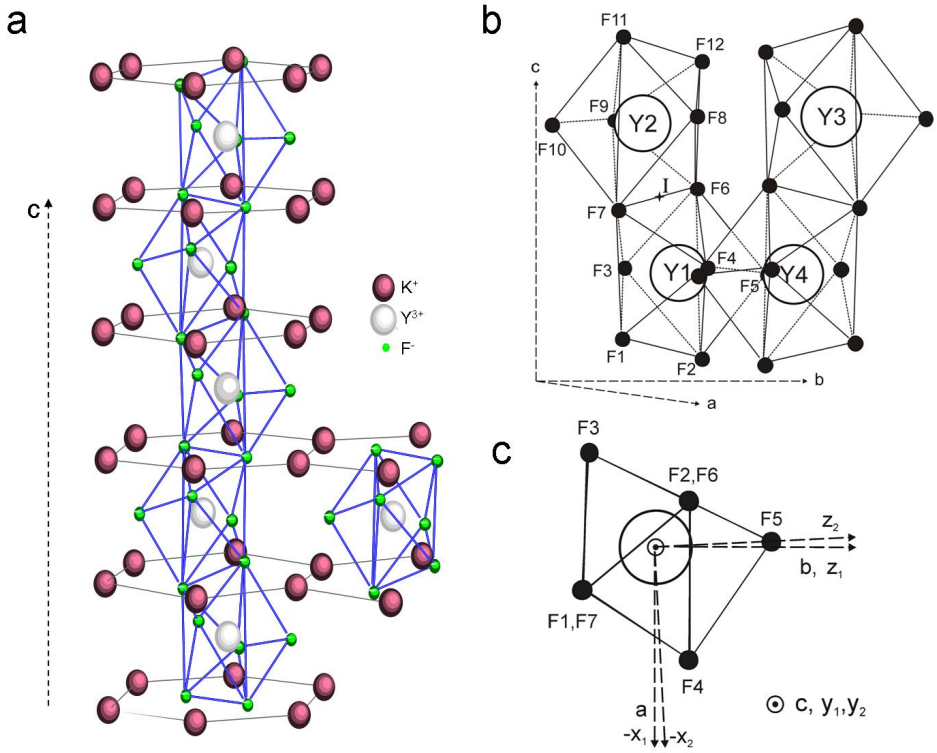

Figure 5.2. **a** The orthorhombic crystal structure of K_2YF_5
b Four symmetry-related YF_7 polyhedra in the unit cell of K_2YF_5
c Top view (along c axis) of the coordination polyhedron for site Y1 (see **b**), defining the reference frames used in the EPR analysis.

and monoclinic (C_h) symmetry. The central Y^{3+} and three F^- ions (F3/8, F4/9, F5/10) lie in these mirror planes. Inversely, the horizontal mirror plane symmetry restriction in combination with the twofold screw axis implies that I is a centre of inversion symmetry. Thus, there is a one-to-one relation between the space group and the Y^{3+} site symmetry for the K_2YF_5 structure. Accordingly, one can determine the space group of K_2YF_5 with EPR spectroscopy using RE^{3+} ions substituting for Y^{3+} as paramagnetic probes.

As the site symmetry of the paramagnetic centre (mono- or triclinic) is lower than the symmetry of the host (orthorhombic), we can make use of the fact that for arbitrary magnetic field orientations several inequivalent orientations of the centre occur, whose EPR spectra do not coincide. The number of inequivalent orientations is related to the site symmetry, as explained below for this particular case.
Gd^{3+} and Ce^{3+} may substitute for Y^{3+} in all four coordination polyhedra in the unit cell, which have the same symmetry but different orientations (figure 5.2b). In the case of *triclinic* site symmetry C_1, EPR spectra of *four* differently oriented coordination polyhedra for the same RE^{3+} centre can simultaneously be observed

at an arbitrary orientation of the magnetic field. However, when the magnetic field is parallel to the a, b or c axis, these four spectra coincide. At an arbitrary orientation in the ab plane (bc, ca) the spectra for RE^{3+} in positions 1 and 2 (1 and 3, 1 and 4) as well as 3 and 4 (2 and 4, 2 and 3), are coincident and, accordingly, in these planes a superposition of only two (sets of) lines is expected. On the other hand, in the case of *monoclinic* C_h site symmetry, the YF_7 polyhedra 1 and 2 are connected by inversion symmetry and the EPR spectra of RE^{3+} ions occupying these sites coincide for all magnetic field orientations. The same holds for polyhedra 3 and 4, and thus, at an arbitrary orientation of the magnetic field, the four differently oriented YF_7 polyhedra give rise to only *two* different components in the EPR spectrum. For magnetic field orientations in the bc and ca planes, the EPR spectra of RE^{3+} in all four polyhedra are coincident.
Both figures 5.3 and 5.4 include angular variations taken at planes who do not correspond to principal planes. At maximum 2 components can be seen, so we can already conclude that both Gd^{3+} and Ce^{3+} have monoclinic symmetry.

5.3 THE SPIN HAMILTONIAN DESCRIBING GD^{3+} AND CE^{3+}

Gd^{3+}, present as accidental impurity at the ppm level, has an (Xe)$4f^7$ configuration and a $^8S_{7/2}$ ground state. As was the case for Fe^{3+}, we expect an isotropic g value close to g_e. No (S)HF structure is resolved in the EPR spectrum. Fitting of the data revealed that the g anisotropy and the sixth rank ZFS parameters have an insignificant influence on the total fitting error and therefore, in order to reduce the number of fitting parameters, have been ignored. The following SH has been used :

$$\hat{H} = \beta_e g \vec{B} \cdot \hat{\vec{S}} + \sum_{k=2,4} \sum_{-k \leq q \leq k} B_k^q \hat{O}_k^q \tag{5.1}$$

In principle, for this S-state ion, the EPR spectrum can be recorded at any temperature, but it readily saturates at low temperature. The ZFS is of the order of the X band MW quantum. Accordingly, at X band frequencies, this spectrum is much more complicated due to the appearance of forbidden transitions with intensities comparable with those of the allowed lines. Therefore the spectra for Gd^{3+} have been recorded at Q band and at RT.

Ce^{3+} has a (Xe) $4f^1$ configuration, with a $^2F_{5/2}$ ground state. A low symmetry site splits the six-fold degenerated ground state into three degenerate levels, referred to as Kramers doublets. Due to fast spin-lattice relaxation, the spectrum can only be recorded at low temperatures, and then only the lowest doublet is populated.

Therefore the system can be described by an effective spin $\tilde{S} = \frac{1}{2}$. In a crystal field with a low symmetry, the ground state Kramers doublet $|\frac{5}{2}, \pm\frac{1}{2}>$ is a linear combination of states with $|M_J| = \frac{1}{2}, \frac{3}{2}$ and $\frac{5}{2}$ values.
As Cerium has no isotope with non-zero nuclear spin and no SHF structure is resolved, the SH consists only of $\hat{H}_{EZ}$ and the EPR spectrum of a Ce^{3+} defect is composed of a single line. Since the g tensor for this ion is expected to be very anisotropic, with principal values ranging between 0 and 4.29 [4], its EPR angular dependence has been recorded at X band.

5.4 Analysis of the Gd^{3+} spectra

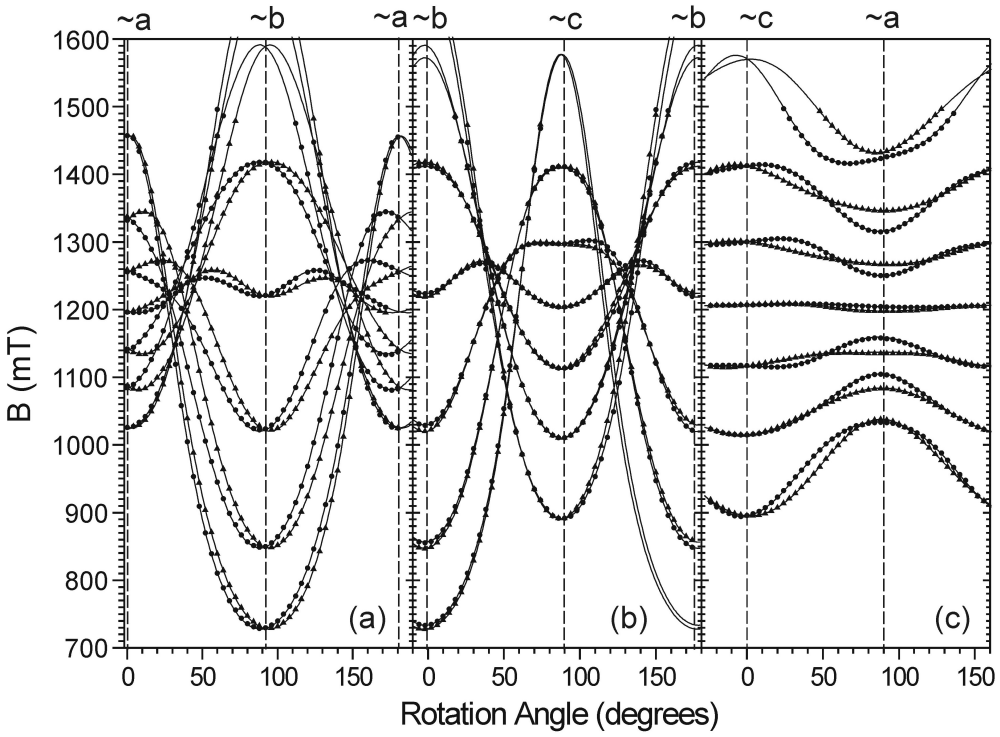

Figure 5.3. Angular dependence of the Q band EPR spectrum of Gd^{3+} in K_2YF_5 at RT, in planes with polar angles in the $x_1y_1z_1$ crystal lattice frame ($\theta = 0$ corresponds to the b axis) : (a) $\theta = 92\,^\circ, \phi = 91\,^\circ$ ($\approx ab$ plane); (b) $\theta = 96\,^\circ, \phi = -3\,^\circ$ ($\approx bc$ plane); (c) $\theta = 9\,^\circ, \phi = -27\,^\circ$ ($\approx ac$ plane).
Magnetic field orientations close to principal crystal orientations have been indicated with dashed lines. The ▲ and • represent the experimental points for two magnetically equivalent sites. The full lines represent simulations using table 5.1 for ▲ and with opposite sign for $B_k^{q=odd}$ for •.

Considering the symmetry of the crystal, it seems natural to take x, y and z along a, b and c, respectively, but other reference frames are possible and this choice is

not necessarily best adapted to the local symmetry of the Y^{3+} site. Because the ZFS of the EPR spectrum exhibits a maximum in the ab plane near the b axis (see figure 5.3), we have chosen to analyse the spectra in a reference frame taking the z axis along b, y along the twofold screw symmetry axis c, and x along $-a$. We refer to this reference frame as $x_1y_1z_1$ and it is displayed in figure 5.2c. For this particular choice of axes frame for a monoclinic defect, the B_k^q parameters with negative q are zero [66]. The two sites inequivalent from the viewpoint of EPR spectroscopy, e.g. positions 1 and 4, are transformed into one another by the coordinate transformation (ignoring the translation) :

$$x_1^{'} = x_1 \qquad y_1^{'} = y_1 \qquad z_1^{'} = -z_1 \tag{5.2}$$

From the explicit form of the Stevens operators [4, 24], it can be verified that they are affected by this transformation as :

$$\left(\hat{O}_k^{q=even}\right)^{'} = \left(\hat{O}_k^{q=even}\right) \qquad \left(\hat{O}_k^{q=odd}\right)^{'} = -\left(\hat{O}_k^{q=odd}\right) \tag{5.3}$$

Hence, the ZFS SH parameters for the two sites are identical except for the sign of the B_k^q parameters with odd q. The SH parameters obtained by simultaneous fitting of the resonance positions for the two sites in this reference frame are given in the second column of table 5.1. The perfect match between experimental and calculated resonance fields using the ZFS in monoclinic form serves as an additional proof for the monoclinic symmetry of the Gd^{3+} dopant site in K_2YF_5. We note in the angular dependence in figure 5.3 (ab plane) that the resonance positions for the various EPR transitions exhibit coincident extremes near the b axis (about 3° tilted away from it, on either side). Bearing this in mind, we define another reference frame, $x_2y_2z_2$ (figure 5.2c), defined by a rotation around the y_1 axis over approximately 3°. The ZFS parameters can be found in the third column of table 5.1. In this reference frame, $B_2^1 = 0$, implying that the defect has in a good approximation orthorhombic symmetry in this axes frame.
In [65] a third reference frame and its ZFS parameters were characterized, but we omitted it here since it does not contribute to the crystal symmetry assignation.
A detailed quantitative analysis of the ZFS parameters is not attempted here, but some qualitative features can readily be interpreted. Evaluation of the ZFS Hamiltonian matrix elements shows that the dominant second rank term is B_2^0 and the dominant terms of fourth rank are B_4^0 and B_4^3. Although the Gd^{3+} centre is clearly monoclinic, the ZFS SH parameters thus indicate that, to a first approximation, the GdF_7 coordination polyhedron has axial (trigonal) symmetry around (an axis close to) the b axis of the K_2YF_5 crystal. This is in agreement with earlier symmetry assignations for the Y^{3+} site as deduced from the XRD data in [58] and

Gd^{3+} (S = 7/2)		
	$g = 1.990_2$	
reference frame	$x_1y_1z_1$	$x_2y_2z_2$
B_2^0	818.1_5	822_5
B_2^1	254.8_{20}	0
B_2^2	186.1_5	183_5
B_4^0	-0.87_5	-0.90_5
B_4^1	-1.09_{75}	-0.25_{75}
B_4^2	-0.73_3	-1.2_3
B_4^3	$-19.2_{2.5}$	$-19.0_{2.5}$
B_4^4	-0.95_{40}	-0.40_{40}

Table 5.1. g value (no unit) and ZFS parameters (in MHz) of Gd^{3+} in K_2YF_5 at RT. The two sets of ZFS parameters correspond to two choices of right handed reference frames : (1) $x_1||-a$, $y_1||c$, $z_1||b$; (2) $y_2||c$ and z_2 tilted $3.2_3°$ away from the b axis in the ab plane. We have chosen the B_2^0 parameter to be positive, which fixes the sign of the other B_k^q parameters. The errors in the last digits are given as subscripts.

[60] and as suggested in [59]. The 3° tilting in the ab plane of the z_2 axis of the second axes system with respect to the b axis might be related to a small off-b-axis position of the seventh F^- ligand. In figure 5.2c, a rotation over +3° for the site Y_1 is shown, which suggests that the z_2 direction lies along the Y_1-F_5 direction. However, from the EPR data alone, it cannot be unambiguously determined which ZFS parameter set (with positive or negative signs for the B_k^q parameters with odd q) corresponds to which Y site. An ENDOR study of the hyperfine interactions with the first ^{19}F coordination shell may lead to a further understanding of the relation between the ZFS parameters and the geometry of the $(RE)F_7$ polyhedra.

5.5 Analysis of the Ce^{3+} spectra

From the angular dependence of the X band EPR spectrum of Ce^{3+}, recorded in three planes (see figure 5.4), the effective g tensor for this centre can be deduced. The data are again analysed in the $x_1y_1z_1$ axes system. The g tensor has four free parameters: the three principal values and the tilting angle Θ_g in the x_1z_1 plane (i.e. the ab plane). The tensors for the two magnetically inequivalent sites only differ in the sign of the tilting angle. The best-fit values for these parameters are listed in table 5.2 and simulations using these parameters are included in figure 5.4. The obtained principal g values are typical for the Ce^{3+} ion in a crystalline environment [4].

From the knowledge of the g value and the ground state wave function in case of C_2 symmetry, Pidol et al. [67] could calculate the contribution of each $|J, \pm M_J>$ to the ground state. But the g values can also give useful information concerning the ground state, without a complete knowledge of the ground state function. From table 5.2 we see that the g values are relatively close to the values $g_{||} = 2.57$ and $g_{\perp} = 0$ expected in purely axial symmetry for a $|J, \pm M_J >= |\frac{5}{2}, \pm\frac{3}{2} >$ ground state ([4], page 308). The deviation from these values is mainly due to admixture of $|\frac{5}{2}, \pm\frac{1}{2} >$ and $|\frac{5}{2}, \pm\frac{5}{2} >$ in the ground state by low symmetry crystal field terms. We may thus conclude that $|\frac{5}{2}, \pm\frac{3}{2} >$ represents the main contribution to the ground state of Ce^{3+} in K_2YF_5.

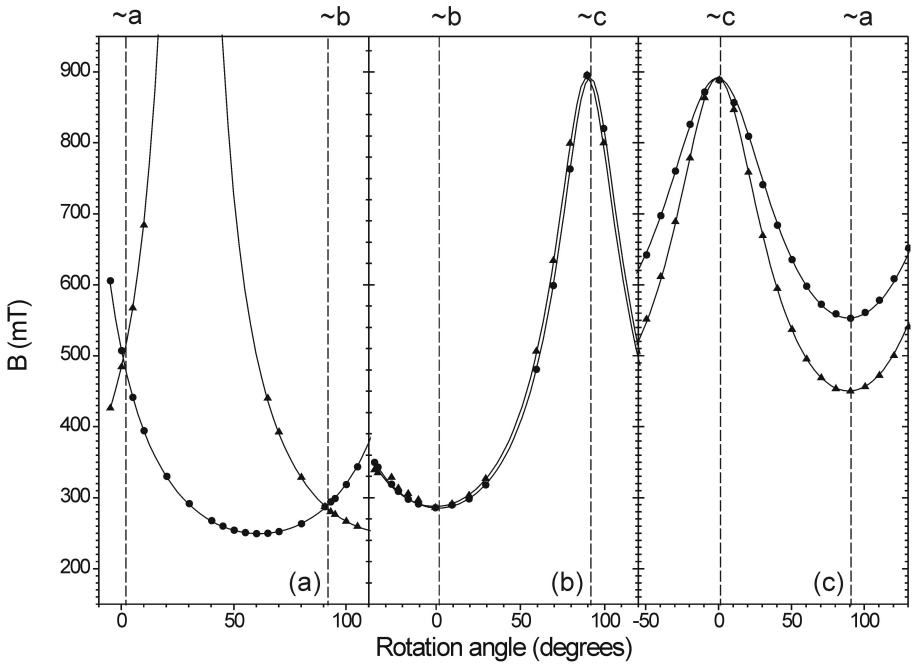

Figure 5.4. Angular dependence of the Q band EPR spectrum of Ce^{3+} in K_2YF_5 at 10 K, in planes with polar angles in the $x_1y_1z_1$ crystal lattice frame ($\theta = 0$ corresponds to the b axis) : (a) $\theta = 97.5°, \phi = 92.0°$ ($\approx ab$ plane); (b) $\theta = 89.5°, \phi = -1.5°$ ($\approx bc$ plane); (c) $\theta = 3.5°, \phi = 0°$ ($\approx ac$ plane).
Magnetic field orientations close to principal crystal orientations have been indicated with dashed lines. ▲ and • represent the experimental points for two magnetically equivalent sites. The full lines represent simulations using table 5.2 for ▲ and with negative Θ_g for •.

A further quantitative or even qualitative interpretation in terms of the geometry of the CeF_7 polyhedron is, however, far from obvious. It should be noted that the effective spin $\tilde{S} = \frac{1}{2}$ used in the EPR analysis does not correspond to the real angular momentum $J = 5/2$ for this ion. The interpretation of the g tensor therefore requires the knowledge of the crystal field splitting of the $^2F_{5/2}$ ground level,

Ce^{3+} (S = 1/2)	
g_x	0.25_5
g_y	0.75_2
g_z	2.74_4
Θ_g	$29.7_5{}^\circ$

Table 5.2. g tensor values and orientation of Ce^{3+} in K_2YF_5 at 10 K in the $x_1y_1z_1$ reference frame. Θ_g is the angle between the principal g axis and the z_1 axis (b) in the x_1z_1 (ab) plane. The errors in the last digits are given as subscripts.

which is at present lacking, but could in principle be extracted from, e.g., optical absorption spectroscopy. The tilting angle of approximately 30° observed for the principal g directions in the ab plane, does not in an obvious way relate to a crystal direction.

A direct comparison between the principal g tensor directions for the two ions is not possible as the Gd^{3+} g tensor was assumed isotropic in the analysis. The deviation by 3° from the b axis of the principal ZFS tensor axes system for Gd^{3+}, which has an obvious geometrical interpretation, is nonetheless remarkable. This might indicate that upon doping, the CeF_7 polyhedron undergoes a distortion that preserves the monoclinic symmetry, e.g. a shift of the RE ion in the mirror plane. However, the effect of a slightly distorted trigonal crystal field on the effective g tensor is not easily predicted. Crystal field calculations should be performed before drawing any further conclusions on this matter. ENDOR measurements may also be helpful in determining the exact location of the F^- ligands in this polyhedron.

5.6 Conclusions and outlook

In section 5.2 we have shown that there is a one-to-one relation between the Y^{3+} site symmetry in K_2YF_5 and its lattice space group. The number of symmetry related EPR inequivalent positions in the unit cell for the Gd^{3+} and Ce^{3+} paramagnetic substitutional impurities in these crystals has been demonstrated to be only two. This clearly shows that the dopant site has monoclinic (C_h) symmetry. Thus, it is concluded that the K_2YF_5 lattice has the Pnam space group.

The analysis of the angular dependence of the EPR spectra using monoclinic forms of the spin Hamiltonian further supported the site symmetry assignation. These findings are quite relevant for future EPR studies on this material aiming to identify the nature of the radiation-induced defects involved in the TL processes. For the identification of trapped carrier (electron/hole) centres placed at

single substitutional impurities or vacancies (F centre, e.g.), the symmetry at each ionic site in the unit cell should be known. Our results imply that four substitutional sites in the primitive cell, one Y^{3+} and three F^-, have ab mirror plane (C_h) symmetry, while the remaining F^- and K^+ positions are triclinic (C_1). In addition, the four F^- ions in the YF_7 polyhedron outside of the mirror plane are symmetry related: they are transformed into one another by the twofold screw and mirror site symmetry operations. More generally, one may state that the symmetry of the radiation-induced paramagnetic defects in this crystal, which can unambiguously be deduced from the angular dependence of EPR and ENDOR spectra, will be an important tool in determining their location in the lattice.
Zverev *et al.*, continued the research on RE (Ce^{3+}, Gd^{3+} and Tb^{3+}) doped K_2YF_5. After irradiation at RT [68] and at 77 K [69], they found several irradiation-induced paramagnetic defects and the knowledge about the crystal symmetry and the different site symmetries facilitated their identification.

CHAPTER 6

EU^{2+} RELATED DEFECTS IN CSBR NEEDLE IMAGE PLATES

"You want to know how two chemicals interact, do you ask them? No, they're going to lie through their lying little chemical teeth. Throw them in a beaker and apply heat."
— DR. G. HOUSE

This chapter contains the major part of the research done during the PhD. In sections 3.4 (at page 38) and 3.5 (page 42) respectively, the morphology of NIPs and the practical consequences of measuring NIPs with EPR were already described. Microsized needles of CsBr (simple cubic crystal lattice) are via PVD deposited to a substrate and Eu^{2+} and Eu^{3+} are incorporated in the needles, Eu^{3+} being EPR silent. XRD showed that a <100> CsBr crystal axis coincides with the needle axis. When the magnetic field is aligned along this axis (perpendicular to the plate) a <100> single crystal-like EPR spectrum is obtained.
In the first section of this chapter, the transition in medical imaging from analogous screen-film technology to digital techniques will be described. One of the digital techniques is based on the X-ray phosphor investigated here.
The principles of how X-ray storage phosphors work will be explained in section 6.2 on the basis of BaFBr:Eu^{2+}. At the workplace a digital imaging plate (IP) goes through several processes: writing, reading and erasing. We will see that EPR and ENDOR played a major role in characterizing several defects involved in the writing and the reading process. However, BaFBr:Eu^{2+} based IPs still have some major drawbacks and consequently, we will report the convincing advantages that CsBr:Eu^{2+} NIPs have in comparison with the commercial more widespread BaFBr:Eu^{2+} IPs.
In section 6.3 an extensive EPR literature review is given. Although there exists an abundant amount of articles on Eu^{2+} doped alkali halides, literature on CsBr do-

ped with Eu^{2+} is very rare. In general, little EPR and ENDOR work on CsCl-type crystals has been published. Anyhow, since NIPs will appear to be substantially different from single crystals, the literature on single crystals should only be regarded as a source of inspiration in search for defect models. From the moment (late 1990s) companies began the research on and the production of NIPs, they started to publish their work in collaboration with several universities and the first articles appeared around 1999. The papers on NIPs will be summarized in section 6.4, revealing that almost no EPR has been done before our study.
Finally, starting from section 6.5 our own results on NIPs will be discussed: different defects occur after annealing at roughly the following temperatures:

- The concentration of the defects occurring after annealing on air at around 170 °C appeared proportional to the sensitivity of the plate (section 6.6)
- Annealing from 300 °C destroys these defects, leading to a stable phase (section 6.7) without X-ray phosphor activity
- Freezing NIPs after over-annealing at temperatures close to the melting point leads to highly unstable Eu^{2+} defects, similar to those reported in single crystals (section 6.8)

We conclude this chapter with the results of additional experiments on NIPs 6.9.

6.1 The need for X-ray phosphors in medical radiography

The use of X-rays (Röntgen rays [70]) in medical imaging was already proposed in 1896, the year of their discovery [71]. In those days the imaging was based on the detection of X-rays with silver halide films. The latter were initially developed for optical photography and their sensitivity towards high-energy X-ray irradiation was quite low. This led to high absorbed doses for the patients. The problem was dealt with by adding an intensifying screen to the film: this screen includes a scintillator that absorbs X-rays and emits visible light, subsequently absorbed by the silver halide film. This film-screen system was also already proposed in 1896 [72] and has in the course of time been further optimized to reduce the absorbed dose by the patient and to enhance the spatial resolution.
Nevertheless, the analogous film-screen technology faced some considerable unsolved issues. First, the development of the films leads to economical (manpower) and ecological (wet chemistry) costs and afterwards, it is hard to manipulate the developed films to facilitate the diagnostics. The S-shaped sensitivity characteristics of all photographic films [73], finally, can cause over- or underexposure, possibly making retakes necessary and thus leading to a higher absorbed dose for patients.
These problems led to the development of digital X-ray systems in the early 1980s [74]. Nowadays there are two digital techniques in medical radiography: computed radiography (CR) and direct digital radiography (DR). CR and DR have many similarities. Both CR and DR use a medium to store X-ray energy and produce a digital image that can be enhanced for diagnosis or further review. They both present an image within seconds after exposure. CR generally involves the use of a cassette that houses the imaging plate (IP, see below) to record the image, similar to traditional film-screen systems, whereas DR typically captures the image directly onto a flat panel detector.
Compared with CR, the DR workflow is typically faster due to the removal of the cassette processing step. However, facilities considering a transition from analogue to digital should carefully consider the substantial costs in upgrading to DR. Initial cost investment is the primary disadvantage of DR as compared to CR. DR in the form of a portable detector starts around $150.000, while a basic low volume CR can start as low as $30.000. DR systems are generally sold as a fully equipped X-ray room and is tied to a single X-ray generator. CR IPs can be retrofitted to existing exam rooms and used at multiple X-ray sites since IPs are processed through a CR reader (scanner) that can be shared between multiple exam rooms. Currently available DR systems take up less space than CR

units, which may be an important factor in facilities challenged by limited space. However, CR systems can offer clear advantages in the portability of the cassettes, especially if the facility regularly serves patients who are not easily moved.
A census [75] conducted in 2005 and 2006 by IMV Medical Information Division, Inc shows that the use of digital technology in diagnostic medical imaging is rapidly expanding. They reported that of 4860 hospitals surveyed in the US 56% had installed CR systems and 30% had installed DR systems. CR systems are the most common in medical applications because they have proven reliability over more than two decades, flexibility to address a variety of clinical applications and lower costs to make multiple exam rooms digital.
We conclude this chapter by enumerating the advantages CR has over analogous film-screen technology, which also led to new uses in non-medical fields [76].

- Substantial reduction of the absorbed dose per take by patients.
- CR often requires fewer retakes due to under- or over-exposure, because of a dynamic range larger than 5 orders of magnitude in X-ray dose, leading to a further reduction of the absorbed dose.
- By adjusting image brightness and/or contrast, a wide range of thicknesses may be examined in one exposure, unlike conventional film based radiography, which may require a different exposure or multiple film speeds in one exposure to cover the wide thickness range in a component.
- No silver based film or chemicals are required.
- Reduced film storage costs/space because the images can be stored digitally.
- Image acquisition is much faster - image previews can be available in less than 15 seconds.
- Images can be enhanced digitally to aid in interpretation.
- Images can be stored on disc or transmitted for off-site review.

Growing technology makes the CR more affordable than ever and one could, depending upon the size of the radiography department, own a CR system for the same monthly cost as an analogous system, since the latter continuously needs chemicals, dark room storage, ...
The IPs are based on X-ray storage phosphors, which are the subject of our investigation. Their working will be explained in the next section.

6.2 THE WORKING AND LIMITATIONS OF THE BAFBR BASED X-RAY STORAGE PHOSPHORS

6.2.1 X-ray storage phosphor : how does it work ?

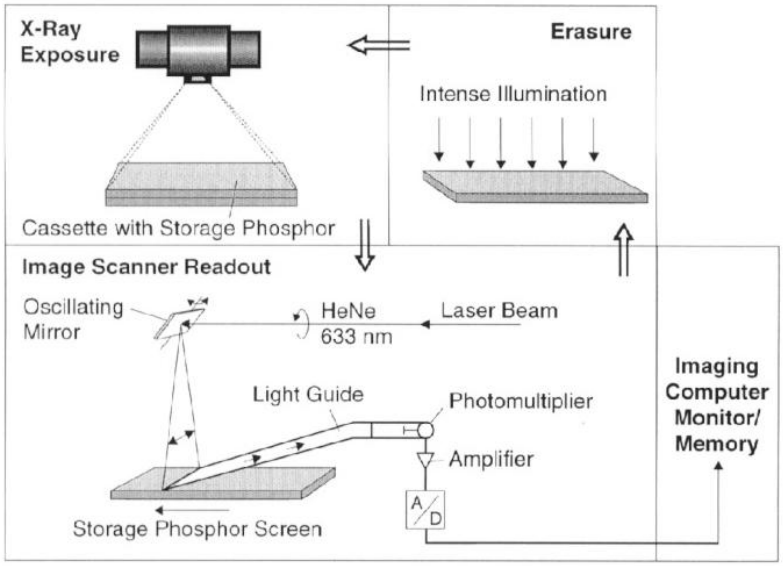

Figure 6.1. Schematic representation of a CR system (from [77])

The process of imaging with IPs consists of three parts (see figure 6.1:

1. *writing* : the X-ray exposure
2. *reading* : the information read-out
3. *erasing* : the optical erasure of the residual information

During the *writing process* the ionizing radiation (X-rays) penetrates the patient and exposes the image plate. This generates a latent image consisting of trapped electron-hole pairs in the phosphor layer of the image plate, the concentration of which is proportional to the absorbed dose. The *read-out* is performed by means of photostimulated luminescence (PSL) by a laser beam that scans the image plate point by point. While 10 years ago, HeNe (633 nm) lasers were used, nowadays mostly diode lasers emitting at 650 to 700 nm are used to excite the PSL. Very recently, also the (more expensive) frequency doubled Nd:YAG lasers (532 nm) are put into use. The trapped electrons are thereby liberated and recombine with the trapped holes under the emission of light (with wave lengths around 400 nm). The light is collected in, e.g., a photomultiplier (PM) which converts the luminescence into an electrical signal. This signal, correlated with the scanning laser

spot position, is digitized and submitted to a computer for the reconstruction of the image. The remaining information in the image plate will then be *erased* by a strong halogen lamp so that the IP can be reused (over 10000 times).

6.2.2 Physics and models of the BaFBr:Eu^{2+} storage phosphor.

In this section the physical model [78, 79, 80] for the BaFBr storage phosphor is explained. Special attention is paid to the EPR and ENDOR work.

6.2.2.1 The crystal structure of BaFBr

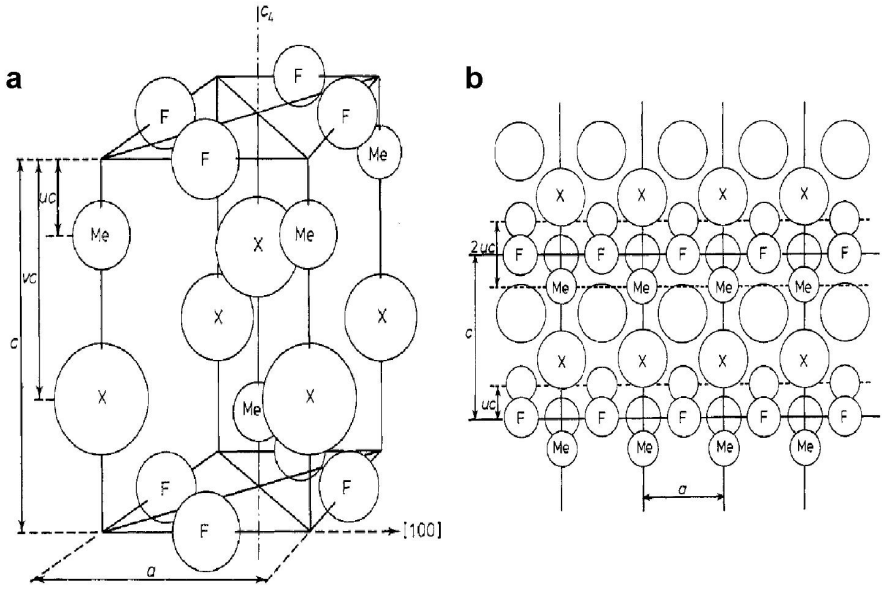

Figure 6.2. a Unit cell for the MeFX-type compound
b Projection of a portion of an MeFX crystal on an ac plane. The atoms labelled Me, F and X pertain to the same plane (plane of the figure). The blank atoms are also contained in a common plane parallel to the former but displaced by the distance $a/2$ (from [81])

BaFBr has the so-called matlockite structure. The crystal has the tetragonal space group P4/nmm and one choice of representation of the unit cell is shown in figure 6.2a. The close neighbourhood of the cation Ba consists of a shell of four F^- and five Br^- ions. Among the latter only four are equivalent, the fifth being further away. The local symmetry of the cationic site corresponds to the C_{4v} group.
This somewhat schematic way to look at the structure, however, does not really satisfactorily describe the actual interaction scheme within the crystal. Figure 6.2b shows a pictorial representation of the crystal more appropriate for a better

insight into the structural characteristics of these compounds. The crystals can be visualised as being built up from sheets, perpendicular to the figure plane in 6.2b, consisting of Ba^{2+} and F^- atoms with a double layer of Br^- ions between two adjacent sheets.
Single crystals can be grown with the Stockbarger method or the Shteber method [82]. The melting point is at about 1010°C. BaFBr decomposes during PVD.

6.2.2.2 Intrinsic defects in a lattice

Several intrinsic defects are present before or are created upon irradiation. Many of them play an important role during the writing, reading or erasing of X-ray storage phosphors. A few important defects are given below in the case of an MX alkali halide.

vacancy (V) : an unoccupied anion (X^-) or cation (M^+) site

F centre : an electron trapped in an anion (X^-) vacancy

F_A centre : an F centre with an impurity cation (M'^+) as closest neighbour

M centre : two F centres on nearest anion sites

V_K centre : two neighbouring X^- anions trapping a hole, thus forming an X_2^- molecular ion placed on two adjacent X^- positions

H centre : an X_2^- molecular ion placed on an X^- position

6.2.2.3 The electron trap centre

There is general agreement [80] that free electrons, created upon X-irradiation, are trapped at F centres. In BaFBr, two F centres are possible : F(Br^-) (stimulation maxima at 495 nm and 590 nm) and F(F^-) (470 nm) centres, where electrons are trapped at Br^- or F^- vacancies, respectively. It has been shown [83, 84] that both F centres contribute to the PSL. This is illustrated in figure 6.3. Their generation mechanism, however, is controversial. In order to form an F centre after creating electron-hole pairs by X-irradiation, one either needs to have a halide vacancy present in the crystal or one must generate it during the radiation damage process.
It was long overlooked that BaFBr produced by firing stoichiometric mixtures of BaF_2 and $BaBr_2$ or by growing single crystals from the melt of such mixtures with the Bridgman method are all contaminated with oxygen. All attempts to eliminate oxygen could only reduce the oxygen contamination. Oxygen can be

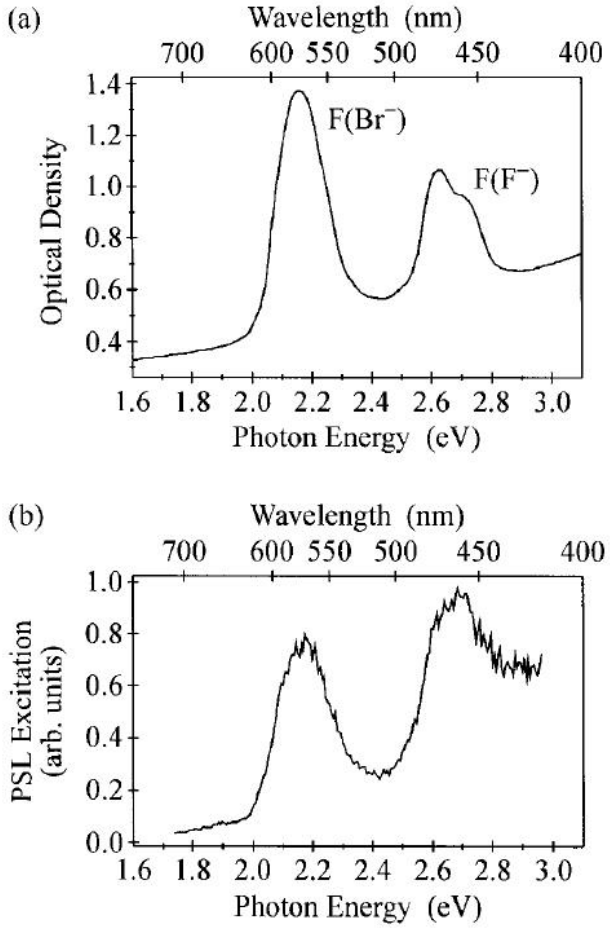

Figure 6.3. a Optical absorption spectrum of $F(Br^-)$ and $F(F^-)$ centres in BaFBr. **b** PSL excitation spectrum of Eu^{2+} in BaFBr.
Both spectra were recorded at 10 K after X-ray irradiation at RT (from [80]).

incorporated in many ways: it was found by EPR and ENDOR investigations as O^{2-}_F (detected by EPR as O^-_F in oxygen enriched BaFBr after hole-trapping, at 1.5 K and after X-ray irradiation at 4.2 K [85]), as O^{2-}_{Br} (analogously detected [86]) and as $(O_F\text{-}O_{Br})^{3-}$ (at 80 K, after RT X-ray irradiation [87]). It is assumed that Br^- vacancies are present and react upon X-irradiation with O^{2-}_F via [88, 89, 90, 91]

$$V^-_{Br} + O^{2-}_F \xrightarrow{X-ray} F(Br^-) + V_K(Br^-_2) + O^{2-}_F \xrightarrow{T>120K} F(Br^-) + O^-_F \qquad (6.1)$$

$V_K(Br_2^-)$, $F(Br^-)$ and O^-_F can be detected by EPR [92, 83]. The mechanism leading to $F(F^-)$ in stochiometric BaFBr remains still unclear. The microscopic structure of the two F centres was established by detailed ENDOR investigations [93, 94].
Non-stochiometric $BaF_{1.1}Br_{0.9}$ does not contain any oxygen impurities and another mechanism leads to the formation of $F(Br^-)$ centres. This mechanism originates from so-called F^- antisites [92] : F^- on a Br^- site.

6.2.2.4 The hole trap centre

The initial hole trap centre after X-ray irradiation is the $V_K(Br^-_2)$ centre (see (6.1)), but the nature of the hole trap centre taking part in the PSL process is still controversial. In [95, 96] it was claimed that upon X-ray irradiation holes are trapped at Eu^{2+} and form Eu^{3+}. Upon photostimulation of F centres, the F electrons move through the conduction band and recombine with Eu^{3+}, producing Eu^{2+} in an excited state, from which the 390 nm luminescence occurs. This simple pair model for the PSL mechanism was questioned by several authors. The EPR signal of Eu^{2+} did not change upon prolonged X-irradiation [83]. Furthermore, the observation of an almost temperature independent PSL effect by stimulating $F(Br^-)$ centres from 4.2 K to RT [97] contradicts the model that electrons move through the conduction band upon photostimulation of F centres.
It has been proposed on the basis of several different experimental findings that the recombination between electrons and holes takes place via tunnelling and that a kind of (triple) *aggregate* between F centres, hole trap centres and the activator Eu^{2+} must be formed [98, 91, 89, 99, 100] during X-irradiation (called triple aggregate centres [83]). It was found that the increase in the PSL intensity is proportional to the X-ray dose [97], which implies that retrapping of electrons after photostimulation does not occur, which makes electron-hole recombination via tunnelling more likely than via the conduction band. Tunnelling, however, requires a spatial correlation between the F centre and the activator. Direct evidence for a spatial correlation between F centres, $V_K(Br^-_2)$, O^-_F centres and Eu^{2+} was given with cross-relaxation spectroscopy using magneto-optical techniques [89] (see figure 6.4). This leads to the speculation that an exciton decay occurs at the Eu^{2+} activator forming electron and hole trap centres and that there is a spatial correlation between the O^{2-}_F - anion vacancy pairs and the Eu^{2+} activators generated during the production of the material.
The role of O^{2-}_F centres is certainly hole trapping with the formation of O^-_F centres. The question is, though, whether it is also the hole trap centre active in the PSL process. It is not very likely [80] that the O^-_F centres are those active hole trap centres in the aggregates described above. On the other hand, it was found that the variation of the oxygen content influences the PSL intensity. A low oxygen content results in a low PSL intensity. Also, the stimulation energy needed for the read-out process is higher for oxygen-poor BaFBr. Thus, it seems that oxygen is involved in two ways in the PSL mechanism: it provides vacancies for the $F(Br^-)$ generation and it somehow seems to influence favourably the photostimulation of the triple aggregate centres in that less stimulation energy is needed for read-out and a high PSL intensity results after short stimulation.

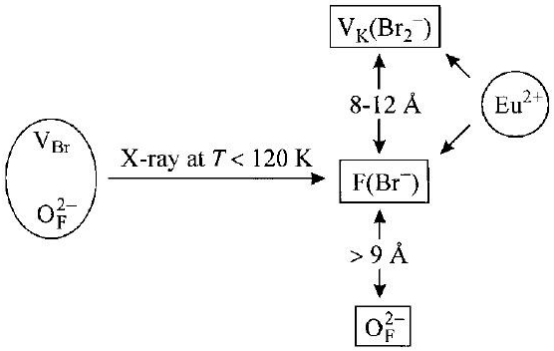

Figure 6.4. Schematic model for the spatial correlation between $F(Br^-)$, $V_K(Br^-_2)$, O^{2-}_F and Eu^{2+} after LT X-irradiation [80]

After X-irradiation of non-stochiometric $BaF_{1.1}Br_{0.9}$ a new hole centre was detected via EPR by Schweizer *et al.* [92], considered to be an H centre in the F lattice. This hole centre is stable up to RT, in contrast to the $V_K(Br^-_2)$, which decays at T $>$ 120 K.

6.2.2.5 The Eu^{2+} activator

It is reasonable to assume that Eu^{2+} substitutes for Ba^{2+} in BaFBr. An EPR investigation yielded a tetragonal centre with the z axes of the ZFS and HF tensors along the c axis as expected for such a site [81]. Unfortunately, no EPR spectrum was shown in this publication; the SH parameters can be found in table 6.1. An MCDA-EPR[1] spectrum (with B along the c axis) of BaFBr:Eu^{2+} is shown in [98]; seven allowed ($\Delta M_S = \pm 1$) were detected in the high-field region and six forbidden transitions ($\Delta M_S = \pm 2$) at lower magnetic fields.
What could not be inferred from EPR was whether or not there are lattice relaxations about the Eu^{2+}. The ionic radius of the replaced Ba^{2+} is larger than that of Eu^{2+} (0.134 nm vs. 0.109 nm). Therefore, a substantial lattice relaxation about Eu^{2+}, or a non-central position of Eu^{2+}, can be anticipated. This is of interest since a lattice relaxation could in principle explain the observation of a spatial correlation between the electron and hole trap centres and Eu^{2+}, an important feature for the functioning of BaFBr:Eu^{2+} as a storage phosphor. However, ENDOR analysis [101] suggested no significant shift of Eu^{2+} away from the regular Eu^{2+} position.

[1]The EPR detected with Magnetic Circular Dichroism of Absorption method is based on the differential absorption of right and left circularly polarized light, where the light is propagating along the direction of an externally applied static magnetic field B_0. More information about this method can be found, e.g., in [13]

BaFBr:Eu^{2+} (290 K)			
g	1.9921	B_2^0	245.9
		B_4^0	0.45
$\|^{151}A\|$	97.3	B_4^4	1.42
		B_6^0	6.3 10^{-3}
		B_6^4	6.3 10^{-2}

Table 6.1. EPR parameters (g : no unit; A,B_q^k : MHz) of Eu^{2+} in BaFBr (from [81]).

6.2.3 Progress in science and technology of BaFBr based IPs

The performance of an IP includes sharpness, sensitivity, reusabilily, ... and is quantified by various quality factors [102, 77, 103, 104]:

conversion efficiency (CE) the light energy emitted by a storage phosphor per exposed X-ray dose and per unit area

stimulation spectrum the read-out of the IP should be done with cheap and compact available diode lasers

emission spectrum the emission of the IP should allow efficient detection with a commercial PM or a charge-coupled device (CCD) camera

dynamic range over which the PSL response vs. X-ray dose should be linear

fast read-out can be obtained by a small decay time constant of the PSL signal

erasability an efficient and fast signal reduction due to exposure to the erasure source

stimulation energy (SE) the stored information should be easily accessible (without the need for high intensity lasers)

spatial resolution is quantified by the modulation transfer function (MTF)

stability the signal should exhibit little fading at RT as it should be possible to store the information for a long time

noise level

These quality factors can roughly be divided into *IP related quality factors* and *storage phosphor related quality factors*. Extensive research on both topics has been done, in order to improve the performance of the IP. Li *et al.* [105], for example,

assessed the influence of the median grain size on the noise level and the spatial resolution, while, from a more fundamental point of view, other related systems like BaFCl:Eu^{2+} [106, 107] and BaFI:Eu [108] were proposed.

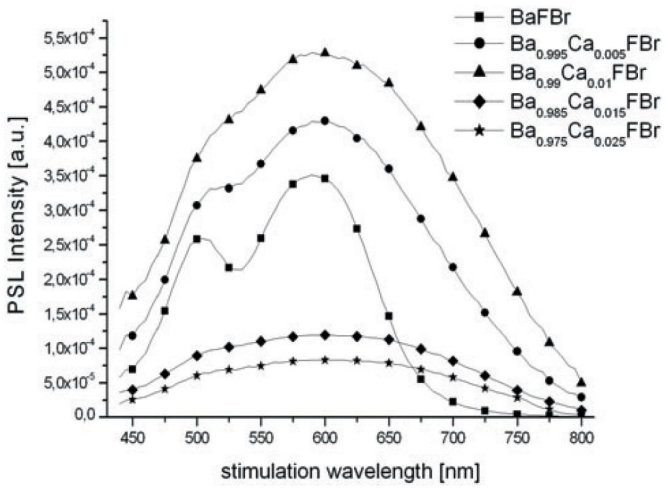

Figure 6.5. Influence of Ca co-doping on the PSL spectrum of BaFBr:Eu^{2+} [109]
■ : PSL curve of BaFBr:Eu^{2+}
● : PSL curve of $Ba_{0.995}Ca_{0.005}FBr:Eu^{2+}$
▲ : PSL curve of $Ba_{0.990}Ca_{0.010}FBr:Eu^{2+}$
♦ : PSL curve of $Ba_{0.985}Ca_{0.015}FBr:Eu^{2+}$
★ : PSL curve of $Ba_{0.975}Ca_{0.025}FBr:Eu^{2+}$

We do not want to give an extensive review of all research done on IPs, but mention only one remarkable finding, possibly important for the CsBr case. Codoping with Sr^{2+} [110] or Ca^{2+} [111, 109] shifts the photostimulation further to the red. This results in a better match with the wavelength of the practically used HeNe lasers (633 nm) or the frequency doubled Nd:YAG lasers (532 nm), and consequently a lower laser light intensity is needed during the read-out process. The shift is attributed to the formation of F_A centres. The influence of Ca co-doping on the PSL is shown in figure 6.5: both the PSL intensity as its spectrum display an optimum at 1 mol% of calcium.

6.2.4 Limitations of BaFBr based IPs

Nowadays the BaFBr based IPs, initially developed for medical radiography, have found new uses [76, 112] in nondestructive testing, XRD, protein crystallography, ... However, the spatial resolution (5 line pairs per mm [113]) of the images remains unsatisfactory for several applications in medicine (e.g. mammography). A BaFBr IP consists in fact of randomly ordered BaFBr grains (microcrystals) embedded in an organic binder on a substrate and light scattering of

the scanning laser beam during the read-out process is certainly one of the reasons of loss in resolution. Furthermore, the BaFBr is birefringent, a consequence of the matlockite structure. With respect to the latter it would be advantageous to replace the BaFBr crystallites by optically isotropic cubic crystals. One of the challenges for new generations of CR IPs was thus to find such X-ray storage phosphor systems which have a similarly high performance as a standard BaFBr:Eu^{2+} phosphor screen.
Two cubic systems have proved to have such storage properties and have been investigated intensely (mostly by luminescence spectroscopy): alkali halides doped with Ga^+, In^+ or Tl^+ and Ce^{3+} or Pr^{3+} doped elpasolites (already mentioned in chapter 4) [41]. However, neither their CE nor SE was comparable with the BaFBr system. Most of them had other disadvantages as well, like KBr:In^+ with low X-ray stopping power (since K is a light element) and RbI:Tl^+ where the stored image fades away within minutes.
More recently, also other materials have been proposed as possible X-ray storage phosphors: glasses and glass ceramics which can resolve features as small as 17 μm [114] and MBrCl:Eu^{2+} (M = Ca, Sr, Ba) [115].

6.2.5 CsBr based needle IPs : the solution

A new CR system, based on CsBr grown in needles, was developed by the end of the 1990s by Agfa-Gevaert NV, and first presented in 1999. Thanks to the specific needle growth (already discussed in section 3.4) the resolution could be improved to the size of the needle diameter (down to a few μm) : the needles act like wave guides for the light. While at first, Ga^+ was used [116], Eu^{2+} quickly became the favoured dopant [117].
Besides a higher spatial resolution, CsBr:Eu^{2+} NIPs show excellent IP quality factors [118, 113, 119, 120]:

- The heavy Cs and the close packing in the needle structure cause a high absorption of X-rays
- Under the same irradiation conditions [118] the *CE* of CsBr:Eu^{2+} is higher than for a commercial BaFBr:Eu^{2+} NIP
- The stimulation band, centred around 680 nm, allows efficient *read-out* with cheap and compact diode lasers (compare figures 6.6 (measured at 10 K) and 6.3 (at RT))
- The blue emission, centred around 440 nm, allows efficient *detection* with both a PM and a CCD (see figure 6.6)

- Under the same *erasure* conditions the signal in CsBr:Eu^{2+} is reduced to 7.10^{-5} of the original signal (7.10^{-3} for BaFBr:Eu^{2+})
- Much less *SE* is needed to set the stored information free as PSL emission than in BaFBr:Eu^{2+}

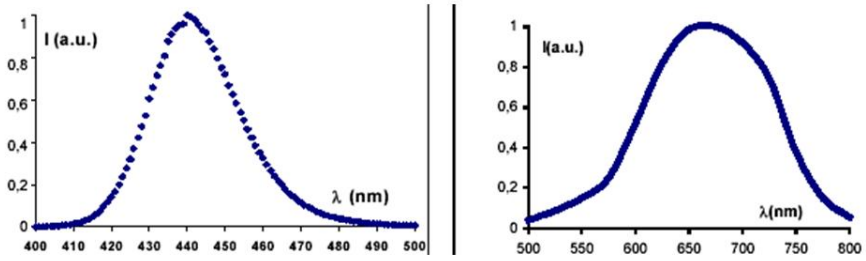

Figure 6.6. Emission (left) and stimulation (right) spectra of a CsBr:Eu^{2+} NIP at RT (from [117]).

The present work contributes in understanding the physics behind the writing and read-out processes in the CsBr:Eu^{2+} NIPs. It was expected that the simpler crystal lattice (simple cube vs. matlockite) would simplify the research, but this soon proved to be not the case.

6.3 Literature overview of EPR on Eu^{2+} and related ions in alkali halide single crystals

EPR literature about Eu^{2+} in cesium halides and in CsBr in particular, is scarce, at variance with the abundance of results reported for the alkali halides with the NaCl structure. Only Savel'ev *et al.* reported a Eu^{2+} centre in CsBr single crystals, obtained by (vacuum) heating at 500°C and subsequent quenching. In subsection 6.3.2, the literature on Eu^{2+} in NaCl-like alkali halides is discussed, while subsection 6.3.3 deals with the work of Savel'ev *et al.* on CsBr:Eu^{2+}. In the next subsection the EPR/ENDOR results on CsCl-type single crystals, doped with different ions, are discussed. Finally, we report the results of the EPR and ENDOR investigations on the F centre in CsBr.

6.3.1 EPR on Eu^{2+} in various lattices

Eu^{2+} has the same $^8S_{7/2}$ ground state as Gd^{3+}. An isotropic g value close to g_e is expected and since S = 7/2, $\hat{H}_{ZFS}$ can include ESO's up to the sixth rank. Eu^{2+} has many different optical applications and can readily be detected with EPR, even at RT. Because of that, Eu^{2+} became a "grateful" ion to study with EPR and ENDOR in a very diverse collection of hosts. This resulted in a tremendous amount of literature.

In the 1960s and 1970s simple binary systems ($PbCl_2$ [121], CaF_2 [122], alkali halides, ...) were under investigation, but soon more complicated hosts with a variety of applications became the centre of interest. Aluminates ($SrAl_2O_4$ and $Sr_4Al_{14}O_{25}$ [123, 124]) and elpasolites (Cs_2NaXCl_6 [125, 126]), for example, are studied for their interesting optical properties. $BaSO_4$:Eu is a promising TL phosphor [127], while the in the previous section mentioned BaFBr [101, 81] shows excellent X-ray storage phophor characteristics.

The first thing that catches the eye, while browsing through the literature, is that the HF interaction of Eu^{2+} is isotropic and that its value is fairly constant. Indeed, as expected,this value does not depend much on the host, since the valence electrons are shielded from the environment by the filled $5p^6$ and $6s^2$ shells. Roughly, the absolute value for ^{151}Eu is around 90 - 100 MHz and the authors who could determine the sign of the HF interaction found that $A < 0$. In section 2.5.3 on page 20 it was noted that $A_{iso} = \frac{2\mu_0}{3} g_e g_N \beta_e \beta_N \rho_S(\vec{0})$. When several nuclear isotopes occur, the HF values are connected via

$$A(^{151}Eu) = A(^{153}Eu)\frac{g_N(^{151}A)}{g_N(^{153}Eu)} \tag{6.2}$$

An analogous equation can be used for the quadrupole interaction

$$Q(^{151}Eu) = Q(^{153}Eu)\frac{\tilde{Q}(^{151}A)}{\tilde{Q}(^{153}Eu)} \tag{6.3}$$

with $\tilde{Q}$ the electric quadrupole moment (see equation (2.43)). This can seriously simplify EPR and ENDOR analysis, since A and Q of only one (^{151}A or ^{153}A) isotope have to be determined.

6.3.2 Eu^{2+} in alkali halides with the NaCl structure

In this section, the results of Eu^{2+} in alkali halides with the NaCl structure are treated in greater detail, since they are very similar to CsBr. Both have a cubic crystal structure, but the NaCl crystal structure (face centred cube) causes a six-fold surrounding of the ions, while in CsCl (simple cube) the ions are eight-fold surrounded. In both types of crystals, the host ions are monovalent, while the dopant Eu^{2+} is divalent, so charge compensation via a cation vacancy V is expected when Eu^{2+} substitutes a cation.

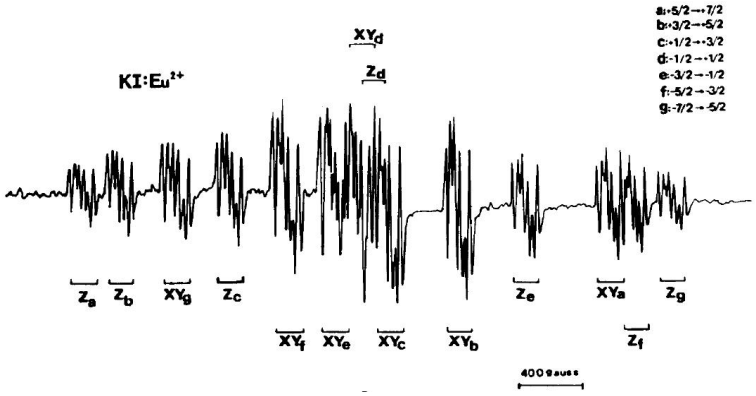

Figure 6.7. The X band EPR spectrum of KI:Eu^{2+} at RT and with the magnetic field along a crystal axis (from [128]).

It is indeed [129] well recognized that the introduction of the divalent Eu in the alkali halide matrix results in the formation of a complex composed of the impurity ion and a vacancy on the nearest cation position [130, 131, 132, 133]. A Eu^{2+} ion, only accompagnied by one or more vacancies in the vicinity, will be labelled as *a Eu monomer* in the following. The most common Eu^{2+} monomer has orthorhombic I symmetry[2]. In almost all of these studies, the EPR analysis was based

[2]There are two types of orthorhombic symmetry :
orthorhombic I : one principal axis lies along a crystal <001> axis; the others along <110> directions
orthorhombic II : all axes lie along <100> directions

KI:Eu^{2+} (RT)			
$g_{\|\|}$	1.993	B_2^0	336.8
$g_\perp$	1.991	B_2^2	89.3
		B_4^0	-0.76
$\|^{151}A\|$	91.5	B_4^2	-0.14
		B_4^4	3.49
		B_6^0	0.006
		B_6^2	-0.002
		B_6^4	-0.035
		B_6^6	0.011

Table 6.2. SH parameters for KI:Eu^{2+} at RT. All parameters (except g) are in units of MHz (from [128]).

on an angular variation of the magnetic field in the (100) and (110) planes. The EPR parameters for Eu^{2+} in KI, for example, can be found in table 6.2. In figure 6.7 its spectrum is shown when the magnetic field lies along a <100> crystal axis. Contributions can be seen of defects with their z axis along this <100> axis (labelled 'Z' in figure 6.7) and equivalent contributions of defects with their x or y axis (labelled 'XY') along this <100> axis. The 14 ZFS lines are further split via (S)HF interaction.

When comparing the magnitudes of B_2^0, which reflects the main axial distortion, for the different alkali halides, an interesting feature pops up with regard to their dependence on the Eu^{2+}-V distance. It was ascertained that the magnitude of B_2^0 was roughly inversely proportional to the Eu^{2+}-V distance. This is shown in figure 6.8.

It appeared that the EPR spectra analysed by Boldu *et al.* [135] in KF and RbF (represented with • in figure 6.8) do not have the same origin as those studied by Iwasaki and coworkers [132]. Since Iwasaki *et al.* firmly established that their observed EPR spectra were due to a complex consisting of a Eu^{2+} ion and a cation vacancy at one of its nearest neighbour (NN) sites, it may be inferred that the complexes responsible for the spectra analysed by Boldu *et al.* are of a quite different nature.

Investigations dealing with the behaviour of Eu^{2+}-V dipoles have a long history, since the problem of solution and precipitation of doubly-valent impurity ions in ionic crystals is of considerable importance both from fundamental and technological points of view. Already from the 1960s [129] there exists controversy about the kinetics of the aggregation. Muñoz *et al.*, among others, analysed the aggregation kinetics of Eu^{2+}-V dipoles in a variety of alkali halides (NaCl, KCl,

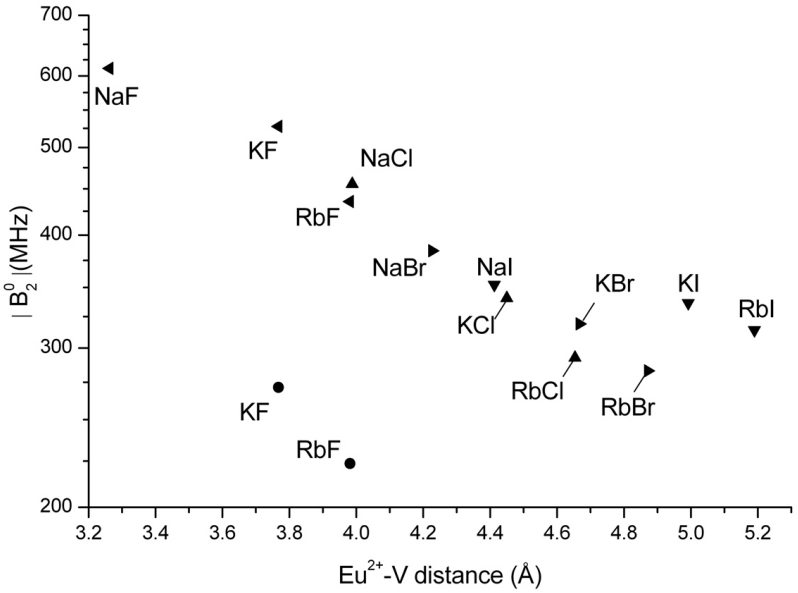

Figure 6.8. $|B_2^0|$ as a function of the Eu^{2+}-V distance in various systems. Data from [131] (▲), [134] (►), [128] (▼), [132](◄) and [135](•)

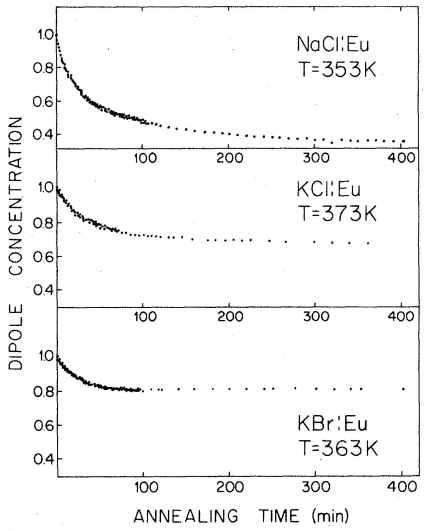

Figure 6.9. Dipole-decay curves for Eu^{2+}-V dipoles at several temperatures (from [136])

KBr and RbBr) with EPR [136] as a function of different annealing temperatures and europium concentrations. The dipole concentration was determined from the EPR signal intensity. Figure 6.9 shows some of the dipole-decay curves.

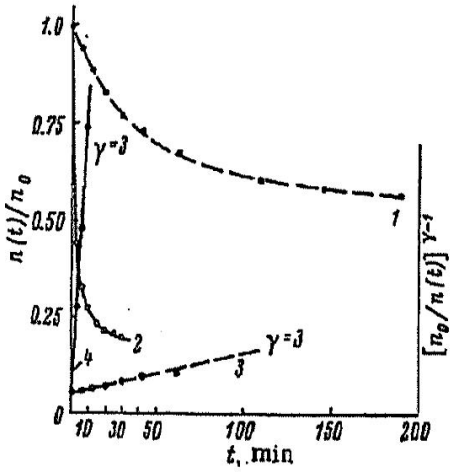

Figure 6.10. **1,2** Relative concentrations of isolated dipoles on the aggregation time
3,4 Plots used to determine the order (γ) of the aggregation kinetics
1,3 NaBr:Eu^{2+}, T = RT
2,4 CsBr:Eu^{2+}, T = 240 K (from [137])

6.3.3 Eu^{2+} in CsBr

Savel'ev *et al.* [137] reported the only EPR results on Eu^{2+} in CsBr single crystals, but unfortunately, no EPR spectrum is shown in their article. They studied the aggregation of Eu^{2+}-V dipoles to clusters of dipoles. Figure 6.10 shows this for NaBr and CsBr doped with Eu^{2+}. Even at 240 K the dipole concentration in CsBr has dropped to a mere 25 % after 10 minutes, while in NaBr the dipole concentration is much more stable, even at RT. The latter is more in correspondence with figure 6.9.

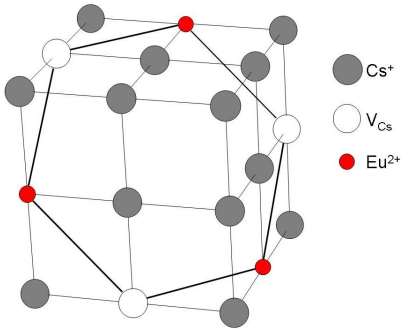

Figure 6.11. The model for the $(Eu^{2+}\text{-}V)_3$ trimer according to [137]

According to their findings, they concluded that the Eu^{2+}-V dipoles quickly agglomerate to $(Eu^{2+}\text{-}V)_3$ complexes, even at extremely low temperatures. They attributed this behaviour to the difference in size between the Eu^{2+} and Cs^{+} ion.

In figure 6.11 their suggested model for the trimer is shown.
In 2001 Spaeth et al. [113, 138] were the first with a renewed interest in CsBr:Eu^{2+}, motivated by the publications on NIPs by Leblans *et al.* [117, 116, 118]. No EPR could be observed in Bridgman grown single crystals. They concluded that almost all of the doped Eu^{2+} is present under the form of diamagnetic aggregates. Attempts to break the aggregates by annealing and quenching failed, in contradiction with the work of Savel'ev *et al*.

6.3.4 EPR literature on cation doped CsCl-type crystals

Since we did find RT stable EPR signals in Eu^{2+} doped CsBr NIPs, we considered it interesting to check whether there exists EPR literature on other crystals with the same crystal structure (CsCl, NH_4Cl and NH_4Br (see figure 6.12)), doped with aliovalent cations.

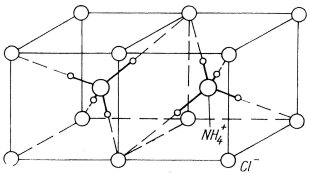

Figure 6.12. The two orientations of the NH_4^+ tetrahedra in NH_4Cl (from [139]).

Iri *et al.* [140] studied Mn^{2+} in CsBr single crystals. Mn^{2+} has a (Ar)$3d^5$ configuration, with a $^6S_{5/2}$ ground state. The single crystals were grown from a saturated aqueous solution of CsBr containing $MnBr_2$ and the EPR spectra were recorded at RT. The observed spectra consisted of two contributions: an isotropic broad line (width = 40 mT, g close to 2) and an anisotropic spectrum with fine structure, each packet consisting of six Mn HF splitted lines. The relative intensity of the latter increased after heating it for 10 minutes at 300°C and quenching (dropping it into liquid nitrogen). They assigned the broad line to a Mn-aggregate and interpreted the anisotropic spectrum as due to Mn^{2+}, substituting a Cs^+, with a NN cation vacancy. They explained the extremely large D value (D = 11.7 GHz) of this tetragonal defect by an appreciable displacement of the Mn^{2+} towards the vacancy. In NH_4Cl:Mn^{2+}, two axial centres were identified as interstitially located Mn^{2+}, coplanar with 4 chlorine ions [141]. The difference between these centres was attributed to the axial ligands which were proposed to be two H_2O molecules in one case and one H_2O and one NH_4^+ in the other.
Boettcher and Spaeth [139, 142] combined ENDOR and EPR to investigate two centres in NH_4Cl:Cu^{2+} (see figure 6.13). Cu^{2+} has a $3d^9$ configuration, with a $^2D_{5/2}$ ground state. Since Cu^{2+} has only one unpaired electron, the 'effective' spin

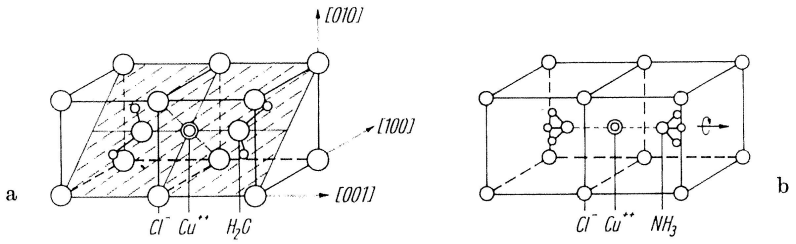

Figure 6.13. Models of centre I (a) and centre II (b) in $NH_4Cl:Cu^{2+}$ (from [139]).

is equal to the real spin of the ion, i.e. S = 1/2. Consequently, no ZFS interaction is needed in the Hamiltonian. They found that in both cases the Cu^{2+} takes an interstitial position, in the centre of four Cl^- ions (cfr. $NH_4Cl:Mn^{2+}$) and is charge compensated by neighbouring cation vacancies on the same <100> axis. In one of the centres (centre I), which changes its symmetry from tetragonal to orthorhombic I when cooling below 20 K, the ion has H_2O as fifth and sixth ligand, taking these cation vacancy positions. The other centre (centre II) remained tetragonal down to 1.6 K and was identified as having NH_3 molecules as axial ligands. Watanabe *et al.* [143], on the other hand, found another centre, very similar to centre II, but with one NH_3 molecule replaced by a vacancy. Centre II was also characterized by Sano *et al.* [144] in $NH_4Br:Cu^{2+}$.
Although being trivalent ions, similar models have also been proposed for Cr^{3+}[145] and Fe^{3+} [146] centres in CsCl and NH_4Cl,

6.3.5 F centre in CsBr

As already mentioned in section 6.2.2.3, F centres are the electron trap centres in the $BaFBr:Eu^{2+}$ phosphor and in section 6.4.1 we will see that the F centre is also the electron trap centre in $CsBr:Eu^{2+}$. Pawlik *et al.* [147] investigated this F centre in CsBr with EPR and ENDOR. In order to obtain the high F centre concentrations necessary for ENDOR, the F centres have been produced via additive colouration in Cs vapour for which the sample was kept at 630 °C, close to its melting point. *Additive colouration* is the change of the colour of a crystal when its stoichiometry is disturbed, for example, when the crystal is heated in a reducing atmosphere or an ionic current is transmitted through it. During this process, anions are replaced by electrons in the volume of the crystal maintaining its charge neutrality.
In CsBr only a broad unresolved EPR line at g = 1.996 with a peak-to-peak derivative linewidth of 70 mT has been detected, indicating a fairly large SHF interaction with the neighbouring Cs nuclei. In CsCl, however, the EPR spectrum, centred around g = 1.984 [148], does show structure due to resolved SHF interac-

tions.
With ENDOR, Pawlik *et al.* could resolve up to five Cs and three Br shells and thus irrefutably characterize the F centre. Using the dipole approximation (2.39), the distance of the shells was calculated, and the calculated values corresponded very well with the distances in the undistorted CsBr lattice.
Using their experimental settings and determined SH parameters, we will be able to easily identify an F centre in NIPs when they occur before or after irradiation.

6.4 Optical and structural research on NIPs

The first papers on NIPs were published around 2000 and originate from Agfa-Gevaert NV (now known as Agfa HealthCare NV). These articles were already mentioned in section 6.2.5. Leblans *et al.* [117, 116, 118] and Schmitt *et al.* [149] mainly focussed on the IP related quality factors (SE, CE, MTF, ...), proving that NIPs are superior to BaFBr IPs.
In this section, the literature on CsBr:Eu^{2+} NIPs and related systems will be reviewed.

6.4.1 The electron trap centre in CsBr:Eu^{2+}

At 4 K for CsBr the F centre absorption band is at 633 nm [150]. Considering the broadening and red-shift of the F centre absorption bands at RT [150] the observed PSL stimulation spectra of CsBr:Eu^{2+} NIPs(figure 6.6) agree quite well with the corresponding F centre absorption bands. Thus, the electron trap centres taking part in the PSL process are F centres [138].

6.4.2 Enhanced PSL after annealing

Hackenschmied *et al.* [28, 151] prepared CsBr:Eu^{2+} powders with various Eu^{2+} concentrations and detected an increased PSL intensity when the powders were annealed around 500 K. This is illustrated in figure 6.14. They explained this, based on XRD measurements, by the formation of $CsEuBr_3$ phases via a mechanism proposed by Nikl for CsCl:Pb^{2+} [152] (figure 6.15). They assumed that a Eu^{2+}-V dipole is the starting point for the formation of perovskite-like cells. The enhanced PSL is attributed to a better localization of charge carriers in the vicinity of the phase boundaries which means in the direct neighbourhood of Eu^{2+}. They also tried to clarify the role of oxygen impurities, and found that the PSL intensity enhancement of the sample annealed in N_2 gas was only 9% of the comparative one annealed on air. They suggested that a centre, similar to the in BaFBr encountered Eu^{2+}-O^- centre (see section 6.2), is responsable for the hole trapping within the precipitations.
To test this hypothesis about the $CsEuBr_3$ precipitations, Hesse *et al.* [153] grew single crystals of $CsEuBr_3$. They concluded that, after preparation, $CsEuBr_3$ degrades in normal atmosphere into at least two phases, one of which is the orthorhombic structure of $Cs_2EuBr_5.10H_2O$. The XRD powder diffraction pattern of this compound is very similar to that of the segregations observed within CsBr:Eu^{2+} and reported by Hackenschmied *et al*. However, they stated that the increased PSL yield in CsBr:Eu^{2+} after annealing cannot be due to the segregations, because

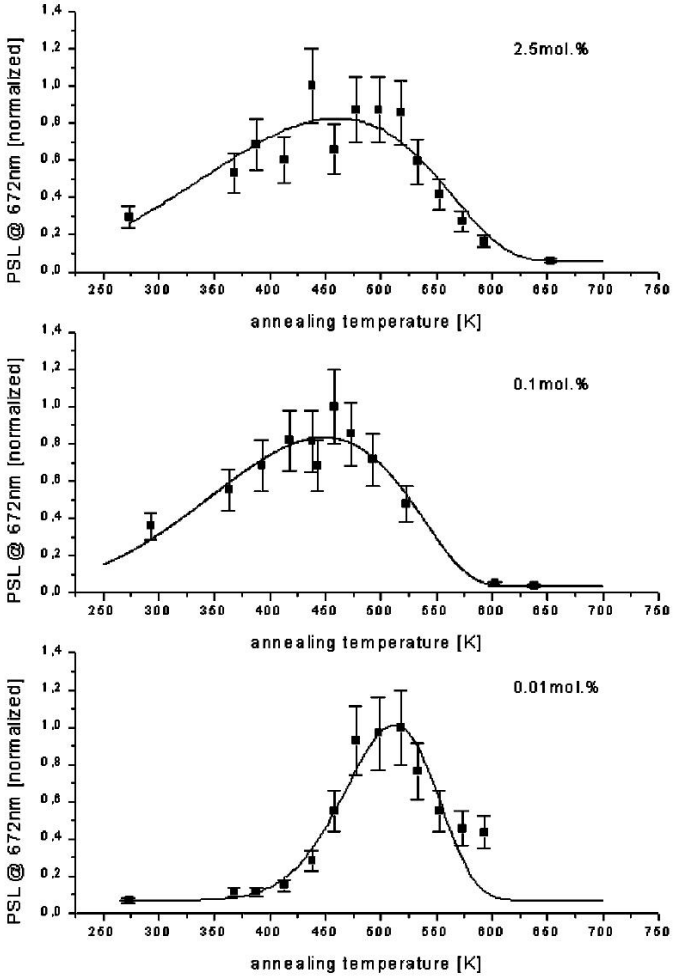

Figure 6.14. PSL intensity of CsBr:Eu^{2+} powders as a function of annealing temperature for different Eu^{2+} concentrations (from [28])

the trivalent nature of the europium in the segregations renders them PSL inactive. Moreover, in their study the increased PSL yield is not proportional to the concentration of the segregation compound, in contrast to what Hackenschmied *et al.* reported. On the other hand, they also found a strong increase in PSL yield after annealing.

Finally, they came up with an alternative explanation for the increased PSL after annealing [154] : during annealing Eu^{2+}-O^{2-} dumbbells are created as PSL active emission centres. In figure 6.16 a picture is show of how such a dumbbell is supposed to look : both ions are placed on neighbouring cation positions, resulting in a <111> oriented dipole. In order to prove that oxygen is the cause of the increased PSL, annealing has been performed in a sulphur atmosphere (H_2S) which yielded an even larger gain in PSL yield (figure 6.17). PSL lifetime measurements indicated furthermore a reduced lifetime for the sulphur treated samples compa-

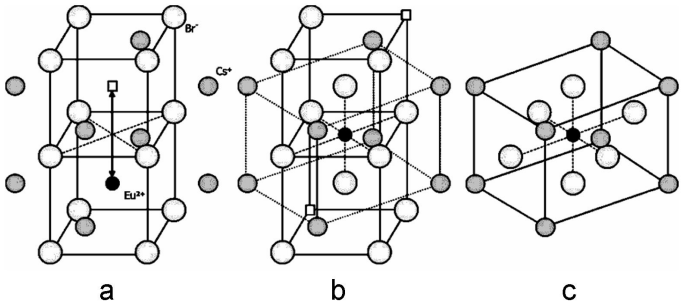

Figure 6.15. Mechanism for the formation of the $CsEuBr_3$-like unit cell in $CsBr:Eu^{2+}$
a Eu^{2+}-V dipole in the CsBr lattice
b transformation of the local structure towards the $CsEuBr_3$ unit cell
c amplification of the $CsEuBr_3$ unit cell (from [28])

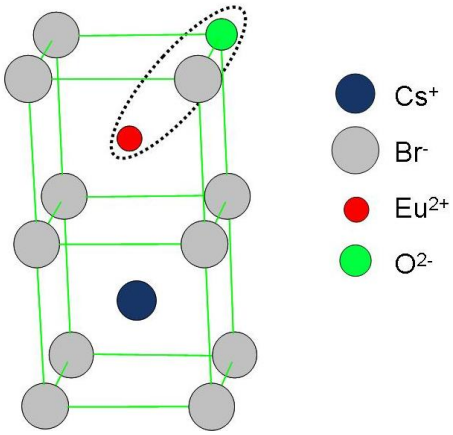

Figure 6.16. The model for the Eu^{2+}-O^{2-} dumbbell according to [154]

red to the oxygen treated ones (which PSL lifetime was equal to the PSL lifetime of the untreated samples) indicating a spatial correlation between the sulphur ion and the Eu^{2+} ion.
This finding supports their speculation of the existence of a Eu^{2+}-O^{2-} dumbbell (or a Eu^{2+}-S^{2-} dumbbell in case of the H_2S treatment). In such a situation the Cs vacancy for the charge compensation of the Eu^{2+} ions would not be needed anymore since O^{2-} would directly compensate the Eu^{2+} ion charge.
In 2007, Schierning *et al.* [155] found a correlation between the dielectric constant ϵ and the PSL efficiency. They concluded that a polarization, or, more generally, an electric dipole (e.g. Eu^{2+}-O^{2-}) is of importance in the PSL process.
Very recently, Appleby *et al.* [156, 157] detected the significance of water during the annealing process. It was proposed that the influence of moisture permits a more efficient incorporation of oxygen into the $CsBr:Eu^{2+}$ lattice, resulting in

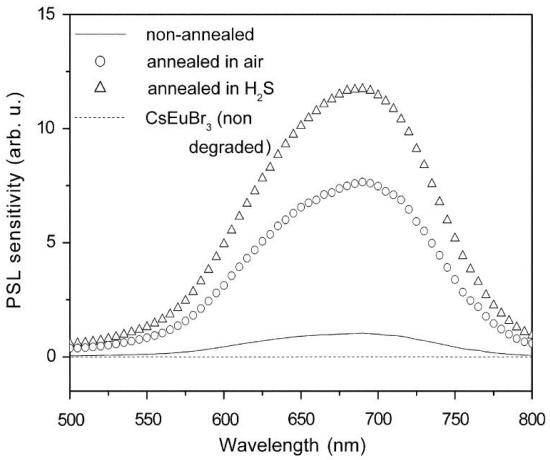

Figure 6.17. PSL excitation spectra of differently treated NIPs as indicated. The annealing is performed at 190 °C for 3 h. For comparison the PSL spectrum of $CsEuBr_3$ immediately after sintering (non-degraded) is shown as (dashed) line indicating the complete absence of photostimulability (from [154])

more Eu^{2+}-O^{2-} dipoles and a subsequent PSL increase, although the mechanism remains unclear.
Meng *et al.* [158], finally, tested the role of hydrogen- and hydroxyl-doping in CsBr:Eu^{2+}. They sintered a mixture of CsBr, $EuCl_3$ and ethanol for 3h at 600°C in a 5% H_2 atmosphere. They found that both hydrogen- and hydroxyl-doping had an influence on the PSL yield, but did not provide an explanation.

6.4.3 Radiation hardness of NIPs

It has been claimed that CsBr:Eu^{2+} NIPs show a significant deterioration of the PSL after high absorbed X-ray doses. One observes an almost exponential drop in PSL yield and consequently a decrease in radiation sensitivity of almost 90% for a total dose of 100 Gy. This implies, according to Zimmerman *et al.* [159], a poor radiation hardness of CsBr:Eu^{2+} and questions the commercial applicability of such a material in image plate applications. It should be noted, however, that typical medical doses are much lower, e.g. a pelvic X-ray examination accounts for about 1.3 mGy, a chest examination for about 0.1 mGy [160]. In other words, only after thousands of takes, the NIPs lose sensitivity, so the results for medical use of NIPs are not so dramatic as stated by Zimmerman *et al*.
They attributed the loss of sensitivity to X-ray induced vacancy centres (e.g. M centres), which enhance the diffusion of the Eu^{2+} activators, resulting in the formation of PSL inactive europium clusters or second phases of europium compounds. To counter this diffusion, Li-codoping was proposed [161] : the integra-

tion of Li^+ would suppress the generation of M centres during X-ray irradiation, thus improving the radiation hardness.
Recently, Batentschuk *et al.* [162] reinvestigated the radiation stability and their results differ considerably from the results of Zimmerman *et al.*. Batentschuk *et al.* found a lower rate of degradation of the PSL. Furhermore, they found a range, in which the PSL intensity does not decrease but rather slightly increases. A possible cause for the significant difference should lie in the microstructure and/or the composition of the samples. Both research groups used a similar deposition technique, described in section 3.4.2. However, information about the precursor for Eu doping has not been given by Zimmermann *et al.*, despite the fact that the composition of the precursor is very important due to a possible incorporation of a large quantity of additional impurity ions in the CsBr lattice. Batentschuk *et al.* suggest a negative impact of the possible oxygen-containing Eu precursors used in the study of Zimmermann *et al.*.

6.4.4 Luminescence spectroscopy on NIPs

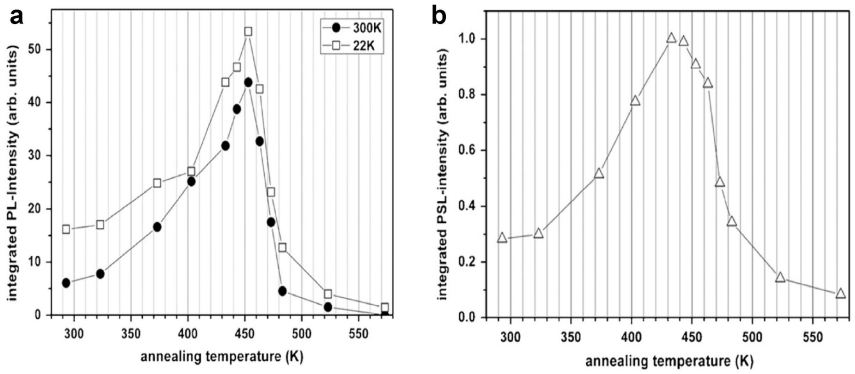

Figure 6.18. **a** Integrated intensity of the broadband Eu^{2+} PL of NIPs depends on the annealing temperature. Measured at RT (circles) and 22 K (squares). **b** Integrated intensity of the PSL emission spectra of NIPs, depending on the annealing temperature. Measured at RT. (from [163])

During our collaboration with Agfa HealthCare NV, they had a parallel collaboration with the University of Erlangen existed. Weidner *et al.* [163, 164] investigated similar NIPs using luminescence spectroscopy, in particular PL and PSL.
The PL spectra of the NIPs at RT show a broad band structure originating from the 5d-4f emission band of Eu^{2+}. It is peaking around 440 nm (2.8 eV), as shown in [151]. The spectral shape of this broad band is quite independent of the temperature treatment the samples were exposed to. However, the intensity of the

band changes (figure 6.18a) according to the annealing status of the NIPs. Unannealed samples show only weak PL intensities, but the intensity increases with the annealing temperature (annealing on air), until a maximum of about 10 times the intensity of the unannealed samples is reached, when the NIPs are tempered at about 170 °C (constructive annealing). Annealing at higher temperatures causes a loss of the PL intensity again, until the band nearly disappears after 300 °C (over)annealing. This temperature behaviour of the intensity of the broadband luminescence occurs when measured at RT and at LT. Analogously, the PSL intensity varies in the same way, as published for powder samples in [28, 151] (see also figure 6.14) and demonstrated for NIPs in figure 6.18b.

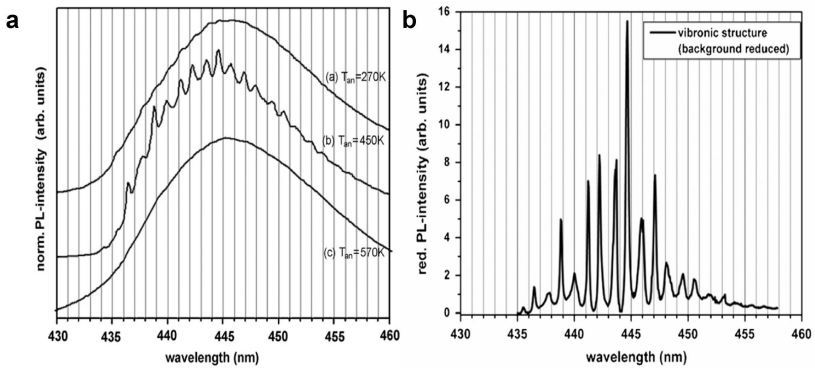

Figure 6.19. **a** Normalized PL emission spectra of NIPs measured at 5.5 K in different stages of annealing: (a) not annealed, as grown; (b) constructively annealed at 170 °C; (c) overannealed at 300 °C. The zero level is shifted for clarity.
b Sharp vibronic peak structure of a constructively annealed NIP (3 h at 170 °C) measured at 5.5 K, obtained by subtraction of the underlying broad band emission (fitted by two Gaussian functions). (from [163])

In addition to the broad band emission, the LT PL emission spectra of the constructively annealed NIPs also contain a series of sharp lines, which are interpreted as vibronic structure (see figure 6.19a). The intensity of the vibronic peak structure undergoes an evolution in agreement with the PL/PSL intensity evolution as a function of the annealing temperature. The authors concluded that the slightly irregular spacing and complicated intensity distribution of the vibronic lines do not allow an interpretation based on a single electronic transition coupled to a single local vibration. They did not give an interpretation for this formation and decay of luminescence centres during the constructive annealing process.
Finally, Weidner *et al.*, also tested different annealing atmospheres. While keeping the NIP at 180 °C, a constant gas flow with different composition was guided over the sample for 3 hours. The results on NIP CB 72425 can be found in figure 6.20

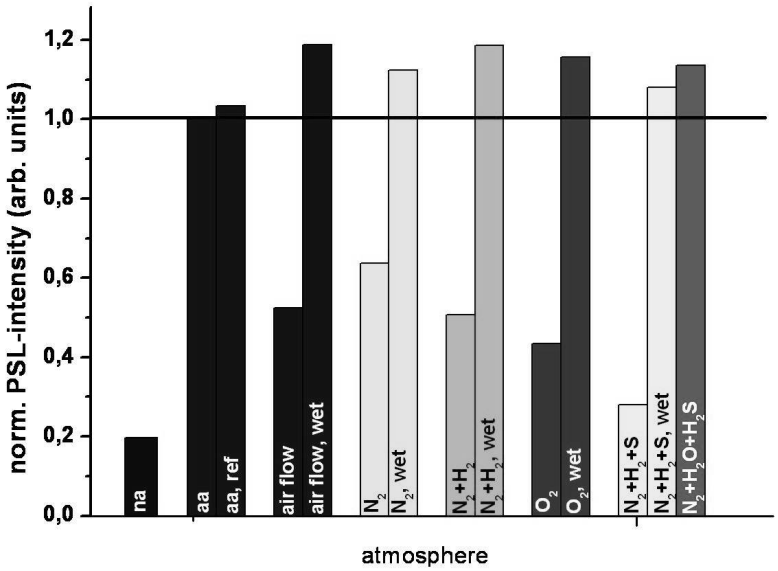

Figure 6.20. Normalized PSL intensity of a NIP (CB 72425) which was annealed for 3 hours at 180°C in different atmospheres. na = not annealed, aa = annealed on air at Agfa HealthCare NV (from [164])

and one can see clearly the positive effect of water on the PSL intensity.

6.4.5 EPR on NIPs

Before our study started, the only published EPR work on NIPs was done by Komiyama *et al.* [165]. In a US patent, by Fuji Photo Film Co., they presented Q band EPR spectra at 10 K on (probably powdered) NIPs. The authors found a difference in the resistance to X-ray damaging for two features appearing at effective g values of 1.90 and 1.88 respectively. They did not analyse the two components, but described them as Eu^{2+} defects with a different oxygen concentration in the neighbourhood of the Eu^{2+} ion. The feature with an effective g value of 1.90 showed a higher resistance to X-irradiation and was designated as the one with the comparatively smallest neighbouring oxygen quantity.

6.5 FIRST EXPERIMENTS ON CSBR:EU^{2+} NIPS

In the previous sections it was shown that constructive annealing of the NIPs at 170°C improved the PSL yield, thus the sensitivity of the plate. Agfa HealthCare NV took advantage of this knowledge, and all NIPs are now systematically annealed after the deposition. Therefore, the 4h constructive annealing at 170 °C on air, will from now on be referred to as *Agfa-annealing*.
As annealing at 170°C had a beneficial influence on the PSL properties of NIPs, we decided to start our EPR research by annealing NIPs at different temperatures up to (close to) the melting point. To avoid oxidation from Eu^{2+} to the EPR silent Eu^{3+} we performed the annealing under vacuum conditions. Figure 6.21 shows an annealing cyclus of the first NIP delivered to us by Agfa HealthCare NV. This NIP (batch CB 50804 AA) was produced in 2004 and already Agfa-annealed.

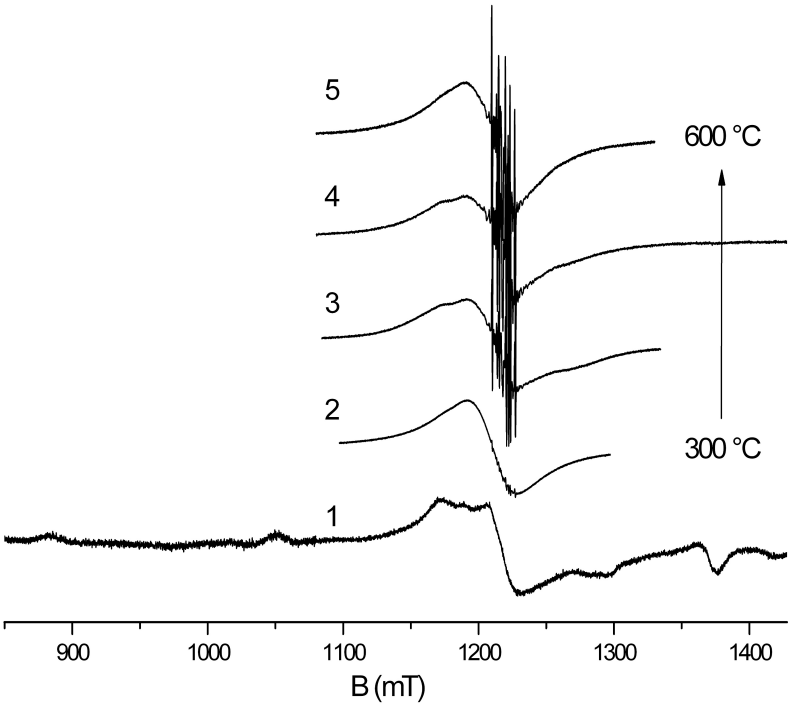

Figure 6.21. Q band EPR spectra of a powdered NIP (CB 50804_AA, produced in 2004) measured at T = 20 K displaying the effect of an annealing cyclus.
1. Spectrum with no extra annealing (only Agfa-annealed).
2.-5. Spectra after vacuum annealing at 300°C, 400°C, 500°C and 600°C respectively, followed by freezing to 77K.

We found different Eu-related signals at different stages of the annealing cycle :

- From RT up to 300 °C we measured the signals present after the deposition and later we could prove that these signals were correlated to the sensitivity

of the plate. The characterization of the defects responsible for these signals constitutes the main part of the work and is described in section 6.6. It was not possible to grow CsBr:Eu^{2+} single crystals nor to manipulate them afterwards in such a way that they show these EPR signals. This meant that we could only use the poly-crystalline NIPs to characterize the signals. This will obviously not facilitate their analysis.

- Around 300 °C these signals disappear and a broad stable signal appears around $g \approx 2$. This signal will be discussed in section 6.7. This broad signal was already observed in the spectrum of certain Agfa-annealed NIPs, but as the quality of the NIPs and/or the Agfa-annealing procedure improved, this signal was no longer detected in as-received Agfa-annealed NIPs. Here it becomes clear why it was not possible to Bridgman grow single crystals containing the defects present at RT, since Bridgman growth starts from the melt (T_m = 636 °C).

- From ca. 500 °C another signal could be detected, if the measurements were done quickly after the annealing and/or when the sample was frozen (in liquid nitrogen) after annealing. These unstable defects will be described in section 6.8 and are attributed to Eu^{2+} monomers.

6.6 ANNEALING AT 170 °C OF NIPS

6.6.1 Correlation between the EPR spectrum and the sensitivity of the NIPs

At RT, all Agfa-annealed NIPs display, with a varying intensity, a characteristic EPR spectrum extending over several hundreds of mT (which will be called the *AA-EPR* spectrum). The occurrence of these intense EPR lines was rather surprising as both from the literature [138] and our own experience it appeared that similarly doped single crystals (see section 6.8) do not show any resembling signal. Because the NIP structure (needles on a substrate) is quite brittle, the first EPR measurements were performed on powdered NIPs. The analysis of the EPR spectrum, however, appeared impossible, all the more since in earlier NIPs a broad signal around $g \approx 2$ overlaps the AA-EPR spectrum.
Fortunately, when the NIPs were cut in a very careful way, it was possible to recover intact pieces of sufficient size. The small pieces of NIP were placed in a Q band quartz tube or on an X band sample holder (see figure 3.10 on page 42). From the beginning, it was clear that the NIPs were preferably measured in Q band[3]: the S/N ratio was noticeably higher in Q band and the sample dimensions were a better match for the Q band cavity.
After measuring several types of Agfa-annealed NIPs, we suspected that the AA-EPR signal intensity shows correlation with the PSL intensity, but it was not so obvious to prove it. The intensity of both the AA-EPR signal and the PSL depends on two aspects : the morphology of the plate and the type of annealing the plate goes through. The morphology of the plate is determined during the deposition, and the following aspects both affect the EPR and PSL intensity :

- the Eu concentration and the Eu^{2+}/Eu^{3+} ratio
- the thickness of the plate
- the packing density of the plate : loosely packed needles will lead to a small filling factor η

These parameters can have a different influence on both the EPR intensity and the PSL intensity. In house Agfa HealthCare NV measurements showed, for example, that the presence of Eu^{3+} has a beneficial influence on the PSL yield, while the influence on the EPR intensity could not be proven. Also the needle diameters have an influence on the PSL while this does, again, not affect the EPR intensity (if the packing density is kept constant).

[3]We will see later that the size of the ZFS (which is larger than the X band quantum) also favours Q band measurements.

The only way to prove unambiguously the correlation between the AA-EPR signal and the PSL intensity, is to anneal several pieces of the same NIP under different conditions. Since all the pieces have the same morphology (coming from the same plate), the EPR and PSL intensity of all pieces can be compared without further problems. Agfa HealthCare NV prepared a high coating weight (thickness = 1 mm) NIP (24 by 18 cm^2) with an Eu^{2+} concentration of about 500 ppm. An Ar gas stream (with a maximal pressure of 10 Pa and at a temperature of 20-30°C) cools both the vapour and the Al support. The plate was cut into seven pieces with comparable sizes and seven different treatments were given (see table 6.3). Sample 1 is the as-prepared NIP, while samples 2, 3 and 4 were annealed at 170 °C under different humidity conditions. Samples 5 and 6 were given an extra aging treatment and sample 7 was overannealed at 300 °C. All treatments had a marked influence on both the PSL and EPR intensities.

sample	1[a]	2	3	4
4h annealing temperature (°C)	RT	170	170	170
annealing atmosphere[b]	room	vacuum	0.19	0.35
PSL intensity (a.u.)	233	408	582	584
EPR intensity (a.u.)	38	80	115	117
sample	5	6	7	
4h annealing temperature (°C)	170	170	300	
annealing atmosphere[b]	0.19	0.19	<0.02	
aging treatment	72h at 35°C with 80% RH[c]	15 min with 254 nm UV irradiation	none	
PSL intensity (a.u.)	517	563	74	
EPR intensity (a.u.)	78	102	≤6	

Table 6.3. Overview of the different treatments on the seven NIP pieces (batch CB 12708), with their respective PSL and EPR intensities.
[a]Sample 1 did not receive any special treatment and was stored at room conditions.
[b]Gram H_2O per m^3 air.
[c]RH = relative humidity of the room where the oven was placed

The PSL measurements were carried out at Agfa HealthCare NV, by integrating the blue-green light intensity emitted upon photostimulation with a HeNe laser at 632.8 nm after applying an X-ray writing dose of 20 μGy to each sample. The PSL values in table 6.3 were calculated as the average intensity from five different spots on the same plate.
The AA-EPR spectra of the seven pieces (with the magnetic field perpendicular to the plate : $\vec{B}||$ <100>) are shown in figure 6.22. The AA-EPR signal intensity

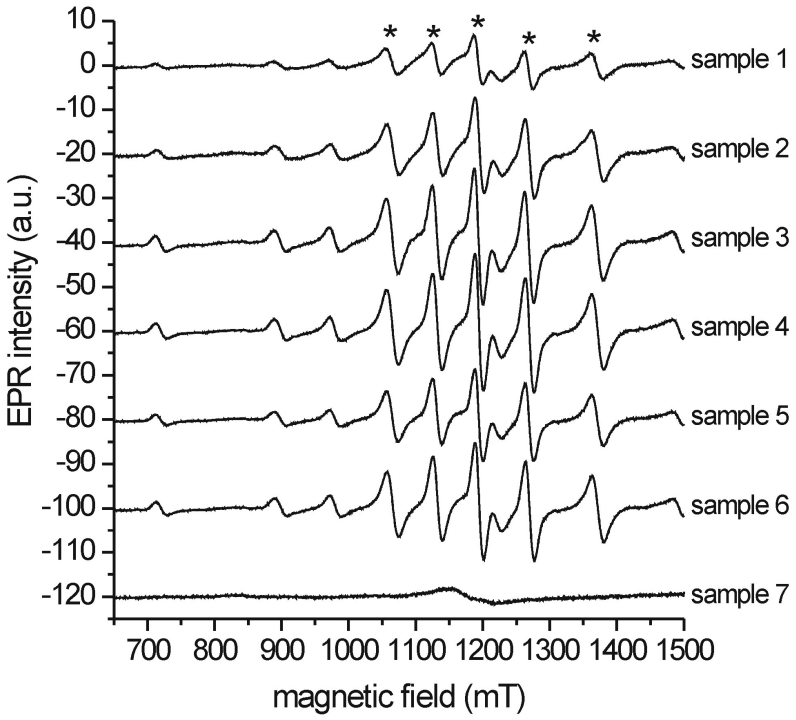

Figure 6.22. Overview of the AA-EPR signals for the seven samples. For all plates, the averaged spectrum from five pieces is shown and all spectra are on the same intensity scale. For clarity, an offset was applied starting from sample 2. The five lines used to calculate the total EPR intensity are marked with an asterisk.

was calculated from the sum of the peak-to-peak amplitudes of the five most intense peaks in the spectrum (marked with an asterisk in figure 6.22). The single sample reproducibility was determined by repeatedly measuring the same sample in between recordings of other samples resulting in an error of about 10%. This percentage comprises both the time dependence of the spectrometer sensitivity and the error in positioning the sample in the cavity. The plate homogeneity, determined by measuring five different pieces, was found to be better than 20%. The average of these five measurements on each plate can be found in table 6.3. The intensity of the AA-EPR signal of sample 7 has been estimated to be less than 5% of that of sample 4 and this estimation is added in the table. In part due to its low intensity, the signal of sample 7 is dominated by a possibly oxygen related signal around $g = 2.06$ which disappears after long term (months) shelf storage.
In figure 6.23, the results of table 6.3 are presented in an EPR intensity versus PSL intensity plot, with the appropriate error bars for a 95% confidence interval. The

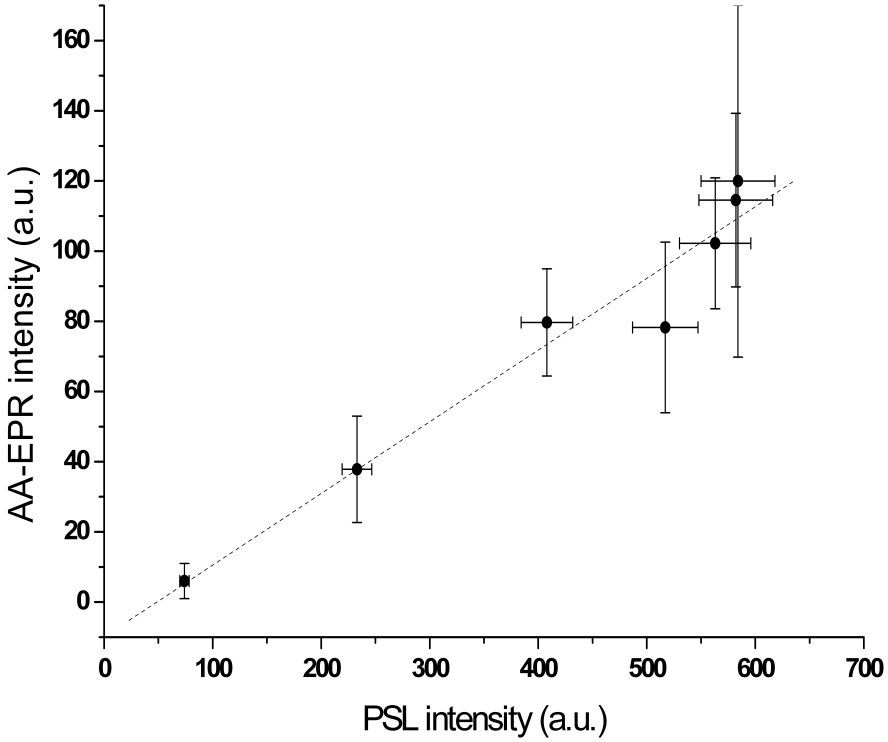

Figure 6.23. AA-EPR intensity vs PSL intensity plot of seven differently treated (see table 6.3) samples of the same NIP. The error bars represent a 95% confidence interval. The dashed line is the calculated linear correlation.

error bars were determined by using the Student's t distribution on the values obtained for the five different spots. The plot in figure 6.23 strongly suggests a linear dependence between the AA-EPR signal and the PSL intensity. Analysis of the 31 available data points (five measurements for six samples, one estimated point for sample 7) gave a Pearson correlation coefficient of r=0.81, with $p<0.001$, which indicates a significant linear correlation. The calculated regression line is shown in figure 6.23 and follows $I_{EPR}=A.I_{PSL}+B$, with A = 0.204±0.056 and B = -9.9±27.5, where the errors delimit a 95% confidence interval. We note that B is zero within the experimental error, indicating that no PSL processes occur uncorrelated to the AA-defect.

Another, albeit less strong, proof for the correlation between the AA-EPR signal and the PSL intensity is found in the comparable overannealing behaviour. It was shown before [28, 163] that gradually increasing the annealing temperature to 300 °C irreversibly quenches the PSL intensity. Additional annealing of the sample for 30 min at 300 °C, both in air and in vacuum, accordingly reduces the AA-EPR signal, while a new broad EPR signal appears (already mentioned on page 102). This new signal, shown in figure 6.24, is isotropic with g = 1.998 and a peak-to-

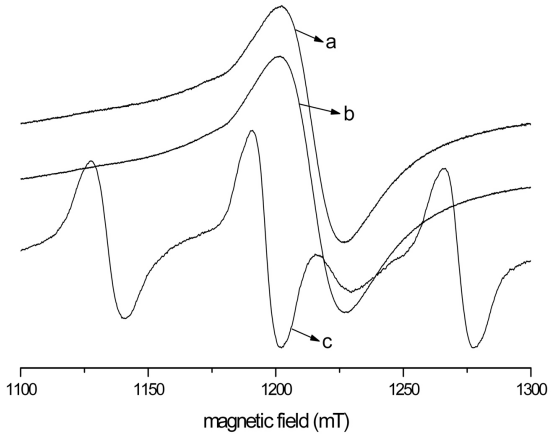

Figure 6.24. The isotropic EPR spectrum of sample 3 after overannealing for 30 min at 300 °C in air (spectrum a) or in vacuum (spectrum b). For comparison, (part of) the AA-EPR spectrum of sample 3 before annealing is also shown (spectrum c), and an offset was applied for clarity.

peak linewidth of about 25 mT at RT. No significant intensity difference could be detected between annealing in air and in vacuum. This signal will be further discussed in section 6.7. It is somewhat surprising that this signal is different from the one in sample 7 (figure 6.22) as the overannealing temperature is the same. Possibly, the AA-EPR defect is a necessary precursor for the broad EPR signal in figure 6.24. Alternatively, prolonged annealing at 300 °C may lead to oxidation from Eu^{2+} to Eu^{3+}.

These findings suggest that the AA-EPR centre is involved in the storage and/or readout processes in CsBr:Eu NIPs, e.g., as luminescence or carrier trapping centre. In the following, we will characterize the signal and try to identify the defect responsible for it.

6.6.2 The EPR spectrum of NIPs at RT

6.6.2.1 The single crystal-like <100> and powder spectrum

In figure 6.25a the single crystal-like <100> spectrum of a typical NIP (sample 1 from previous section, CB 12708_73) is shown, measured at Q band at RT. All spectra shown in the following were recorded using this sample, unless explicitly mentioned otherwise. This spectrum is compared with the spectrum of the powdered NIP (6.25b). The comparison of the two spectra demonstrates that the same features occur at the same field positions. This is a strong indication that all tensors in the SH governing the angular dependence of the EPR lines have their principal directions along <100> orientations. The symmetry in the spectrum

with respect to g ≈ 2 strongly suggests that a few higher field lines are missing due to the limited range of our magnet (1.5 T). As the spectrum was measured in many different samples and under diverse experimental conditions, without changing its shape, we can be sure that it is non-composite.

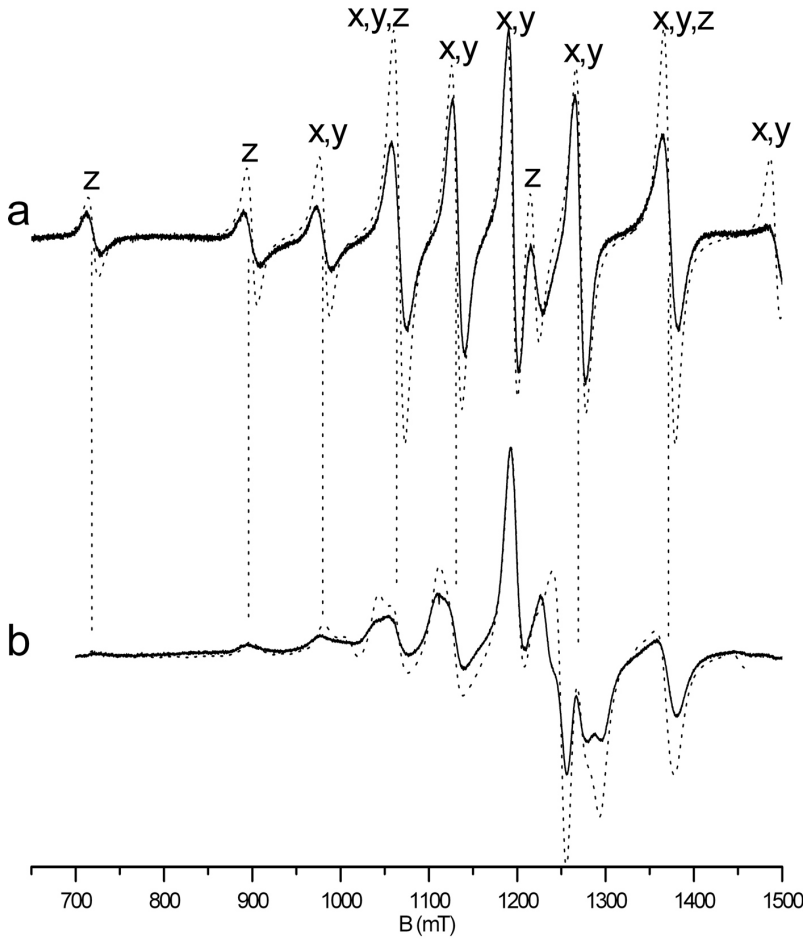

Figure 6.25. Q band EPR spectrum of an intact NIP with the magnetic field along the needles' axis (a) and of a powdered NIP (b). All spectra were recorded at RT, with P_{mw} = 54 mW and A_{mod} = 0.4 mT. The vertical lines illustrate the presence of common features in the two spectra. The dotted lines show the simulations, using the parameters in table 6.4.

As no (S)HF interaction is resolved and an isotropic g tensor is expected, we could convincingly simulate the spectrum with the following SH :

$$\hat{H} = \beta_e g \vec{B} \cdot \hat{\vec{S}} + \sum_{k=2,4,6} \sum_{-k \leq q \leq k} B_k^q \hat{O}_k^q \tag{6.4}$$

It proved possible to reproduce all resonance line positions in the single crystal-like <100> spectrum (figure 6.25a), with an axial centre, with the fourfold axis

along <100> . This resulted in two different contributions to the <100> spectrum: both the perpendicular (x=y) and the parallel (z) orientations of the centre are visible. Each resonance line could be assigned to the appropriate orientation of the defect. As a convention, we will label the defects which have their fourfold symmetry axis along the needle axis as z oriented, and those with the tetragonal axis perpendicular to the needle axis x or y oriented. The best fit parameters are listed in table 6.4 and the simulations are shown in figure 6.25. Only the ZFS parameters up to fourth order have been used, since including non-zero B_6^q's in the fitting led to shifts in the resonance positions considerably smaller than the observed linewidths, as did including g anisotropy. Therefore, B_6^q's and g anisotropy have been ignored. From the RT spectra, only the relative signs of the ZFS could be determined, and we chose $B_2^0 < 0$ (see section 6.6.4 for justification of this choice). We have attributed an equal weight to the calculated spectra of the three defect orientations (x, y and z) in the simulation of the <100> spectrum. Whereas the resonance field positions are perfectly reproduced by the simulation, the intensities are not. We assume this is caused by random strain of the ZFS parameters, as was already the case in Fe^{3+} doped Cs_2NaYF_6 (see figure 4.2), and by the underlying polycrystalline seedling layer (see section 3.4).

AA-EPR (RT)	
g	1.9913_{51}
B_2^0	-755_{11}
B_4^0	-0.27_{18}
B_4^4	3.47_{99}

Table 6.4. g value and ZFS parameters (in MHz) of the AA-EPR defect in a CsBr:Eu^{2+} NIP at RT

6.6.2.2 Angular variation of the needle plate spectrum

As ultimate test for the correctness of the analysis we recorded the angular variation, for sample rotation around an axis perpendicular to the needles. In figure 6.26, rotation angle 0° (and 180°) corresponds to a magnetic field orientation parallel to the needles, hence giving rise to the single crystal-like <100> spectrum. The 90° spectrum is recorded with the magnetic field perpendicular to the needles and, for a random in-plane needle orientation, would correspond to the 2D powder spectrum (see section 3.4.4). Inspection of the 0° and 90° spectra shows that they are, however, very much alike. In particular, it can be seen that the two lines at low fields (marked with an asterisk), which correspond to z components

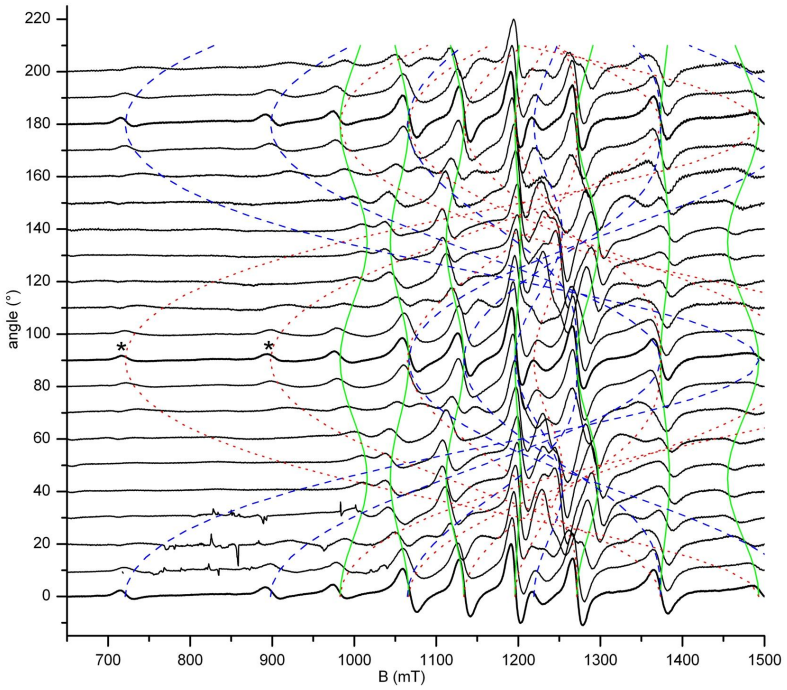

Figure 6.26. Q band EPR angular variation of a NIP around an axis perpendicular to the needles at RT. At 0° and 180° a <100> orientation is found, while at 90° a 2D powder spectrum is present. The lines represent simulations of the angular variations of the single crystal resonance fields, using the SH parameters in table 6.4. The two asterisks indicate two low field z component features of the 2D powder spectrum.

of the spectrum, have slightly decreased in relative intensity and have acquired an asymmetric line shape, as expected in powder spectra, but their intensities relative to the x and y components is much higher than expected for a true 2D powder spectrum. This can be attributed to the fact that the needles also show an appreciable in-plane ordering, as could be seen earlier from the pole figure of this NIP (figure 3.9 on page 41). This is confirmed by the EPR angular dependence in a plane. Indeed, for a random in-plane orientation of the needles, no angular dependence should be observed when rotating the sample along the needle axis, whereas a periodic angular pattern is observed in figure 6.27.

The full, dotted and dashed lines in figure 6.26 represent simulations of the single crystal angular dependence in a (100) plane using the parameters in table 6.4. Again, like in section 3.5.2, the angular variation contains three possible path-

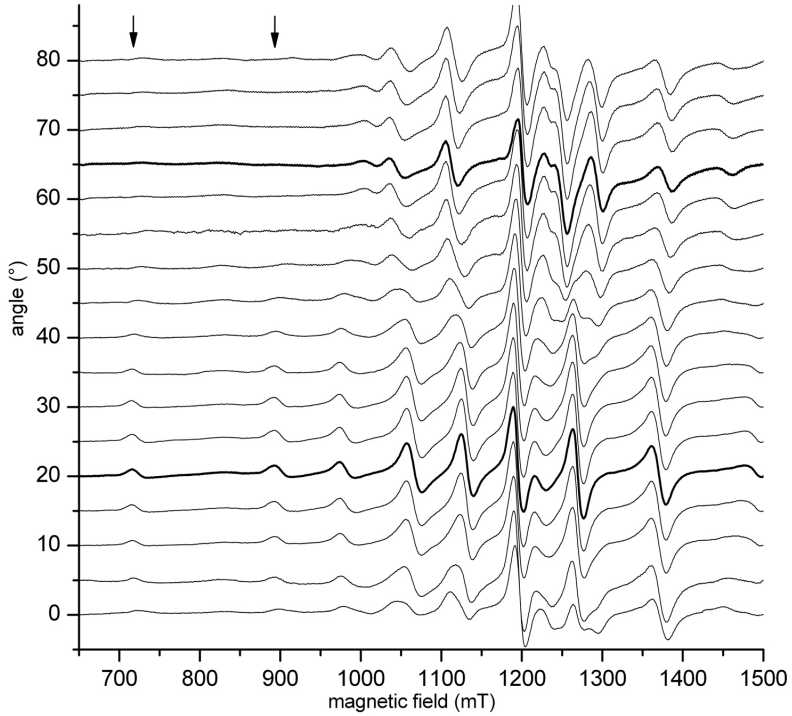

Figure 6.27. Q band EPR angular variation of a NIP around the axis of the needles at RT. A periodic angular pattern is observed, e.g., in the intensity of two low field z components, the positions of which are marked with arrows.

ways :

$$\begin{aligned} x &\rightarrow y \qquad \text{(in solid green, equivalent with } y \rightarrow x\text{)} \\ z &\rightarrow x \qquad \text{(in dashed blue, equivalent with } z \rightarrow y\text{)} \\ x &\rightarrow z \qquad \text{(in dotted red, equivalent with } y \rightarrow z\text{)} \end{aligned} \tag{6.5}$$

The perfect agreement between the simulation lines and the spectra, confirms the SH parameters in table 6.4.

One final remark should be made about these simulations. There will obviously be more than these three paths in the angular dependence. For a random in-plane orientation of the needles, an x oriented defect, e.g., can turn to an arbitrary direction in the yz plane, and not only to the exact y or z direction. Two examples are shown in figure 6.28, where the possible paths of only one EPR transition (M_S=$|\frac{5}{2}> \leftrightarrow |\frac{7}{2}>$) of an x (green solid lines) and z oriented (blue dashed lines) defect are drawn. We note that the possible paths for the x (or y) oriented defect spread out widely, mainly due to the large B_2^0. The spread of the paths originating from the z oriented defect is much smaller and is only caused by the small B_4^4, which induces a variation of the resonance fields in the plane perpendicular to the four-fold symmetry axis of the centre. Due to averaging, only the extremal

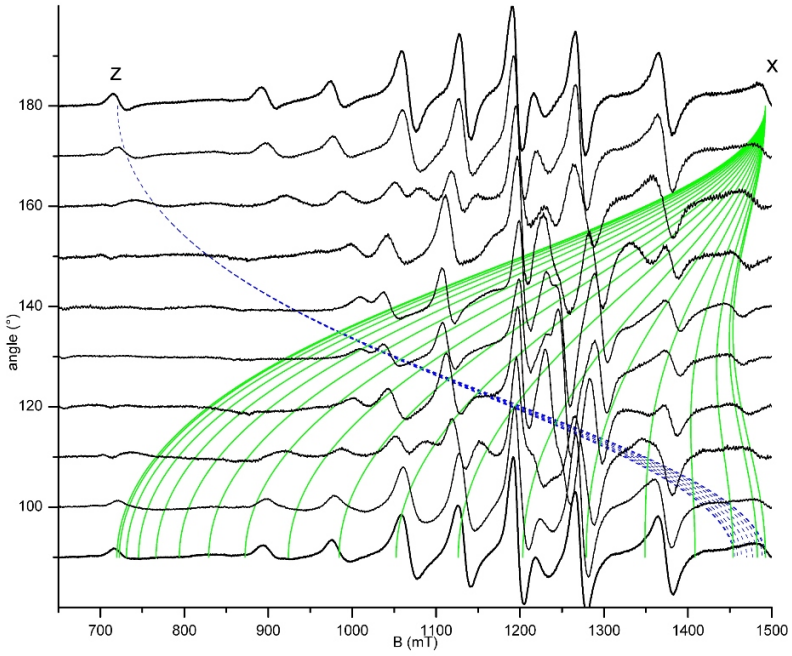

Figure 6.28. Detail of figure 6.26, with a simulation of possible paths for the M_S=$|\frac{5}{2}> \leftrightarrow |\frac{7}{2}>$ transition of an x (green solid lines) and a z (blue dashed lines) oriented defect.

positions (which correspond with the paths in equation (6.5)) are expected to be found in the 2D powder spectrum. As shown in figure 6.27 the in-plane orientation of the needles is not random. An intermediate picture between a single crystal and a 2D powder spectrum arises. The in-plane orientation of a specific needle determines which of the possible paths in figure 6.28 is followed by its EPR angular dependence.

6.6.2.3 NIP:Mn

Before we discuss the effects of T on the Eu spectrum, we want to report the results of a small side project. As will become evident in the following, obtaining ENDOR spectra from NIPs is not that obvious. Therefore we looked for alternative systems that might help in the identification of the Eu centres. We chose Mn^{2+} for three reasons : (i) it is divalent, as is Eu^{2+}, (ii) it is also an S-state ion ((Ar)$3d^5$ configuration with a $^6S_{5/2}$ ground state), but with a lower effective spin (S = 5/2) than Eu^{2+} and (iii) there exists a lot more of EPR and ENDOR literature on Mn^{2+} ions in various crystal lattices (e.g. in CsBr, section 6.3.4), so we hoped that it would be easier to acquire ENDOR spectra from Mn^{2+} doped NIPs.
On our request, Agfa HealthCare NV deposited NIPs doped with Mn^{2+} instead of Eu^{2+} with various concentrations : 0, 20, 100 and 1000 ppm. In figure 6.29 the

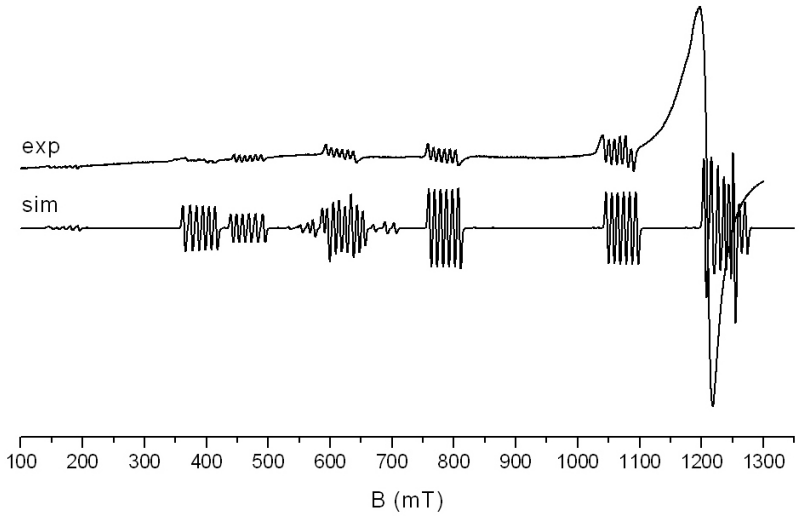

Figure 6.29. Q band experimental and simulated <100> spectrum of Mn^{2+} doped CsBr NIP at RT. Simulations are done using the parameters from Iri *et al.*, listed in table 6.5.

<100> spectrum at RT is shown for the NIP with the highest concentration (CB 267022). When simulating a <100> single crystal EPR spectrum with the same

CsBr:Mn^{2+}				
S	$g_\perp$	$g_{\|\|}$	A (MHz)	B_2^0 (MHz)
5/2	2.00	1.95	270	3900

Table 6.5. EPR values at RT of aqueous solution grown CsBr:Mn^{2+} single crystals (from [140]).

experimental parameters and using the EPR parameters listed by Iri *et al.* (see table 6.5), we see a good agreement between simulation and experiment. It seems very plausible that we detected the same defect. As already mentioned in section 6.3, they attributed it to a Mn^{2+}, substituting a Cs^+, with a vacancy at its NN cation site and with an appreciable displacement of the Mn^{2+} towards the vacancy. The broad signal around g≈2 with a peak-to-peak width of 22 mT resembles on the one hand the broad signal found after annealing CsBr:Eu^{2+} NIPs at around 300 °C and on the other hand the broad signal in the CsBr:Mn^{2+} single crystals, as both are centred around g≈2. The fact that the relative intensity of the broad signal was smaller in lower Mn^{2+}-doped NIPs, corresponds well to the assignation of Iri *et al.* to a Mn-aggregate.
In these NIPs no ENDOR could be detected. It was nevertheless interesting to see that Mn^{2+} doped NIPs and (aqueous solution grown) single crystals contain the

same EPR signals at RT, whereas no EPR signal was detected in Eu^{2+} (Bridgman grown) doped single crystals. Our preliminary assumption is that Iri *et al.* did not reckon with the possible influence of H_2O : while in Bridgman grown single crystals all water is removed before and during the growth[4], this is not the case for solution grown crystals.

6.6.2.4 Conclusion

The analysis of the RT EPR spectrum of Eu-doped CsBr NIPs has shown that it is due to a single paramagnetic centre with S = 7/2 exhibiting a large axial ZFS. Its spin state and the fact that its spectrum can be detected at RT, allow us to conclude that this defect is Eu^{2+} centred. Its spectrum does, however, not correspond to that of Eu^{2+} monomers observed after Agfa-annealing CsBr:Eu^{2+} Bridgman grown single crystals at higher temperatures and decaying at RT due to aggregation of the ions (see section 6.8).
We may, therefore, conclude that the here studied defect has a complex structure, either involving multiple (i.e., an odd number of) Eu^{2+} ions and/or a nearby lattice defect or an accidental impurity, which makes it stable against (further) aggregation. Both the results on Mn^{2+} doped NIPs and the enhanced PSL yield after annealing, suggest that such an impurity could be water (related).
In order to obtain a more detailed picture of the structure and surroundings of this centre, low temperature EPR and ENDOR measurements were needed. These will be described in the following sections.

6.6.3 The EPR spectrum of NIPs at 4K

6.6.3.1 The <100> and powder spectrum at 4 K

As will be shown later, temperatures $\leq$ 4 K are needed for ENDOR measurements on these centres, but when cooling the sample from RT to 4 K, the EPR spectrum undergoes a dramatic change. In figure 6.30 the <100> Q band EPR spectra at RT and 4 K are shown. Comparing both spectra, the similar field range and the size of the line splittings suggest that they originate from the same type of centre. On the other hand, it is clear that these spectra exhibit several differences which complicate finding the link between them; for example, at 4 K the number of line groups is considerably larger than at RT and a complex (S)HF structure is visible on several transitions. Analyzing this structure from the EPR spectra alone is not

[4]This is done via heating the quartz ampoule, containing both the host material and the dopant, at around 300°C for at least three days. During this process, all evapourating water is extracted via a pump. Afterwards, the ampoule is sealed, keeping the vacuum.

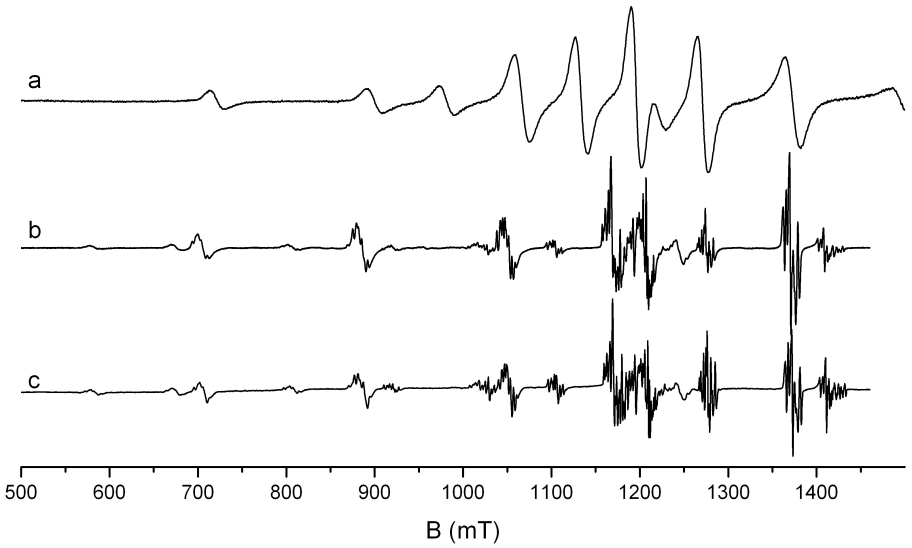

Figure 6.30. Normalized Q band <100> spectrum of a 1 mm thick NIP at RT (a) and at 4 K (b) and of a commercial plate (Hamamatsu A0 605490) at 4 K (c).

obvious. In figure 6.30c, the <100> spectrum at 4 K is shown for a commercial plate, demonstrating that essentially the same signal is found in both materials, which substantiates the relevance of these spectra for actual applications.
Varying both the experimental recording and sample conditions, we attempted to obtain additional information that would help for the complete analysis of this complex Q band <100> spectrum.

- When the MW power is varied, in order to separate the spectra of defects with different relaxation behaviour, no relative intensity changes between the resonance lines in the <100> spectrum occur.

- The W band (ν = 95 GHz) <100> spectrum (figure 6.34) reveals several transitions which cannot be reached in the Q band setup. Since the complete spectrum consists of more than 14 line packets, the RT interpretation in terms of only one tetragonal centre cannot be complete here.

- When comparing the <100>, the 2D powder, and the 3D powder spectrum (see figure 6.31), essentially the same features occur at the same field positions. This indicates that the g and ZFS tensors in the SH have their principal axes along or close to <100> orientations.

The extra information obtained in this way appeared anyhow still insufficient for a complete analysis of the EPR spectrum.

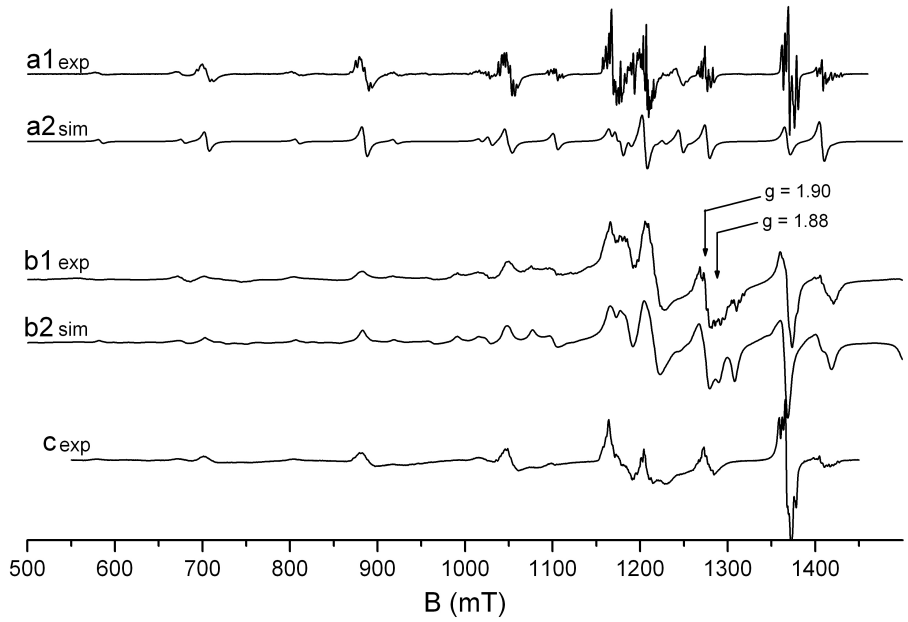

Figure 6.31. 4 K Q band spectrum of a NIP with the magnetic field perpendicular to the plate [(a) <100> spectrum], of a powdered NIP [(b) 3D powder spectrum] and of a NIP with the magnetic field parallel to the plate [(c) 2D powder spectrum]. An optimized sum of the simulations of both AA-EPR I and II has been used (a2 and b2) to reproduce the experimental (a1 and b1) spectra. With arrows, the resonance fields belonging to two effective g values have been indicated (see section 6.6.5).

6.6.3.2 The angular variation at 4 K

The angular variation around an axis perpendicular to the needles proved to be the key to solving this problem. The angular variation is shown in figure 6.32; 0° corresponds with the <100> spectrum, 90° with the 2D powder (not shown in the picture). From figure 6.32a, it is clear that, due to an enhanced broadening at larger angles, the lines in the angular variation can only be easily followed close to the <100> orientation. Nevertheless, the angular variation was decisive in understanding the complex EPR spectrum. In figure 6.32b, several branches exhibiting little anisotropy were found. These were attributed to the perpendicular component of a centre with tetragonal symmetry, leading to the prediction of the other perpendicular and parallel components. As can be observed in figure 6.32a, these transitions appear to belong to a minority species, labelled *AA-EPR I*. The remaining strong lines can all be attributed to a second centre with orthorhombic symmetry, *AA-EPR II*, as clearly shown in figure 6.32b and further explained in the next subsection.

The SH parameters determined from the angular variation were optimized using

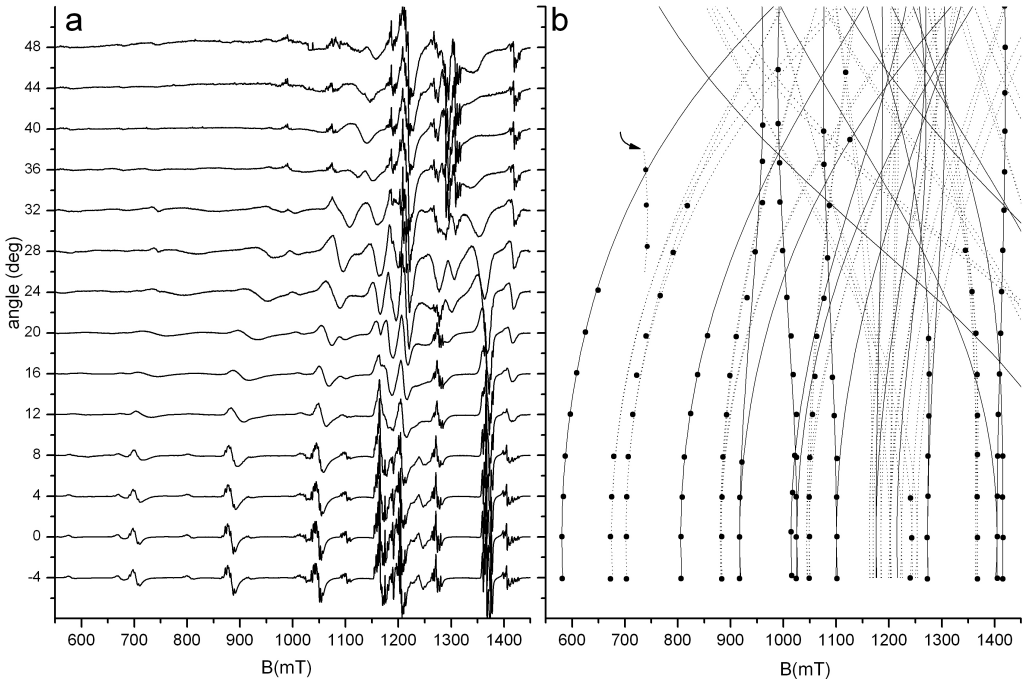

Figure 6.32. a 4 K Q band angular variation with the magnetic field rotated in a plane perpendicular to the plate, at 0° the <100> spectrum is visible.
b For both centres, the resonance positions and the simulations (solid and dashed lines for AA-EPR I respectively AA-EPR II) are shown. The dotted line and resonance positions marked with an arrow represent a forbidden $|-\frac{3}{2}>\leftrightarrow|\frac{1}{2}>$ transition of AA-EPR II on a zy oriented line.

the Q and W band spectra in the <100> orientation and can be found in table 6.6. The solid and dashed lines in figure 6.32b, representing the simulations of AA-EPR I and II, respectively, as well as all other simulations in this section, were calculated using these parameters.

	AA-EPR I (4 K)	**AA-EPR II (4 K)**
g	1.993_5	1.991_4
B_2^0	$-964.6_{6.9}$	$815.6_{9.1}$
B_2^2	0	788_{21}
B_4^0	-0.27_{10}	0.59_{14}
B_4^2	0	$-1.7_{1.2}$
B_4^4	4.77_{65}	$-2.2_{1.2}$

Table 6.6. g value (no unit) and ZFS parameters (in MHz) of the AA-EPR I and the AA-EPR II defect in a CsBr:Eu^{2+} NIP at 4 K

6.6.3.3 Reproduction of the <100> and powder spectrum at 4 K

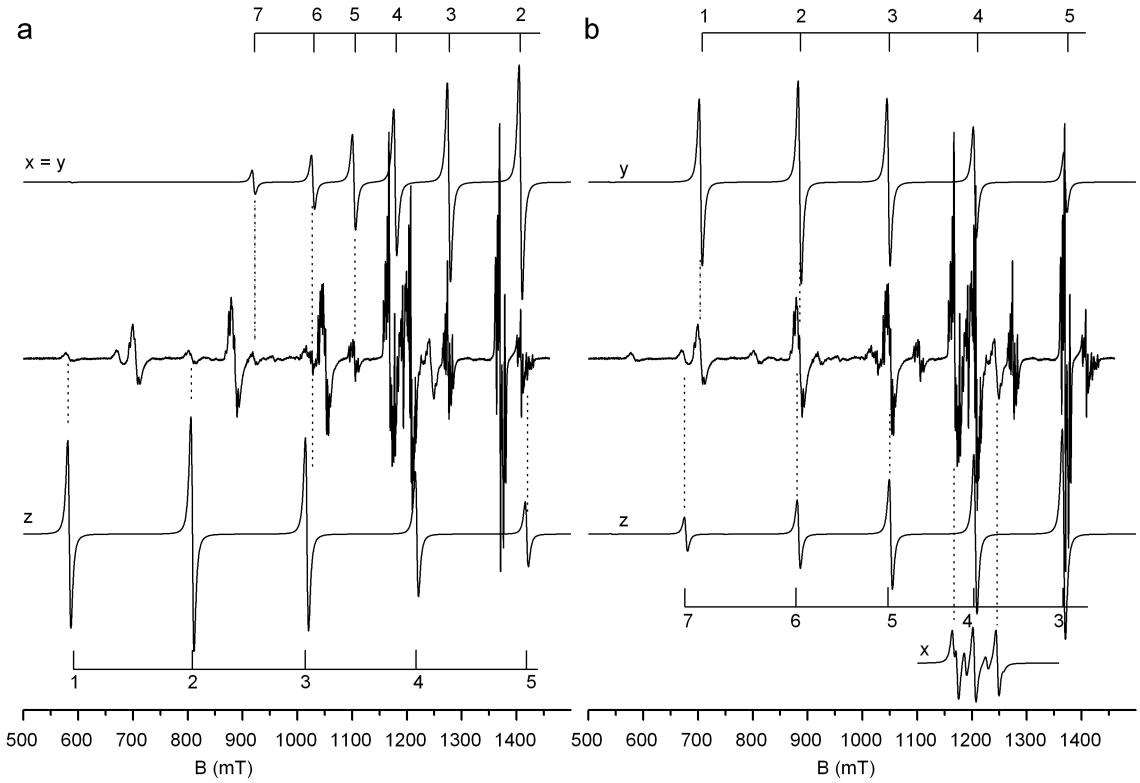

Figure 6.33. Experimental and simulated 4 K Q band <100> spectrum. On the simulations of AA-EPR I (a) and AA-EPR II (b) both the orientation as well as the transition is indicated: 1 represents the $|-\frac{7}{2}> \leftrightarrow |-\frac{5}{2}>$ transition, ..., 7 represents the $|\frac{5}{2}> \leftrightarrow |\frac{7}{2}>$ transition. The simulation parameters can be found in table 6.6; no (S)HF was included.

The *AA-EPR I* centre has the same tetragonal symmetry as the AA-EPR centre. The spectrum is, except for SHF structure, perfectly reproduced with the use of only three ZFS parameters : g, B_2^0 and B_4^0. Within experimental error the defect has an isotropic g tensor, as is expected for an S-state ion. The <100> simulation of AA-EPR I can be found in figures 6.33a and 6.34a, where both the orientation and the $|M_S> \leftrightarrow |M_S + 1>$ transition are indicated. Because of the low temperature the absolute signs of the ZFS parameters could be determined from the population differences of the energy levels. This is (see also section 4.5.3) particularly clear in W band (figure 6.34a), where certain simulated[5] and experimental resonance lines have very low intensities.

For the simulation of the *AA-EPR II* spectrum, which dominates the 4 K spectrum,

[5]Another, so far unmentioned, feature of ES is the possibility to account for population differences between energy levels as a result of the temperature. By default, the temperature is set to infinity, and no population differences are taken into account.

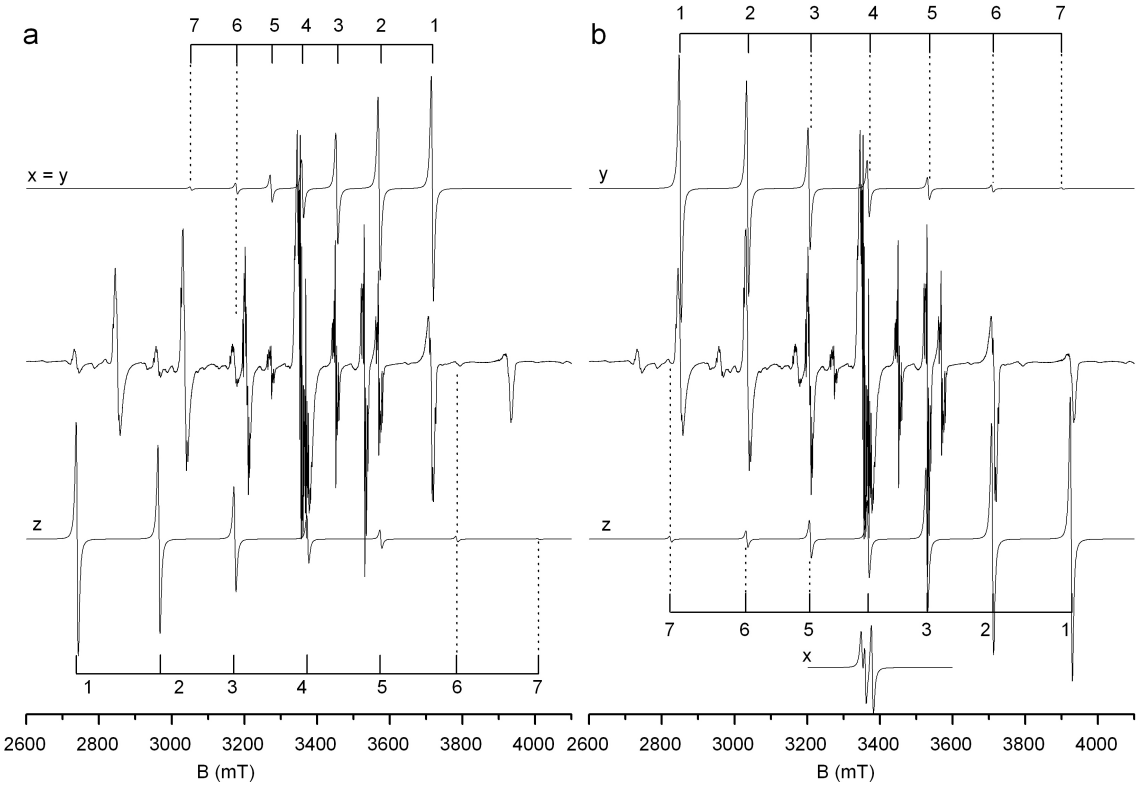

Figure 6.34. Experimental and simulated 4 K W band <100> spectrum. On the simulations of AA-EPR I (a) and AA-EPR II (b) both the orientation as well as the transition is indicated: 1 represents the $|-\frac{7}{2}> \leftrightarrow |-\frac{5}{2}>$ transition, ..., 7 represents the $|\frac{5}{2}> \leftrightarrow |\frac{7}{2}>$ transition. The simulation parameters can be found in table 6.6; no (S)HF was included.

two more ZFS parameters are necessary, reflecting its orthorhombic II symmetry. Three orientations (x, y and z) of the defect are represented in the <100> spectrum (figures 6.33b and 6.34b). In table 6.6 one can find that $B_2^0 \approx B_2^2$ implying that the centre has nearly extreme rhombic symmetry, better known under the condition $E/D = 1/3$. Extreme rhombic symmetry has earlier been found and discussed for several defects in various lattices [166, 167]. When higher order ZFS parameters are neglected, this special ratio for the ZFS parameters creates an identical ZFS in two main orientations (y and z) whereas in the third main orientation (x) the ZFS reduces to zero.

In figure 6.31a the experimental <100> spectrum in Q band is shown, together with an optimized sum of the simulations of the AA-EPR I and AA-EPR II spectra. This figure shows that, like in the case of AA-EPR, while the resonance positions are reproduced perfectly, the intensities are not. In figure 6.31b the corresponding spectra are shown for a powdered NIP. Taken again into account that in the simulations no SHF interaction was included, there is a convincing corres-

pondence between experiment and the simulations for AA-EPR I and AA-EPR II. The 2D powder spectrum in figure 6.31c shows the same features that occur in the <100> and 3D powder spectrum.

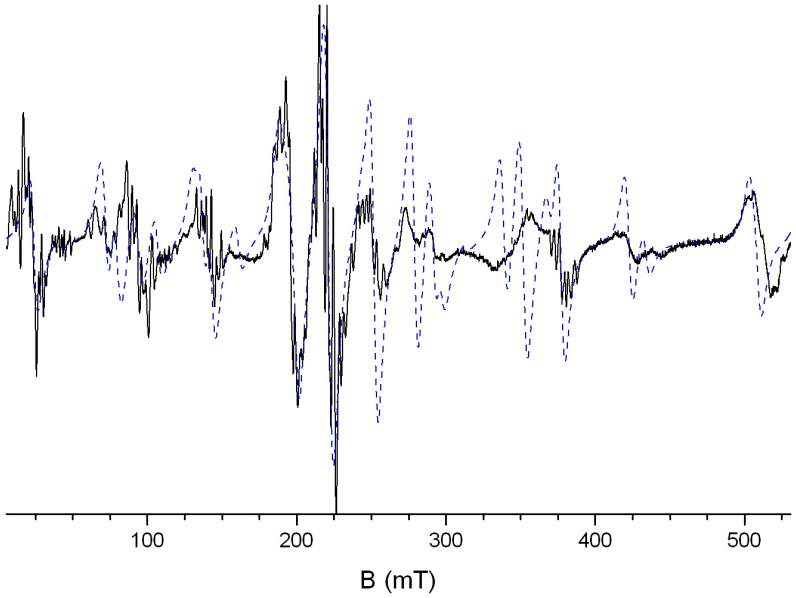

Figure 6.35. Experimental (solid line) and simulated (dashed line) X band <100> spectrum at 4 K. The simulation is an optimized sum of the simulations of AA-EPR I and AA-EPR II.

In figure 6.35 the <100> spectrum in X band is shown. As can be seen, the agreement between the experimental (full line) and simulated (dashed line) spectrum is not as good as in Q and W band. This is, in our opinion, mainly caused by a spread of the needle axes around the <100> crystal axis, since at X band several NIPs are mounted on top of each other (see figure 3.10 on page 42). The spreading can be enhanced by the fact that mainly forbidden transitions are present in the X band spectrum.

6.6.4 The temperature dependence of the EPR spectrum of NIPs

To make the link between the RT (one tetragonal centre) and the 4K (one tetragonal and one orthorhombic centre) spectra, the <100> spectrum was recorded at various intermediate temperatures as shown in figure 6.36. As the spectra were collected from experiments on several days and as sample positioning has an effect on the EPR intensity, the differences in S/N ratio are not believed to be relevant. The x=y (perpendicular) and z (parallel) components are indicated in the RT spectrum. From RT down to about 40 K, the AA-EPR spectrum can be

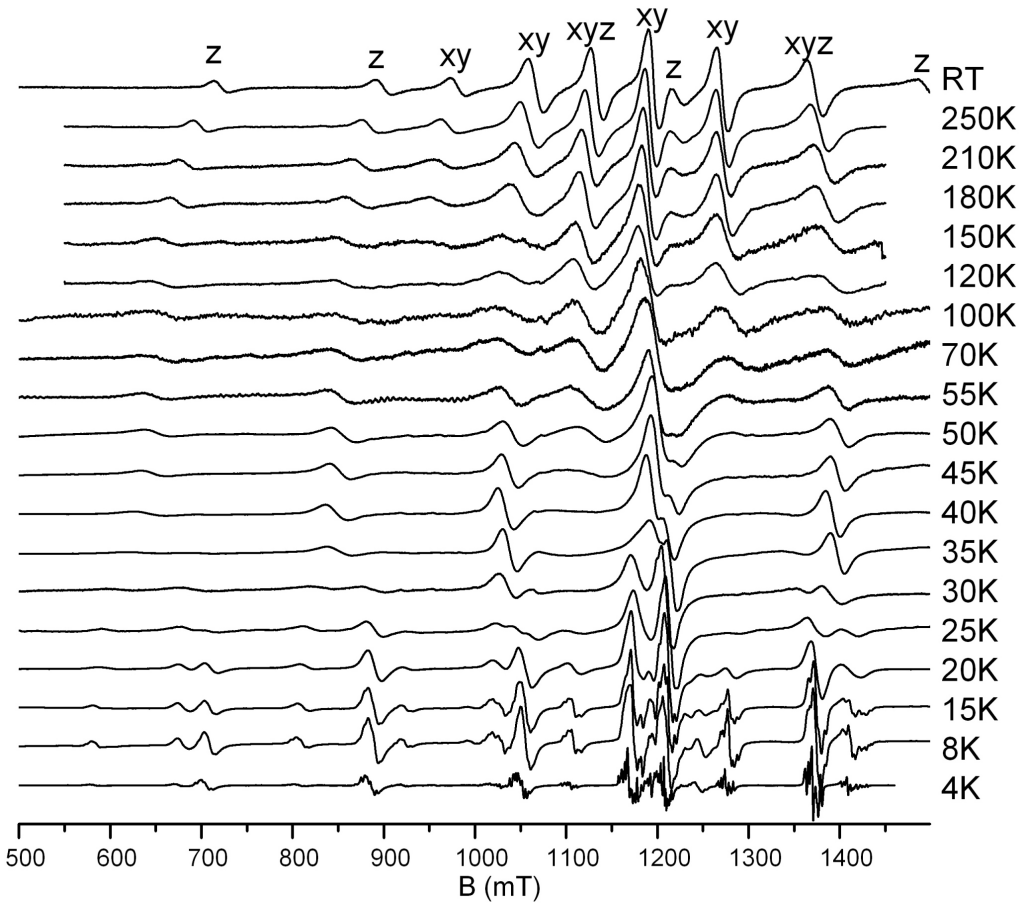

Figure 6.36. Temperature dependence of the <100> spectrum at Q band. All spectra have been recorded at optimal measuring conditions.

followed, albeit with T dependent ZFS parameters. It should, however, be noted that only the parallel component can be clearly followed in this temperature range, whereas the perpendicular component broadens and eventually seems to disappear at lower temperatures. Around 35 K, the spectrum gradually undergoes a more drastic change by the appearance of extra lines and an interpretation in terms of a single centre is no longer possible. From 15 K down to 4 K, (S)HF

structure is increasingly better resolved and the spectrum contains the two components, AA-EPR I and II, as described above. In figure 6.37 the T behaviour of B_2^0, the ZFS parameter reflecting the main axial distortion of AA-EPR and AA-EPR I, is depicted. The absolute signs of the ZFS parameters of AA-EPR, can, however, not be determined at higher temperatures and we have chosen (see section 6.6.2.1) them to match the sign of B_2^0 for AA-EPR I. The T dependence of the other ZFS parameters is indebted with larger experimental errors and shows a less smooth behaviour. At T $>$ 40 K resp. T $<$ 25 K B_2^0 clearly applies to AA-EPR resp. AA-EPR I. The fundamental changes in the spectra around 35 K are also reflected in the behaviour of B_2^0 and in this T region it is not possible to assign B_2^0 unambiguously to either one of the tetragonal defects.

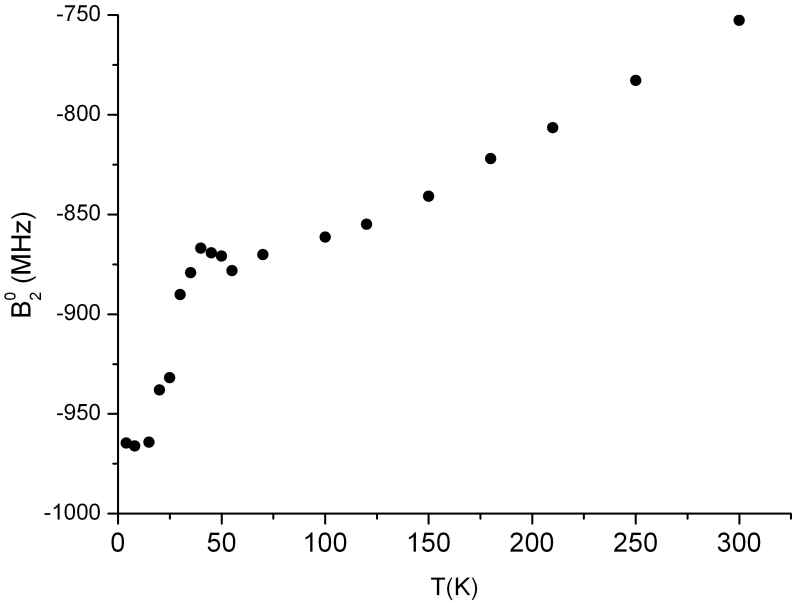

Figure 6.37. Temperature dependence of the B_2^0 parameter of AA-EPR (35 K-RT) and AA-EPR I (4K - 35 K).

6.6.5 Influence of X-ray irradiation on AA-EPR, AA-EPR I and AA-EPR II

Also the influence of X-ray irradiation on these EPR signals was investigated. Neither spectral changes nor new signals have been detected after irradiation at LT or RT, although it should be noted that possible new signals, expected around $g \approx 2$, could be overlapped by the intense AA-EPR-like signals in that magnetic field range. In section 6.9 more details will be given about the search for radiation-induced centres.

Figure 6.38 shows the intensity of the AA-EPR spectrum when irradiated at RT. The intensity was again calculated as the sum of the peak-to-peak heights of the

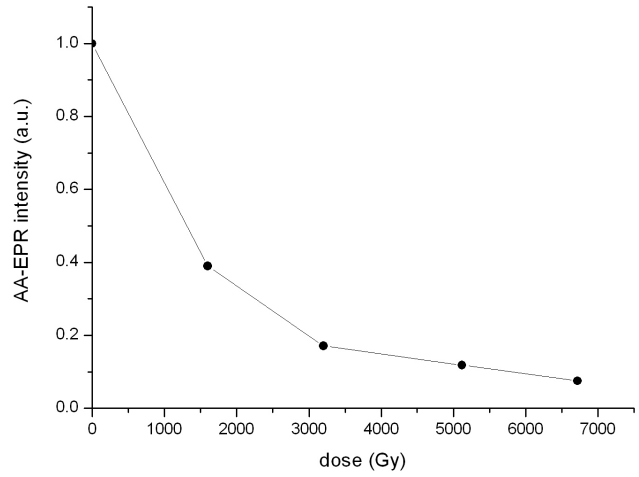

Figure 6.38. AA-EPR signal intensity as a function of absorbed dose.

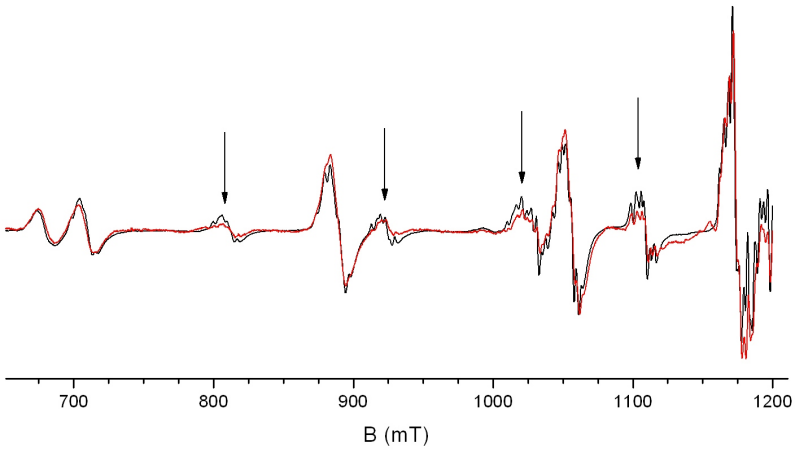

Figure 6.39. Part of the <100> spectrum at Q band (T = 10 K) of a NIP before (black) and after (red) 10 K X-ray irradiation. The spectrum after irradiation has been normalized in such a way that the AA-EPR II spectrum intensities match. The AA-EPR I spectrum is indicated with arrows.

5 most intense peaks in the <100> spectrum (marked with an asterisk in figure 6.22). A drastic decrease of EPR signal intensity is seen at high doses, as was already reported for the PSL yield in section 6.4.3.
When irradiating NIPs at LT (10 K), neither the spectrum of AA-EPR I nor that of AA-EPR II changes, but their relative intensities do. This was not the case after RT irradiation and subsequent cooling to 10 K. In figure 6.39 part of the 10 K spectrum is shown before (black) and after (red) 10 K X-ray irradiation. The intensity of the spectrum after irradiation was much lower and it has been normalized so

that the intensity of the AA-EPR II spectrum was equal in both spectra. AA-EPR II turned out to have a higher resistance to LT irradiation than AA-EPR I.
One can compare this with the results of Komiyama *et al.* (section 6.4.5). In figure 6.31, two resonance fields are indicated corresponding to the two g values they mentioned [165]. When simulating the powder spectra of AA-EPR I and II using the values of table 6.6, one can derive that the effective g value of 1.90 resp. 1.88 points to a feature present in the powder spectrum of AA-EPR I resp. AA-EPR II. So it seems very likely that they referred to these two centres, although they did not report any further spectrum analysis. In their patent, they stated that the defect with the highest resistance to X-ray irradiation, corresponds to the g = 1.90 feature, thus with AA-EPR I. This is in disagreement with our findings.

6.6.6 ENDOR experiments on AA-EPR I and II

From the analysis of the EPR spectra of the AA-EPR-like defects in NIPs the g value and the ZFS parameters have been determined, without leading to a conclusive model however. Therefore also ENDOR measurements have been performed. ENDOR spectra could only be recorded at temperatures below 4 K. To improve the detection stability of the cavity at these temperatures, an extra pump had to be installed (see figure 3.1, part E4). In addition, measurements were time consuming and usually were limited to one magnetic field orientation per day. Similar as for EPR, the recorded ENDOR signals rapidly broadened when rotating the sample away from the <100> orientation. As a result, only ENDOR spectra within 20° from that direction could be detected.

6.6.6.1 Europium interaction

In agreement with the corresponding EPR intensities, the AA-EPR II ENDOR spectra are considerably stronger than for AA-EPR I. In figure 6.40 three typical ENDOR spectra are shown. Although they are recorded on the same broad AA-EPR II line (see figure 6.33) and have only slightly different field positions, they differ substantially. Four packets of 5 quadrupole split lines are expected (2 M_S multiplets and 2 isotopes with I(^{151}Eu) = I(^{153}Eu) = 5/2), but in none of the spectra this pattern is easily recognized. This is due to the size of the Eu interaction : only a single EPR transition is saturated per ENDOR experiment and not all ENDOR transitions occur in the detection range 0 - 150 MHz. In 2D ENDOR, however, the picture got clearer.
In figure 6.41I the 2D ENDOR spectrum is shown over the 1150 - 1250 mT range. As can be seen from the EPR spectrum in figure 6.41II (part of figure 6.33), all transitions belonging to the x oriented AA-EPR II defects occur in this range, as

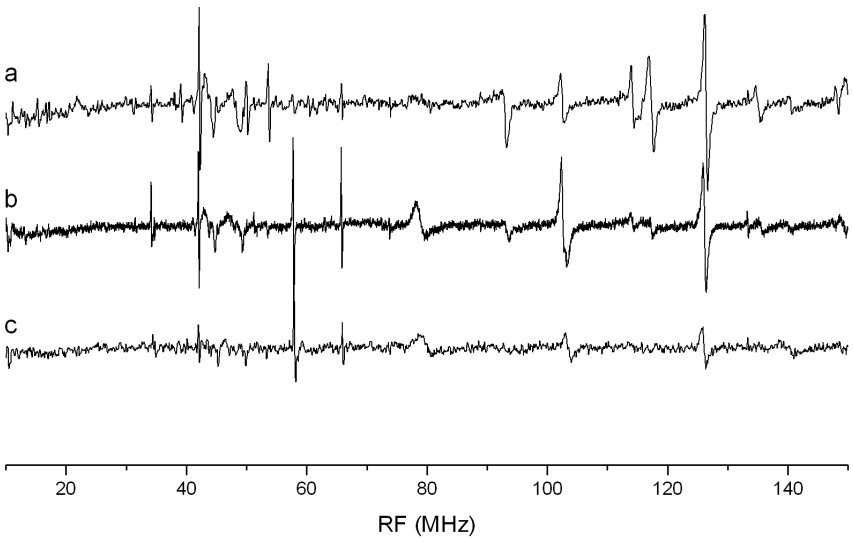

Figure 6.40. ENDOR spectra on three different positions of one resonance line of AA-EPR II (T = 3.8 K, P_{MW} = 0.5574 mW, 100 kHz modulation depth) with B along <100>
a B = 882 mT **b** B = 887 mT **c** B = 892 mT

well as the $M_S = \frac{1}{2} \leftrightarrow -\frac{1}{2}$ transition of the y and z oriented AA-EPR II defects. Also two transitions of the AA-EPR I defect are present in that region, but these have a smaller intensity and are not shown.
In figure 6.41I two kinds of ENDOR lines are present : the lines around 50 MHz vary strongly with the magnetic field, while the majority of the lines shows little field dependence. Via the slope of the field dependence, we could determine that the lines around 50 MHz originate from hydrogen nuclei (g_N = 5.58, ν_L = 51.09 MHz at B = 1200 mT). Hydrogen interactions are not *a priori* expected in CsBr:Eu^{2+}, but as the samples were annealed in a wet atmosphere they were not so surprising. The hydrogen interaction will be discussed in the next subsection.
The lines that show smaller field dependence belong to nuclei with smaller g_N. Both ^{151}Eu and ^{153}Eu have small g_N values (1.389 and 0.6134 respectively) and are the most logical candidates. In figure 6.41I, around 1170 mT and 1200 mT, a five-line pattern in the 100 - 150 MHz range originates from quadrupole split nuclei with I = 5/2. From the figure it can also be understood why no five-line patterns can be observed in regular (1D) ENDOR spectra. Starting from a typical A value for Eu^{2+} (see table 6.2), it was possible to satisfactorily simulate the 2D ENDOR spectrum, fitting these 10 quadrupole split lines. All 10 lines belong to ^{151}Eu (A and Q of ^{153}Eu could be found via equations (6.2) and (6.3)). The A and Q values

are reported in table 6.7 and are only obtained from this <100> orientation : only the principal values of Q were determined and A was assumed to be isotropic. Figure 6.41III shows the simulation of the $^{151/153}$Eu interaction for AA-EPR II. It was possible to reproduce and explain most of the experimental lines, using the parameters obtained from only 10 lines in the 2D ENDOR spectrum. For example, the three lines, centred around 1160 mT at 64.5, 70.1 and 73.1 MHz belong to the $M_S = \frac{1}{2}$ energy level of ^{151}Eu, the (96 MHz, 1190 mT) point to the $M_S = \frac{3}{2}$ energy level of ^{153}Eu.

Eu HF interaction in AA-EPR II (4K)		
	^{151}Eu	^{153}Eu
A	-93.5	-41.28
Q_x	2.87	7.30
Q_y	5.32	13.53
Q_z	-8.21	-20.84

Table 6.7. A and Q (both in MHz) of $^{151/153}$Eu in AA-EPR II (4K) in a CsBr:E^{2+} NIP

The A value found for the Eu interaction is in agreement with the literature and the principal values of the quadrupole interaction reflect the (orthorhombic II) symmetry of the defect. As the intensity of the ENDOR lines for AA-EPR I is much smaller and because the Eu HF interaction in itself does not provide new information about the defects, we did not perform sufficient measurements up till now to characterize the Eu interaction in AA-EPR I.

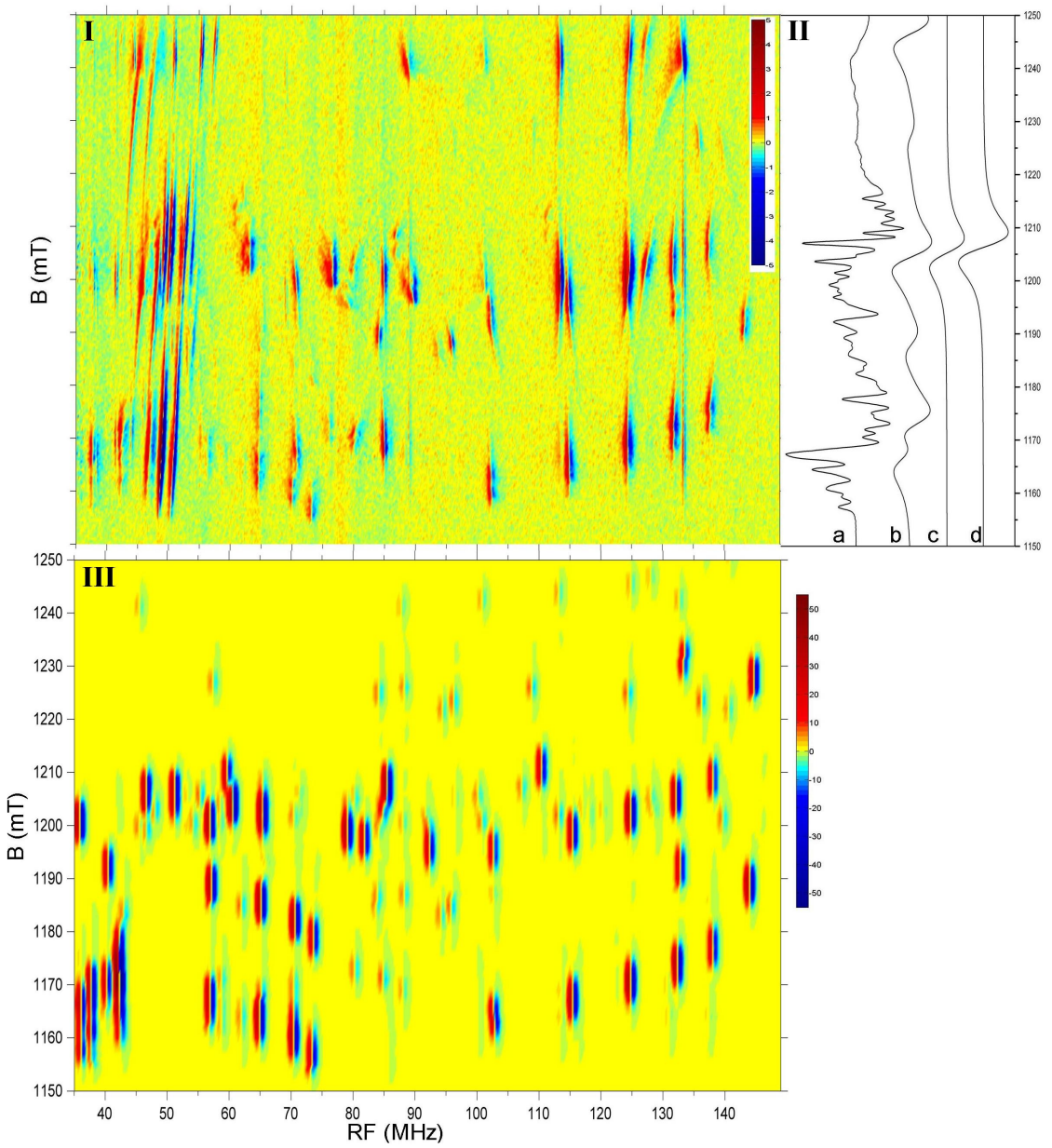

Figure 6.41. **I** 2D ENDOR spectrum of a CsBr:Eu^{2+} NIP (CB 12708_73) in the 1150 - 1250 mT magnetic field range, with the magnetic field oriented along <100> (T = 3.4 K, P_{MW} = 0.5620 mW, 200 kHz modulation depth).
II A part of figure 6.33 : the experimental EPR spectrum (**a**) and the simulations of the x (**b**) (and y (**c**) respectively z (**d**)) oriented AA-EPR II defect.
III Simulation of the $^{151/153}$Eu interaction for AA-EPR II in the 1150 - 1250 mT range, using the ENDOR parameters from table 6.7 and the EPR parameters from table 6.6

6.6.6.2 Hydrogen interaction

Since $I(^1H) = 1/2$, two ENDOR lines are expected for each nucleus (set of equivalent nuclei) per EPR transition. In a first order approximation, the same formulas (4.3) can be used as for the ^{19}F interaction in the elpasolites to fit their positions.

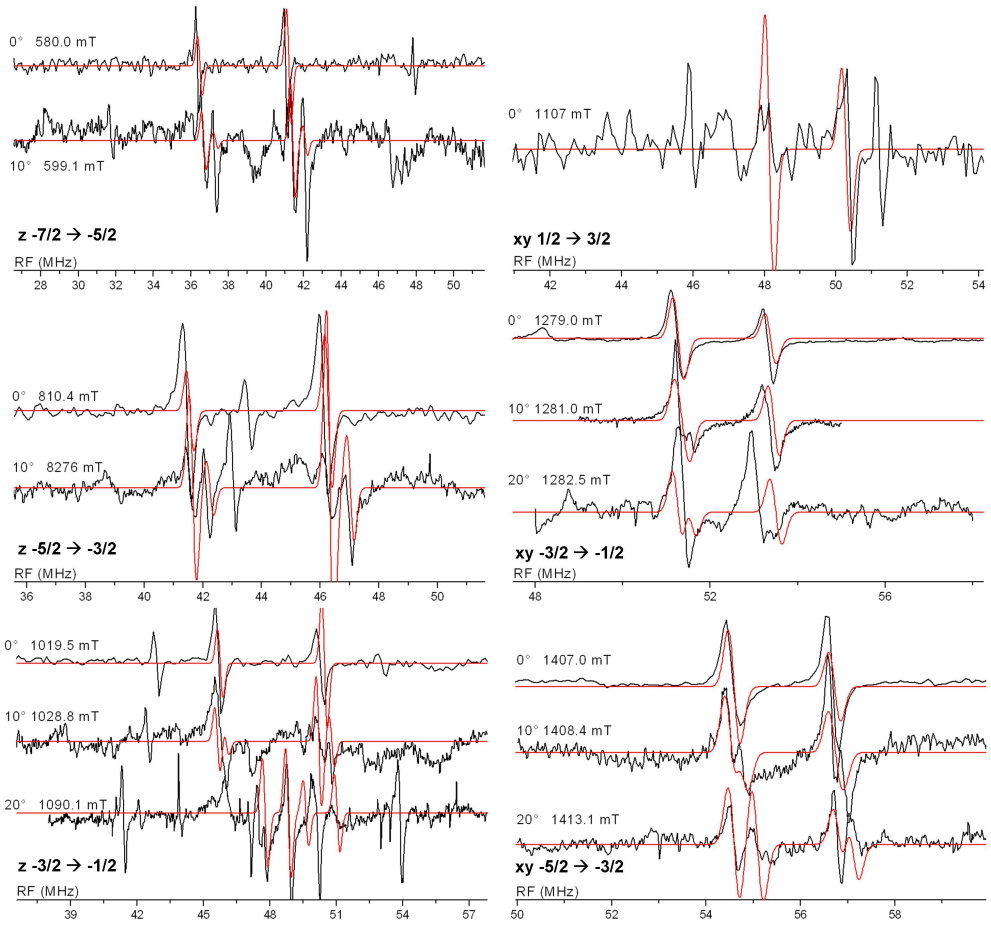

Figure 6.42. ENDOR spectra (black) of AA-EPR I at several magnetic fields and orientations. The indicated angles are referred to <100>, in an arbitrary plane through <100>. The simulations (red) are performed with the parameters from table 6.8. The orientation of the defect (z or xy) and the $M_S \rightarrow M_S + 1$ transition are indicated for each spectrum.

We start with the analysis of the hydrogen interaction in AA-EPR I, since the centre has a simpler (axial) symmetry and EPR transitions belonging to a single defect orientation can easily be found, in contrast to the situation for the (nearly) extreme rhombic AA-EPR II centre (compare parts **a** and **b** of figure 6.33). We could record ENDOR spectra up to 20° from the <100> orientation for some EPR peaks and line splitting was detected on all hydrogen lines when rotating away from <100>. The experimental (in black) and the simulated (red) spectra

are shown in figure 6.42. One could argue that the simulation is not so good; this has several reasons. It is possible to perfectly reproduce the ENDOR spectra in the <100> orientation but then neither the splitting nor the position of the peaks at other orientations will be reproduced. When including the resonance lines of off-<100> orientations in the analysis, one should not forget that these orientations are not really single crystal orientations. As already illustrated for the EPR angular variation in section 6.6.2.2 and in figure 6.28, the specific morphology of the NIPs makes that several orientations are simultaneously present at off-<100> orientations. This means that (i) the positions in the off-<100> ENDOR spectra are only approximations and (ii) the further away from the <100> orientation, the less reliable these positions are. Nevertheless, one has to include them, to get at least an idea of the size and multiplicity of the splitting. The best fit ENDOR parameters are listed in table 6.8. The largest principal value is found along the Eu-H direction. For AA-EPR I, this direction is slightly tilted away from the [100] orientation.

^{1}H interaction at 4K				
	principal value	eigenvectors x	y	z
AA-EPR I				
A_x	-2.4	0.703	-0.703	0.108
A_y	-2.0	0.707	0.707	0.000
A_z	4.8	-0.076	0.076	0.994
AA-EPR II				
A_x	-2.4	-0.966	0.260	0
A_y	-2.4	0	0	1
A_z	4.6	0.260	0.966	0.000

Table 6.8. Principal values and eigenvectors in the xyz crystal lattice frame of the ^{1}H SHF interaction for AA-EPR I and AA-EPR II.

One can estimate the distance of the hydrogen atom to the central Eu atom with equation (2.39). Using the approximation $\frac{\mu_0}{4\pi} g_e g_N \beta_e \beta_N \frac{1}{r^3} \approx 2.3$ MHz and the conversion table on page 163, one gets r = 3.3 Å.
Experimental spectra of the AA-EPR II centre can be found in figure 6.43 and the colour of the simulations depends on the orientation, as different orientations can occur in the same spectrum. The parameters can be found in table 6.8. The Eu-H direction for AA-EPR is slightly tilted away from the [010] orientation.

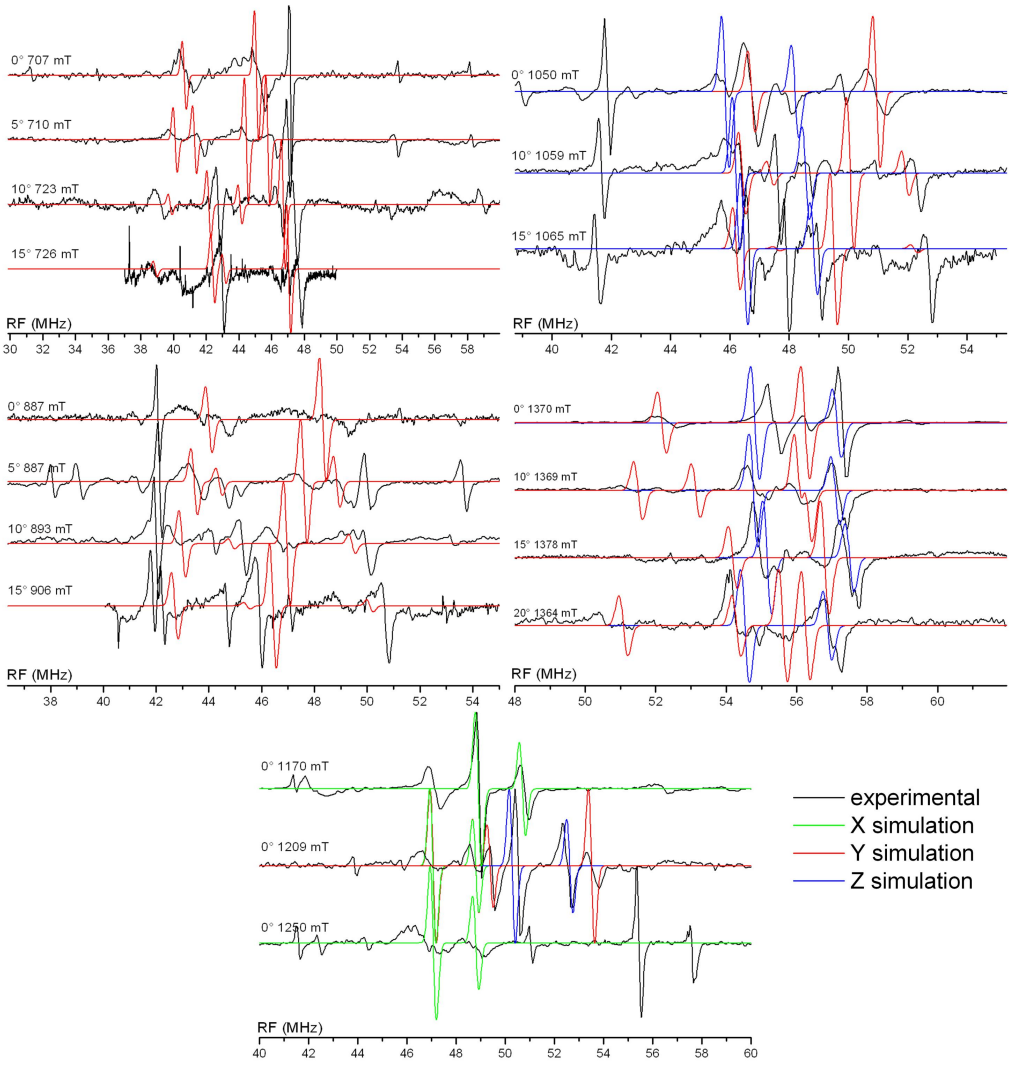

Figure 6.43. ENDOR spectra (black) of AA-EPR II at several magnetic fields and orientations. The indicated angles are referred to <100>, in an arbitrary plane through <100>. The simulations are performed with the parameters from table 6.8 and are done for a x (green), y (red) resp. z (blue) oriented defect in the <100> direction.

6.6.7 Interpretation and possible models for the AA-EPR-like defects

In this final subsection, we try to find plausible models for AA-EPR and AA-EPR I/II.

Firstly, the large ZFS of the AA-EPR-like defects (tables 6.4 and 6.6) indicates the presence of a nearby distortion, as the ZFS in alkali halides, where Eu^{2+} is present as a monomer with only a nearby vacancy, is much smaller (figure 6.8).

Subsequently, the following facts strongly suggest that the impurity is water or a water-related fragment like OH^- :

- On the one hand, the AA-EPR intensity, and consequently the AA-EPR I and AA-EPR II intensity, is linearly correlated with the PSL yield (section 6.6.1). On the other hand, the PSL yield increases when the annealing occurs in the presence of water (figure 6.20).
- The ENDOR spectra clearly show ^1H interaction, which originates most probably from water in the atmosphere during growth and/or post-annealing, as, for example, no H_2 is involved in the production process.
- The similarities between the RT EPR spectra from aqueous solution grown CsBr:Mn^{2+} crystals and CsBr:Eu^{2+}/Mn^{2+} NIPs (section 6.6.2.3) suggest some influence of water, since no EPR spectrum is observed from as-grown CsBr:Eu^{2+} Bridgman single crystals.

Furthermore, this 'water-like' impurity should be in the close vicinity of the Eu^{2+} ion, since ENDOR measurements show that the ^1H nucleus is located approximately 3.3 Å away from the Eu atom.
However, ENDOR gives no direct information about the number of equivalent nuclei. Furthermore, it was not possible to detect the presence of oxygen, since the only isotope with $I \neq 0$, ^{17}O (I = 5/2), has a natural abundance of 0.038 %.
From the knowledge that the symmetry axes of the AA-EPR-like centres correspond to <100> crystal axes, we can already discard with certainty some proposed models. The simple model with a Eu^{2+} ion and a H_2O (or OH^-) on a NN anion position will have its main symmetry axis along a <111> orientation and can thus not correspond to an AA-EPR-like centre.

In view of similarities in the temperature-induced change in symmetry, the model for the H_2O-associated Cu^{2+} centre in NH_4Cl, as determined by Boettcher and Spaeth (section 6.3.4), deserves special attention. In this model, a thermally activated rotation of the H_2O molecule around its C_2 axis (see figure 6.13), parallel to the main symmetry axis of the complex, setting in above 20 K, was held responsible for the temperature induced change from orthorhombic I to axial symmetry for centre I. An analogous model for the AA-EPR-like centres would consist of an interstitial Eu^{2+} ion, in the centre of a plane of four Br^- ions, with two H_2O ligands along the axis perpendicular to that plane. When at high temperature the H_2O ligands rotate around their C_2 axis, an axial centre is expected, conform observations (AA-EPR). In order for the model to explain the symmetry of the centres at $T < 35$ K, this rotation should freeze out leaving the H_2O molecules in {100} planes, at variance with the situation in NH_4Cl. Moreover, for AA-EPR I the H_2O planes would be perpendicular to each other, whereas for AA-EPR II both H_2O molecules would lie in the same {100} plane.

Also the ENDOR results seem to favour the model of Boettcher and Spaeth. Indeed, a set of equivalent ^1H atoms at 3.3 Å away, tilted a few degrees from a <100> axis is in agreement with (a) water molecule(s) placed 2.7 Å away from the Eu^{2+} ion on the C_2 axis, with the H atoms oriented away from the Eu^{2+} ion.
Although this model gives a qualitatively correct picture of the temperature-induced symmetry changes for the centres and explains the ENDOR results, its validity is less obvious if one regards the problem in a more quantitative way. Indeed, in all three models the $(EuBr_4O_2)^{6-}$ core of the complex is expected to impose the main axial symmetry, while the (static/dynamic) arrangement of four protons induces a small perturbation that only in the case of AA-EPR II lowers the symmetry. It seems hard to imagine that this perturbation would provide an explanation for the difference between the AA-EPR I centre with perfectly axial and the AA-EPR II with nearly extreme rhombic symmetry.

One plausible and simple alternative model consists of a Eu^{2+} ion positioned on a Cs^+ site with one NN Cs^+ ion replaced by a H_2O molecule and a vacancy in one of the remaining NN Cs^+ positions. In figure 6.44, the five possible positions of the vacancy are drawn. When the vacancy substitutes for Cs^+ ion nr. 1, the tetragonal symmetry fits the AA-EPR I defect. The orthorhombic II defect, which appears when the vacancy substitutes one of the other four neighbouring Cs^+ ions, then corresponds to AA-EPR II. This model also explains the lower EPR intensity of AA-EPR I in comparison with AA-EPR II, as the latter has a 4 times higher probability of appearing. If both Eu^{2+} and H_2O are exactly positioned at Cs^+ lattice positions, the distance between H^+ and Eu^{2+} should be 4.9 Å, but relaxation of Eu^{2+} and $H_2{}^{2+}O^{2-}$ towards each other may be expected. This may lead to a slight shift of the main orientations of the defect tensors away from <100> crystal axes. The attraction between Eu^{2+} and O^{2-} could prevent Eu^{2+} to aggregate. This attraction is not present in Eu^{2+}-V complexes in water-free single crystals.
The temperature induced symmetry change around T = 35 K, could be explained by a rapid motion of the vacancy between the 5 possible positions, averaging to a tetragonal defect without any resolved (S)HF interaction in the AA-EPR spectrum. Annealing at higher temperatures (T > 300 K) can break the Eu-O bond, and thus allow H_2O (and/or the vacancy) to migrate through the lattice. This irreversibly destroys the AA-EPR defect.
It should be noted that this model has one negative charge in excess. The vacancy is not required for local charge compensation of the centre, but may accommodate local stress[6] induced by the impurity substitution. As it is however generally ac-

[6]Stress is induced in the lattice when an impurity ion (Eu^{2+}, ionic radius r = 109 pm) substitutes a larger lattice ion (Cs^+, r = 167 pm)

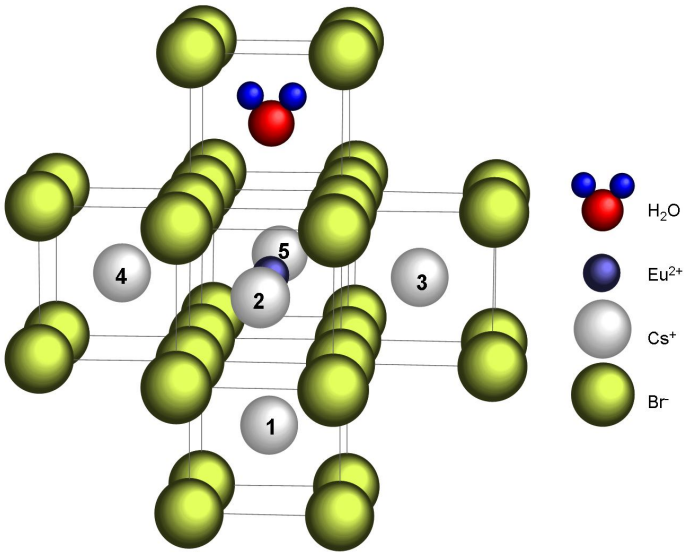

Figure 6.44. Possible models for AA-EPR I and AA-EPR II in the CsBr lattice.

cepted that F centres are created upon irradiation and Br^- vacancies are present before irradiation, the latter can be seen as distant charge compensators.
It cannot be ruled out that other similar defects are also present in the lattice, e.g. a defect with two axial water molecules and a vacancy. Such model is, however, less likely and has already two negative charges in excess.

6.7 ANNEALING AT 300 °C OF NIPS

When annealing a NIP at 300 °C, the AA-EPR-like centres disappear, in favour of a broad isotropic line with a peak-to-peak amplitude of around 25 mT and centred around $g \approx 2.00$. This line will be labelled the *A-EPR* spectrum. A-EPR is stable up to temperatures of about 500 °C, after which it disappears in favour of an Eu^{2+} monomer spectrum also observed in single crystals (see next section).
Its stability and its presence in the earlier generation NIPs, when the PVD process was not optimized yet, leads to the proposition that a $Cs_xEu_yBr_z$ microphase is responsable for the A-EPR signal. This assignation is further supported by figure 6.45. In this figure the EPR spectrum at Q band (RT) of two $Cs_xEu_yBr_z$ powders is compared with spectrum a from figure 6.24. Both powders were produced by Agfa HealthCare NV by firing CsBr with either $EuBr_2$ (in a 1:1 ratio, CEBLA 3301/01/1) or with $EuBr_3$ (in a 7:3 ratio, CEBLA 0212/05/1). The surprising resemblance between the three spectra supports the assignation of A-EPR.

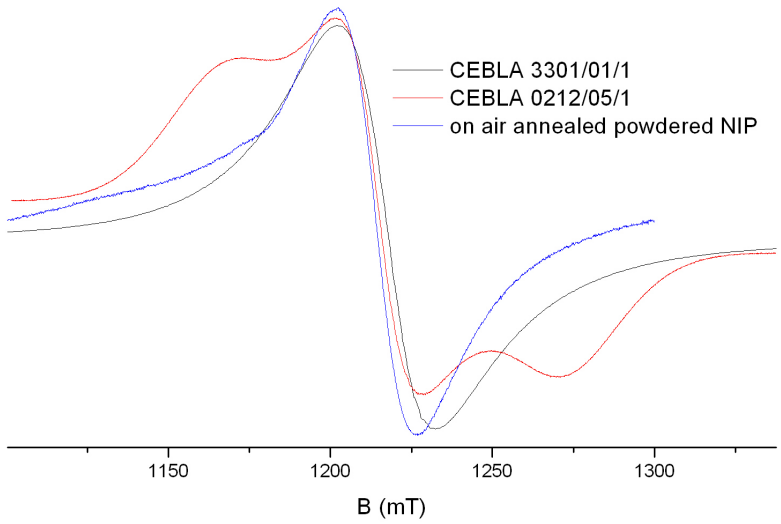

Figure 6.45. Q band EPR spectrum at RT of two $Cs_xEu_yBr_z$ powders and of an on air at 300 °C annealed NIP

No ENDOR could be detected to support this assignation.
The attribution of A-EPR to microphases is somewhat in contradiction with the work of Hackenschmied *et al.* (section 6.4.2). They attributed certain lines in the 2θ XRD spectrum of annealed CsBr:Eu powders to $CsEuBr_3$ phases, and the intensity of these lines followed the PSL intensity : these lines disappeared by annealing at temperatures above 250°C. So, either these lines or A-EPR do not

correspond to $CsEuBr_3$ phases. A-EPR can also correspond to other $Cs_xEu_yBr_z$ phases. Also specific differences in the two setups can hamper the direct comparison in annealing temperature and time in the two sets of experiments.

6.8 Annealing at 600 °C of NIPS and CsX single crystals

After (vacuum) annealing a NIP at temperatures higher than 500-600 °C, both the AA-EPR-like and A-EPR signal disappear, in favour of a new signal, labelled as the *EU-EPR spectrum*. This signal decays rapidly at RT, but is nevertheless worthwile to be investigated, mainly for the following reasons.
Firstly, unambiguous identification with EPR and/or ENDOR of the defect(s) responsible for the EU-EPR spectrum, would eliminate these models as explanation for the AA-EPR-like defects. As we will show, we have strong indications that the defects producing EU-EPR are Eu^{2+} monomers, without any impurity in the close vicinity. As these defects aggregate and AA-EPR-like defects do not, impurity association for the latter seems very plausible.
Secondly, Savel'ev *et al.* [137] were until now the only group to report the aggregation of Eu in CsBr single crystals (see section 6.3.3). They concluded that Eu monomers fastly (see figure 6.10) agglomerate to $(Eu^{2+}\text{-}V)_3$ trimers. Since many authors working on CsBr:Eu^{2+} cite this publication and often use the trimer hypothesis in their theories [163, 28, 154], it is certainly useful verifying their results.
Finally, as already mentioned earlier, Savel'ev *et al.* do not show any EPR spectrum. It is anyhow interesting to find the EPR signals they might have detected and distinguish them from the AA-EPR type spectra.
Vacuum annealing at high temperatures ($T \geq 500$ °C), followed by freezing in liquid nitrogen, will be referred to as *over-annealing* in the following.

6.8.1 Experimental details

The EU-EPR spectrum in CsBr:Eu can only be detected in the temperature range 5 - 50 K and standardly we measured at 20 K. Over-annealing of a sample brings along two main problems.
After the XRD orienting of a single crystal, it is glued to a quartz rod, without any loss of orientation. With this method, accuracies down to 2° can be obtained [168]. However, we did not find any glue which can sustain a temperature range from -268 °C (EPR measurements at 5 K) up to 600 °C (during annealing). Thus we had no other choice but to try to minimize the loss of orientation during the transfer from the XRD setup to the sample holder. Therefore the crystal was cylindrically sawn along the rotation axis (usually a <100> crystal axis).
Secondly, contact with air at temperatures above 300 °C, leading to oxidation from Eu^{2+} to Eu^{3+} [169], should be avoided for both NIPs and single crystals. This can be attained in several ways. For *Q band* samples, the sample remains inside the quartz tube (which sustains smoothly these temperatures), which al-

ready simplifies the problem. At first, the sample tube was wrapped in Al foil. As annealing times increased (beyond one hour at T = 600 °C) in order to improve the S/N ratio of the EPR signal, this method soon proved to be unsatisfactory. As intermediate solution the sample tube was put in a larger tube, which was continuously pumped during the annealing. However then the sample could not be cooled down fast enough due to the isolating outer tube. Finally we used quartz tubes with thicker tube walls than those regularly used, in which the sample could be sealed of in vacuum. The smaller inner diameter (0.8 mm vs. 1.35 mm) however reduced drastically the sample size.
For *X band* samples, we could not use the regular plexy sample holders (for single crystals and NIP plates, see figure 3.10) or teflon boxes (powders) because they would melt. Once more, wrapping the sample in Al foil nor melting the sample in a larger vacuum tube sufficed for NIPs, and thus long vacuum melted quartz tubes were used. The reduction in sample size was even more drastic than in Q band.

6.8.2 Characterization of the EU-EPR defect at 20K

6.8.2.1 EU-EPR in NIPs

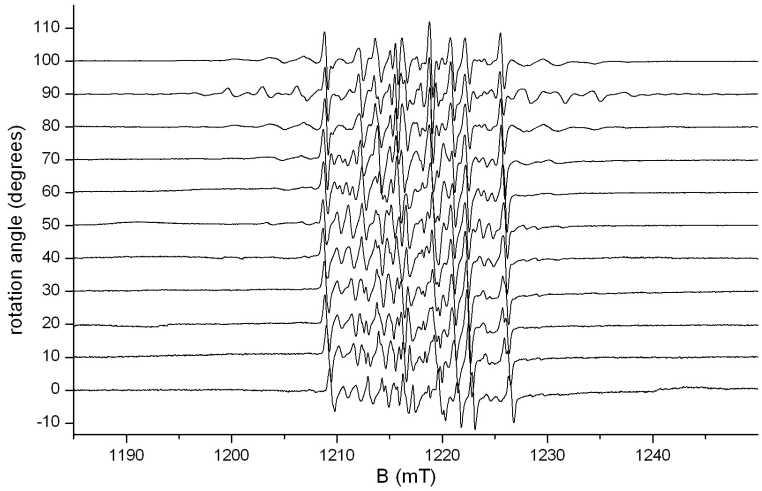

Figure 6.46. Q band angular variation (T = 20 K, P_{MW} = 1.74 mW) of a NIP (CB 12708_73), vacuum annealed at 600 °C for 30 minutes and subsequently frozen at 77 K. 90° corresponds to the single crystal-like <100> spectrum.

In figure 6.46 the angular variation of an over-annealed NIP is shown. The EPR signal shows a complex underlying structure extending over a limited magnetic field range. The latter is in contrast with the AA-EPR-like defects and Eu^{2+}

monomers in alkali halides (see section 6.3). For one Eu^{2+} site, 7 zero field split packets are expected (S = 7/2), each containing 12 HF lines (6 lines per isotope, I(^{151}Eu) = I(^{153}Eu) = 5/2), making a total of 84 lines per Eu site. This number is further increased (times 2, 3, ...), when the symmetry of the defect is lower than cubic. In contrast the alkali halides (e.g. KI in figure 6.7) the HF packets are not separated from one another, most probably due to much smaller ZFS. This makes the analysis considerably more complicated. It proved impossible to determine the ZFS parameters of this (these) Eu-related defect(s) from the complex angular dependence of the NIP EPR spectrum.

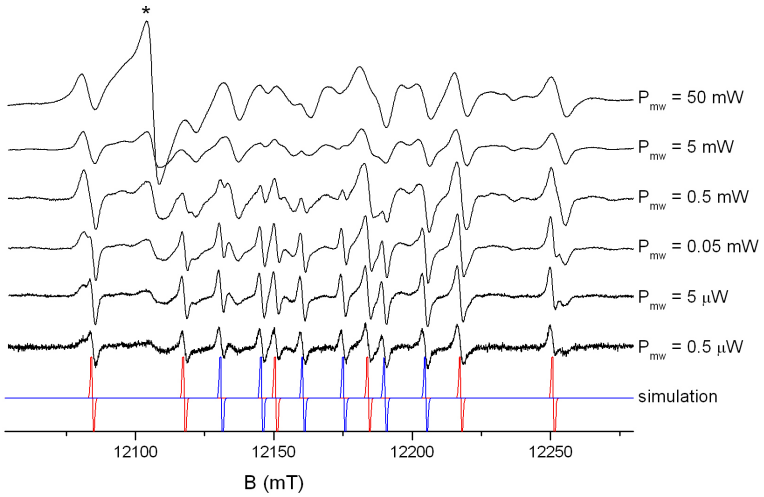

Figure 6.47. Q band spectra (black) of a powdered NIP (CB 50804_AA), vacuum annealed at 600 °C for 72 minutes and recorded with different MW power (T = 20 K). For clarity, all spectra are normalized. The single line from an unknown impurity is marked with an asterisk. The simulation of the ^{151}Eu (in red) and the ^{153}Eu (in blue) spectrum was done using the parameters in table 6.9.

Powdering the NIPs removes the angular dependence of the spectrum, and at low MW powers the NIP powder spectrum (see figure 6.47) shows mainly the 12 HF split lines of the $M_S = \frac{1}{2} \leftrightarrow -\frac{1}{2}$ transition. When increasing the MW power, the spectrum becomes more complicated, due to one or more other underlying defects. The peak present at high MW power and marked with an asterisk, at g = 2.001, is most probably due to an impurity[7]. From the low P_{mw} EU-EPR spectrum, it was possible to determine g and A, which are both isotropic. In figure 6.47 the

[7]It is most probably a surface impurity, since the NIPs and single crystals are brown coloured after longtime annealing. The impurity signal, however, was only to a much lesser extent present in the single crystals.

simulation is shown and the simulation parameters, which are typical for a Eu defect, can be found in table 6.9.

EU-EPR (20 K)	
g	1.9913
^{151}A	-92.9
^{153}A	-41.2

Table 6.9. g and A (in MHz) of the EU-EPR defect in a CsBr:Eu NIP at 20 K

In the next section, we will try to determine the ZFS parameters of the EU-EPR defect from the angular variation of over-annealed CsBr:Eu^{2+} single crystals.

6.8.2.2 EU-EPR in CsBr:Eu^{2+} single crystals

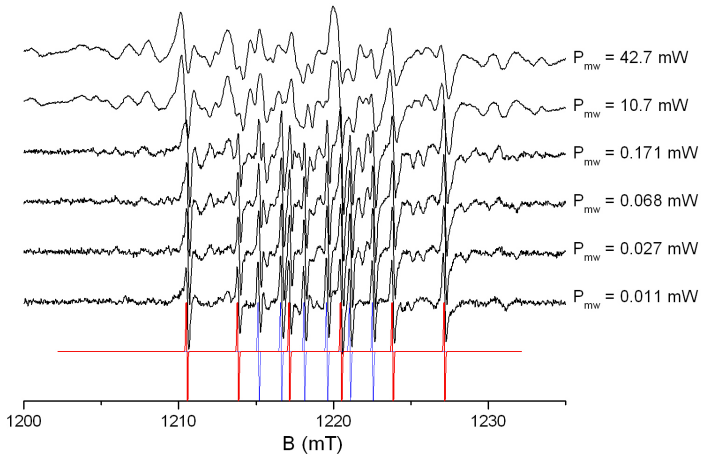

Figure 6.48. Normalized Q band spectra (T = 20 K, black) of an over-annealed CsBr:Eu^{2+} single crystal. The simulation of the ^{151}Eu (red) and the ^{153}Eu (blue) spectrum was done using the parameters in table 6.9.

In figure 6.48 the Q band EPR spectra of an over-annealed CsBr:Eu^{2+} single crystal is shown for an unknown orientation as a function of P_{MW}. Again, several defects seem to be responsabe for the signal at higher P_{MW}. At low P_{MW}, the 12 line structure becomes more pronounced and could be simulated with EU-EPR parameters from table 6.9, strongly indicating that the same defect is present in the low P_{mw} spectrum of NIPs and single crystals after over-annealing.

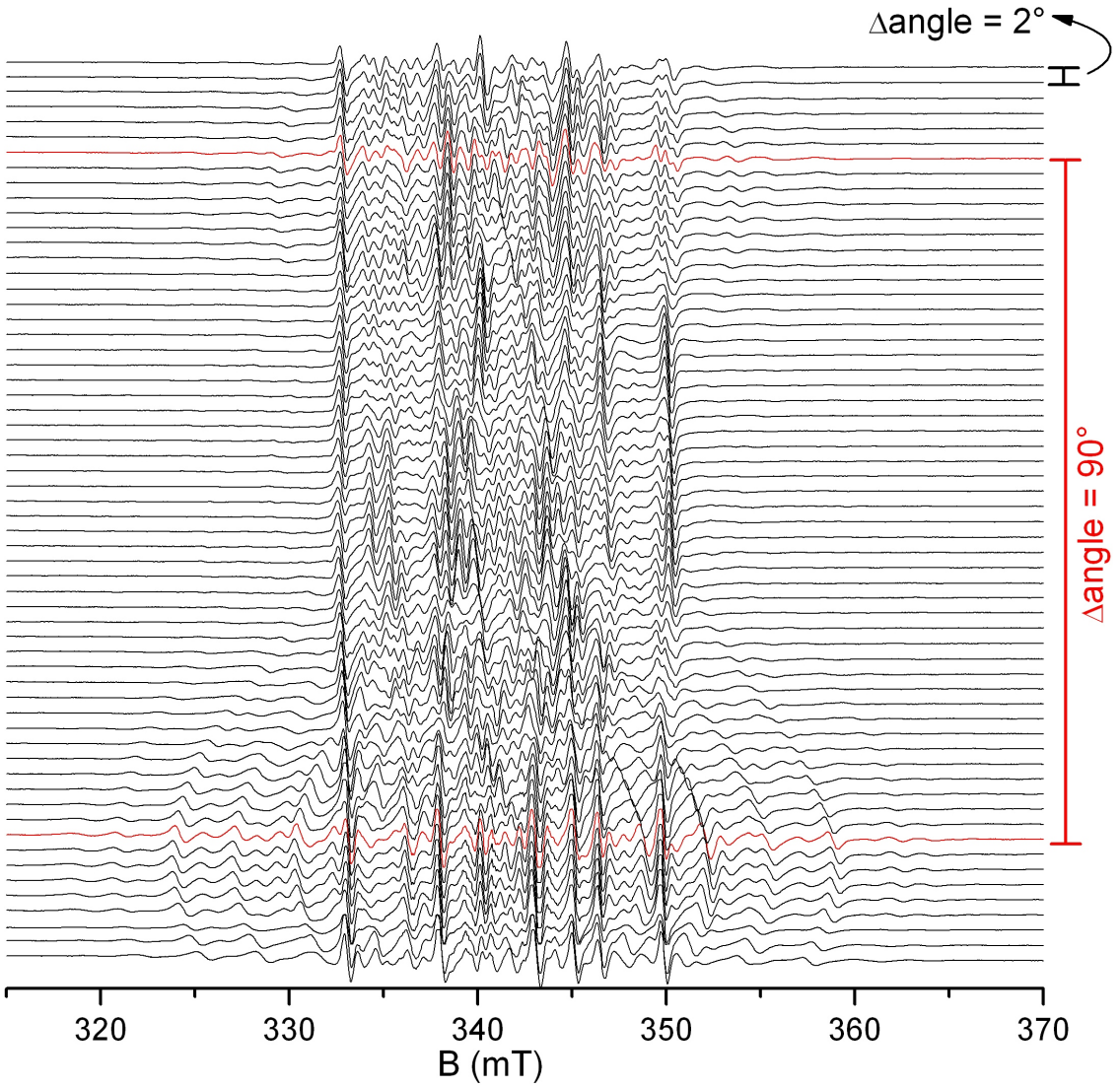

Figure 6.49. Normalized X band (20 K) angular variation (per 2°) of an over-annealed CsBr:Eu^{2+} single crystal. Two spectra, which are showing extremal resonance positions and are recorded over a 90° interval, are coloured in red.

The biggest problem with respect to characterizing the EU-EPR spectrum in over-annealed single crystals is the lack of accuracy in crystal orientation. This is illustrated in figure 6.49, where the angular variation (recorded with an interval of only 2°) is shown. We attempted to orient this crystal along a <100> crystal axis, but the angular variation shows that this is clearly not the case. Two spectra, which are showing extremal resonance positions and are recorded at 90° orientation difference, are coloured in red and should be identical when the angular variation was performed around a perfect <100> axis of a cubic crystal. The angular variation was recorded in X band, since this setup provides the opportunity

to tilt the rotation plane up to 10° to compensate for such misorientations, but this was clearly not sufficient.
Figure 6.49 illustrates that it is not possible to follow the resonance positions of the different central peaks, although the angular variation was recorded every 2°. The outer resonance lines were plenty and sometimes difficult to discriminate from the background noise. It was impossible to known to which isotope the different lines belong neither to which electronic and nuclear transition.
In figure 6.50 the comparison is made between the <100> spectrum of an over-annealed NIP (from figure 6.46) and the spectrum with maximal splitting of figure 6.49. The resemblance between both is striking, all the more as they are recorded in different bands, and leaves little doubt that the EU-EPR spectrum in NIPs and single crystals is the same.

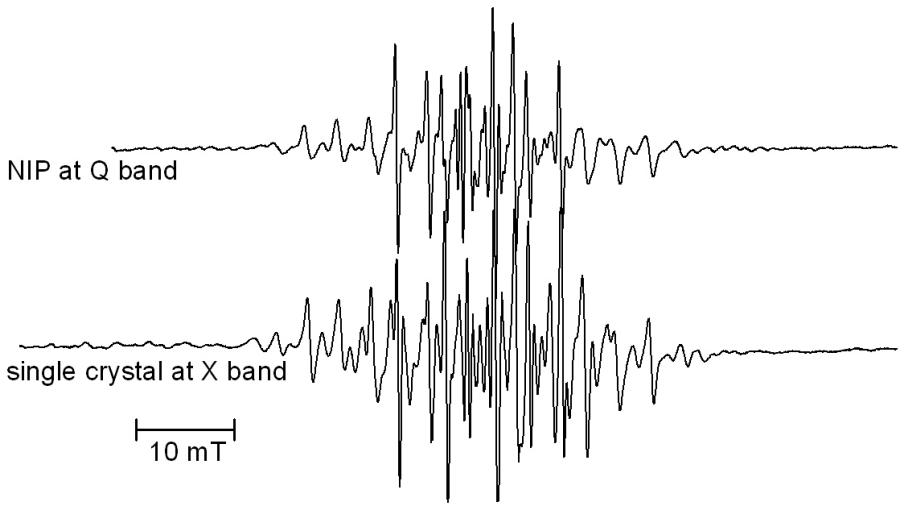

Figure 6.50. Comparison between the EU-EPR spectra of an over-annealed NIP at Q band (90° spectrum of figure 6.46) and an over-annealed single crystal at X band (spectrum with maximal splitting of figure 6.49).

6.8.2.3 ENDOR on EU-EPR in single crystals

ENDOR spectra could be recorded on EU-EPR in over-annealed single crystals. Transitions were only detected at (or very close to) the Larmor frequencies of ^{133}Cs, ^{79}Br and ^{81}Br. Some unresolved splitting of the ^{133}Cs-line was found in both bands, but proved insufficient to analyse and hence also gives no further information about the structure.

6.8.3 The decay of the EU-EPR signal

6.8.3.1 The decay of the EU-EPR signal in NIPs

In this subsection, we focus on the fading of the EU-EPR spectrum. We want to check whether the EU-EPR spectrum is the unstable EPR spectrum in the publication of Savel'ev *et al.* The first experiments showed that the EU-EPR spectrum in NIPs was more stable than they reported (see figure 6.10). It meant that, in order to observe a reasonable decay, the sample had to be kept at RT for a few minutes, rather than, for example, at 240 K. This imposed that the sample had to be removed from the cavity, kept at RT[8] for a few minutes and then put back at the cavity, for measurements at 20 K. This brought along problems in keeping the orientation of the sample. For this, we worked with powdered NIPs.
In figures 6.51 and 6.52 the Q and X band spectra of over-annealed powdered pieces of the same NIP are shown respectively. All spectra were recorded at very low MW powers (5.6 μW in Q band and 50 μW in X band), to minimize saturation effects and in the hope to detect only one defect. The impurity peak, shown in figure 6.47, is present and marked with an asterisk.

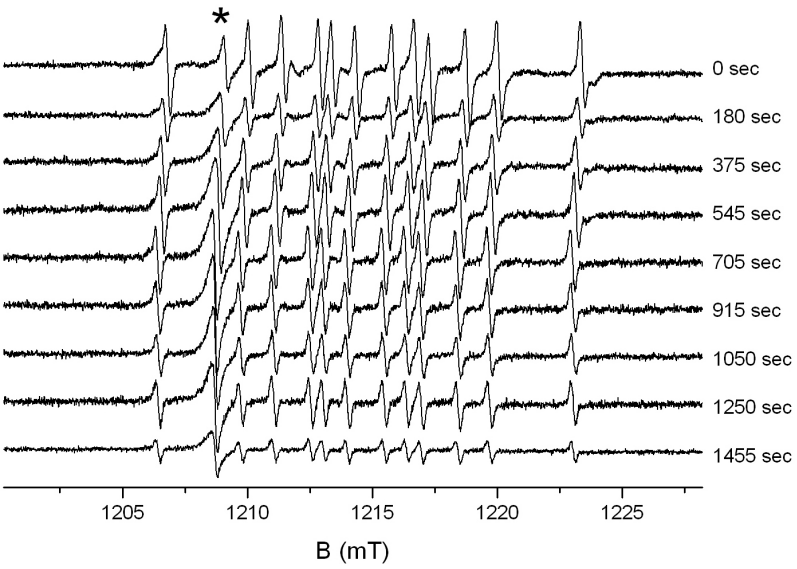

Figure 6.51. Q band EU-EPR spectra of a powdered NIP (CB 71605), vacuum annealed at 580 °C for 30 minutes and subsequently frozen at 77 K. The total time the sample is afterwards exposed at RT is indicated for every spectrum. The single line of an unknown impurity is marked with an asterisk. (T = 20 K, $P_{MW\,=\,0.0056\,mW}$).

[8]Annealing the sample at RT was done by quickly putting the sample in a cup with ethanol. This procedure is preferred over simply keeping it on air, to minimize both the effects of ice on the tube walls and the 'heating' time of the sample.

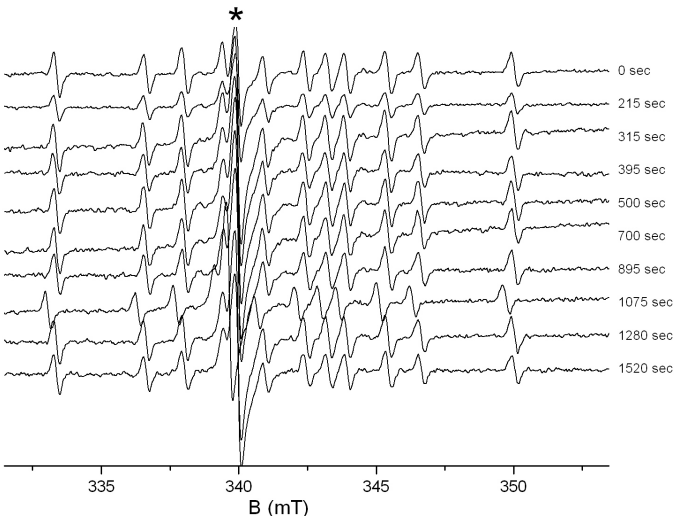

Figure 6.52. X band EU-EPR spectra of a powdered NIP (CB 71605), vacuum annealed at 570 °C for 30 minutes and subsequently frozen at 77 K. The total time the sample is afterwards exposed at RT is indicated for every spectrum. The single line of an unknown impurity is marked with an asterisk. ((T = 20 K, $P_{MW = 0.0502\ mW}$).

The intensity of the spectrum is calculated as

$$I = \sum_i h_i w_i^2 \tag{6.6}$$

where h_i and w_i are respectively the height and the peak-to-peak linewidth of those of the 12 resonance lines not overlapping the impurity signal. However, when plotting the intensity vs. time, especially for the powdered NIP measured at X band, this did not result in a monotonously decaying curve. Considerable improvement was obtained by using the impurity signal as an intensity normalization reference, certainly when the complexity of the experimental procedure is taken into account. The 'outlier' for the X band NIP curve (at t = 215 sec) can probably be explained by the overlap between the impurity signal and one of the HF lines. In figure 6.53 $\frac{I(t)}{I_0}$ is shown as a function of annealing time at RT, with I_0 the EPR intensity at t = 0 sec. In both bands, the intensity loss is smaller than in figure 6.10. There is a distinct difference between the two bands, which can possibly be explained by the size of the samples. As the X band sample is larger, it takes a longer time to obtain a constant T throughout the sample than in the smaller Q band sample. This delay can cause the apparent slower decay of the EU-EPR signal.

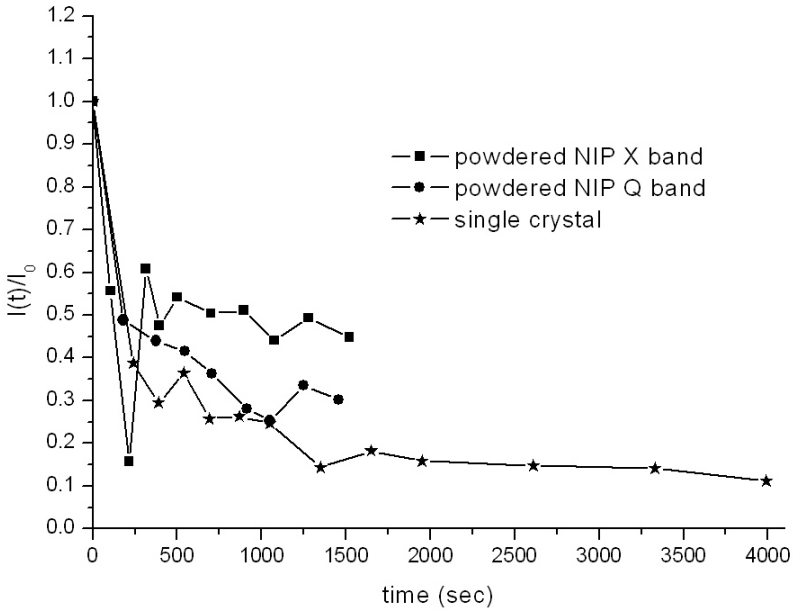

Figure 6.53. Normalized EPR intensity of the EU-EPR spectra shown in figures 6.51 (•), 6.52 (■) and 6.54 (★).

6.8.3.2 The decay of the EU-EPR signal in CsX single crystals

As there were differences between our results on NIPs and Savel'ev's, we decided to redo the experiments with CsBr:Eu^{2+} single crystals. After over-annealing, we rotated the not *a priori* oriented crystal to find an orientation where the EPR spectrum is the narrowest. In figure 6.54 the spectra can be found and in figure 6.53 the EPR intensity (calculated with (6.6)) is shown. CsBr single crystals exhibit a faster decay than CsBr NIPs, but the decay is still somewhat slower than reported by Savel'ev. An explanation for the difference between NIPs and single crystals could be the better heat conduction and higher mobility in the latter.
We repeated the measurements with CsCl:Eu^{2+} and CsI:Eu^{2+} single crystals. The same over-annealing procedure as for NIPs was carried out. The intensity of the spectra was calculated using (6.6). In figure 6.55 a comparison of $\frac{I_0}{I(t)}$ as a function of time for all three CsX:Eu^{2+} single crystals is shown. For clarity, $\frac{I_0}{I(t)}$ was preferred over $\frac{I(t)}{I_0}$. The decay speed is clearly related with the lattice constant (table 6.10); the larger the lattice constant, the faster the decay.

6.8.3.3 Conclusion

In this subsection we showed the first EPR spectra of over-annealed CsBr:Eu NIPs and single crystals. The spectrum, labelled EU-EPR spectrum, is in both samples the same and it decays at RT. In single crystals the decay is slightly faster than

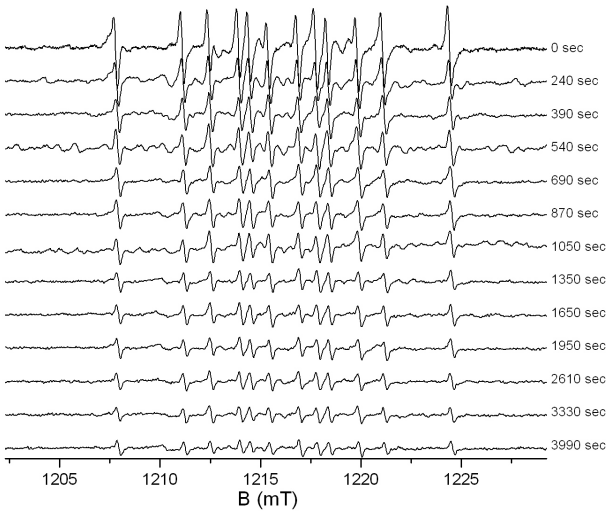

Figure 6.54. Q band EU-EPR spectra of a CsBr:Eu^{2+} single crystal with an unknown orientation, vacuum annealed at 570 °C for 32 minutes and subsequently frozen at 77 K. The total time at RT is indicated for every spectrum. (T = 20 K, $P_{MW = 0.0178\,mW}$).

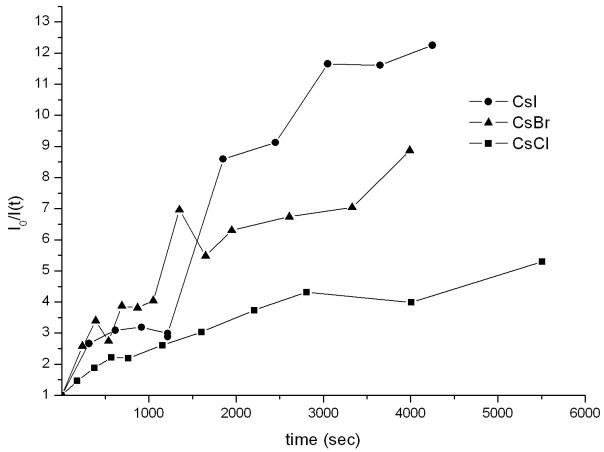

Figure 6.55. $\frac{I_0}{I(t)}$ of the Q band EPR spectrum from a annealed CsX:Eu^{2+} single crystal

in NIPs, but somewhat slower than reported by Savel'ev *et al.* We have no explanation for this small discrepancy, and can only regret that no EPR spectra are shown in the publication [137]. It seems safe to assume that Savel'ev detected the same EU-EPR spectrum. It should however be clear that their conclusions and especially the resulting model (the $(Eu^{2+}\text{-}V)_3$ trimer) should be treated with more scepticism than has been done up to now and not be used thoughtlessly as a basis for other models.

	CsCl	CsBr	CsI
melting point (°C)	646	636	621
lattice constant (Å)	4.11	4.29	4.64

Table 6.10. Melting point [170] and lattice constant [171] of cesium halides

We were unable to fully characterize the EU-EPR defect. The isotropic A and g could be determined and their values are typical for Eu^{2+}. Neither the symmetry nor the surroundings of the Eu^{2+} ion could be found.
We can however estimate the maximal value of B_2^0. If one neglects (S)HF, quadrupole and nuclear Zeeman interaction and only uses the D term of the ZFS interaction, equation (2.54) simplifies to

$$E\left(M_S\right) = g\beta_e B M_S + \frac{D}{3}\left(3M_S^2 - S(S+1)\right) \tag{6.7}$$

The positions of the seven allowed EPR transitions when the magnetic field is oriented along the axial distortion axis, can be calculated as

$$\begin{cases} B_{5/2\leftrightarrow 7/2} = \frac{h\nu}{g\beta_e} + 6\frac{D}{g\beta_e} \\ \dots \\ B_{-7/2\leftrightarrow -5/2} = \frac{h\nu}{g\beta_e} - 6\frac{D}{g\beta_e} \end{cases} \tag{6.8}$$

These seven positions are in turn the centre of 12 HF split lines. If ΔB is the distance between the two outer HF packets, than $\Delta B = 12\frac{D}{g\beta_e}$ and an estimation of D can be made from the spectrum. In our opinion 50 mT is a safe upper limit for ΔB, as can be checked in figure 6.50. This value for ΔB results in D = 116 MHz and $B_2^0 \leq 40$ MHz (see equation (2.29)) respectively. This value has been derived when the magnetic field is oriented along the main axial distortion, thus when the spectrum is measured with the maximal ΔB. We did several measurements with arbitrarily oriented crystals and did not find any spectrum with $\Delta B > 50$ mT.
$B_2^0 \leq 40$ MHz is a very small ZFS compared with Eu in the NaCl-type alkali halides and with the B_2^0 of AA-EPR-like defects. The small value excludes a any drastic distortion of the cubic CsBr lattice in the vicinity of the Eu^{2+} ion. In figure 6.56, $|B_2^0|$ is shown as a function of the Eu^{2+}-V distance. This was already shown in figure 6.8, but now the off-trend results of Boldu *et al.* [135] are omitted. Also, the $|B_2^0|$ values of AA-EPR and AA-EPR I are added, in the assumption that the vacancy is on the closest cation position (i.e. one lattice constant, 4.29 Å, away). The latter illustrates again that the AA-EPR-like defects cannot be explained with a Eu^{2+} and a vacancy on NN cation positions. Finally, a trendline,

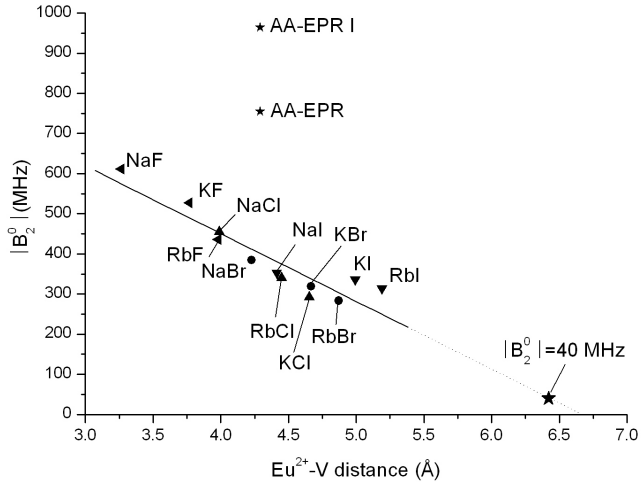

Figure 6.56. $|B_2^0|$ as a function of the Eu^{2+}-V distance in various systems. Data from figure 6.8 and table 6.6. A linear fit has been made to the alkali halides data, and extrapolated to $|B_2^0| = 40$

fitted to the results in the alkali halides, is added and extrapolated to $|B_2^0|$ = 40 MHz. When the EU-EPR defect follows the trend of the alkali halides, the cation vacancy would be present at a distance of roughly 6 to 7 Å. A closer look at the cation site in the CsBr lattice, shows that the NN cations lie at 4.29 Å (6 cation positions, all oriented in a <100> direction from the central cation), the next-nearest neighbour (NNN) cations lie at 6.07 Å(12, <110>) and the third shell at 7.43 Å (8, <111>). From these considerations, V-compensation at the NN cation positions seems in any case excluded.

As a final conclusion, we propose that the EU-EPR signal is the sum of the spectra from several Eu^{2+} monomers, where the Eu^{2+} ion is positioned on a regular cation position. The different monomers differ from each other by the positioning of the vacancy, but none of them have a vacancy closer than on a NNN cation position. Over-annealing NIPs brings the Eu^{2+} dopant (ionic radius = 1.09 Å) in a solid state matrix similar to that of melt-grown CsBr single crystals, and hence removes the defects/impurities necessary to stabilize the AA-EPR like centres.

6.9 Additional experiments on NIPs

6.9.1 Irradiation of NIPs

When investigating the effects of X-ray irradiation on a NIP, two main questions arise

- What is the influence of the irradiation on the defects which were present before the irradiation ?
- Which new defects are created upon irradiation ?

No AA-EPR signal intensity difference could be found after 'medical' irradiation, i.e. RT irradiation with a dose less than 1 mGy. A high dose ($>$ 1 kGy) X-ray irradiation, however, decreases irreversibly the AA-EPR-like defect concentration, both at LT and at RT. This was already discussed in section 6.6.5, as well as the fact that AA-EPR II has a higher resistance to LT irradiation than AA-EPR I. The irreversible decrease in AA-EPR-like signal intensity following high X-ray doses is probably due to an oxidation of Eu^{2+} to the EPR silent Eu^{3+} or, less likely, to an aggregation of the Eu^{2+} ions.
Neither after medical nor high dose irradiation of CsBr:Eu^{2+} NIPs, any new signals could be detected. The NIPs were nevertheless deeply blue coloured after high dose irradiation, meaning that F centres were created upon irradiation. These centres could however not be detected, probably because X-ray irradiation is not able to induce a sufficient concentration of F centres to be detected by EPR. This is in correspondence with the EPR/ENDOR work of Pawlik *et al.* [147] on the F centre in CsBr single crystals (see section 6.3.5) : their measurements were performed on additively coloured crystals instead of irradiated crystals.
The fact that no new signals are detected, can be due to the intense AA-EPR signal, which overlaps possible new signals in the region $g \approx 2$. To avoid this, Agfa HealthCare NV grew CsBr NIPs without (intentional) Eu^{2+} doping. Before irradiation, no signal could be detected at RT nor at LT. Despite the intense blue colouring after high doses of X-ray irradiation, no EPR signals could yet again be detected.

6.9.1.1 Illumination of NIPs

During the read-out, red light is used to photostimulate the NIP, which subsequently emits blue light. We wanted to see whether in situ illumination under varying conditions could lead to the discovery of new defects.
Via a quartz rod, in situ illumination of the sample is possible with wavelengths

between 350 nm and 900 nm. No new signal could be detected after a long series of experiments in which parameters like X-ray irradiation temperature, wavelength of the in situ illumination, ... have been tested. This is most probably again due to the insufficient number of defects created/annihilated upon irradiation and/or illumination.

6.9.2 Doping the NIPs with water-like molecules

Attempts have been made to replace the water during the Agfa-annealing process by other, analogous molecules. Agfa Healthcare NV and M. Weidner [172] tried to incorporate H_2S in NIPs, since Hesse *et al.* [154] described its beneficial influence on the PSL yield, but both failed.
Both did succeed in incorporating D_2O in NIPs, but the D_2O did not replace enough H_2O molecules to be detected in ENDOR.

6.9.3 Oxygen codoping in CsBr:Eu^{2+} single crystals

As oxygen played a crucial role in the working of the BaFBr:Eu^{2+} storage phosphor (section 6.2.2.4), we tried codoping of a CsBr:Eu^{2+} single crystal with oxygen. The oxygen was incorporated by oxidizing pure Cs, but it is unknown in which state exactly the Cs_xO_y entered the Bridgman tube. A Eu^{2+} CEBLA powder was used for the Eu doping.
After the growth, luminescence revealed that no Eu^{2+} was present anymore in the crystal. A small, new signal did however appear at 10 K after X-ray irradiation and the angular variation around an unknown axis is shown in figure 6.57. We did not detect this small defect in NIPs, but it can be easily overlapped by the AA-EPR-like signals. We did not finish the analysis of this defect, but it is most probably an oxygen defect.

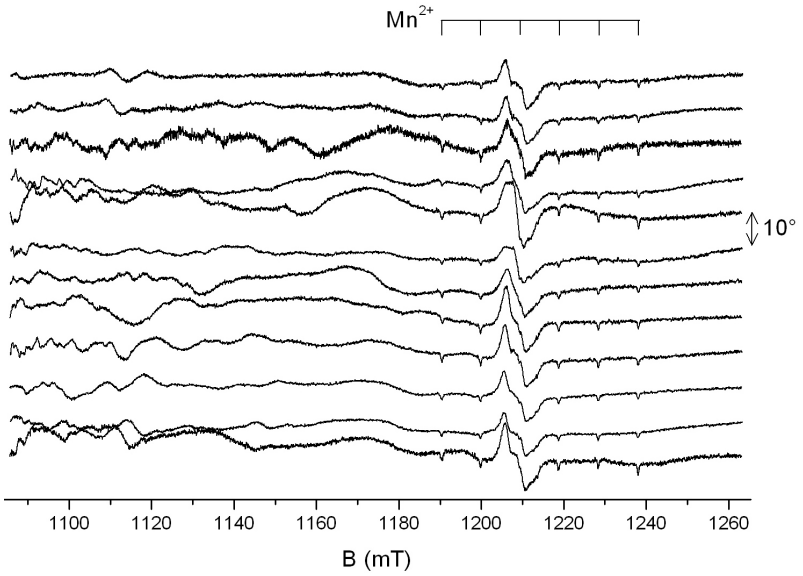

Figure 6.57. Normalized Q band angular variation around an unknown axis (T = 10 K, P_{MW} = 54.81 mW) of a CsBr:Eu,O single crystal, after RT irradiation

CHAPTER 7

SUMMARY AND OUTLOOK

"Goodbye for now, and good mental health."
— DR. F. CRANE

In this work we investigated dopant related defects in three different types of X-ray storage phosphors. We performed this study mainly from a fundamental point of view: our research efforts were more oriented towards the identification of the microscopic structure of the defects, than towards the dependence of the material properties on the type and concentration of the defects.

In hexagonal and cubic $Cs_2NaM^{III}F_6$ elpasolites (Chapter 4), we characterized the Fe^{3+} defect that, in all investigated elpasolites, is incorporated at an M^{III} site. Although Fe^{3+} is an unintentional impurity and has no direct applications, it was a very good probe for investigating the environment of the trivalent cation site in elpasolites. At variance with the unique cubic site in cubic elpasolites, in their hexagonal counterparts, Fe^{3+} can be positioned on two trigonal sites : site C and site E. Both can be essentially seen as a cubic site, which is compressed, respectively elongated along a C_3 symmetry axis. It was possible to unambiguously determine the signs of the ZFS and the SHF parameters, combining 2D ENDOR and W band measurements at (very) low temperatures.
EPR and ENDOR appeared excellent tools to identify paramagnetic defects with a very low (impurity) concentration. From an applied point of view, our results can be used to facilitate the detection and identification of Fe^{3+} in many materials, where Fe^{3+} is often unintentionally present. From a more fundamental point of view, the availability of ZFS and SHF parameters of a high spin ion in three very similar sites, can be used as a starting point for, or to check theoretical calculations. The latter is already the case for our earlier work on Cr^{3+} (S = 3/2) doped elpasolites [173, 174].

The microscopic structure of the RE dopants in K_2YF_5 crystals (Chapter 5) is highly determined by the rarely encountered seven-fold surrounding by F^- ions of the trigonal cation. Both Gd^{3+} and Ce^{3+} substitute for Y^{3+} at a monoclinic site. The knowledge of this local symmetry allowed us to determine the space group symmetry as Pnam and to solve a long lasting ambiguity in the literature. The knowledge of the RE^{3+} defect in K_2YF_5 facilitated further research on the effect of irradiation on these crystals. Very recently, Zverev *et al.* could already identify several radiation-induced paramagnetic defects in RE (Ce^{3+}, Gd^{3+} and Tb^{3+}) doped K_2YF_5.

The main focus of our work was on Eu^{2+} doped CsBr medical imaging plates consisting of cylindrical microcrystals, the so-called 'needles', all aligned with their longest axis perpendicular to the plate. It appeared that the PVD growth provides the plates with interesting X-ray storage properties, since Bridgman-grown CsBr:Eu^{2+} single crystals do not exhibit such behaviour. Earlier research on NIPs revealed that annealing them in a wet atmosphere enhances their overall performance, without providing a satisfying explanation for this beneficial effect. One of our main aims was to make a contribution to the understanding of this behaviour and to the characterization of the defects involved in the working of the NIP. At RT, we detected the AA-EPR defect, a Eu^{2+} related defect with its main tetragonal symmetry axis along a crystal <100> direction. We demonstrated that its EPR signal intensity is linearly correlated with the PSL intensity, and thus the sensitivity of the plate. In other words, the AA-EPR defect is involved in the writing and/or reading process of the NIP.
ENDOR measurements were the next step towards the detailed identification of the environment of the Eu^{2+} ion. Lowering the temperature to saturate the EPR signal, led to a drastic change in the EPR spectrum and its analysis revealed that the LT spectrum was composed of spectra from two defects : AA-EPR I, which has tetragonal symmetry, and AA-EPR II, which exhibits nearly extreme rhombic symmetry. For both defects, all principal axes were again oriented along <100> directions. Up to now it is not clear whether AA-EPR I and AA-EPR II both transform to AA-EPR or whether the AA-EPR II spectrum or defect disappears at higher temperatures.
The problems encountered during the EPR study and related to the partial ordering of the NIPs, also severely complicated the ENDOR analysis. Next to the characterization of the Eu HF interaction, we also detected ^1H SHF interactions, originating from H nuclei at about 3.3 Å from the Eu^{2+} ion. Whereas the Eu-H bond is slightly tilted from the <100> crystal axis for AA-EPR I, it lies nearly in a <110> orientation for AA-EPR II.

Up to now, we could not provide a conclusive model for the AA-EPR-like defects, that would explain both the symmetry (and its temperature behaviour) and the Eu-H interaction. From its beneficial influence on the PSL/EPR intensity, we can assume that water-related defects have a stabilizing influence on the Eu^{2+} ion, preventing it from aggregating. This is supported by the fact that in water-free as-grown Bridgman-grown single crystals, no Eu^{2+} related EPR signals could be detected. We suspect that water-related defects "fill" cation vacancies preventing Eu^{2+} from diffusing. It is, e.g., not unlikely that a water molecule substitutes for a Cs^{+} ion, since both the charge (neutral vs. +1) and size difference is minimal (ionic radii of O^{2-} and Cs^{+} are 1.3 Å and 1.7 Årespectively). Also substitution for Br^{-} (r = 1.96 Å) is not impossible, but less likely as the Eu^{2+} ion causes already one excess positive charge.
When over-annealing the NIP at 300 °C, the stabilizing defects diffuse away and the Eu^{2+} ion probably aggregates to $Cs_xEu_yBr_z$ microphases. Over-annealing at 600 °C brings the Eu^{2+} dopant in a solid state matrix similar to that of melt-grown CsBr single crystals, and no EPR signal can be detected anymore.
High dose X-ray irradiation also irreversibly destroys the AA-EPR-like defects. No new defects could however be detected after irradiation and/or illumination of NIPs.
To gain more detailed information about the AA-EPR-like defects, ideally, a single crystal containing them should be available. Unfortunately, it is neither possible (i) to grow CsBr:Eu^{2+} crystals which contain these defects nor (ii) to after-treat CsBr:Eu^{2+} crystals in such way that these defects are introduced. This is compatible with the fact that the AA-EPR-like defects irreversibly decay at temperatures higher than 300°C.
In practice, the best strategy is probably to (try to) measure a single needle, which is - as far we know - a single crystal. The size of the average needle is, however, too small to allow detection of the spectrum of a single needle in Q band. With the present knowledge about the PVD, it was not yet possible to grow a needle with dimensions in the mm range.
On the other hand, measuring a single needle should be possible in a high frequency setup, e.g. the J band (ν = 275 GHz) EPR/ENDOR spectrometer at the University of Leiden.

APPENDIX A

EASYSPIN BASED MATLAB PROGRAMS

A.1 THE PROGRAM EXAMPLE.M

```
clear;     % removes all variables from the workspace
orientation = [0;0];
    % defines the euler angles [phi,theta] of the magnetic field in a
    % fixed molecular frame. Here phi = theta = 0; thus the magnetic field
    % is oriented along the z orientation of the defect.

% First we define our spin system
sys.S = 1;                      % electron spin S = 1
sys.g = [2 2 2];                % isotropic g tensor
sys.lwpp = 0.1;                 % a peak-to-peak gaussian EPR linewidth of 0.1 mT
sys.D = 500;                    % D = 500 MHz
sys.Nucs = '14N';               % the system interacts with 1 nucleus (I = 1)
sys.A = 50 ;                    % isotropic HF interaction of 50 MHz
sys.Q = 10;                     % e²qQ_tilde = 10 MHz -> Q = 10/4 MHz, eta = 0
sys.lwEndor = 1;                % a FWHM ENDOR linewidth of 0.1 MHz

% Secondly we define the experimental settings for all bands
exp.nPoints= 4000;              % 4000 points will be calculated
exp.Orientations = orientation;% z orientation
exp.Temperature=5;              % temperature = 5K

% Calculating the EPR Q band spectrum : freq = 34 GHz, field up to 1.5 mT
exp.mwFreq = 34;                % defines the MW frequency
exp.Range = [1190 1240];        % defines the range of the magnetic field
subplot(2,1,1);pepper(sys,exp);
    % ES routine pepper.m calculates the EPR spectrum of system 'sys' under
    % experimental conditions 'exp'.
title('EPR spectrum at 34 Ghz');

% Calculating 3 ENDOR Q-band spectra : freq = 34 GHz, field up to 1.5 mT
% First we define the experimental settings for ENDOR
expend.ExciteWidth = 1;         % excitation width of the MW in MHz
expend.mwFreq=34;
expend.Harmonic = 1;            % results in the first derivative
expend.Orientations = [0;0];
expend.Range=[0 70];            % The RF range in Q band can go up to 150
      % MHz, but for clarity we restricted it here to 70 MHz

expend.Field = 1195;            % selects the magnetic field (in mT)
subplot(2,3,4);salt(sys,expend);
title('ENDOR spectrum at 1195 mT');
    % ES routine salt.m calculates the ENDOR spectrum of system 'sys' under
    % experimental conditions 'expend'.

expend.Field = 1197;
subplot(2,3,5);salt(sys,expend);
title('ENDOR spectrum at 1197 mT');

expend.Field = 1234;
subplot(2,3,6);salt(sys,expend);
title('ENDOR spectrum at 1234 mT');
```

A.2 THE PROGRAM FREQUENCIES.M

```
clear;
orientation = [0;0];

sys.S = 3/2 ;
sys.g = [2 2 2];
sys.lwpp = 10;
sys.D = 15000;

exp.nPoints= 4000;
exp.Orientations = orientation;
exp.Temperature=300;


% X band : frequency = 9.5 GHz, field up to 1.5 mT
subplot(2,3,1);                 % placement of the plot in a 2-by-3 arrangement
levelsplot(sys,orientation,[0 1500],9.5)
    % ES routine levelsplot.m display the level diagram of system 'sys'
    % with the magnetic field directed along 'orientation' within a range of
    % '[0 1500]' mT.
    % Since also the MW frequency is given '9.5' GHz, the resonances for
    % this frequency are also plotted. Red lines indicated allowed
    % resonances, gray ones indicate forbidden ones. If the lines are
    % terminated with dots, the relative transition intensity is above 1%.
subplot(2,3,4);
exp.mwFreq = 9.5;               % defines the MW frequency
exp.Range = [0 1500];           % defines the range of the magnetic field
pepper(sys,exp);
    % ES routine pepper.m calculates the EPR spectrum of system 'sys' under
    % experimental conditions 'exp'.

% Q band : freq = 34 GHz, field up to 1.5 mT
subplot(2,3,2);
levelsplot(sys,orientation,[0 1500],34)
subplot(2,3,5);
exp.mwFreq = 34;
exp.Range=[0 1500];
pepper(sys,exp);

% W band : freq = 95 GHz, field up to 5.5 mT
subplot(2,3,3);
levelsplot(sys,orientation,[0 5500],95)
subplot(2,3,6);
exp.mwFreq = 95;
exp.Range = [0 5500];
pepper(sys,exp);
```

A.3 THE PROGRAM SAMPLES.M

```
clear;

sys.S = 1 ;
sys.g = [2 2 2];
sys.lwpp = 10;
sys.D = 7000;

exp.nPoints= 4000;
exp.Temperature=300;
exp.Range=[500 1500];
exp.mwFreq=34;

% powder spectrum
subplot(3,1,1);
pepper(sys,exp);
    % When exp.Orientations is undefined, a full powder spectrum is calculated
text(600,1e-3,'\fontsize{15}3D powder');

% 2D powder spectrum
subplot(3,1,2);
step=0.5; % The resolution in degrees in the plane
spectrum=zeros(exp.nPoints,1)';
for i=0:step:90
    angle=i*pi/180;
        % MATLAB works with radians
    exp.Orientations=[angle;pi/2];
        % Magnetic field is oriented in all directions, varying from
        % X to Y, in a 0.1° interval. Varying the field from Y to X results
        % in the same spectra since our system is axial symmetric.
    [x,y]=pepper(sys,exp);
    spectrum=spectrum+y;
        % We sum all simulated spectra
end
for i=0:step:90
    angle=i*pi/180;
    exp.Orientations=[0;pi/2-angle];  %XZ, equivalent to YZ
    [x,y]=pepper(sys,exp);spectrum=spectrum+y;
end
for i=0:step:90
    angle=i*pi/180;
    exp.Orientations=[angle;pi/2];  %XY, equivalent to YX
    [x,y]=pepper(sys,exp);spectrum=spectrum+y;
end
plot(x,spectrum);
    % We plot the resulting spectrum.
xlabel('magnetic field [mT]');ylabel('intensity [a.u.]');
text(600,0.3,'\fontsize{15}2D powder');

% Single crystal spectrum
subplot(3,1,3);
exp.Orientations=[0 pi/2 0;pi/2 pi/2 0];
    % The single crystal spectrum consists of contributions with the
    % magnetic field along resp. x, y and z.
pepper(sys,exp);
text(600,1e-3,'\fontsize{15}single crystal');
```

A.4 THE PROGRAM ANGVAR.M

```
clear;

sys.S = 1 ;
sys.g = [2 2 2];
sys.lwpp = 2;
     % A smaller peak-to-peak linewidth, in order to see more clearly the
     % angular variation
sys.D = 7000;

exp.nPoints= 4000; exp.Temperature=300; exp.mwFreq=34;

figure;hold on;

for i=0:5:90
    angle=i*pi/180;

    exp.Orientations=[angle;pi/2];
        % Magnetic field varies from X to Y, in a 5° interval. Varying the
        % field from Y to X results in the same spectra since our system is
        % axial symmetric.
    exp.Range=[800 1500];
        % This range comprises all allowed transitions attainable by our
        % electromagnet
    [x1,spectruma]=pepper(sys,exp);
    exp.Range=[500 800];
        % This range comprises all forbidden transitions.
    [x2,spectrumb]=pepper(sys,exp);
    plot(x1,70*spectruma+i,'r');
        % We plot all simulated spectra, with an offset equal to the
        % corresponding angle (in degrees).To make the picture more clear,
        % we increased the simulated spectra (by a factor 70)
    plot(x2,20*70*spectrumb+i,'r');
        % Since the forbidden transitions have a lower intensity, we had to
        % increase these spectra 20 times as much as the spectra coming
        % from the allowed transitions.
        % The spectra from the XY angular variation are plotted in red.

    exp.Orientations=[0;pi/2-angle];  %XZ, equivalent to YZ
    exp.Range=[800 1500]; % allowed transitions
    [x1,spectruma]=pepper(sys,exp);plot(x1,70*spectruma+i,'k');
    exp.Range=[500 800]; % forbidden transitions
    [x2,spectrumb]=pepper(sys,exp);plot(x2,20*70*spectrumb+i,'k');
        % The spectra from the ZX angular variation are plotted in black.

    exp.Orientations=[0;angle];  %ZX, equivalent to ZY
    exp.Range=[800 1500]; % allowed transitions
    [x1,spectruma]=pepper(sys,exp);plot(x1,70*spectruma+i,'b');
    exp.Range=[500 800]; % forbidden transitions
    [x2,spectrumb]=pepper(sys,exp);plot(x2,20*70*spectrumb+i,'b');
        % The spectra from the XY angular variation are plotted in blue.
end

xlabel('Magnetic Field [mT]'); ylabel('Angle [°]'); axis([500 1500 -5 95 ]);
a=line([800 800],[-5 95],'LineStyle','--','LineWidth',1,'Color','black');
        % We plot a vertical line at 800mT to emphasize the difference
        % between the spectra on the right (allowed transitions) and on the
        % left (forbidden transions, increased by a extra factor of 20).
text(700,92,'\fontsize{15}x 20');
text(810,92,'\fontsize{15}x 1');
```

APPENDIX B

CONVERSION TABLE FOR ENERGY UNITS

	J	eV	cm^{-1}	K	Hz	nm
J	1	$6.242\ 10^{18}$	$5.035\ 10^{22}$	$7.244\ 10^{22}$	$1.509\ 10^{33}$	$4.525\ 10^{50}$
eV	$1.602\ 10^{-19}$	1	8065	$1.1605\ 10^{4}$	$2.418\ 10^{14}$	$7.246\ 10^{31}$
cm^{-1}	$1.986\ 10^{-23}$	$1.240\ 10^{-4}$	1	1.439	$2.998\ 10^{10}$	$8.992\ 10^{27}$
K	$1.380\ 10^{-23}$	$8.617\ 10^{-5}$	$6.950\ 10^{-1}$	1	$2.084\ 10^{10}$	$6.247\ 10^{27}$
Hz	$6.626\ 10^{-34}$	$4.136\ 10^{-15}$	$3.336\ 10^{-11}$	$4.799\ 10^{-11}$	1	$2.998\ 10^{17}$
nm	$2.210\ 10^{-51}$	$1.380\ 10^{-32}$	$1.112\ 10^{-28}$	$1.601\ 10^{-28}$	$3.335\ 10^{-18}$	1

The table can be read as follows : 1 J = $6.242\ 10^{18}$eV

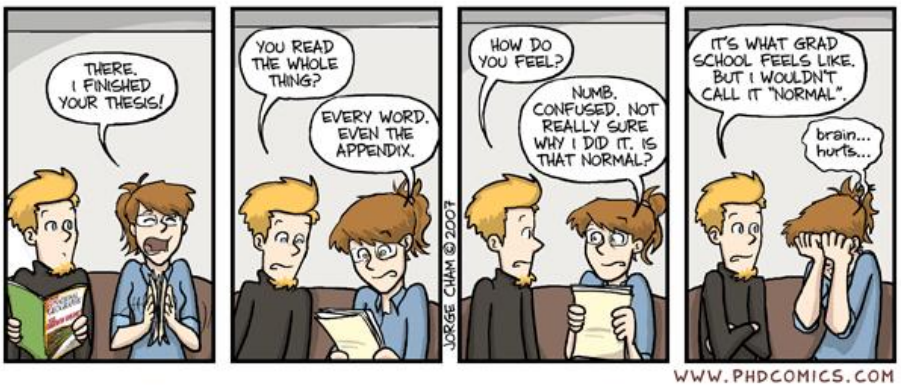
THERE. I FINISHED YOUR THESIS!
YOU READ THE WHOLE THING?
EVERY WORD. EVEN THE APPENDIX.
JORGE CHAM © 2007
HOW DO YOU FEEL?
NUMB. CONFUSED. NOT REALLY SURE WHY I DID IT. IS THAT NORMAL?
IT'S WHAT GRAD SCHOOL FEELS LIKE. BUT I WOULDN'T CALL IT "NORMAL".
brain... hurts...
WWW.PHDCOMICS.COM

BIBLIOGRAPHY

[1] J. W. Orton. *Electron Paramagnetic Resonance : An introduction to transition group ions in crystals*. Iliffe books Ltd., London, 1968.

[2] R. Kirmse and J. Stach. *ESR Spektroskopie : Anwendungen in der Chemie*. Akademie-Verlag Berlin, 1985.

[3] J. R. Pilbrow. *Transition Ion Electron Paramagnetic Resonance*. Oxford Science Publications, Clarendon Press, Oxford, 1990.

[4] A. Abragam and B. Bleaney. *Electron Paramagnetic Resonance of transition ions*. The international series of monographs on physics, Clarendon Press, Oxford, 1970.

[5] G. E. Pake and T. L. Estle. *The physical principles of Electron Paramagnetic Resonance*. W. A. Benjamin, Inc., 1973.

[6] P. Zeeman. The effect of Magnetisation on the Nature of Light Emitted by a Substance. *Nature*, 55:347, 1897.

[7] N. Bohr. On the constitution of Atoms and Molecules, Part I and II. *Philosophical Magazine*, 26:1–25,476–502, 1913.

[8] H. Haken and H. C. Wolf. *Atom- und Quantenphysik*. Springer-Verlag, 2001.

[9] W. Gerlach and O. Stern. Das magnetische Moment des Silberatoms. *Z. Phys.*, 9:353–355, 1922.

[10] G. E. Uhlenbeck and S. Goudsmit. Ersetzung der Hypothese vom unmechanischen Zwang durch eine Forderung bezüglich des inneren Verhaltens jedes einzelnen Elektrons. *Die Naturwissenschaften*, 13(47):953–954, 1925.

[11] E. Zavoisky. Relaxation of liquid solutions for perpendiculat fields. *J. Phys. U.S.S.R.*, 9:211–216, 1945.

[12] G. R. Eaton, S. S. Eaton, and K. M. Salikhov. *Foundations of modern EPR*. World Scientific, 1998.

[13] J.-M. Spaeth, J. R. Niklas, and R. H. Bartram. *Structural Analysis of Points Defects in Solids : An introduction to multiple magnetic resonance spectroscopy*. Springer-Verlag, 1992.

[14] C. Rudowicz and S. K. Misra. Spin-Hamiltonian formalisms in electron magnetic resonance and related spectroscopies. *Appl. Spectr. Rev.*, 36(1):11–63, 2001.

[15] J. H. Van Vleck. The Jahn-Teller Effect and Crystalline Stark Splitting for Clusters of the Form XY_6. *J. Chem. Phys.*, 7:72, 1939.

[16] J. H. Van Vleck. Paramagnetic relaxation times for titanium and chrome alum. *Phys. Rev.*, 57:426–447, 1940.

[17] M. H. L. Pryce. A modified perturbation procedure for a problem in paramagnetism. *Proc. Phys. Soc.*, A63(1):25–29, 1950.

[18] C. Rudowicz and H. W. F. Sung. Can the electron magnetic resonance techniques measure the crystal (ligand) field parameters? *Physica B*, 300:1–26, 2001.

[19] K. W. H. Stevens. Matrix elements and operator equivalents connected with the magnetic properties of rare earth ions. *Proc. Phys. Soc.*, 65:209–225, 1952.

[20] C. Rudowicz. Transformation relations for the conventional and normalised Stevens operators equivalents with k = 1 to 6 and -k $\leq$ q $\leq$ k. *J. Phys. C : Solid State Phys.*, 18:1415–1430, 1985.

[21] C. Rudowicz. Concept of spin Hamiltonian, forms of zero field splitting and electronic Zeeman Hamiltonians and relations between parameters used in EPR. A critical review. *Magn. Res. Review*, 13:1–89, 1987.

[22] C. Rudowicz. On the relations between the zero-field splitting parameters in the extended Stevens operator notation and the conventional ones used in EMR for orthorhombic and lower symmetry. *J. Phys. : Condens. Matter*, 12:L417–l423, 2000.

[23] C. Rudowicz and S. B. Madhu. Monoclinic and orthorhombic standardization of spin-Hamiltonian parameters for rare-earth centers in various crystals. *Physica B*, 279:302–318, 1987.

[24] C. Rudowicz and C. Y. Chung. The generalization of the extended Stevens operators to higher ranks and spins, and a systematic review of the tables of the tensor operators and their matrix elements. *J. Phys. Condens. Matter*, 16:5825–5847, 2004.

[25] S. Stoll and A. Schweiger. Easyspin, a comprehensive software package for spectral simulation and analysis in EPR. *J. Magn. Reson.*, 178(1):42–55, 2006.

[26] J. A. Weil, J. R. Bolton, and J. E. Wertz. *Electron Paramagnetic Resonance : Elementary Theory and Practical Applications*. John Wiley & Sons, Inc., 1994.

[27] Bruker Analytische Messtechnik GMBH. *ER Series User's Manual*. Bruker, 1983.

[28] P. Hackenschmied, G. Schierning, M. Batentschuk, and A. Winnacker. Precipitation-induced photostimulated luminescence in CsBr:Eu^{2+}. *J. Appl. Phys.*, 93(9):5109–5112, 2003.

[29] F. E. Mabbs and D. Collison. *Electron Paramagnetic Resonance of d Transition Metal Compounds*. Elsevier, 1992.

[30] A. D. Rae. Relationship between the experimental Hamiltonian and the point symmetry of a paramagnetic species in a crystal. *J. Chem. Phys*, 50(6):2672–2685, 1969.

[31] F. Callens. *EPR van enkele atomaire en moleculaire defecten in alkalihalogeniden, synthetische en biologische carbonaatbevattende apatieten - Aggregaatsproefschrift*. UGent, 1991.

[32] D. T. J. Hurle. *Handbook of Crystal Growth. Part 2a : Bulk Crystal Growth - Basic Techniques*. North-Holland, 1994.

[33] R. Haegele, W. Verscharen, and D. Babel. Single crystal structural data of some fluorides and cyanides $A_2^{I}B^{I}M^{III}X_6$ of elpasolite family. *Zeit. Naturforsch. B*, 30(5-6):462–464, 1975.

[34] E. Bucher, H. J. Guggenheim, K. Anders, G. W. Hulle, and A. S. Cooper. Magnetic properties of some cubic rare-earth elpasolite hexafluorides. *Phys. Rev. B*, 10:2945–2951, 1974.

[35] H. N. Bordallo, R.W. Henning, L. P. Sosman, R. J. M. da Fonseca, A. D. Tavares Jr., K. M. Hanif, and G. F. Strouse. Structural and vibrational

study of chromium doped elpasolite crystals Cs_2NaAlF_6. *J. Chem. Phys.*, 115(9):4300–4305, 2001.

[36] H. N. Bordallo, X. Wang, K. M. Hanif, R. J. M. Strouse, G. F. da Fonseca, L. P. Sosman, and A. D. Tavares Jr. Structure determination and a vibrational study for the hexagonal elpasolite Cs_2NaGaF_6:Cr^{3+}. *J. Chem. Phys.*, 115(9):4300–4305, 2001.

[37] M. Ahrens, G. Scholz, and E. Kemnitz. Synthesis and crystal structure of $RbKLiAlF_6$ - the first Al-elpasolite with three different alkali metals. *Z. Anorg. Allg. Chem.*, 634:2978–2981, 1998.

[38] P. Greenough and A. G. Paulusz. 2eg 4a2g phosphorescence spectrum of the Cr^{3+} ion in K_2NaAlF_6. *J. Chem. Phys.*, 70:1967, 1979.

[39] L. P. Sosman, A. D. Tavares Jr., R. J. M. da Fonseca, T. Abritta, and N. M. Khaidukov. Study of optical properties of Cr^{3+} ions in Cs_2NaAlF_6 single crystals. *Solid State Commun.*, 114:661–665, 2000.

[40] R. J. M. da Fonseca, A. D. Tavares Jr., P. S. Silva, T. Abritta, and N. M. Khaidukov. Investigation of Cr^{3+} ions in Cs_2NaGaF_6 single crystals by optical spectroscopy. *Solid State Commun.*, 110:519–524, 1999.

[41] T. Pawlik and J.-M. Spaeth. Investigation of the x-ray storage phosphors Cs_2NaYF_6:Pr^{3+} or Ce^{3+}. *J. Appl. Phys.*, 82(9):4236–4240, 1997.

[42] T. Pawlik, J.-M. Spaeth, M. Otte, and H. Overhof. ENDOR investigations of rare earth and transition metal ions in the cubic elpasolite Cs_2NaYF_6. *Rad. Eff. Def. Solids*, 135:49–54, 1995.

[43] T. Pawlik and J.-M. Spaeth. Investigation of radiation-induced defects in Cs_2NaYF_6. *phys. stat. sol. (b)*, 203:43–52, 1997.

[44] E. Fargin, B. Lestienne, and J. M. Dance. ESR of Cr^{3+} in the 12r hexagonal perovskite Cs_2NaAlF_6. *Solid State Commun.*, 75(10):769–771, 1990.

[45] J. L. Boldu, R. J. Gleason, and E. Muñoz. Single crystal EPR study of trivalent gadolinium in $Cs_2NaInCl_6$ in the 6-300 K interval. *Revista Mexicana de fisica*, 51(2):199–202, 2005.

[46] H. Vrielinck, F. Loncke, F. Callens, P. Matthys, and N. M. Khaidukov. Identification of Cr3+ centers in Cs_2NaAlF_6 and Cs_2NaGaF_6 crystals by EPR and ENDOR paramagnetic resonance techniques. *Phys. Rev. B*, 70:144111, 2004.

[47] F. Loncke. *Magnetische resonantiestudie van Cr^{3+} centra in hexagonale en kubische elpasolieten - Master Thesis*. UGent, 2003.

[48] H. De Cooman. *Magnetische-resonantiestudie van zeldzame-aardionen in kubische elpasolieten - Master Thesis*. UGent, 2005.

[49] H. A. Mares, A. B. Eitlerova, M. Nikl, N. Solovieva, K. Nitsch, M. Kucera, M. Kubova, V. Gorbenko, and Y. Zorenko. Scintillation and optical properties of YAG : Ce films grown by liquid phase epitaxy. *2007*, 42(4-5):533–536, Radiat. Meas.

[50] M. Luo, N. Y. Garces, N. C. Giles, U. N. Roy, Y. Cui, and A. Burger. Optical and electron paramagnetic resonance spectroscopies of diffusion-doped Co2+: ZnSe. *2006*, 99(7):073709, J. Appl. Phys.

[51] M. H. Cao, J. Jiang, H.X. Liu, and J. Yuan. The nature of Fe impurity phase in ferromagnetic CaB6. *Physica B*, 364(1-4):150–156, 2005.

[52] F. Loncke, H. De Cooman, N. M. Khaidukov, H. Vrielinck, E. Goovaerts, P. Matthys, and F. Callens. EPR and ENDOR analysis of Fe^{3+} impurity centres in fluoroelpasolite lattices. *Phys. Chem. Chem. Phys.*, 9:5320–5329, 2007.

[53] D. Babel, R. Haegele, G. Pausewang, and F. Wall. Cubic and hexagonal elpasolites $A_2^{I}B^{I}M^{III}X_6$. *Mater. Res. Bull.*, 8:1371, 1973.

[54] J. A. Aramburu, J. I. Paredes, M. T. Barriuso, and M. Moreno. Local relaxation around Fe^{3+} in fluorides : Influence on electronic properties. *Phys. Rev. B*, 61(10):6525–6534, 2000.

[55] J. Marcazzo, M. Santiago, E. Caselli, N. Nariyama, and N. M. Khaidukov. Effect of Pr^{3+} concentration on thermoluminescene from $K_2Y_{1-x}Pr_xF_5$. *Opt. Mater.*, 26:65–70, 2004.

[56] L. O. Faria, D. Lo, H. W. Kui, N. M. Khaidukov, and M. S. Nogueira. Thermoluminescence response of K_2YF_5:Tb^{3+} crystals to photon radiation fields. *Radiat. Prot. Dosim.*, 112(3):435–438, 2004.

[57] H. W. Kui, D. Lo, N. M. Khaidukov, and V. N. Makhov. Thermoluminescence of double potassium yttrium fluorides singly doped with Ce^{3+}, Tb^{3+}, Dy^{3+} and Tm^{3+}. *J. Lumin.*, 117:29–38, 2006.

[58] **Y. A. Kharitonov, Y. A. Gorbunov, and B. A. Maksimov. The crystal-structure of potassium yttrium fluoride K_2YF_5. *Kristallografiya*, 28(5):1031–1032, 1983.**

[59] **R. E. Peale, H. Weidner, F. G. Anderson, and N. M. Khaidukov. Spectroscopy of Er^{3+} in K_2YF_5. *Trends in Optics and Photonics, Advance solid state lasers*, 10:262–466, 1997.**

[60] **K. Güde and C. Hebecker. Ueber die Darstellung und röntgenographische Untersuchung von Verbindungen des Formeltyps K_2LnF_5. *Z. Naturforsch. B*, 40:864–867, 1985.**

[61] **H. M. Lu and J. R. Hardy. Simulations of phase transitions in Rb_2ZnCl_4. *Phys. Rev. B*, 45(14):7609–7620, 1992.**

[62] **W. H. Baur and M. Lerch. On deciding between space groups Pnam and $Pna2_1$ for the crystal structure of Zr_3N_4. *Z. Anorg. Allg. Chem.*, 622:1729–1730, 1996.**

[63] **D. Wang, Y. Min, S. Xia, V. N. Makhov, N. M. Khaidukov, and J. C. Krupa. Upconversion fluorescence of Nd^{3+} ions in K_2YF_5 single crystal. *J. Alloys Compd.*, 361:294–298, 2003.**

[64] **Y. Li, M. Yin, N. Dong, N. M. Makhov, N. M. Khaidukov, and J. C. Krupa. Spectra analysis of Tm^{3+} in K_2YF_5. *J. Phys. Chem. Solids*, 65:1059–1063, 2004.**

[65] **F. Loncke, D. Zverev, H. Vrielinck, N. M. Khaidukov, P. Matthys, and F. Callens. K_2YF_5 crystal symmetry determined by using rare-earth ions as paramagnetic probes. *Phys. Rev. B*, 75:144427, 2007.**

[66] **S. K. Misra and C. Rudowicz. Effect of monoclinic symmetry on the EPR spectra of Gd^{3+}-doped hydrated single crystals of rare-earth trichlorides. *phys. stat. sol. (b)*, 147:677–684, 1988.**

[67] **L. Pidol, O. Guillot-Noël, A. Kahn-Harari, B. Viana, D. Pelenc, and D. Gourier. EPR study of Ce^{3+} ions in lutetium silicate scintillators $Lu_2Si_2O_7$ and Lu_2SiO_5. *J. Phys. Chem. Sol.*, 67:643–650, 2006.**

[68] **D. Zverev, H. Vrielinck, F. Callens, P. Matthys, S. Van Doorslaer, and N. M. Khaidukov. EPR, ENDOR and HYSCORE study of X-ray induced centres in K_2YF_5 thermoluminescent phosphors. *Phys. Chem. Chem. Phys.*, 10:1789–1798, 2008.**

[69] D. Zverev, H. Vrielinck, P. F. Smet, D. Poelman, and F. Callens. Structure of F_2^- centers in K_2YF_5 and their relation to thermoluminescence below room temperature. *Phys. Rev. B*, 79(22):224110, 2009.

[70] W. C. Röntgen. On a new kind of Rays. *Science*, 59:227–231, 1896.

[71] E. B. Frost. Experiments on the X-Rays. *Science*, 59:235–236, 1896.

[72] M. I. Pupin. Röntgen Rays. *Science*, 59:231–235, 1896.

[73] T. Tani. *Photographic sensitivity - Theory and Mechanisms*. Oxford University Press, 1995.

[74] M. Sonoda, M. Takano, M. S. Miyahara, and H. Kato. Computed Radiography utilizing scanning laser stimulated luminescence. *Radiology*, 148:833–838, 1983.

[75] IMV. X-Ray/CR/DR Overview. `http://www.imvinfo.com/index.aspx?sec=xray&sub=dis&itemid=200095`, September 2006.

[76] Y. Amemiya and J. Miyahara. Imaging plate illuminates many fields. *Nature*, 336:89–90, 1988.

[77] M. J. Yaffe and J. A. Rowlands. X-ray detectors for digital radiography. *Phys. Med. Biol.*, 42:1–39, 1997.

[78] H. von Seggern. Photostimulable X-ray storage phosphors : a review of present understanding. *Braz. J. Phys.*, 29(2):254–268, 1999.

[79] H. von Seggern, T. Voigt, W. Knüpfer, and G. Lange. Physical model of photostimulated luminescence of X-ray irradiated BaFBr:Eu^{2+}. *J. Appl. Phys.*, 64(3):1405–1412, 1988.

[80] S. Schweizer. Physics and current understanding of X-ray storage phosphors. *phys. stat. sol. (a)*, 2:335–393, 2001.

[81] D. Nicollin and H. Bill. Experimental contribution to the study of S-state ions in single crystals. *J. Phys. C: Solid State Phys.*, 11:4803–4813, 1978.

[82] A. A. Shalaev and E. A. Radzhabov. Single crystal growth of BaFBr:Eu storage phosphor with alkali impurities. *J. Crystal Growth*, 275:775–777, 2005.

[83] T. Hangleiter, F. K. Koschnick, J.-M. Spaeth, R. H. D. Nuttall, and R. S. Eachus. Temperature dependence of the photostimulated luminescence of x-irradiated BaFBr:Eu^{2+}. *J. Phys.: Condens. Matter*, 2:6837–6846, 1990.

[84] T. Hangleiter, F. K. Koschnick, J.-M. Spaeth, and R. S. Eachus. Photostimulated emission of x-irradiated BaFBr:Eu^{2+}. *Radiat. Eff. Defects Solids*, 119:615–620, 1991.

[85] R. S. Eachus, W. G. McDugle, R. H. D Nuttall, M. T. Olm, F. K. Koschnick, Th. Hangleiter, and J.-M.. Spaeth. Radiation-produced electron and hole centers in oxygen-containing BaFBr : I. EPR and ODEPR studies. *J. Phys.: Condens. Matter*, 3:9327–9338, 1991.

[86] R. S. Eachus, R. H. D Nuttall, M. T. Olm, W. G. McDugle, F. K. Koschnick, Th. Hangleiter, and J.-M.. Spaeth. Oxygen defects in BaFBr and BaFCl. *Phys. Rev. B*, 52(6):3941–3950, 1995.

[87] S. Schweizer and J.-M. Spaeth. New oxygen hole centres in the x-ray storage phosphor BaFBr. *J. Phys.: Condens. Matter*, 11:1723–1733, 1999.

[88] H. H. Rüter, H. von Seggern, R. Reininger, and V. Saile. Creation of photostimulable centres in BaFBr:Eu^{2+} single crystals by vacuum-ultraviolet radiation. *Phys. Rev. Lett.*, 65(19):2438–2441, 1990.

[89] F. K. Koschnick, J.-M. Spaeth, and R. S. Eachus. Study of spatial correlations between radiation-induced defects and the activator Eu^{2+} in the X-ray storage phosphor BaFBr:Eu^{2+} with optical detection of electron paramagnetic resonance. *J. Phys.: Condens. Matter*, 4:8192–8932, 1992.

[90] F. K. Koschnick, Th. Hangleiter, K. S. Song, and J.-M. Spaeth. Optically detected magnetic resonance study of an oxygen-vacancy complex in BaFBr. *J. Phys.: Condens. Matter*, 7:6925–6937, 1995.

[91] F. K. Koschnick, J.-M. Spaeth, and R. S. Eachus. The influence of oxide impurity on the generation by x-irradiation of F centers in BaFBr. *J. Phys.: Condens. Matter*, 4:3015–3029, 1992.

[92] S. Schweizer, J.-M. Spaeth, and T. J. Bastow. Generation of F centres and hole centres in the nonstoichiometric x-ray storage phosphor BaFBr. *J. Phys.: Condens. Matter*, 10:9111–9122, 1998.

[93] R. U. Bauer, J. R. Niklas, and J.-M. Spaeth. 2 types of F-centers in alkaline-earth fluoro-halides.1. superhyperfine interactions and electronic structure. *phys. stat. sol. (b)*, 118(2):557–566, 1983.

[94] F. K. Koschnick, Th. Hangleiter, J.-M. Spaeth, and R. S. Eachus. Structure and optical properties of two types of F centers in BaFBr. *J. Phys.: Condens. Matter*, 4(11):3001–3013, 1992.

[95] K. Takahashi, J. Miyahara, and Y. Shibahara. Photostimulated luminescence (PSL) and color centers in BaFX:Eu^{2+} (X = Cl, Br, I) phosphors. *J. Electrochem. Soc.*, 132(6):1492–1494, 1985.

[96] K. Takahashi, K. Kohda, and J. Miyahara. Mechanisms of photostimulated luminescence in BaFX:Eu^{2+} (X = Cl, Br) phosphors. *J. Lumin.*, 31-32:266–268, 1984.

[97] H. von Seggern, T. Voigt, W. Knüpfer, and G. Lange. Physical model of photostimulated luminescence of x-ray irradiated BaFBr:Eu^{2+}. *J. Appl. Phys.*, 64(3):1405–1412, 1988.

[98] J.-M. Spaeth, F. K. Koschnick, R. S. Eachus, W. G. McDugle, and R. H. D. Nuttall. Investigation of the storage phosphor BaFBr:Eu by multiple resonance techniques. *Nucl. tracks rad. meas.*, 21(1):73–79, 1992.

[99] M. Thoms, H. von Seggern, and A. Winnacker. Spatial correlation and photostimulability of defect centers in the x-ray-storage phosphor BaFBr:Eu^{2+}. *Phys. Rev. B*, 44(17):9240–9246, 1991.

[100] F. K. Koschnick, J.-M. Spaeth, R. S. Eachus, W. G. McDugle, and R. H. D. Nuttall. Experimental evidence for the aggregation of photostimulable centers in BaFBr:Eu^{2+} single crystals by cross relaxation spectroscopy. *Phys. Rev. Lett.*, 67(25):3571–3574, 1991.

[101] S. Assmann, S. Schweizer, and J.-M. Spaeth. ENDOR investigation of the Eu^{2+} activator in the X-ray storage phosphor BaFBr. *phys. stat. sol. (b)*, 212:325–334, 1999.

[102] Rowlands J. A. Topical review : the physics of computed radiography. *Phys. Med. Biol.*, 47:R123–R166, 2002.

[103] H. von Seggern. X-ray imaging with photostimulable phosphors. *Nucl. Instr. and Meth. A*, 322:467–471, 1992.

[104] A. R. Cowen, A. G. Davies, and S. M. Kengyelics. Advances in computed radiography systems and their physical imaging characteristics. *Clinical Radiology*, 62:1132–1141, 2007.

[105] H. Li, P. Hackenschmied, E. Epelbaum, and M. Batentschuk. Imaging performance of polycrystalline BaFBr:Eu^{2+} storage phosphor plates. *Mat. Sci. Eng. B*, 94:32–39, 2002.

[106] M. Secu, L. Matei, T. Serban, E. Apostol, Gh. Aldica, and C. Silion. Preparation and optical properties of BaFCl:Eu^{2+} X-ray storage phosphor. *Opt. Mater.*, 15:115–123, 2000.

[107] V. R. Kumar, K. V. Narasimhulu, N. O. Gopal, J. L. Rao, and R. P. S. Chakradhar. EPR and optical investigations of Eu^{2+}-doped BaFCl phosphor. *Physica B*, 348:446–453, 2004.

[108] Y. Nakano, T. Gido, S. Honda, A. Maizawa, H. Wakamatsu, and T. Yanagita. Improved computed radiography image quality from a BaFI:Eu photostimulable phosphor plate. *Med. Phys.*, 29(4):592–597, 2002.

[109] M. Schlapp, E. Bulur, and H. von Seggern. Photo-stimulated luminescence of calcium co-doped BaFBr:Eu^{2+} x-ray storage phosphors. *J. Phys. D: Appl. Phys.*, 36:103–108, 2003.

[110] C. Dietze, Th. Hangleiter, P. Willems, P. Leblans, L. Struye, and J.-M. Spaeth. Photostimulation redshift for nonstoichiometric $Ba_{1-x}Sr_xFBr:Eu^{2+}$. *J. Appl. Phys.*, 80(2):1074–1078, 1996.

[111] S. Schweizer, P. Willems, P. Leblans, L. Struye, and J.-M. Spaeth. Electron traps in Ca^{2+}- or Sr^{2+}-doped BaFBr:Eu^{2+} x-ray storage phosphors. *J. Appl. Phys.*, 79(8):4157–4165, 1996.

[112] K. Takahashi. Progress in science and technology on photostimulable BaFX:Eu^{2+} (X = Cl,Br,I) and imaging plates. *J. Lumin.*, 100:307–315, 2002.

[113] J.-M. Spaeth. Recent developments in X-ray storage phosphor materials. *Radiat. Meas.*, 33:527–532, 2001.

[114] S. Schweizer and J. A. Johnson. Fluorozirconate-based glass ceramic X-ray detectors for digital radiography. *Radiat. Meas.*, 42:632–637, 2007.

[115] X. Meng, Y. Wang, and D He. Luminescence studies of MBrCl:Eu^{2+} (M = Ca, Sr, Ba). *J. Rare Earths*, 27(2):316–319, 2009.

[116] P. Leblans, L. Struye, and H. Gebele. A new detector for digital radiography : the best of two worlds. *Physica Medica*, XV(4):301–304, 1999.

[117] P. Leblans, L. Struye, and P. Willems. New needle-crystalline CR detector. *J. Dig. Imag.*, 13:117–120, 2000.

[118] P. Leblans, P. Willems, and L. B. Alaerts. New needle-crystalline detector for X-ray computer radiography (CR). *J. Nondestr. Testing*, 7(12), 2002.

[119] H. Nanto, A. Nishimura, M. Kuroda, Y. Takei, Y. Nakano, T. Shoji, T. Yanagita, and S. Kasai. X-ray imaging plate using CsBr:Eu phosphors for computed radiography. *Nucl. Instr. and Meth. A*, 580:278–281, 2007.

[120] N. Kurata, N. Kubota, Y. Takei, and H. Nanto. Eu-doped CsBr phosphor as a new optically-stimulable phosphor material for medical X-ray imaging sensor. *Radiat. Prot. Dosim.*, 119(1-4):398–401, 2006.

[121] Q. H. F. Vrehen and J. Volger. Paramagnetic resonance of divalent Europium in Lead Chloride. *Physica*, 31(6):845–&, 1965.

[122] R. Nakata, K. Kawano, M. Sumita, and E. Higuchi. ESR study of Europium ions in hydrolyzed CsF_2:Eu crystals. *J. Phys. Chem. Sol.*, 40(12):955–959, 1979.

[123] K. Kaiya, N. Takahashi, T. Nakamura, T. Matsuzawa, G. M. Smith, and P. C. Riedi. EPR studies of europium(II)-doped strontium aluminate phosphors. *J. Lumin.*, 87-89:1073–1075, 2000.

[124] T. Nakamura, T. Matsuzawa, C. C. Rowlands, V. Beltran-Lopez, G. M. Smith, and P. C. Riedi. EPR investigations on europium(II)-doped aluminates. *J. Chem. Soc., Faraday Trans.*, 94:3009–3012, 1998.

[125] J. L. Boldu, R. J. Gleason, C. Quintanar, and E. P. Muñoz. Europium paramagnetic resonance studies Eu^{2+} of in Cs_2NaYCl_6 crystals. *J. Phys. Chem. Solids*, 57(3):267–270, 1996.

[126] M. A. Mondragon, R. J. Gleason, E. P. Muñoz, and J. L. Boldu. Trigonal sites of Eu^{2+} in single crystals of Cs_2NaYCl_6. *J. Chem. Phys.*, 89(12):7189–7192, 1988.

[127] S. S. Shinde, T. K. Gundu Rao, S. S. Sanaye, and B. C. Bhatt. TL and ESR characteristics of $BaSO_4$:Eu co-doped with Na/P : influence of method of preparation. *Radiat. Prot. Dosim.*, 84(1-4):215–218, 1999.

[128] J. O. Rubio, H. S. Murrietta, E. P. Muñoz, J. O. Boldu, and G. S. Aguilar. Electron paramagnetic resonance of Eu^{2+} in the alkali iodides. *J. Chem. Phys.*, 63(10):4222–4229, 1975.

[129] J. O. Rubio. Doubly-valent rare-earth ions in halide crystals. *J. Phys. Chem. Solids*, 52(1):101–174, 1991.

[130] J. O. Rubio, E. P. Muñoz, and G. S. Aguilar. Electron paramagnetic resonance of Eu^{2+} in orthorhombic sites of RbCl single crystals. *J. Chem. Phys.*, 61(12):5273–5274, 1974.

[131] G. S. Aguilar, E. P. Muñoz, H. S. Murrietta, L. A. Boatnerr, and R.W. Reynolds. EPR investigations of Eu^{2+} in orthorhombic sites of NaCl. *J. Chem. Phys.*, 60(12):4665–4669, 1974.

[132] T. Iwasaki, Y. Nakamura, and H. Wakabayashi. Electron Spin Resonance study on the ^{151}Eu-Vacancy complexes in Alkali Fluorides. *J. Phys. Soc. Japan*, 50(2):563–568, 1981.

[133] R. Nakata, M. Suzuki, K. Kawano, and M. Sumita. ESR study of new Eu^{2+} complex in additively colored KCl:Eu crystals. *J. Phys. Soc. Japan*, 41(6):1996–2000, 1976.

[134] G. S. Aguilar, H. S. Murrietta, J. O. Rubio, and E. P. Muñoz. Studies by electron paramagnetic resonance of K- and Na-bromides doped with Eu^{2+}. *J. Chem. Phys.*, 62(4):1197–1200, 1975.

[135] J. O. Boldu, E. P. Muñoz, W. K. Cory, and J. O. Rubio. Divalent europium in the alkali fluorides. *J. Chem. Phys.*, 67(5):2391–2393, 1977.

[136] A. F. Muñoz, E. B. Cabrera, H. R. Rivereros, M Patron, and J. O. Rubio. Aggregation kinetics of Eu^{2+}-cation vacancy dipoles in the alkali halides : dimer versus trimer formation. *Phys. Rev. B*, 31(12):8196–8205, 1985.

[137] V. P. Savelev, V. P. Avdonin, L. D. Dugarova, A. P. Nedashkovskii, and B. T. Plachenov. Aggregation of Eu^{2+}-V^{-}_{C} in europium-activated alkali halide crystals. *Sov. Phys. Solid State*, 16(4):700–702, 1974.

[138] S. Schweizer, U. Rogulis, S. Assmann, and J.-M. Spaeth. RbBr and CsBr doped with Eu^{2+} as new competitive X-ray storage phosphors. *Radiat. Meas.*, 33:486–486, 2001.

[139] F. Boettcher and J.-M. Spaeth. ENDOR investigation of Cu^{2+} centres in NH_4Cl I. Experimental results. *phys. stat. sol. (b)*, 61:465–473, 1974.

[140] T. Iri and G. Kuwabara. Paramagnetic resonance of Mn^{2+} in CsBr. *J. Phys. Soc. Jap.*, 23(3):536–539, 1967.

[141] S.-Y. Chou and J.-T. Yu. Electron paramagnetic resonance of the thermally-produced Mn^{2+} in single crystals of NH_4Cl doped with MnO_4^{-}. *Chin. J. Phys.*, 29(3):253–262, 1991.

[142] F. Boettcher and J.-M. Spaeth. ENDOR investigation of Cu^{2+} centres in NH_4Cl II. Theoretical interpretation. *phys. stat. sol. (b)*, 62:65–72, 1974.

[143] K. Watanabe and A. Hidetaro. Temperature dependence of an $NH_4Cl:Cu^{2+}$ system studied by EPR. *J. Phys. Soc. Jap.*, 38(3):755–765, 1975.

[144] W. Sano and E. Di Mauro. EPR of Cu^{2+} in NH_4Br : ortorhombic centre. *J. Phys. Chem. Solids*, 58(3):391–392, 1997.

[145] F. S. Stibbe and N. J. Trappeniers. ESR of Cr^{3+} in CsCl and NH_4Cl single crystals. *Physica B*, 95:81–92, 1978.

[146] T. Behner and G. Lehmann. EPR of Fe^{3+} in CsCl and NH_4Cl. *J. Phys. Chem. Solids*, 48(6):555–558, 1987.

[147] T. Pawlik, V. Dierolf, and J.-M. Spaeth. An electron-nuclear double-resonance study of the F centre in CsBr. *J. Phys.:Condens. Matter*, 9:1857–1862, 1997.

[148] F. Hughes and J. G. Allard. Electron Paramagnetic Resonance in irradiated CsCl. *Phys. Rev.*, 125(1):173–176, 1962.

[149] B. Schmitt, M. Fuchs, E. Hell, W. Knüpfer, and A. Hackenschmied, P. Winnacker. Structured alkali halides for medical applications. *Nucl. Instr. and Meth. B*, 191:800–804, 2002.

[150] W. B. Fowler. *Physics of Color Centres*. Academic Press, New York, London, 1968.

[151] P. Hackenschmied, G. Zeitler, M. Batentschuk, A. Winnacker, B. Schmitt, M. Fuchs, E. Hell, and W. Knüpfer. Storage performance of X-ray irradiated CsBr. *Nucl. Instr. and Meth. in Phys. Res. B*, 191:163–167, 2002.

[152] M. Nikl, K. Nitsch, K. Polak, G. P. Pazzi, P. Fabeni, D. S. Citrin, and M. Gurioli. Optical properties of the Pb^{2+} -based aggregated phase in a CsCl host crystal: Quantum-confinement effects. *Phys. Rev. B*, 51(8):5192–5199, 1995.

[153] S. Hesse, J. Zimmerman, H. von Seggern, H. Ehrenberg, Fuess H., C. Fasel, and R. Riedel. $CsBrEu_3$: crystal structure and its role in the photostimulation of $CsBr:Eu^{2+}$. *J. Appl. Phys.*, 100:083506, 2006.

[154] S. Hesse, J. Zimmerman, H. von Seggern, H. Ehrenberg, and Fuess H. The role of segregations and oxygen doping in the photostimulation mechanism of $CsBr:Eu^{2+}$. *Radiat. Meas.*, 42(4-5):638–643, 2007.

[155] G. Schierning, M. Batentschuk, A. Osvet, A. Winnacker, L. Struye, J.-P. Tahon, and P. Leblans. Correlation of the dielectric properties and the PSL-sensitivity in CsBr:Eu plates. *Radiat. Meas.*, 42:657–660, 2007.

[156] G. A. Appleby, J. Zimmerman, S. Hesse, O. Karg, and H. von Seggern. Sensitization of the photostimulable X-ray storage-phosphor CsBr:Eu^{2+} following room-temperature hydration. *J. Appl. Phys.*, 105:073511, 2009.

[157] G. A. Appleby, J. Zimmerman, S. Hesse, O. Karg, and H. von Seggern. Sensitization of radiation hardening of the photostimulable X-ray storage-phosphor CsBr:Eu^{2+} . *J. Mater. Sci.: Mater Electron*, 20:S54–S58, 2009.

[158] J. Meng, L. Zhao, J. Wu, and L. Song. The role of hydrogen- and hydroxyl-doping in CsBr:Eu^{2+}. *J. Lumin.*, 129:850–853, 2009.

[159] J. Zimmerman, S. Hesse, H. von Seggern, M. Fuchs, and W. Knüpfer. Radiation hardness of CsBr:Eu^{2+}. *J. Lumin.*, 114:24–30, 2005.

[160] E. Vano, J. M. Fernandez, J. I. Ten, C. Prieto, L. Gonzalez, R. Rodriguez, and H. de Las Heras. Transition from Screen-Film to Digital Radiography: Evolution of Patient Radiation Doses at Projection Radiography. *Radiology*, 243:461–466, 2007.

[161] J. Zimmerman, S. Hesse, H. von Seggern, M. Fuchs, and W. Knüpfer. Radiation hardness of CsBr:Eu^{2+}. *J. Appl. Phys.*, 101:113711, 2007.

[162] M. Batentschuk, S. Neudert, M. Weidner, A. Osvet, L. Struye, J.-P. Tahon, and P. Leblans. Radiation stability of CsBr:Eu needle image plates. *J. Appl. Phys.*, Accepted for publication, 2009.

[163] M. Weidner, M. Batentschuk, F. Meister, A. Osvet, A. Winnacker, J.-P. Tahon, and P. Leblans. Luminescence spectroscopy of Eu^{2+} in CsBr:Eu needle image plates. *Radiat. Meas.*, 42:661–664, 2007.

[164] M. Weidner. *Einfluss der Temperbedingungen auf Lumineszenz- und Speicherzentren in CsBr:Eu^{2+} Nadelbildplatten - PhD Thesis*. Hut Verlag, 2009.

[165] T. Komiyama, M. Murofushi, and K. Takahashi. Radiation image storage panel and process for producing the same. *US PATENT*, page 2007/0075282 A1, 2006.

[166] D. M. Wang and E. de Boer. Electron paramagnetic resonance of $Cr(CN)_6^{3-}$ in NaCl: Evidence for motion of the associated cation vacancies. *Phys. Rev. B*, 39(16):11272–11279, 1989.

[167] D. Wang and G. R. Hanson. Extreme rhombic distortion in electron paramgnetic resonance and a superposition model account. *J. Magn. Reson.,Ser. A*, 118:1–6, 1996.

[168] H. De Cooman. *A combined EMR and DFT study of radiation-induced defects in sucrose and glucose 1-phosphate - PhD Thesis*. UGent, 2009.

[169] Agfa HealtCare NV. *private communication*. 2007.

[170] CRC. *Handbook of Chemistry and Physics*. The Chemical Rubber Co., Ohio, 1970.

[171] CaRIne Crystallography 3.1. The Crystallographic software for research and teaching, 1998.

[172] Martina Weidner. *private communication*. 2008.

[173] M. G. Brik, C. N. Avram, and N. M. Avram. Calculations of spin Hamiltonian parameters and analysis of trigonal distortions in $LiSr(Al,Ga)F_6 : Cr^{3+}$ crystals. *Physica B - Condens. Mat.*, 384(1-2):78–81, 2006.

[174] M. G. Brik and N. M. Avram. Analysis of trigonal distortions in $Cs_2Na(Al,Ga)F_6 : Cr^{3+}$ using experimental EPR data. *J. Optoelec. Adv. Mater.*, 8(1):102–106, 2006.